INSTITUT NATIONAL POLYTECHNIQUE DE GRENOBLE

N° attribué par la bibliothèque |__|__|__|__|__|__|__|__|__|__|

THESE EN COTUTELLE INTERNATIONALE

pour obtenir le grade de

DOCTEUR DE L'INP Grenoble
et
de l'Université de Vilnius

Spécialité : « Energétique Physique »

préparée au laboratoire des Matériaux et du Génie Physique
dans le cadre de **l'Ecole Doctorale** « Mécanique et Energétique »
et à la Faculté de Chimie de l'Université de Vilnius

présentée et soutenue publiquement

par

Ausrine Bartasyte

le 18 Décembre 2007

Effet des contraintes et transition de phase dans des couches minces de $PbTiO_3$ obtenues par MOCVD

Stress effects and phase transitions in $PbTiO_3$ thin films deposited by MOCVD

DIRECTEUR DE THESE: François Weiss
CO-DIRECTEUR DE THESE: Adulfas Abrutis

JURY

M. Ibanez Alain,	**Président**
M. Karkut Michael,	**Rapporteur**
Mme. Guilloux-Viry Maryline,	**Rapporteur**
M. Weiss François,	**Directeur de thèse**
M. Abrutis Adulfas,	**Co-encadrant**
M. Banys Juras,	**Examinateur**
Mme. Chaix-Pluchery Odette,	**Examinateur**
M. Santiso José	**Invité**

Remerciements – Padėka - Aknowledgments

J’exprime tout d’abord mes sincères remerciements aux membres du jury pour l’honneur qu’ils m’ont fait de juger mon travail de doctorat : à Madame Maryline Guilloux-Viry (Université de Rennes 1) et à Monsieur Michael Karkut (Université de Picardie Jules Verne) pour avoir accepté d’être rapporteurs de mon manuscrit ; à Monsieur Alain Ibanez (Institut Néel ; CNRS) pour avoir présidé ma soutenance ; à Madame Odette Chaix-Puchery (INPG, CNRS) et à Messieurs José Santiso (ICMAB , Spain)et Juras Banys (Université de Vilnius, Lituanie) pour avoir eu la bienveillance de s’intéresser à mon travail et d’assister à ma soutenance. [Nuoširdžiausia padėka Prof. Jurui Baniui už sutikimą atvykti į Grenoblį ir būti disertacijos gynimo komisijos nariu.]

Je tiens particulièrement à remercier François Weiss, le directeur de cette thèse, pour la liberté, sa confiance et son soutien pendant ces années. Je garde un souvenir précieux de ses encouragements et du financement qui m’a permis de réaliser mes idées même dans les moments difficiles.

Iš visos širdies noriu padėkoti mano disertacijos vadovui Prof. Adulfui Abručiui už MOCVD pagrindus, įgytą praktiką ir suteiktą galimybę pažinti LMGP laboratoriją bei Prancūziją.

Ce travail de thèse a été effectué au sein du Laboratoire des Matériaux et du Génie Physique (LMGP) et Faculté de Chimie de l’Université de Vilnius. Je remercie chaleureusement Bernard Chenevier pour m’avoir accueilli dans son laboratoire.

Un immense merci revient bien sûr à Carmen Jiménez (LMGP) qui m’a conduit et guidé pendant ma thèse. Je te suis reconnaissante pour ton aide, ton enthousiasme et ta disponibilité.

Je remercie tout autant Odette Chaix-Pluchery pour ta disponibilité, tes critiques, ta précision et … ta patience tout au long de ce travail. Plus que les autres, tu auras été exposée à mon *stress doctoral* et j’espère que tu ne m’en tiendras pas rigueur !

Ce travail n’aurait pas pu se réaliser sans l’aide précieuse de Jens Kreisel qui m’a transmis une partie de ses connaissances et son enthousiasme en spectroscopie Raman et en transitions de phase. Merci pour m’avoir invité et accompagné dans les *aventures du monde des phonons*.

Je tiens à remercier Samuel Margueron, qui m’a fait profiter de sa compétence scientifique en spectroscopie Raman, c’est sans aucun doute à lui que je dois ma petite faiblesse pour *les contrainte et les quasimodes.* Merci pour ton sacrifice, ton soutien, ton aide et ta patience pendant la rédaction de thèse... et tout le bonheur...

Je tiens à remercier de ma sincère gratitude José Santiso pour la chaleur de nos rencontres et pour avoir mis à ma disposition les équipements DRX de l’ICMAB. En particulier je te suis reconnaissant de m’avoir aidé pendant la rédaction de ma thèse à me retrouver dans *l’espace réciproque*.

Je remercie également Michel Boudard pour les mesures par DRX et nos discussions longues et fructueuses dans le traitement et l’interprétation des données.

Didelis ačiū Zitai Šaltytei už puikios kokybės prekursorius, palaikymą, gerą nuotaiką bei skanią arbatą ir mano *mėgstamiausius kūginius saldainius*.

Nuoširdus ačiū Virgaudui Kubiliui už impedanso matavimus, pagalbą *klaidingame kompiuterių pasaulyje*, išaiškinimą „sudėtingo“ oscilografo veikimo principą ir kaip gauti skraidančius batus, patarimus *Moksle ir Gyvenime* bei nepamirštamas akimirkas praleistas kartu.

Ypatingas ačiū Arūnui Teišerskiui už draugiškumą, konsultacijas apie grafikų braižymą ranka bei su Originu, patarimus, pagalbą bei ypatingą palaikymą (už „Nelūžk“) disertacijos gynimo metu.

Ne kuo mažesnis ačiū Valentinai Plaušinaitienei už nuoširdžius patarimus *Moksle ir Motinystėje* bei palaikymą sunkiais gyvenimo momentais ir žinoma už puikius manganitų sluoksnius, juk niekas geriau už tave nesodina ir „nejaučia‘ manganitų.

Negaliu nepadėkoti ir mano pirmajam MOCVD mokytojui Sergejui Pasko už išsamias *instrukcijas pateiktas raštu* bei draugiškumą, nuoširdumą ir atvirumą.

Je remercie également: Latitia Rappene, pour avoir effectué les observations TEM et m’avoir initié à leur interprétation ; Patrick Chauduët, pour les observations en AFM, FEG et EBSD ; Hervé Roussel pour ses compétences en DRX ; Rachid Bouregba et Gilles Poullain (CRISMAT), pour les mesures d’hystérésis et de propriétés diélectriques ; Eldhaj Dogheche et Denis Remiens (IEMN), pour les mesures piézoélectriques ; Brahim Dkhil et Jacques Chevreul (ECP), pour les mesures DRX en températures ; Patrice Bourson et Marc Fontana (LMOPS), pour m’avoir permis d’effectuer l’expérience de champ sombre en spectroscopie Raman.

Je tiens à remercier Mario Maglione, Françoise Hippert, Pierre Bouvier, Jean-Pierre Sénateur et Catherine Dubourdieu pour leurs conseils scientifiques.

Thanks for Prof. H. Funakubo (Tokyo Institute of Technology, Japan) for our discussions and his support and confidence in my results.

Esu labai dėkinga doc. R. Raudoniui už manęs pasiūlymą ir pristatymą MOCVD laboratorijoje pirmame studijų kurse. Taip pat nuoširdus ačiū dėstytojams Prof. J. Grigui, Prof. G. Juškai ir Prof. V. Daujočiui už suteiktas žinias kurios be galo pravertė doktorantūros metu.

Je remercie tous les membres du LMGP, en particulier toute l’équipe technique, qui a été disponible, efficace et convivial tout au long de ce travail. Merci à Anne-Marie, Josiane, Virginie, Angélique, Joseph, Jean-Eduard, ….

Merci pour mes colocataires de *biuro*, Igor, Claire, Béatrice et Philipe, pour m’avoir supporté et pour l’ambiance chaleureuse.

Didelis ačiū už palaikymą, nuoširdumą, draugiškumą, pagalbą, gerą nuotaiką ir nepamirštamas akimirkas kartu: Linai, Berniukui - Mindaugui, Rasuolei, Seniūnui - Žygimantui, Annai.

Merci à tous ceux et celles qui m’ont accompagné depuis de longues années, dans le désordre : Sonia, Oscar, Vincent, José, Martin, Pierre, Laura, Sébastien, Dominique,Virginie, Anne-Laure, Isabelle, David, Cécile, Tristan, Benoit, Claire, David, Olivier, Hoi-Pang, Marco et tous les autres….

Taip pat noriu padėkoti savo tėvams, broliui Aurentui ir sesei Aidai už palaikymą ir pagalbą.

Merci à mon fils Deividukas d'être mon soleil…

Je dédis ce manuscrit à mon fils Deividukas et Samuel.

Table of contents

Introduction ________ *1*

Chapter 1

1 *$PbTiO_3$ – prototypical ferroelectric perovskite* ________ *5*

1.1 Perovskites ________ **8**

1.2 Ferroelectrics ________ **8**

1.2.1 Definition and polarization properties ________ 8
1.2.2 Ferroelectric-to-paraelectric phase transition ________ 10

1.3 The ferroelectric $PbTiO_3$ ________ **14**

1.4 $PbTiO_3$ phonon modes ________ **15**

1.4.1 General considerations ________ 15
1.4.2 $PbTiO_3$ Raman spectra ________ 16
1.4.3 Oblique modes ________ 18

1.5 Stresses and relaxation mechanisms in $PbTiO_3$ thin films ________ **19**

1.5.1 Stresses in PbTiO3 thin films ________ 19
1.5.2 Stress relaxation: dislocations and twinning ________ 21
1.4.3 Oblique modes ________ 18

1.6 Theoretical considerations on phase transitions in $PbTiO_3$ thin films ________ **24**

Bibliography ________ **26**

Chapter 2

2 Experimental techniques ________ *29*

2.1 Thin film deposition by pulsed liquid injection MOCVD system ________ **32**

2.1.1 PI MOCVD method 32
2.1.2 Metalorganic precursors 32
2.1.3 Substrates 33

2.2 X-ray diffraction 34

2.2.1 Film characterization in Bragg-Brentano and Shultz geometries 34
2.2.2 Two dimensional ω-2Θ, ω-χ and reciprocal space maps 38
2.2.3 High-temperature XRD 41
2.2.4 Determination of microstrains and average grain size 42

2.3 Raman spectroscopy 44

2.3.1 Theoretical considerations 44
2.3.2 Spectrometer 45

2.4 Other characterization techniques 47

2.4.1 Atomic force microscopy 47
2.4.2 Determination of film thickness 47
2.4.3 Wavelength dispersive X-ray spectroscopy 48
2.4.4 Transmission electron microscopy 48

Bibliography 49

Chapter 3

3 PbTiO$_3$ thin film deposition by PI MOCVD, process optimization 51

3.1 Partial oxygen pressure effect on the film composition 55

3.2 Deposition temperature influence on film composition and morphology 56

3.3 PbO desorption control with film growth rate 59

3.4 Deposition pressure influence on growth rate 60

3.5 Deposition temperature influence on the film microstructure 60

Conclusions 63

Bibliography 65

Chapter 4
4 $PbTiO_3$ thin film structure evolution with misfit strain and film thickness _______ *67*

4.1 Introduction _______ **70**

4.2 Domain structure study by reciprocal space mapping _______ **71**

4.3 Domain structure evolution with misfit strain and film thickness _______ **76**

4.3.1 Domain fraction _______ 76
4.3.2 Twinned and non-twinned *a*- and *c*-domains _______ 79
4.3.3 Twinning angles _______ 81
4.3.4 Mosaicity _______ 86

4.4 HR TEM analysis of dislocations and twin defects _______ **87**

4.5 Lattice parameters in *a*- and *c*-domains _______ **92**

4.6 Residual stress _______ **95**

4.6.1 Theoretical considerations _______ 95
4.6.2 Residual stress in $PbTiO_3$ films _______ 96

4.7 Heterogeneity of strains in $PbTiO_3$ films _______ **97**

4.8 Microstrains and average grain size _______ **100**

4.8.1 Average grain size _______ 100
4.8.2 Microstrains _______ 102

Conclusions _______ **102**

Bibliography _______ **104**

Chapter 5
5 Raman modes and residual stress _______ *107*

5.1 Introduction _______ **110**

5.2 General considerations: Raman modes and their activity in bulk $PbTiO_3$ _______ **111**

5.2.1 Raman selection rules _______ 111

5.2.2 Polarized Raman spectra ____ 112
5.2.3 Origin of the so-called oblique modes (or “quasimodes) ____ 114
5.2.4 Polarized Raman spectra ____ 112

5.3 Effect of polarization in $PbTiO_3$ films ____ 118

5.4 Estimation of residual stress by using the E(TO) modes ____ 120

5.4.1 Theoretical considerations ____ 120
5.4.2 Relation between residual stress and misfit strain ____ 121
5.4.3 Residual stress in *a*- and *c*-domains ____ 123
5.4.4 Effect of thickness on the residual stressing *c*-domains ____ 126

5.5 Analysis of the domain structure from A_1(TO) modes ____ 127

5.5.1 A_1(1TO) soft mode ____ 128
5.5.2 A_1(TO) hard modes and domain structure ____ 129

Conclusions ____ 130

Bibliography ____ 131

Chapter 6

6 Effect of temperature on $PbTiO_3$ powder and thin films ____ 133

6.1 Literature review ____ 136

6.2 Temperature evolution of domain structure and lattice parameters in $PbTiO_3$ thin films ____ 138

6.2.1 Domain structure ____ 139
6.2.2 Lattice parameters ____ 140
6.2.3 Domain fraction ____ 142

6.3 Domain transformations and phase transitions in $PbTiO_3$ ____ 143

6.3.1 High-temperature XRD study of epitaxial system PTO/STO films ____ 143
6.3.2 Raman spectroscopy results ____ 144
6.3.2.1 $PbTiO_3$ powder ____ 144
6.3.2.2 Polycrystalline $PbTiO_3$ films on sapphire substrate ____ 146
6.3.2.3 Strained epitaxial $PbTiO_3$ films on $SrTiO_3$ substrate ____ 147
6.3.2.4 Domain state transformations and structural phase transitions in partially or completely relaxed $PbTiO_3$ films on $LaAlO_3$ and MgO substrates ____ 149

Discussion ____ **157**

Bibliography ____ **160**

Chapter 7

7 Origin of residual stress ____ ***163***

7.1 Misfit strain ____ **166**

7.2 Thermal stresses ____ **168**

7.3 Phase transformation stress ____ **168**

7.4 Stresses and a-domain fraction ____ **169**

Conclusions ____ **170**

Bibliography ____ **170**

General conclusions and perspectives ____ ***171***

Résumé ____ ***177***

Introduction ____ **179**

Dépôt de films de $PbTiO_3$ par PI MOCVD ____ **180**

Evolution de la structure des films de $PbTiO_3$ ____ **182**

Modes Raman et contraintes résiduelles ____ **187**

Effet de température sur $PbTiO_3$ poudre et en films ____ **190**

Origine de contraintes résiduelles ____ **192**

Conclusions générales et perspectives ____ **195**

Annex 1: ICDD 00-006-0452 ____ ***199***

Annex 2: Surface&Coatings Technology 201 (2007) 9340-4 _ ***203***

List of publications ____ ***210***

Abbreviations

2-D **–** two – dimensional;
AFM – atomic force microscopy;
BTO – barium titanate, $BaTiO_3$;
FE – ferroelectric phase;
F-P – ferroelectric-to-paraelectric phase transition;
FWHM – full width at half maximum;
H –horizontal;
HR TEM – high resolution transmission electron microscopy;
HW – Halder – Wagner approximation;
LAO - lanthanum aluminate, $LaAlO_3$;
LO – longitudinal optic phonons;
LWD – long working distance
NA – numerical aperture;
O^{i}Pr – i-propoxide;
PI MOCVD – pulsed liquid injection metalorganic chemical vapour deposition;
PTO – lead titanate, $PbTiO_3$;
PZT – lead zirconium titanate, $PbZr_{1-x}Ti_xO_3$;
Ra – average roughness;
RS – Raman spectroscopy;
RT – room temperature;
SAPH – sapphire;
SEM – scanning electron microscopy;
STO - strontium titanate, $SrTiO_3$;
T$_c$ – Curie transition (ferroelectric-to-paraelectric) temperature;
T$_{Dep}$ – deposition temperature;
TEC – thermal expansion coefficient;
thd – 2,2,6,6-tetramethyl-3,5-heptandionate;
TO – transverse optic phonons;
V – vertical;
WDS – wavelength dispersive X-ray spectroscopy;
WH – Williamson – Hall analysis;
XAFS – X-ray absorption fine-structure;
XRD **–** X-ray diffraction;

Introduction

Introduction

Perovskite-type oxides exhibit an extraordinary richness of physical and structural properties. They are well-known for their common structural instabilities which can be driven by external parameters like temperature, electric field, stress etc. An original way of varying these structural instabilities, and thus the related physical properties, is to use the interfacial strain when a thin film is deposited on a substrate. The physical properties of thin films can be substantially different from those of bulk materials not only due to substrate-film interactions, but also because of grain size effects, defects etc. Stresses can also alter mechanical, optical, structural and electrical properties as well as the nature of phase transitions in thin films which can directly play a part in the reliability of devices.

Ferroelectric perovskite oxides receive considerable attention for their attractive physical properties. Thus, studies about epitaxial ferroelectric thin films are of great interest because of their potential application as elements in static random access memories, high dielectric constant capacitors and optical waveguides. In the past internal stress levels in ferroelectric films were systematically studied by varying of different parameters: the film thickness, the choice of the substrate to obtain different lattice or thermal expansion mismatches, the variation of deposition conditions or post-annealing process, the insertion of a thin layer of a different chemical composition in between the film and the substrate etc. However, the obtained films may have different microstructure or grain size, which also affects electric properties. It can be noted, that most literature works do not present a direct measurement of the residual stress in films and results are generally assigned to be due to one type of stress only (for example, misfit or thermal stress). In studies where residual stress values are given, it is mainly assumed that residual stress originates from only one type of stress and this although residual stress at room temperature is the sum of all stresses developed during the complex process of film preparation. Furthermore, residual stress values are usually estimated using only one method of which the accuracy is only rarely discussed. Thus, simple methods to estimate the residual stress and investigation of its origin using commonly used characterization techniques, such as X-ray diffraction (XRD) and Raman spectroscopy, are of special interest.

Stress effects on phase transitions in ferroelectric thin films have been studied in literature as well. It is known that in high quality strained epitaxial films, the transition temperature can be shifted by a few hundred degrees and primary and secondary order parameters can be decoupled. However, stress effects on partially relaxed epitaxial films remain unclear due to the lack of advanced studies based on the influence of the film relaxation degree on the nature of the phase transition.

For our study we have chosen the perovskite-type ferroelectric lead titanate ($PbTiO_3$ (PTO)) which can be considered as a prototype of the wide class of ferroelectric materials. Also, the physical, structural and spectroscopic properties of bulk PTO are rather well-known which makes this system a good reference for thin film studies. As a matter of fact, PTO thin films also have been intensely studied over the last 15 years as well which allow us to compare and discuss our results with those reported in literature.

The objective of our study was to investigate the origin of residual stress and stress effects on the nature of the phase transitions and domain state transformations in epitaxial PTO films by using standard characterization techniques such as X-ray diffraction and Raman spectroscopy. In order to vary the stress level in the films, a thickness series of PTO films has been deposited on most commonly used substrates, inducing compressive and tensile misfit stresses (Figure I-1).

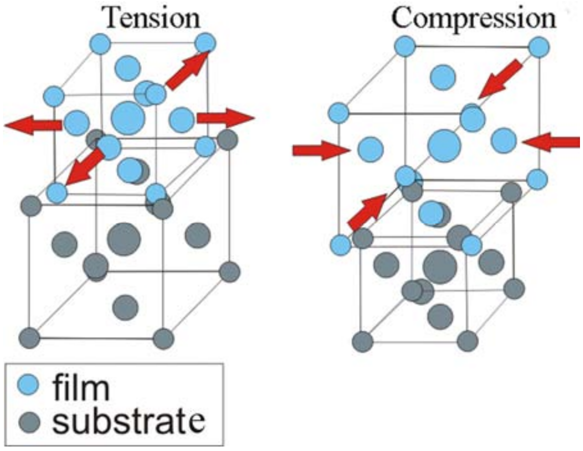

Figure I-1. Schematic representation of a film submitted to tensile and compressive misfit stress.

The thesis is organized as follows.

Before the presentation of our results, the general properties of ferroelectric perovskites are described in *Chapter 1* where we pay particular attention to phase transitions and phonon modes in bulk samples. Stresses of different origins, stress relaxation mechanisms and theories on phase transitions in PTO thin films are presented as well.

The experimental setup, including PTO film growth and characterization techniques are described in *Chapter 2*.

The optimization of the metalorganic chemical vapour deposition (MOCVD) process to obtain PTO films of high quality, stoichiometric composition and with pure tetragonal phase is shortly described in *Chapter 3*.

The influence of thickness and lattice mismatch on domain structure, lattice parameters, epitaxial quality, microstrains and defect density has been investigated in C*hapter 4*. They are the direct traces of stresses induced during the complex process of film preparation. This information will be a guide to understand the stress relaxation and film adaptation to the substrate.

The determination of residual stress from Raman spectroscopy results is presented in *Chapter 5*. In order to determine the phonon mode wavenumbers with accuracy, a polydomain PTO single –crystal has been studied first as it is stress free and other parameters different from stress can modify the peak profiles Thus, the corresponding Raman shifts have been used as reference wavenumbers for all film spectra measured in the same experimental conditions. In order to test the validity of residual stress values determined by Raman spectroscopy, they have been directly compared with those calculated from lattice parameters issued from XRD data presented in chapter 4.

The investigation of stress effects on the domain state transformations and on the nature of the phase transition in epitaxial PTO films using high-temperature XRD and Raman spectroscopy is presented in *Chapter 6*. The obtained results are compared to those obtained for polycrystalline films and bulk PTO.

In *Chapter 7*, our results on film relaxation process are summarized and on this basis the origin of residual stress is discussed. Moreover, a particular attention is paid to the stress related to the phase transformation because it is usually assumed in literature that such a stress does not exist.

In the last part we will present our *General conclusions and perspectives* drawn from our study.

Chapter 1:

$PbTiO_3$ - prototypical ferroelectric perovskite

Chapter 1

1 *$PbTiO_3$ – prototypical ferroelectric perovskite* *5*

1.1 Perovskites 8

1.2 Ferroelectrics 8

- 1.2.1 Definition and polarization properties 8
- 1.2.2 Ferroelectric-to-paraelectric phase transition 10

1.3 The ferroelectric $PbTiO_3$ 14

1.4 $PbTiO_3$ phonon modes 15

- 1.4.1 General considerations 15
- 1.4.2 $PbTiO_3$ Raman spectra 16
- 1.4.3 Oblique modes 18

1.5 Stresses and relaxation mechanisms in $PbTiO_3$ thin films 19

- 1.5.1 Stresses in $PbTiO_3$ thin films 19
- 1.5.2 Stress relaxation: dislocations and twinning 21
- 1.4.3 Oblique modes 18

1.6 Theoretical considerations on phase transitions in $PbTiO_3$ thin films 24

Bibliography 26

1. $PbTiO_3$ – prototypical ferroelectric perovskite

1.1 Perovskites

Perovskite-type oxides, and solid solutions among them, are well known for exhibiting an extraordinary richness of physical and structural properties (1). The perovskite oxides have a general formula ABO_3, where the A site cations are typically larger than the B-site cations and similar in size to the O^{2-}. The A cations are surrounded by twelve anions in a cubo-octahedral coordination and the B cations are surrounded by six anions in an octahedral coordination. The oxygen anions are surrounded by two B-site cations and four A-site cations. The ideal perovskite structure adopts the cubic space group $Pm\bar{3}m$ (for example, $SrTiO_3$ at 300 K) (Figure 1‑1a). However, this ideal perovskite structure is usually distorted, that results in lower symmetries. There are two main types of perovskite structural distortions: (i) rotations of BO_6 octahedra (tilts) and (ii) A and/or B cation displacements with respect to their oxygen cages (Figure 1‑1 b and c). Generally, cationic displacements drive the ferroelectric properties and tilts of the BO_6 octahedra play a critical role in magnetic properties. Even small structural instabilities which can be driven by external parameters like temperature, pressure, stresses, electric and magnetic fields, etc., may change significantly the physical properties of the perovskites.

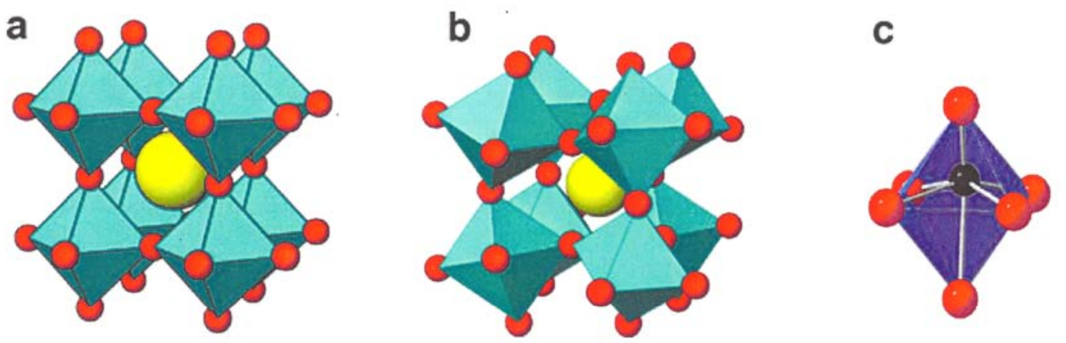

Figure 1-1: Perovskite-type structure: ideal perovskite structure with cubic symmetry (a), example of BO_6 octahedra tilt (b) and illustration of cation displacements.

1.2 Ferroelectrics

1.2.1 Definition and polarization properties

The ferroelectric materials are characterized by a spontaneous polarization, which can be inverted by the application of an electric field. They are named in analogy to ferromagnetic materials, which exhibit a spontaneous magnetization.

From symmetry considerations, it can be shown that a ferroelectric materials necessarily crystallize in a non-centrosymmetric structure with a single rotation axis. At a microscopic scale, the polarization is generally due to the displacement of a cation with respect to the centre of the cage formed by its first anion neighbors. The Figure 1-2 illustrates this point for the ferroelectric perovskite $PbTiO_3$. In that case, the Pb and Ti cations move out of the centre of their cube-octahedral and octahedral cages, respectively, which leads to a tetragonal distortion.

One can define two equivalent polarization states compatible with this symmetry. There is an energy barrier between these two ferroelectric states, which corresponds to the high symmetry (cubic) phase (Figure 1-2). It can be overcome by an external electric field, which unbalances the energy wells and enables the transition between them (Figure 1-3). Due to their finite depths, there is a delay for changing the wells, which results in polarization hysteresis. The electric field needed for switching between two states is called the coercitive field E_c. The polarization in absence of electric field is called remanent polarization P_r.

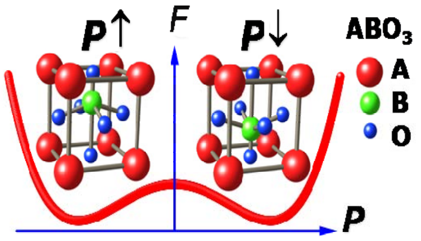

Figure 1-2: Free energy double-well, corresponding to two equivalent ferroelectric states in a tetragonal perovskite. The difference in sizes of balls do not correspond to the difference in atom sizes in perovskites.

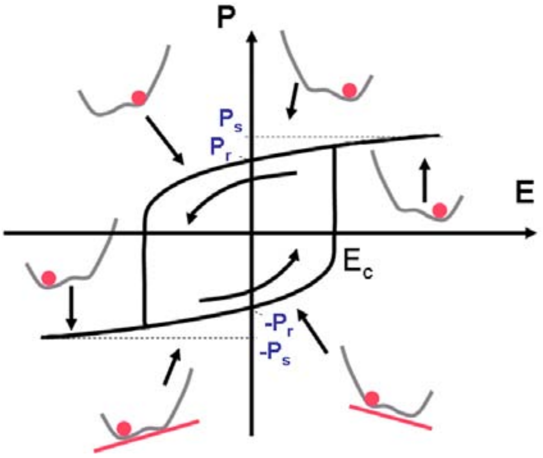

Figure 1-3: Switching between two equivalent ferroelectric states under applied field, and resulting polarization hysteresis.

Ferroelectric materials can display regions with different polarizations, each region with a uniform polarization being called a domain. Two neighboring domains with opposite polarizations are called 180 ° domains. The total polarization therefore corresponds to the difference in volume of the domains with a polarization parallel to the polar axis and those with a polarization anti-parallel to the polar axis. Two domains are separated by domain wall, which displacement leads to a change of domain volumes and hence, of the total polarization.

1.2.2 Ferroelectric-to-paraelectric phase transition

When the temperature is being raised, all ferroelectrics undergo a phase transition at the critical temperature T_c towards a paraelectric state, which corresponds to a null polarization in a centrosymmetric structure. In $PbTiO_3$ for instance, the ideal cubic perovskite structure is recovered above $T_c = 490$ °C.

The application of an electric field to an insulating material (either ferroelectric or not) generates an induced polarization P_i. For a polycrystalline sample, P_i is proportional to the electric field amplitude according to:

$$P = \chi \varepsilon_0 E \tag{1.1}$$

where χ is the susceptibility which depends on the material and ε_0 is the permittivity of free space. In ferroelectric materials, χ diverges at T_c.

The description of ferroelectric-to-paraelectric (F-P) phase transitions may be given at both macroscopic (Ginzburg-Landau-Devonshire theory) and microscopic scales.

1.2.2.1 The Ginzburg-Landau–Devonshire theory

The Ginzburg-Landau-Devonshire theory (2; 3; 4) describes ferroelectricity by considering a polynomial expansion of the free energy F as a function of polarization P (primary order parameter) when applied stress is equal to zero:

$$F = \frac{1}{2}aP^2 + \frac{1}{4}bP^4 + \frac{1}{6}cP^6 .... - EP \quad , \tag{1.2}$$

where b, c are constants and $a = \frac{T - T_0}{C}$ (T - temperature, T_0 - phase transition temperature, C – constant ($C > 0$)).

The equilibrium configuration is determined by the condition $\frac{\partial F}{\partial P} = 0$ thus,

$$\frac{T - T_0}{C} P + bP^3 + cP^5 ... - E = 0 \tag{1.3}$$

For practical purposes, only a coefficient is considered to be temperature dependent, while b and c are constant with temperature. To obtain F-P phase transition, a must pass through zero at transition temperature.

At $E = 0$, for the second order phase transition Eq. 1-3 can be written as

$$\frac{T - T_0}{C} P + bP^3 = 0 \quad (b > 0) \tag{1.4}$$

and for the first order phase transition as

$$\frac{T - T_c}{C} P + bP^3 + cP^5 = 0 \quad (b < 0, c > 0), \tag{1.5}$$

where T_0 and T_c are phase transition and Curie temperatures, respectively. The signs of *a*, *b*, and *c* parameters were chosen in order to get stable paraelectric and ferroelectric phases at $P = 0$ and $P \neq 0$, respectively.

In the case of second order phase transition, the solutions of Eq. 1.4 show that polarization of ferroelectric phase goes continuously $Ps = \sqrt{\frac{3a}{2b}(T - T_0)}$ to zero approaching phase transition temperature and paraelectric phase free energy minimum is at $P = 0$ (Figure 1‑4a and b).

At first order phase transition, $T = T_c$, the free energies of the paraelectric and the ferroelectric phases are equal. Thus, the polarization evolution is discontinuous : P = 0 for $T \geq T_c$ and $P > \sqrt{\frac{-3b}{4c}}$ at $T \leq T_c$ (Figure 1‑4 a and b).

The characteristic macroscopic behaviours of the primary order parameter - polarization parameters of ferroelectrics with associated anomalies and non-linearities are accompanied by corresponding behaviours of the secondary order parameters – other mechanical, thermal, piezoelectric and electrothermal properties. For example, absolute dielectric susceptibility can be expressed as $\chi = \left(\frac{\partial P}{\partial E}\right)_T$, and it can be easily calculated for paraelectric phase ($T > T_0$).

It follows the Curie Law for second order phase transition $\chi = \frac{1}{a(T - T_0)}$ and for the first order phase transition $\chi = \frac{1}{a(T - T_c)}$, where $T_c = T_0 - \frac{3b^2}{16ac}$ (Figure 1‑4 c). In the case of first order phase transition dielectric susceptibility diverges at different temperatures T_c and T_0 in ferroelectric and paraelectric phases, respectively.

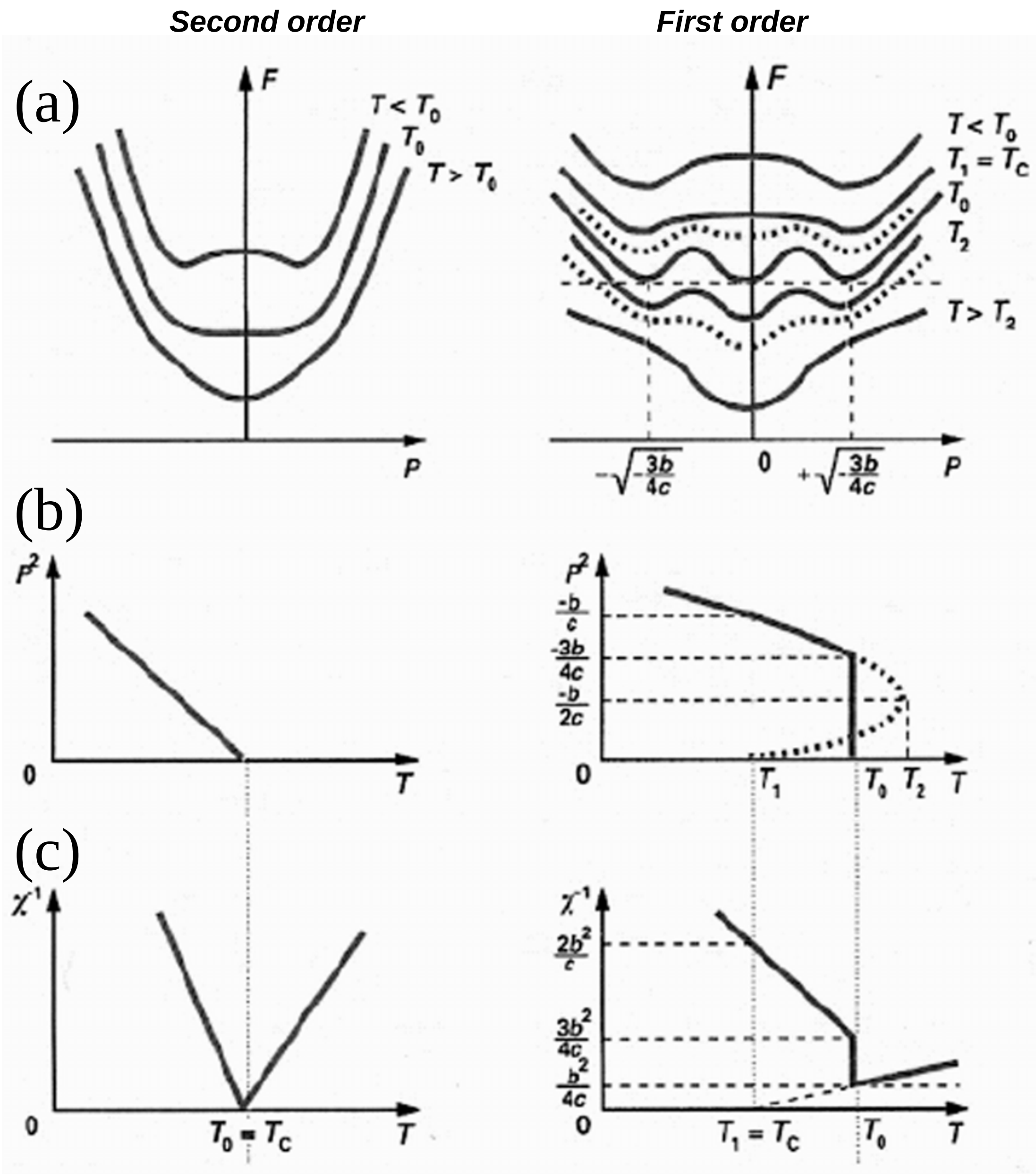

Figure 1-4: Summary of properties of second order (left) and first order (right) ferroelectric phase transitions, as described by Ginzburg-Landau –Devonshire theory: (a) free energy (T_0– phase transition temperature, T_c—Curie temperature, T_2—tangent of horizontal inflection), (b) square of polarization and (c) inverse dielectric susceptibility as a function of temperature at E=0.

1.2.2.2 Microscopic description of ferroelectric-to-paraelectric phase transition

At a microscopic scale, the ferroelectric phase transitions are usually described in the framework of two possible models: the order-disorder and displacive models. The two transition types lead to substantially different local structures.

Displacive phase transition In the case of an ideal displacive transition, the phases below and above the transition temperature are both ordered (except for lattice vibrations) but have different symmetries (Figure 1-5). From Cochran's theory (5; 6), ideal displacive transitions are caused by softening of one of the transverse optical modes.

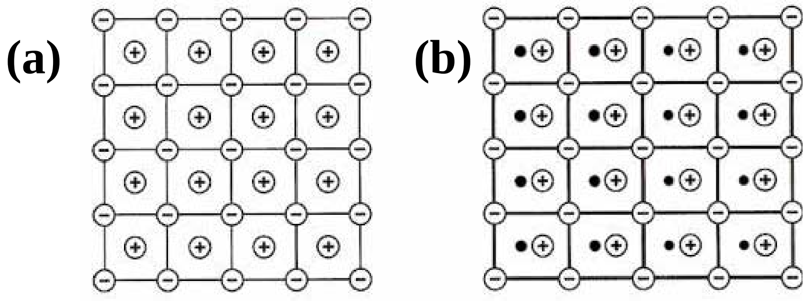

Figure 1-5: Schematic diagram of displacive ferroelectric transition. Positive and negative charge centers in the paraelectric phase (a) and in the ferroelectric phase (b).

Order-disorder phase transition In the case of an order-disorder phase transition, the crystals are disordered above and partially ordered below the transition temperature (Figure 1-6). No soft modes are expected. Comès et al.(7) first reported the possibility of such a behavior in the ferroelectric perovskites. They found diffuse X-ray lines in the paraelectric phase of $BaTiO_3$, indicating the existence of local polar disorder which averages out to a cubic structure (8-site model). The distinction between the displacive and order-disorder models is not absolute. In recent papers, a mixed character of the ferroelectric phase transitions is taken into account (8; 9).

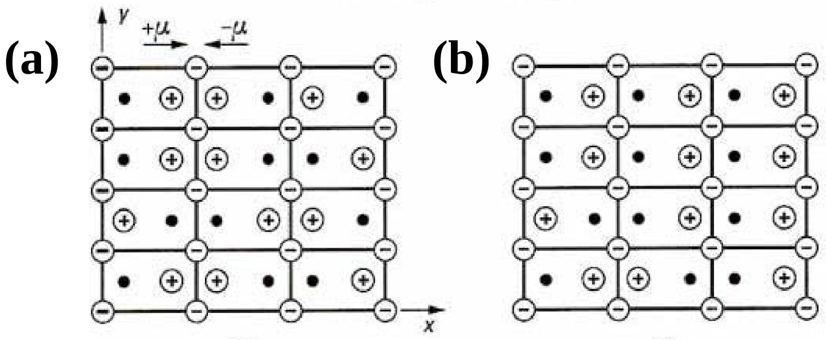

Figure 1-6: Schematic diagram of order-disorder ferroelectric transition. The dipoles are disordered in paraelectric phase (a) and partially ordered in ferroelectric phase (b).

1.3 The ferroelectric $PbTiO_3$ - structural properties

$PbTiO_3$ (PTO) undergoes a first order paraelectric–to-ferroelectric phase transition at T_c = 490 °C (10; 11). This ferroelectric-to-paraelectric phase transition temperature is the highest in the family of ferroelectric perovskites. PTO is cubic above T_c, and tetragonal below T_c (Figure 1‑7); at room temperature, the *c/a* ratio value is 1.065.

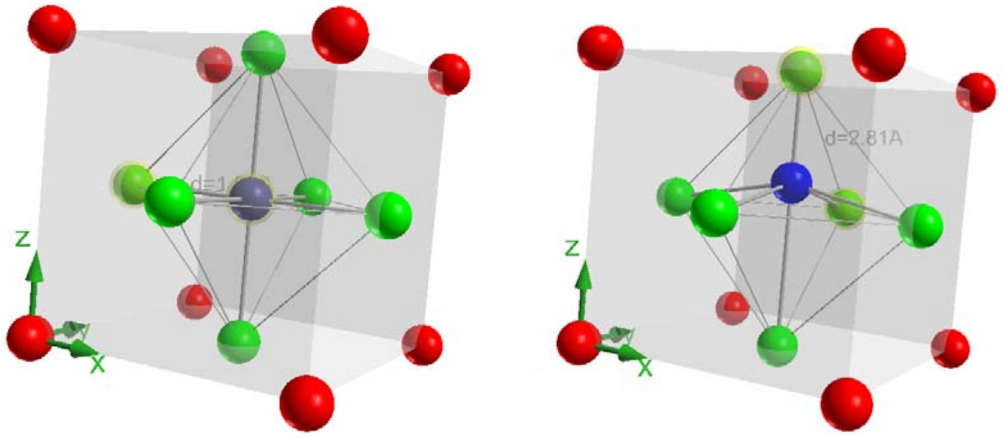

Figure 1-7: Cubic (left) and tetragonal (right) $PbTiO_3$ cells corresponding to paraelectric and ferroelectric phases, respectively (blue balls—Ti^{4+}, red—Pb^{2+} and green—O^{2-}) .

Local dipole moments The value of the polarization is quite larger in PTO than in $BaTiO_3$ (BTO), which is probably due to the presence of lead. Pb is not an alkaline earth metal and it is more deformable and polarizable than Ba. It was pointed out by theoretical studies (12; 13) that the hybridization between the Ti *3d* states and O *2p* states is essential to the ferroelectric instability in both PTO and BTO. Moreover, the orbital hybridization exists between the Pb *6p* states and O *2p* states to play a crucial role for larger ferroelectricity in PTO, whereas the interaction between Ba and O is almost ionic in BTO.

Nature of the phase transition in PTO Due to a large Curie-Weiss constant (~ 8.5×10^4 K (14)) and a well-behaved soft mode, PTO was considered as an exemplary displacive ferroelectric. However, some evidence of order-disorder like behavior in Pb atoms was given by high resolution neutron diffraction (15). Fontana et al. (16; 17) suggested that PTO has partial order-disorder nature in the vicinity of T_c: near the transition, a central peak appears and its area increases approaching the transition, indicating the presence of disorder. Furthermore, the dielectric constant was found larger than that expected from Lydane-Sachs-Teller relation, suggesting that an ordinary displacive type model would not be sufficient to account for the dielectric constant (16). They concluded that up to 430 °C the displacive character governs the PTO properties, while at higher temperatures the ionic disorder becomes important. The order-disorder component of the ferroelectric phase transition in PTO was further shown by X-ray absorption fine- structure (XAFS) experiments (18; 19). It is found that the tetragonality ratio c/a is almost the same as that determined by XRD at ambient conditions and local distortions are orientationally ordered. As the temperature rises, the difference between the local and average distortions increases indicating an increase in orientational disorder. Above the transition XRD data show that *c/a = 1*, whereas c/a measured by XAFS is as high as 1.06, indicating that even above the transition the local PTO structure is tetragonal. Above the transition the local and average structures are different indicating that the system is orientationally disordered: there are equal probabilities that Pb and Ti are displaced in any of the six [00*1*]-type directions (Figure 1‑8). Sani et al. (20) and Sicron et al. (18) proposed that the nonzero distortion in high temperature phase is an indication of the presence of tetragonal domains in the cubic phase and of nonnegligible order-disorder character of the phase transition. These tetragonal domains are ferroelectric clusters which have a nonzero spontaneous polarization at local scale. The progressive increase of disorder makes the spontaneous polarization of the clusters to be strongly disoriented one to another, so the cubic phase is formed by tetragonal clusters of nonzero polarization at local scale. There is no correlation between the long-range order value and the microscopic values of spontaneous polarization.

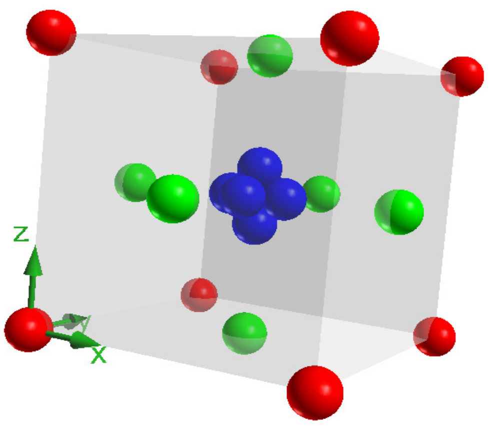

Figure 1-8: Average cubic cell of PTO above phase transition (blue balls—Ti^{4+}*, red—*Pb^{2+}* and green—*O^{2-}*) . The Ti distortions are completely disordered with equal probabilities in displacements in any of six [001] type directions.*

1.4 $PbTiO_3$ phonon modes

1.4.1 General considerations

At room temperature PTO is ferroelectric and adopts tetragonal crystal symmetry (space group C^1_{4v}) with one formula unit per unit cell. At 490 °C, a ferroelectric to paraelectric phase transition takes place. It has been reported that this structural phase transition has both displacive- and order-disorder-like properties (18; 16) just as most ferroelectric perovskites. In the cubic high-temperature phase (space group O^1_h), there are 12 degrees of freedom at $\boldsymbol{k}$=0, which belong to the irreducible representations $3T_{1u}$ + T_{2u} where T_{2u} is a silent mode since it is neither infrared nor Raman active. The T_{1u} modes are only infrared active. Long range electrostatic forces lead to a split of the T_{1u} modes into a $T_{1u}(TO)$ mode (polarization transverse to **k**) and a $T_{1u}(LO)$ mode (polarization parallel to **k**). In the tetragonal phase, each T_{1u} mode splits into A_1 + E modes, resulting in $3A_1$ + $3E$ modes whereas the T_{2u} mode splits into B_1+E modes. The A_1 and E modes are infrared- and Raman-active and the corresponding phonons are polarized in the *z*- direction or in the *xy* plane, respectively; the B_1 mode is only Raman active. The Raman polarization tensors are presented in Eq. (1.6) for each mode, and the direction of polarization is indicated in parentheses.

$$A_1(z)=\begin{bmatrix} a & \cdot & \cdot \\ \cdot & a & \cdot \\ \cdot & \cdot & b \end{bmatrix} \quad E(x)=\begin{bmatrix} \cdot & \cdot & -e \\ \cdot & \cdot & \cdot \\ -e & \cdot & \cdot \end{bmatrix} \quad E(y)=\begin{bmatrix} \cdot & \cdot & \cdot \\ \cdot & \cdot & e \\ \cdot & e & \cdot \end{bmatrix} \quad B_1=\begin{bmatrix} c & \cdot & \cdot \\ \cdot & -c & \cdot \\ \cdot & \cdot & \cdot \end{bmatrix} \qquad (1.6)$$

Table 1-1: TO-LO assignment of E and A_1 modes

Propagation direction	Phonon assignment		
	E(x)	E(y)	A_1(z)
x	LO	TO	TO
y	TO	LO	TO
z	TO	TO	LO

Due to the long-range electrostatic forces, all A_1 and E modes split into transverse (*TO*) and longitudinal (*LO*) components. Depending on the phonon propagation direction (*x*, *y* or *z*), only pure *TO* or *LO* can be observed in Raman spectra as resumed in Table 1- 1.

Lattice dynamics studies showed that $A_1(TO)$ modes correspond to PTO lattice vibrations along the c-axis of the tetragonal cell, while *E(TO)* modes correspond to the lattice vibrations in the *ab*-basal plane (Figure 1‑9) (21).

1.4.2 PbTiO$_3$ Raman spectra

Raman mode assignment and position determination (22; 23; 24; 25) were carried out by using monodomain PTO single crystals (different ferroelectric structure of *c*-domains in general). *TO* and *LO* mode wavenumbers reported by different authors are given in Table 1- 2. In the seventies (22; 23; 24) the difference in reported values can be explained by low resolution spectrometers (4 cm^{-1}), which is not the case in Ref. (25) (0.5 cm^{-1}). Unlike other groups (22; 23; 24), Foster et al. (25) have used single ferroelectric domain crystals (90° and 180° ferroelectric domains were removed) in order to avoid depolarization effects. There was a discrepancy about $A_1(1TO)$ mode assignment in the earliest

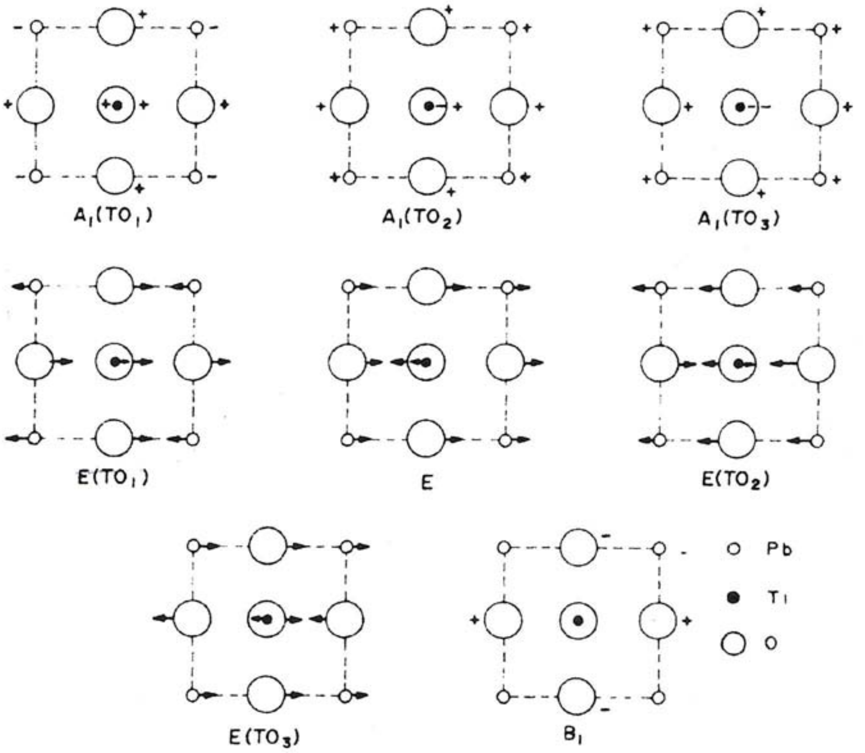

Figure 1-9: Graphical representation of zone-center modes of vibrations for PTO with atoms projected on an ab-basal plane (21).

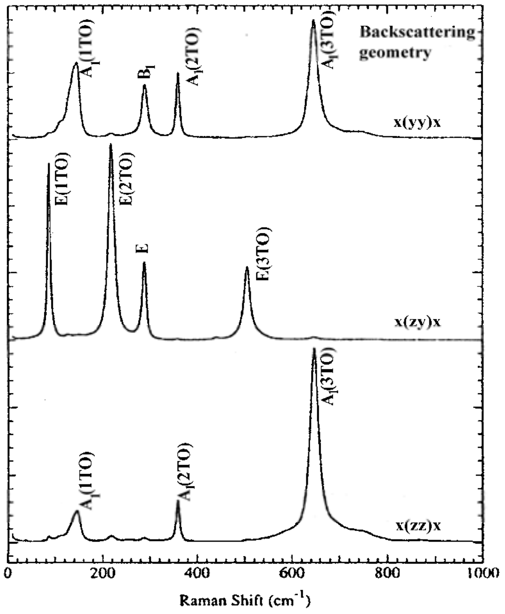

Figure 1-10: Polarized Raman spectra of a single ferroelectric domain PTO single-crystal at 300 K recorded in parallel (x(yy)x, x(zz)x) and crossed (x(zy)x) polarization configurations (28).

studies. In the more recent Raman reports (16; 28; 17), the peak at 148 cm^{-1} was assigned to the $A_1(1TO)$ mode, based on its polarization.

Raman selection rules are strictly obeyed in polarized Raman spectra of single ferroelectric domain PTO single-crystals as shown in Figure 1‑10 (25). In the crossed polarization configuration (*x(zy)x*) only *E(TO)* modes are observed. In parallel polarization configuration, the spectra contain only $A_1(TO)$ modes (*x(zz)x*) or $A_1(TO)+B_1$ modes (*x(yy)x*).

Table 1-2: PTO Raman mode shifts at room temperature

	Burns et al. (22) (1973)	Cerdeira et al. (23) (1975)	Frey et al. (24) (1976)	Foster et al. (25) (1993)
E(TO)	89	85	88	87.5
	221	205	220	218.5
	508	502	505	505
E(LO)	128	-	128	128
	445	-	439	440.5
	717	-	723	687
B_1+E	-	289	289	-
A_1(TO)	127?	117?	147	148.5
	364	350	359	359.5
	651	634	646	647
A_1(LO)	215	-	189	194
	445	-	465	465
	797	-	796	795

1.4.3 Oblique modes

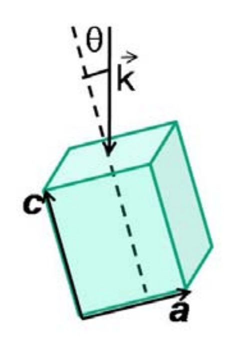

*Figure 1-11: Angle Θ between **k** and the c axis.*

This description of the phonons as LO or TO is valid only when the phonon wavevector **k** is along one of the principal symmetry directions of the crystal. For uniaxial crystals, the phonon mode frequencies disperse as a function of the angle Θ between **k** and the *c* axis (Figure 1-11) (i.e., the direction of the spontaneous polarization in the FE phase). Phonons observed at Θ=0 and π/2 correspond to pure *LO* and *TO* phonons, while at intermediate values of Θ, the modes are termed oblique phonons or "quasimodes". A scheme of the frequency dispersion of the *LO* and *TO* phonons with Θ is given in Figure 1‑12 for cubic O^1_h and tetragonal C^1_{4v} symmetries (25). The angular dependence of the peak positions as obtained by Foster (25) from Raman spectra of single ferroelectric domain PTO single crystal is shown in Figure 1‑13. In passing from k∥a (Θ=90°) to k∥c (Θ=0°), it is observed that high frequency modes as *E(2LO)* and *E(3LO)* disperse upward to become A_1*(2LO)* and A_1*(3LO)*, respectively; A_1*(3TO)* disperses downward to merge with *E(3TO)*; A_1*(2TO)* disperses downward to merge with *E(2TO)*. At low frequencies, *E(1LO)* disperses downward to merge with *E(1TO)* and A_1*(TO)* disperses upward to connect to A_1*(LO)*. All *E(TO)* modes are unchanged by Θ variation.

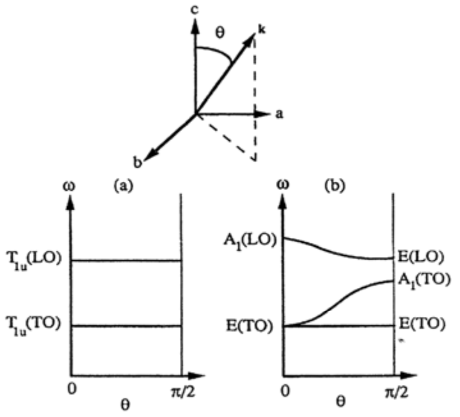

Figure 1-12: Scheme of the hard mode frequency dispersion as a function of Θ for cubic (a) and tetragonal (b) systems (25).

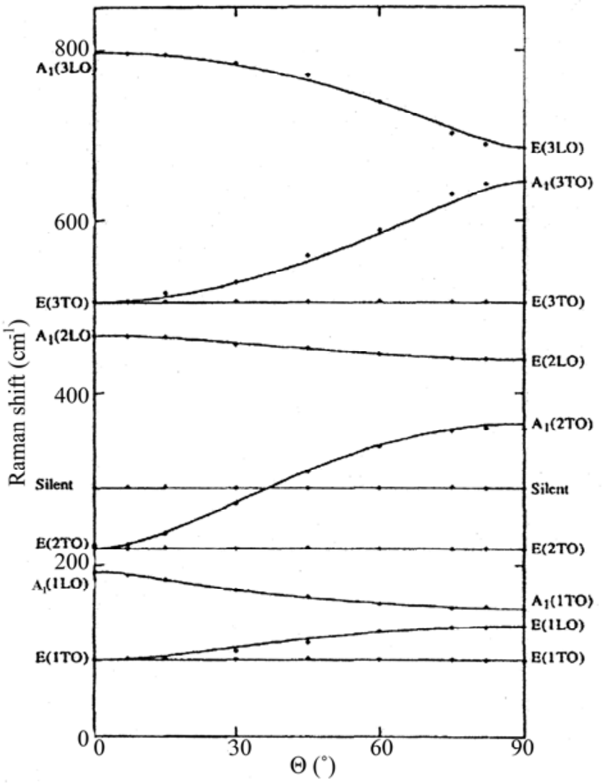

Figure 1-13: PTO phonon frequency dispersion curves (28).

1.5 Stresses and relaxation mechanisms in PbTiO$_3$ thin films

1.5.1 Stresses in PTO thin films

Films are submitted to substantial stresses during growth and subsequent cooling process from deposition temperature to room temperature (RT). The biaxial stresses result in in-plane and out-of-plane strains, $\varepsilon_{\parallel}$ and $\varepsilon_{\perp}$, respectively. The relation between the biaxial stress σ and the in-plane strain $\varepsilon_{\parallel}$ in PTO films can be expressed as follows

$$\sigma = \frac{E}{1-\nu}\varepsilon_{\parallel} \tag{1.7}$$

where υ is the Poisson's ratio (0.22 (26)) and E the Young's modulus (130 GPa (26)) of the PTO film. $\varepsilon_{\perp}$ can be expressed through $\varepsilon_{\parallel}$ as follows

$$\varepsilon_{\perp} = -\frac{2\nu}{1-\nu}\varepsilon_{\parallel} \ . \tag{1.8}$$

At the growth temperature, stresses are mainly misfit (also called epitaxial) and intrinsic stresses. During the cooling process, additional stresses may develop in the film, such as thermal stresses or stresses related to the phase transformation. The different strains are defined hereunder.

Homogenous strains:

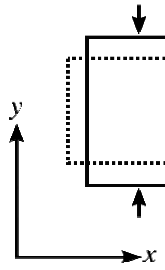

Figure 1-14: Schematic representation of Poisson law.

Misfit, thermal and transformation stresses result in homogenous strains in the PTO film. Homogeneous strains follow Poisson law: when a sample of material is stretched in one direction, it tends to contract (or expand) in the other two directions (Figure 1-14).

Misfit strain ε_m It comes from the lattice mismatch between the film and the substrate at the growth temperature and can be expressed as

$$\varepsilon_m = \frac{(a_s - a_f)}{a_s} \ , \tag{1.9}$$

where a_s and a_f are the lattice parameters of the substrate and of cubic PTO, respectively, assuming that the deposition temperature is higher that the structural phase transition temperature.

Thermal strain ε_{th} It originates from the difference between the film and substrate thermal expansion coefficients, α_f and α_s, respectively, during the cooling down from the deposition temperature to RT $\Delta T=(T_{Dep}-T_c)$. For PTO films, the thermal strain can be expressed as

$$\varepsilon_{th} = \left(\alpha_f - \alpha_s\right)\Delta T \tag{1.10}$$

Phase transformation strain The PTO films undergoes a paraelectric-to-ferroelectric phase transition during the cooling down from the deposition temperature. During the phase transition, the change in bulk PTO volume is 0.45 %, as observed from high temperature XRD measurements. The transformation strain $\boldsymbol{\varepsilon_{PT}}$ in a stress-free PTO single crystal can be expressed as

$$\varepsilon_{PT} = \frac{\left(c_T - a_T\right)}{a_C} \tag{1.11}$$

where a_T and c_T are lattice parameters of tetragonal PTO at transition temperature and a_C is the lattice parameter of cubic phase. The transformation stress is tensile. Any condition of pre-existing strains affects the phase transition.

Heterogeneous strains:

The strains resulted from defects or intrinsic stresses are heterogeneous and do not follow Poisson law. Example of cell under heterogenous strains are given in Figure 1-15.

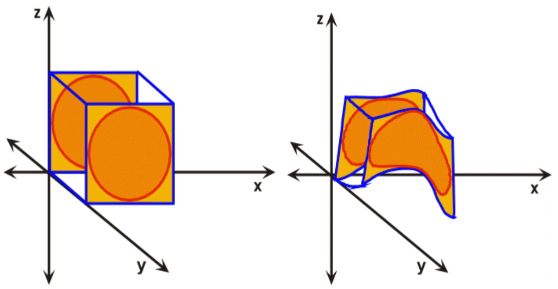

Figure 1-15: Unstrained (a) and heterogeneously strained (b) unit cell.

Defects Defects form in thin films to relax the homogeneous stresses. However, defects such as oxygen vacancies, misfit and threading dislocations locally deform the lattice and introduce heterogeneous strains in the films.

Intrinsic strain It is related to the growth technique. In the case of MOCVD, the intrinsic stress is introduced by the surface energy reduction associated with grain boundary formation during island coalescence. This intrinsic stress inversely proportional to the average grain diameter and is tensile stress as the film density become lower due to grain boundary relaxation. In the case of physical methods, the intrinsic stress is generated by the atomic peening during deposition, that is, the impact of neutrals against the film surface. Whether the intrinsic stress is tensile or compressive is determined by the momentum of scattering neutrals. Usually, it is negligible in the case of MOCVD and rather high when using physical methods.

1.5.2 Stress relaxation: dislocations and twinning

Two principal mechanisms of stress relaxation in PTO films are the formation of dislocations and twinning.

Misfit and threading dislocations Two types of dislocations exist in epitaxial ferroelectric thin films: they are misfit and threading dislocations. During the deposition, when a film exceeds a critical thickness, misfit dislocations form at the film-substrate interface to reduce the mismatch between the film and the substrate (27). Threading dislocations cross through the film thickness and also contribute to the stress relaxation.

The critical thickness for the introduction of the first misfit dislocations is inversely proportional to the misfit strain (27). The misfit strain accommodation initiates at the critical thickness and hyperbolically approaches complete relaxation with increasing film thickness as it was shown by the theory of Speck et al. (27). After a misfit dislocation has developed at the film/substrate interface, the film no longer “sees” the potential of substrate, but rather it experiences the potential of the substrate with an array of misfit dislocations. Thus, effective misfit strain ε_m^* in the film is controlled by an effective substrate lattice parameter b*:

$$\varepsilon_m^* = \frac{b^* - a_c}{b^*} \tag{1-12}$$

The b* value depends on the film thickness; therefore, the effective misfit strain is also thickness dependent.

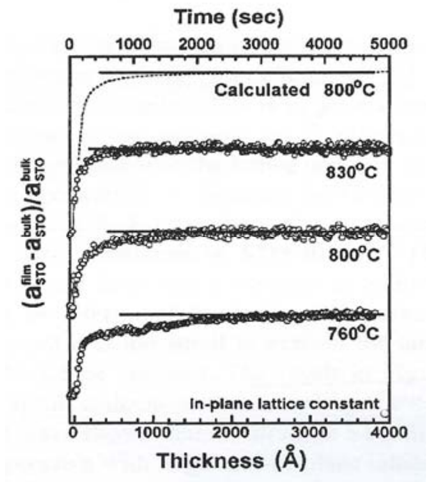

Figure 1-16: Strain in $SrTiO_3$ films on $LaAlO_3$ substrates as a function of film thickness and deposition temperature. A theoretically predicted curve for strain relaxation by misfit dislocations taking into account only the lattice constant mismatch between the film and the substrate at 800 °C is also plotted (28).

Peng et al. (28) reported on *in-situ* reflection high-energy electron diffraction study of strain relaxation during growth of $SrTiO_3$ thin films (Figure 1‑16). They found that the critical thickness that marks the start of strain relaxation is very small for substrates resulting in -3% and 7.5% misfit strains ($LaAlO_3$ and MgO substrates, respectively). The majority of the strain is relaxed quickly, but the complete strain relaxation takes place much more slowly until ~ 50 nm for $SrTiO_3$ films deposited at 830 °C. Furthermore, they showed that the strain relaxes much more slowly when the deposition temperature is reduced. For example, the thickness of complete strain relaxation increases from ~50 to ~250 nm when the deposition temperature changes from 830 to 760 °C. This is because less thermal energy is available at lower deposition temperatures to overcome the kinetic barrier for dislocation formation (29).

Twinning Domain formation in epitaxial films undergoing a phase transformation is a mechanism that relaxes the total strain energy, which is a result of the phase transformation, lattice mismatch, and the differences in thermal expansion coefficients of the film and the substrate (30). The degree of stress relaxation by dislocation generation plays a critical role in the final domain structure (27; 31). The following variants of the orientation of domain walls were assumed to be possible in epitaxial c- and/or a-axis oriented tetragonal PTO films grown on cubic substrates (Figure 1‑17):

(i) c/a/c/a polydomain state, where domain walls are parallel to the {101} crystallographic planes of the prototypic cubic phase so that they are inclined at about 45° to the film/substrate interface. This variant of domain geometry corresponds to the so-called *c/a/c/a* structure widely observed in epitaxial films of perovskite ferroelectrics. It is composed of *c*- and *a*-domains, where the *c*-axis is perpendicular and parallel to the substrate plane, respectively.

(ii) Domain walls are orthogonal to the film/substrate interface and oriented along the {110} planes of the prototypic cubic phase. This domain wall orientation is characteristic of the so-called ***$a_1/a_2/a_1/a_2$* structure**, where the spontaneous polarization develops in the film plane along the [100] and [010] axes within the a_1 and a_2 domains, respectively.

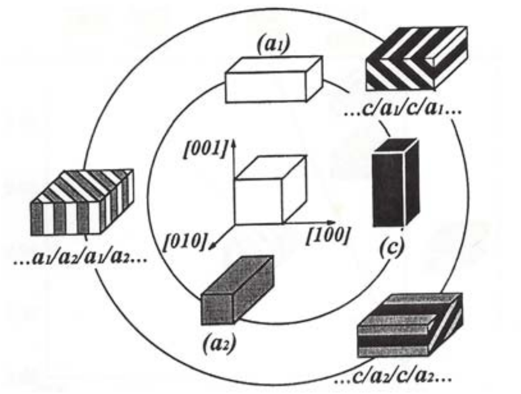

Figure 1-17: Possible domain structures of strained PTO films (30). The c/a$_1$/c/a$_1$ and c/a$_2$/c/a$_2$ polydomain structures are energetically equivalent and will be referred as c/a/c/a structure.

The domains are tilted by a small angle with respect to the film-substrate normal. The theoretical tilt angle α can easily be determined from the geometry of the polydomain structure (32) (Figure 1‑18 a) as

$$\alpha = 2\tan^{-1}\left(\frac{c_T}{a_T}\right) - \frac{\pi}{2} \ . \qquad (1.13)$$

The tetragonality of bulk PTO is 1.065 at room temperature, corresponding to a theoretical tilt angle of ~3.6°. Generally, the tilt is accommodated in both *a*- and *c*-domains, depending on their volume fractions. The tilt accommodation in both *a*- and *c*-domains (32) is schematically illustrated in Figure 1‑18 b. From the geometry, the tilts in each domain are

$$\frac{\tan\alpha_a}{\tan\alpha_c} = \frac{A}{1-A} \ , \qquad (1.14)$$

where A is the fraction of *c*-domains, and α_a and α_c are the tilts in the *a*- and *c*-domains, respectively. This domain structure results in a fourfold tilt of the *(h00)* and *(00l)* planes from the film-substrate normal along [*h00*], [-*h00*], [*0k0*] and [*0-k0*]. Many groups observed by XRD the fourfold splitting of *a*-domains (33; 34; 35; 36; 37). However, the fourfold symmetry of *c*-domains is observed only in films having significant fraction of *a*-domains (38; 39; 40).

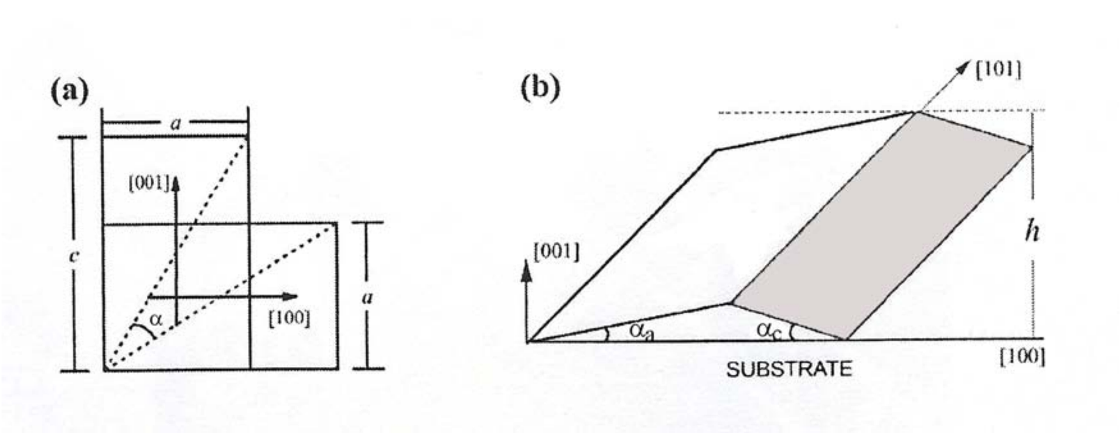

Figure 1-18: (a) The tilt in polydomain films consisting of a- and c-domains when brought together at the (101) interface due to the tetragonality of the lattice. (b) The accommodation of tilt in films consisting of a- and c- domains. The tilt angles are highly exaggerated (32).

1.6 Theoretical considerations on phase transitions in PTO thin films

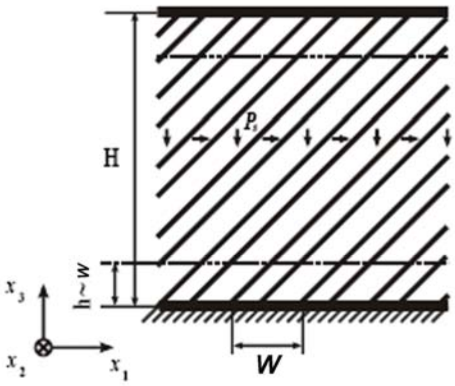

Figure 1-19: Schematic drawing of the dense c/a/c/a domain structure in epitaxial PTO films. The dashed lines indicate a thin layer near the film/substrate interface, where the internal stresses are highly inhomogeneous. The x_3 *axis is normal to the substrate plane, whereas the* x_1 *and* x_2 *axes are parallel to the in-plane crystallographic axes of the film proto-*

Koukhar et al. (31) thermodynamically described the dense laminar polydomain states in epitaxial PTO films using Landau-Ginsburg-Devonshire-type nonlinear phenomenological theory. This theory takes into account the mechanical substrate effect on the polarization and lattice strains in dissimilar elastic domains (twins). It is assumed that the polarization and strain fields are homogeneous within each domain. This approximation may be justified for dense polydomain states, where the domain widths W are much smaller than the film thickness H. In this case of dense structure, the polarization and strain fields become almost uniform within each domain in the inner region of the film, because highly inhomogeneous internal fields can exist only in two thin layers (h~W) near the film surface (Figure 1‑19). Authors also adopted the effective misfit strain concept, proposed by Speck et al. (27), that drives the formation of polydomain structures. For PTO films grown on dissimilar cubic substrates, the “misfit strain – temperature” phase diagrams are constructed, which shows the stability ranges of various possible polydomain and single-domain states (Figure 1‑20). At the negative misfit strains, except for a narrow strain range in the vicinity of $S_m=0$, the paraelectric-to-ferroelectric transformation result in the appearance of the tetragonal *c*-phase with the spontaneous polarization orthogonal to the substrate. Compressive in-plane stresses in the ferroelectric phase prevent the film from twinning at relatively high temperatures. However, during the further cooling the introduction of elastic *a*-domains into the *c*-phase becomes energetically favourable. This leads to the second-order transformation to the *c/a/c/a* polydomain state. At larger positive misfit strains, the $a_1/a_2/a_1/a_2$ polarization configuration becomes the most energetically favourable thermodynamic state in PTO films. Therefore, at positive misfit strains, the *c/a/c/a* structure is expected to form via nucleation of *c*-domains inside the $a_1/a_2/a_1/a_2$ state at critical temperature. The transformation from the *c/a/c/a* state to the $a_1/a_2/a_1/a_2$ state is of the first order. The equilibrium volume fraction of *c*-domains must increase during the film cooling. The ferroelectric-to-paraelectric phase transition is of the second order at positive and negative misfit strains S_m (except for a narrow range near $S_m=0$, where a direct transformation of the paraelectric phase to the polydomain *c/a/c/a* state occurs).

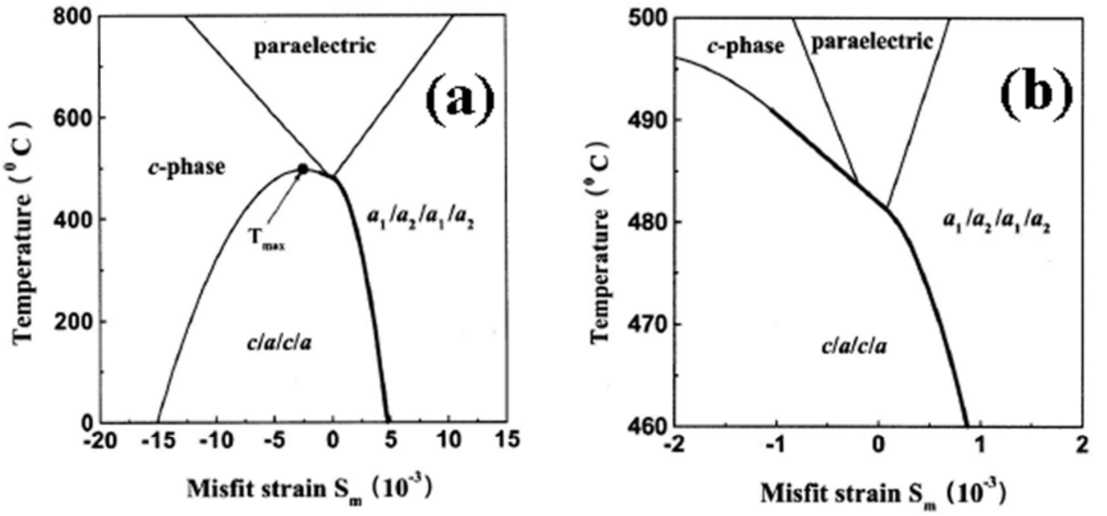

Figure 1-20: Phase diagram of PTO epitaxial films grown on cubic substrates (a). The continuous and discontinuous transformations are shown as thin and thick lines, respectively. Enlarged section of the diagram near S_m=0 is shown in (b).

Bibliography

1. Perovskites: Modern and Ancient. **Mitchell, R.H.** s.l. : Almaz Press, Ontario (C), 2002.

2. **A.F. Devonshire**, Philos. Mag., 1949, Vol. 40, p. 1040.

3. **A.F. Devonshire**, Philos. Mag., 1951, Vol. 42, p. 1065.

4. **A.F. Devonshire**, Adv. Phys., 1954, Vol. 3, p. 85.

5. **W. Cochran**, Phys. Rev. Lett., 1959, Vol. 3, p.412.

6. **W. Cochran**, Adv. Phys., 1960, Vol. 9, p.387.

7. **R.Comes, M. Lambert, and A. Guinier.** 10, s.l. : Solid State Commun., 1968, Vol. 6, p. 715.

8. **Y. Girshberg and Y. Yacobi**, Solid State Communications, 1997, Vol. 103, p. 425.

9. **Y. Girshberg and Y. Yacobi**, J. of Phys.: Condens. Matter, 1999, Vol. 11, p. 9807.10. **G. Shirane and S. Hoshino.** 4, s.l. : J. Phys. Soc. Jap., 1951, Vol. 6, p. 265.

11. **S.A. Mabud and A.M. Glazer.** s.l. : J. Appl. Cryst., 1979, Vol. 12, p. 49.

12. **Cohen, R.E.** s.l. : Nature (london), 1992, Vol. 358, p. 136.

13. **R.E. Cohen and H. Krakauer.** s.l. : Ferroelectrics, 1992, Vol. 136, p. 65.

14. *Principles and applications of ferroelectrics and related materials.* **M.E. Lines, A.M. Glass.** s.l. : Oxford:Clarendon Press, 1977.

15. **R.J. Nelmes and W.F. Kuhs.** s.l. : Solid State Commun., 1985, Vol. 54, p. 721.

16. **M.D. Fontana, H. Idrissi, G.E. Kugel, and K. Wojcik.** s.l. : J. Phys.: Condens. Matter, 1991, Vol. 3, p. 8695.

17. **M.D. Fontana, H. Idrissi, G.E. Kugel, and K. Wojcik.** s.l. : Ferroelectrics, 1988, Vol. 80, p. 117.

18. **N. Sicron, B. Ravel, Y. Yacoby, E.A. Stern, F. Dogan, and J.J. Rehr.** 18, s.l. : Phys. Rev. B, 1994, Vol. 50, p. 13168.

19. **Y. Yacoby, Y. Girshberg and E.A. Stern.** s.l. : Z. Phys. B, 1997, Vol. 104, p. 725.

20**. A. Sani, M. Hanfland, and D. Levy.** s.l. : J. Solid State Chem., 2002, Vol. 167, p. 446.

21. **J.D. Freire and R.S. Katiyar.** 4, s.l. : Phys. Rev. B, 1988, Vol. 37, p. 2074.

22. **G. Burns and B.A. Scott.** 7, s.l. : Phys.Rev. B, 1973, Vol. 7, p. 3088.

23. **F. Cerdeira, W.B. Holzapfel, and D. Bauerle.** 3, s.l. : Phys. Rev. B, 1975, Vol. 11, p. 1188.

24. **R.A. Frey and E. Silberman.** s.l. : Helvetica Physica Acta, 1976, Vol. 49, p. 1.

25. **C.M. Foster, Z. Li, M. Grimsditch, S.-K. Chan, and D.J.Lam.** 14, s.l. : Phys. Rev. B, 1993, Vol. 48, p. 10160.

26. *Ferroelectric Materials and Their Applications.* **Xu, Y.** s.l. : North-Holland, Amsterdam,, 1991.

27. **J.S. Speck and W. Pompe.** s.l. : J. Appl. Phys., 1994, Vol. 76, p. 466.

28. **L.S.-J. Peng, X.X. Xi, B.H. Moeckly, and S.P. Alpay.** 22, s.l. : Appl. Phys. Lett., 2003, Vol. 83, p. 4592.

29. **J.Y. Tsao, B.W. Dodson, S.T. Picraux, and D.M. Cornelison.** s.l. : Phys. Rev. Lett., 1987, Vol. 59, p. 2455.

30. **Roytburd, A.L.** s.l. : Phys. Status Solidi A, 1976, Vol. 37, p. 329.

31. **V.G. Koukhar, N.A.Pertsev, and R. Waser.** s.l. : Phys. Rev. B, 2001, Vol. 64, p. 214103.

32. **C.S. Ganpule, V. Nagarajan, B.K. Hill, A.L. Roytbard, E.D. Williams, S.P. Alpay, A. Roelops, R. Waser, and L.M. Eng.** s.l. : J. Appl. Phys., 2002, Vol. 76, p. 1477.

33. **B.S. Kwak, A. Erbil, J.D. Budai, M.F. Chisholm, L.A. Boatner, and B.J. Wilkens.** 21, s.l. : Phys. Rev.B, 1994, Vol. 49, p. 14865.

34. **M. de Keijser, D.M. de Leeuw, P.J. van Veldhoven, A.E.M. De Veirman, D.G. Neerinck, G.J.M. Dormans.** s.l. : Thin Solid Films, 1995, Vol. 226, p. 157.

35. **W.-Y. Hsu and R. Raj.** 6, s.l. : Appl. Phys. Lett., 1995, Vol. 67, p. 792.

36. **C.M. Foster, W. Pompe, A.C. Daykin, and J.S. Speck.** 3, s.l. : J. Appl. Phys., 1996, Vol. 79, p. 1405.

37. **K. Lee and S. Baik.** 81, s.l. : Annu. Rev. Mater. Res., 2006, Vol. 36, p. 81.

38 **.K. Kim, H. Morioka, R. Ueno, S. Yokoyama, H. Funakubo, K. Lee, and S. Baik.** s.l. : Appl. Phys. Lett., 2006, Vol. 88, p. 252904.

39. **C.M. Foster, Z. Li, M. Buckett, D. Miller, P.M. Baldo, L.E. Rehn, G.R. Bai, D. Guo, H. You, and K.L. Merkle.** 4, s.l. : J. Appl. Phys., 1995, Vol. 78, p. 2607.

40. **K.S. Lee and S. Baik.** 11, s.l. : J. Appl. Phys., 2000, Vol. 87, p. 8035.

Chapter 2:

Experimental techniques

Chapter 2

2 Experimental techniques ________________ *29*

2.1 Thin film deposition by pulsed liquid injection MOCVD system ________________ 32

2.1.1 PI MOCVD method ________________ 32
2.1.2 Metalorganic precursors ________________ 32
2.1.3 Substrates ________________ 33

2.2 X-ray diffraction ________________ 34

2.2.1 Film characterization in Bragg-Brentano and Shultz geometries ____ 34
2.2.2 Two dimensional ω-2Θ, ω-χ and reciprocal space maps ________ 38
2.2.3 High-temperature XRD ________________ 41
2.2.4 Determination of microstrains and average grain size ________ 42

2.3 Raman spectroscopy ________________ 44

2.3.1 Theoretical considerations ________________ 44
2.3.2 Spectrometer ________________ 45

2.4 Other characterization techniques ________________ 47

2.4.1 Atomic force microscopy ________________ 47
2.4.2 Determination of film thickness ________________ 47
2.4.3 Wavelength dispersive X-ray spectroscopy ________________ 48
2.4.4 Transmission electron microscopy ________________ 48

Bibliography ________________ 49

2. Experimental techniques

In this section we will give the main principles of the deposition method and of the characterisation techniques: X-ray Diffraction (Section 2.2), Raman Spectroscopy (Section 2.3) and other used techniques (Section 2.4)

2.1 Thin film deposition by pulsed liquid injection MOCVD system

$PbTiO_3$ thin films were deposited by Metalorganic Chemical Vapor Deposition (MOCVD). The principles of the CVD will not be presented here. Interested authors will find more information in devoted books. In this section, we will present the pulsed injection MOCVD (PIMOCVD). The main parameters to take into account for the process optimization will be resumed in Chapter 3.

2.1.1 PI MOCVD method

PTO thin film depositions were carried out by pulsed liquid injection MOCVD (PI MOCVD) technique in a vertical hot wall reactor (Figure 2- 1). The principle of the film deposition by MOCVD is the thermal decomposition of metalorganic precursor vapours on the surface of heated substrate. Pulsed liquid injection MOCVD is a modification of classical MOCVD (1). During PI MOCVD process, microdoses (few microlitres) of an organic solution containing a mixture of metal-organic precursors were repeatedly injected into a hot evaporator using a special computer controlled injector. The solution in the precursor container is under pressure of 1.5 bar Argon. Vapour mixture (precursor + solvent) formed after flash evaporation of micro-doses was transported by $Ar+O_2$ gas into a reaction chamber to a hot substrate. Main advantages of this technique are the reliability, an easy control of precursor feeding rate (by the drop frequency or the opening time), vapour and film composition (solution concentration). Moreover, precise and reproducible pulsed micro-dosing of precursor solution ensure growth like “digital”, and consequently a simple control of film thickness by pulse number. More details about PI MOCVD system can be found in Ref. (1; 2; 3). In our reactor, the substrate was heated by an external resistive furnace. We worked at low pressure (a few Torr) created by a mixture of oxygen and argon, and ensured by a rotatory pump. A liquid nitrogen trap was used to condensate the non-reacted vapours. After deposition, the system was filled with oxygen and the cooling rate was controlled by a programmed ramp of the furnace.

2.1.2 Metalorganic precursors

$Pb(thd)_2$ (thd – 2,2,6,6-tetramethyl-3,5-heptandionate) and $Ti(thd)_2(O^iPr)_2$ (O^iPr – i -propoxide) dissolved in toluene were used as precursors for PTO film deposition. They were synthesized and purified in our laboratory at Vilnius University. It is worth noting that the quality of precursors, especially of Pb(thd)$_2$, is crucial for obtaining good quality PTO films. For example, we tried to test some commercial Pb(thd)$_2$ precursors and we always had problems to prepare clear solutions without turbidity.

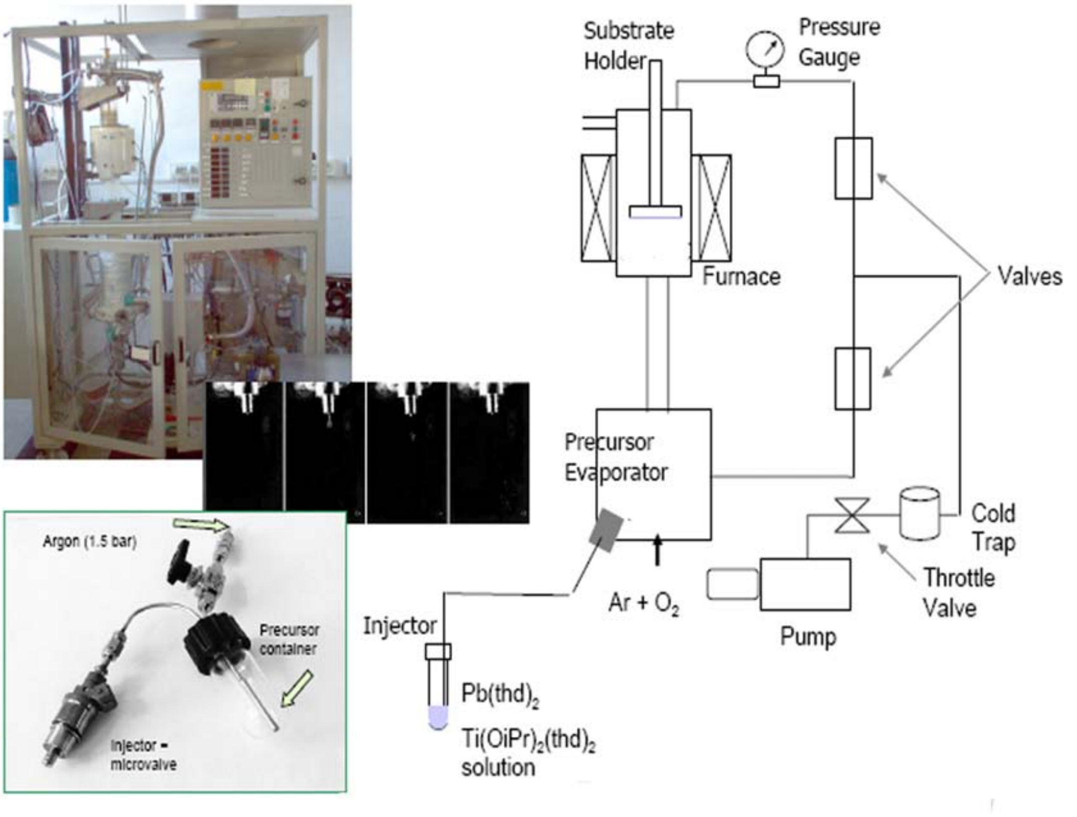
Substrate Holder
Pressure Gauge
Valves
Furnace
Precursor Evaporator
Cold Trap
Throttle Valve
Ar + O$_2$
Pump
Injector
Pb(thd)$_2$
Ti(OiPr)$_2$(thd)$_2$ solution
Argon (1.5 bar)
Precursor container
Injector - microvalve

Figure 2-1: PI-MOCVD reactor photo and schema. Photos of injector and injection process are also presented.

2.1.3 Subtrates

The choice of substrate materials for PTO deposition was based on their commercial availability. In order to span a wide range of misfit strains in epitaxial PTO films, they were deposited on the SrTiO$_3$ (STO), LaAlO$_3$ (LAO) and MgO substrates. In order to deposit polycrystalline PTO films, Al$_2$O$_3$ (sapphire (SAPH)) and Si substrates were used, as they have big lattice mismatch with PTO (Table 2-1). The substrates were supplied by CrysTec (Germany). The main characteristics of used substrates are given in Table 2-1 The substrates were washed for 10 min in toluene with ultrasonic bath before film deposition.

Table 2-1: Main characteristics of substrates and bulk PTO and misfit strains for all film/ substrate systems.

Material	Crystal structure	Surface cut parallel to	Lattice parameters (Å)		TEC (× 10^6 K^{-1})	Misfit strain at RT (%)		Misfit strain at T_{dep} (%)
			At RT	At T_{dep}				
PTO	tetragonal at RT, cubic at T_{Dep}	-	a=3.899 c=4.153	3.974	12.6 (*a*-axis) (4)	With PTO *a*-axis	With PTO *c*-axis	
STO	cubic	*(00l)*	3.905	3.932	11.5***	+0.1	-6.3	-1.1
LAO	pseudo-cubic*, cubic at T_{Dep}	*(00l)***	3.789	3.814	10.2***	-2.9	-9.6	-4.2
MgO	cubic	*(00l)*	4.212	4.251	14.8 (4)	+7.4	+7.4	+6.5
Al_2O_3	rhombo-hedral	R-plane	3.5	-	4.5 (5)	-11.4	-18.7	-
Si	cubic	*(00l)*	5.431	-	2.7 (6)	+28.2	+23.5	-

**rhombohedral with α = 90°05' at RT*
*** indices refer to the pseudo-cubic setting*
**** estimated from our high-temperature XRD results*

2.2 X-ray diffraction

X-ray diffraction (XRD) is a versatile, non-destructive technique that reveals detailed information about the phase composition and crystallographic structure of materials. A crystal lattice is a regular three-dimensional distribution (cubic, rhombic, etc.) of atoms in space. These are arranged so that they form a series of parallel planes separated from one another by a distance *d*, which varies according to the nature of the material. For any crystal, planes exist in a number of different orientations - each with its own specific *d*-spacing (Figure 2-2). Bragg's law says that when a monochromatic X-ray beam with wavelength λ is projected onto a crystalline material at an angle Θ, diffraction occurs only when the distance travelled by the rays reflected from successive planes differs by a complete number *n* of wavelengths.

2.2.1 Film characterization in Bragg-Brentano and Shultz geometries

Crystallization, phase purity, in-plane and out-of plane orientation of the films were studied by XRD in Bragg-Brentano and Schulz geometries using a SIEMENS D5000 diffractometer with monochromatic CuK_α radiation ($\lambda = 0.15418$ nm) and equipped with point detector. Standard Θ/2Θ-, ω- ,χ- and φ-scans and pole figure measurements were performed.

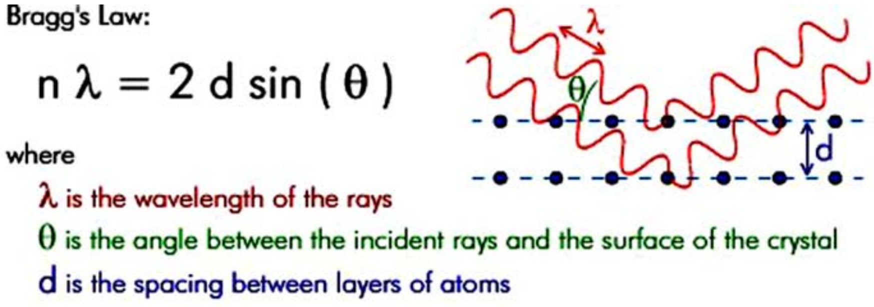

Bragg's Law:

$$n\lambda = 2d\sin(\theta)$$

where

λ is the wavelength of the rays

θ is the angle between the incident rays and the surface of the crystal

d is the spacing between layers of atoms

Figure 2-2: Bragg's law and scheme of X-ray diffraction from atomic planes.

Bragg-Brentano geometry By varying the angle Θ, the Bragg's law conditions are satisfied by different d-spacings in polycrystalline materials (Figure 2- 3). Only planes parallel to the surface will satisfy the Bragg’s law in Bragg-Brentano geometry, as shown in Figure 2- 3. Plotting the angular positions and intensities of the resultant diffracted peaks produces a so- called Θ/2Θ pattern, which is characteristic of the sample. Thus, in the case of thin films, Θ/2Θ scans are used to identify the phases and preferred orientations parallel to the normal of the substrate. In the case of polycrystalline materials, more diffraction reflections are observed than in single crystals due to random grain orientation as illustrated in Figure 2- 4.

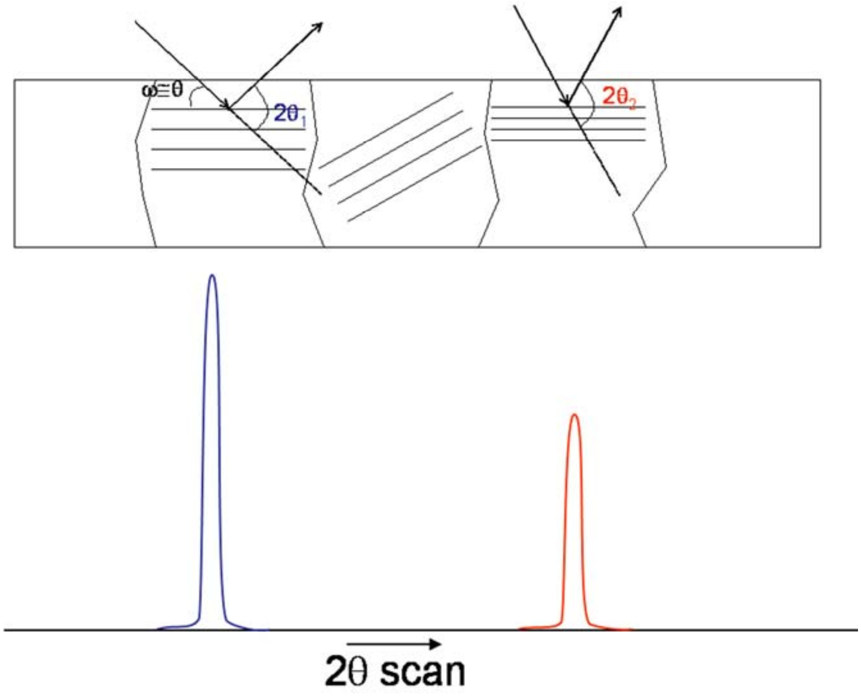

Figure 2-3: X-ray diffraction from planes parallel to the surface and resulting Θ/2Θ scan.

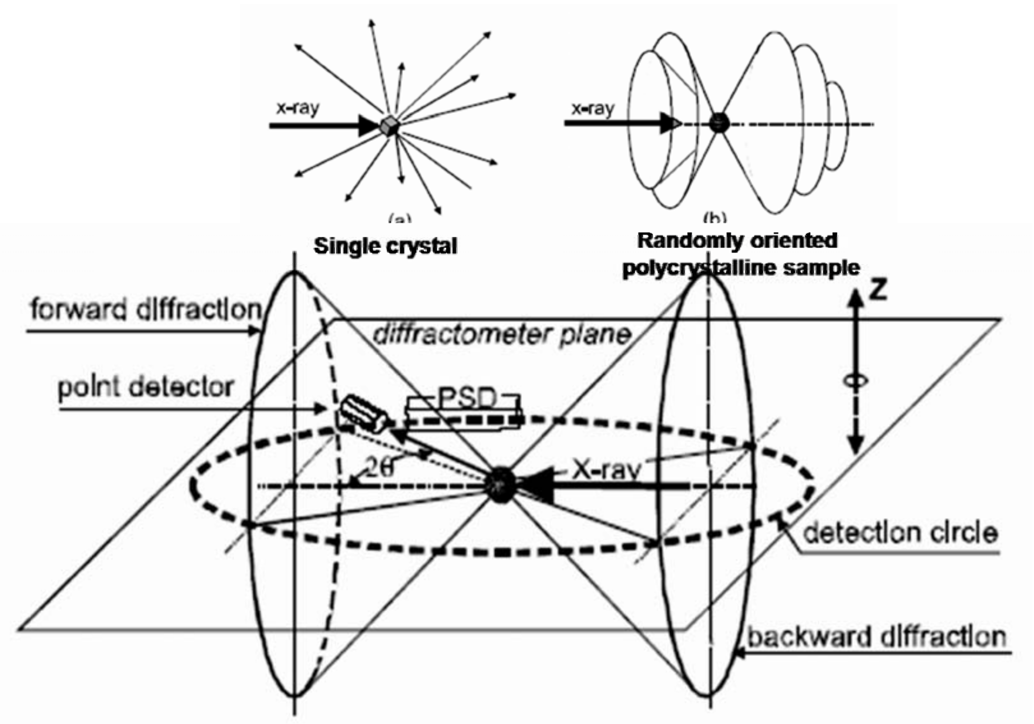
x-ray
x-ray
(a)
(b)
Single crystal
Randomly oriented polycrystalline sample
Z
forward diffraction
diffractometer plane
point detector
PSD
2θ
X-ray
detection circle
backward diffraction

Figure 2-4: Space distribution of X-ray diffraction from a single crystal and a polycrystalline sample. Scheme corresponding to $\Theta/2\Theta$ scan measurement by point detector in Bragg-Brentano geometry.

Shultz geometry Since the properties of the film, especially in epitaxial ones are strongly tied to the degree of texture, it is important to quantify the amount and type of preferred orientation. Moreover, the films may have specific orientation in the plane or twin structure. In order to characterize the microstructure of films, rocking curves (ω-scans), φ-scans and pole figure analysis of a single XRD reflection were performed in Shultz geometry (Figure 2-5).

Rocking curve of *(hkl)* reflection is measured by scanning ω incidence angle from $w=\Theta-\delta\omega$ to $\Theta+\delta\omega$ ($\delta\omega$ is usually a few degrees) at fixed 2Θ detector angle corresponding to Bragg’s position of this reflection. Rocking curve analysis is used to quantify grain size and mosaic spread in crystalline materials.

The ***φ-scans*** of *(hkl)* reflection is measured by scanning the φ-angles from 0 ° to 360 ° at fixed 2Θ, $\omega=\Theta$ and χ-angles, corresponding to each *(hkl)* reflection. The φ-scans are used to determine the film orientation in the film plane and its epitaxial relation with the substrate.

The ω- and φ-scan methods provide useful information about film texture and orientation in the substrate plane, respectively.

The ***pole figure*** analysis enables one to determine the distribution of crystalline orientations within a crystalline thin-film sample. It provides more complete information than the two simple methods mentioned above. Pole figure of *(hkl)* plane family is measured by systematically scanning φ- ($0° \leq \varphi \leq 360°$) and χ- angles ($0° \leq \chi \leq 90°$) at fixed Θ/2Θ angles corresponding to *(hkl)* reflection. The purpose of this measurement is to bring all the *(hkl)* family planes to the diffraction conditions. The diffracted intensity $I_{\Theta}(\chi,\varphi)$ is proportional to the volume of *(hkl)* planes, of which orientation is defined by χ and φ angles after corrections related to χ and 2Θ dependence. The pole figure is a two-dimensional projection of an hypothetical sphere surrounding the crystal to the plane (Figure 2-5).

The interpretation of the PTO diffraction diagrams was performed from the ICDD 00-006-0452 presented in Annexe 1.

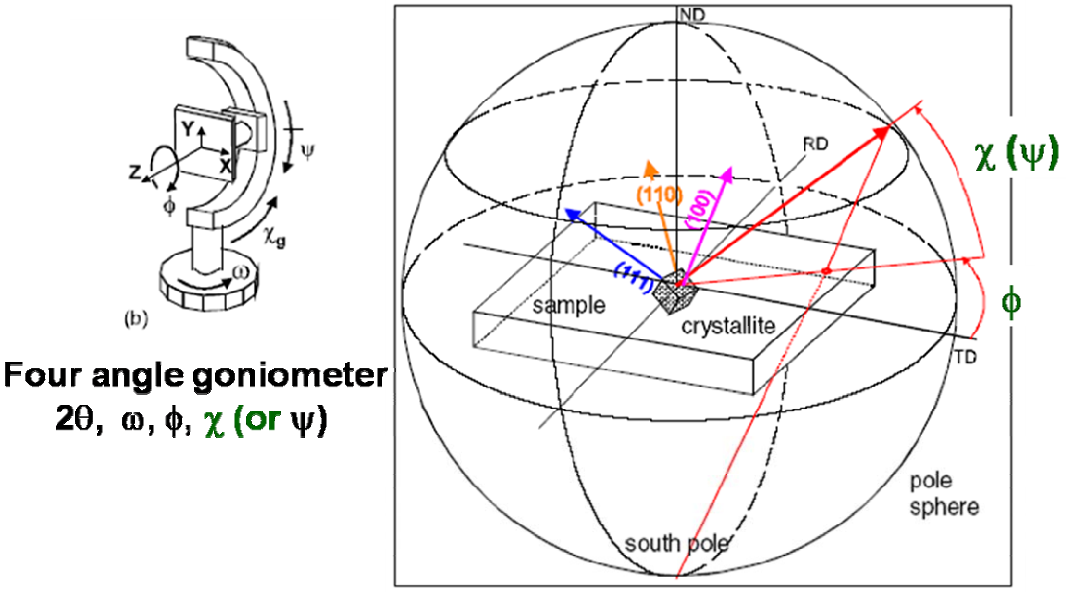

Figure 2-5: Four angles goniometer and the principle of measurements in Shultz geometry.

a-domain fraction estimation

In the case of *(00l)/(h00)* oriented (*c*- and *a*-axis oriented domains) epitaxial PTO films, the percentage of *a*-axis oriented domains (A, %) in the films was calculated by integration of peaks in φ-scans of *(102)* reflection:

$$A = \frac{2*(I(102)_{\chi=58^\circ} + I(102)_{\chi=62^\circ})}{2*(I(102)_{\chi=58^\circ} + I(102)_{\chi=62^\circ}) + I(102)_{\chi=27^\circ}} *100\% \qquad (2.1)$$

where I is the area of the peaks in φ-scans measured at different χ angles, corresponding to *a*-axis and *c*-axis oriented crystallites. χ angles were determined from χ-scans of *(102)* reflection. The χ-scans of *(102)* are measured by scanning χ-angles at fixed Θ/2Θ and

φ angles corresponding to *(102)* XRD reflection. However, the *(102)* reflections corresponding to *a*- and *c*-domains are measured at distinct χ-angles, what may lead to a variation of intensities due to defocusing of XRD beam on the sample surface. The defocusing corrections should be applied in order to take into account the diffracting volume change with the variation of χ-angle. The same fraction of material will give lower intensity at higher χ angles.

Thus, this *a*-domain volume fraction estimation method have been used only during PTO film deposition process optimization, as it is a simple and quick method to observe *a*-domain fraction change trend, despite the lower absolute values. In the case of thickness series of PTO films, which is the main object of our study, we chose a more precise method based on comparing *(103)*, *(301)* and *(310)* reflection peaks at approximately the same χ values, which will be discussed in the following section.

2.2.2 Two dimensional ω-2Θ, ω-χ and reciprocal space maps

Difractometers The reciprocal lattice completely describes a crystal, just as a real space lattice completely describes a lattice. Two dimensional mapping consisting of 10-20 reflections of the reciprocal space was performed using an automatic Nonius Kappa CCD diffractometer with four circles (Mo Kα radiation λ = 0.7071 Å) equipped with a 2-D detector (Figure 2- 6). A detailed study of the PTO film microstructure was carried out by analyzing 2-D ω-2Θ and ω-χ maps near *(103)* and *(301)/(310)* reflections (corresponding to *c*- and *a*-domains, respectively) by using a Bruker D8 Advance diffractometer with a four circles and General Area Detection Diffraction System (GADDS) ($\lambda_{CuK\alpha}$ 1.5418 Å, Ni filter) (Figure 2- 7 a and b). The latter measurements were performed at ICMAB, University of Barcelona, Spain. Large χ and 2Θ angle

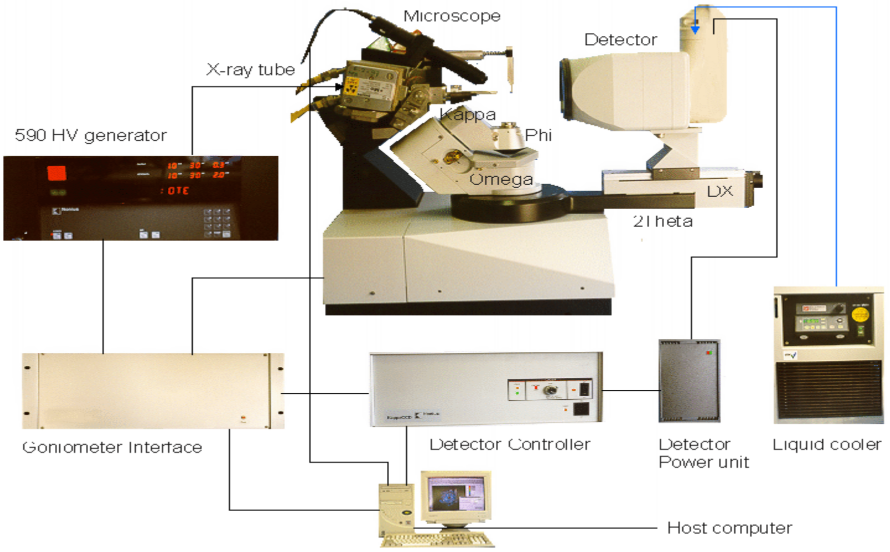

Figure 2-6: Automatic Nonius Kappa CCD diffractometer with four circles and equipped with 2-D detector.

is measured simultaneously by 2-D detectors with both diffractometers. The Bruker D8 Advance diffractometer is also equipped with a sample alignment system, which allows the correction of the sample height.

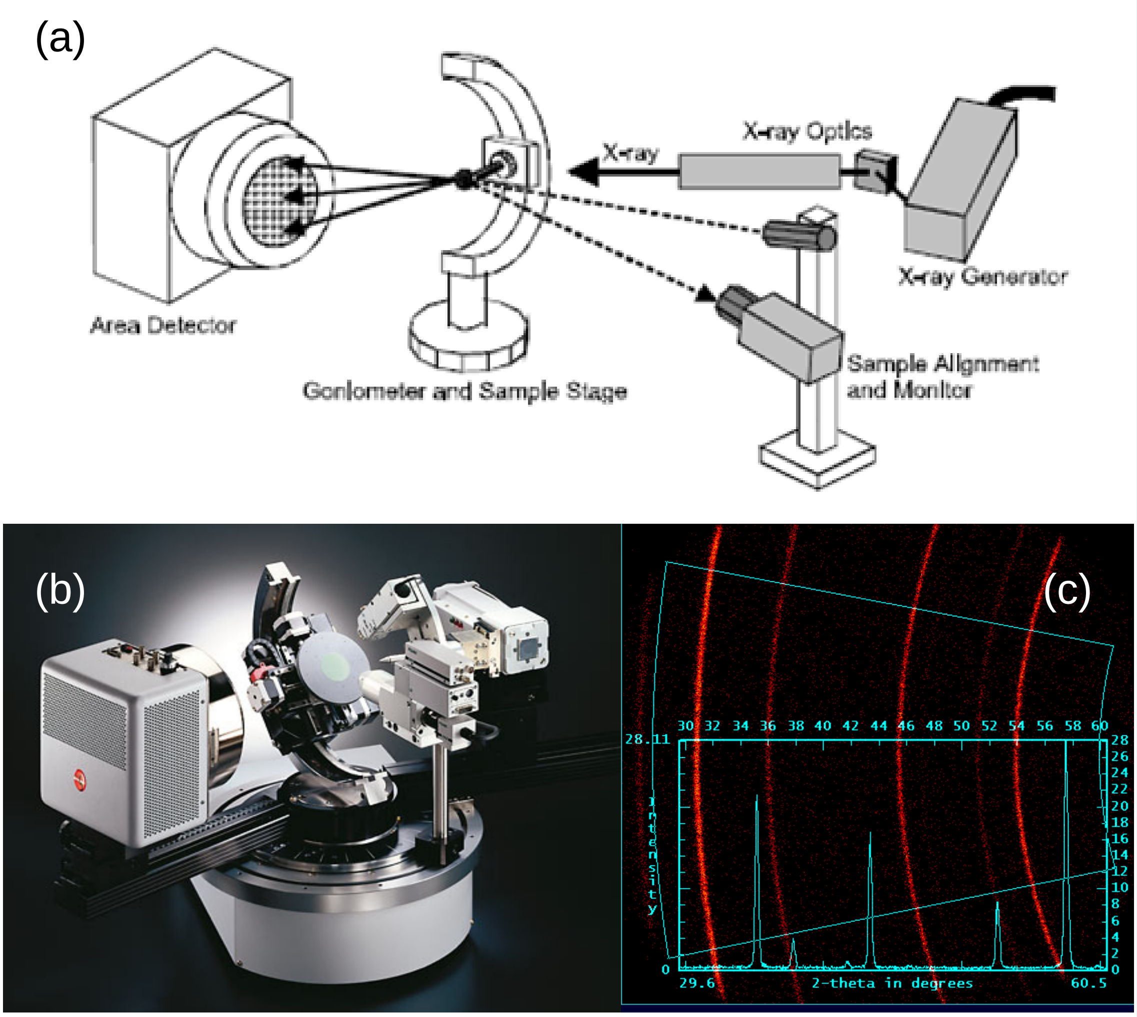
(a)
X-ray Optics
X-ray
X-ray Generator
Area Detector
Sample Alignment and Monitor
Goniometer and Sample Stage
(b)
(c)
30 32 34 36 38 40 42 44 46 48 50 52 54 56 58 60
28.11
Intensity
0
28 26 24 22 20 18 16 14 12 10 8 6 4 2 0
29.6
2-theta in degrees
60.5

Figure 2-7: Bruker D8 Advance diffractometer with a four circles and General Area Detection Diffraction System: scheme (a) and photo (b). Raw 2Θ-χ maps of polycrystalline sample and 2Θ-scan obtained by integration of the χ values (c).

2-D area maps The measurements of 2-D ω-2Θ, ω-χ area maps and reciprocal space maps of PTO thin films are performed with the same way by both diffractometers. Therefore, we will explain only the measurements (of ω-2Θ, ω-χ and reciprocal space maps) performed with the Bruker D8 Advance diffractometer.

The way to get the raw data for ω-2Θ, ω-χ and reciprocal space maps is following. 2Θ-χ map near *(103)* and *(301)/(310)* PTO reflections (in the range of 70 ≤ 2Θ ≤ 84 and -19°≤ χ ≤ 19°) at fixed ω-angle are measured simultaneously with 2-D detector. The example of raw 2Θ-χ map of a polycrystalline film is given in Figure 2-7 c. Two hundred of such 2Θ-χ maps are collected by varying ω-angle from 15° to 25° by step of 0.05°. Hereafter, the integration of χ-values is performed in each 2Θ-χ map that results in simple 2Θ spectrum at corresponding ω-angle. From these data, the matrix (x-2Θ, y-ω and z-intensity) is generated and used to plot ***2-D ω-2Θ area maps***. The reflections observed at the same 2Θ and ω angles but at different χ angles superimpose in 2-D ω-2Θ area maps.

2-D reciprocal space maps can be plotted from Q_x, Q_y and intensity values. The Q_x and Q_y values can be calculated from the 2Θ (from 2Θ scans obtained by integrating χ values) and corresponding ω values

$$Q_x = \sin\Theta \sin(\Theta - \omega) \tag{2- 2}$$

And

$$Q_y = \sin\Theta \cos(\Theta - \omega)\ . \tag{2- 3}$$

The ***2-D ω-χ area maps*** can be obtained by similar way: the integration of 2Θ values is performed and matrix is generated from obtained χ-scans and corresponding ω-angles.

Lattice parameter determination

In-plane and out-of-plane lattice parameters of *a*- and *c*-domains were estimated from *(301)/(310)* and *(103)* reflection positions (2Θ and ω angles), respectively. In the case of reflection split due to twinning (for ex. *(301)* reflection of *a*-domains), the average of 2Θ and ω values corresponding to two spots, were used. The substrate reflections were used as internal standard, assuming that it is strain free. Moreover, as mentioned above, the sample height was corrected. Q_x and Q_y values were calculated from corresponding 2Θ and ω values using Eq.2.2 and Eq. 2.3, respectively. Further, the in- plane ($P_{in\text{-}plane}$) and out-of-plane ($P_{out\text{-}of\text{-}plane}$) lattice parameters can be expressed through Q_x and Q_y of *(hkl)* reflection as follows:

$$P_{in-plane} = \frac{h\lambda_{CuK\alpha}}{2Q_x} \quad \text{or} \quad P_{in-plane} = \frac{k\lambda_{CuK\alpha}}{2Q_x} \tag{2- 4}$$

and $$P_{out-of-plane} = \frac{l\lambda_{CuK\alpha}}{2Q_y}\ . \tag{2- 5}$$

The accuracy in the determination of the cell parameters is about 0.0005 Å if reflections at sufficiently high 2θ are chosen for the analysis.

The out-of-plane lattice parameters of *c*-domains and *a*-domains were also estimated from *(00l)* reflections observed in standard Θ/2Θ scans, using Bragg's law.

In the case of PTO/SAPH films, for the calculation of the cell parameters we proceed in a different way, as films were polycrystalline and corresponding Θ/2Θ-scans have a good collection of peak positions. It was assumed that all the grains with different orientations have the same lattice parameters. The lattice parameters were calculated from a least square fitting, using the program UNITCELL (http://www.esc.cam.ac.uk/astaff/holland/UnitCell.html). The accuracy in the determination of the cell parameters is about 0.0002 Å and 0.0003 Å for *a* and c parameters, respectively.

Domain fraction estimation

The *a*-domain fraction in epitaxial PTO films was estimated from *a*-domain *(301)/(310)* and *c*-domain *(103)* spot in 2Θ-χ scans integrated area ratio.

$$A(\%) = \frac{IA(301) + IA(310)}{IA(301) + IA(310) + IA(103)} * 100\% \qquad (2\text{-}\ 6)$$

where IA- is an integrated area of spot. The intensities of the different reflections were corrected to their corresponding structure factors. The intensities for a PTO powder were used for the corrections (given in Annexe 1). The IA of *(103)*, *(301)* and *(310)* were divided by 6, 8 and 10 before applying Eq. 2.6, respectively.

The accuracy in the determination of the *a*-domain fraction is 1%. This method was used to estimate the domain fraction in thickness series of epitaxial PTO films.

2.2.3 High-temperature XRD

High-temperature XRD measurements were performed by using the Bruker D8 Advance diffractometer with a four circles and GADDS in the temperature range from RT to 300 °C in ICMAB (Barcelona, Spain). The diffractometer is equipped with home-made high-temperature cell. A thermocouple is inserted into a metal block where the sample is fixed. The ω-2Θ area maps for PTO films at different temperatures were obtained by the same way as at RT (section 2.2.2).

High temperature XRD measurements in the temperature range from RT to 650 °C were performed in SPMS (Ecole Centrale Paris). Standard Θ/2Θ scans were collected in Bragg-Brentano geometry, using a high precision goniometer (1 step = 0.0002° in 2Θ) with 18 kW rotating Cu anode generator ($\lambda_{CuK\beta}$ = 1.39223 Å).

2.2.4 Determination of microstrains and average grain size

Line profile analysis is used to obtain micro-structural information of the sample averaged over the diffraction volume. XRD reflections can be described by five parameters: position 2Θ, maximum intensity I_{max}, full width at half-maximum FWHM, integral breadth $\beta = \frac{\int I(2\Theta)d(2\Theta)}{I_{max}}$ and profile factor η (Figure 2- 8). The profile factor depends on the reflection nature (Lorentz, Gauss, pseudo-Voigt). FWHM and β depend on instrumental resolution and sample microstructure. Thus, it is necessary to correct observed profiles for the instrumental broadening.

For this reason, the microstructural analysis was performed using the program *Fullprof* (via the graphical interface *Winplotr*) (7). Within *Fullprof*, the microstructural effects are treated using Voigt approximation: both the instrumental and the sample intrinsic profile are supposed to be described approximately by a convolution of Lorentzian and Gausian components. The pseudo-Voigt profile function (the linear combination of Gauss and Lorentz functions) has been used to mimic the exact Voigt function. The pseudo-Voigt, Gauss and Lorentz functions are given in Table 2-2. All the profile functions (Table 2-2) used in Fullprof are normalized to 1.

Table 2-2: Mathematical functions used for fitting of XRD reflection profiles.

Pseudo-Voigt function	**Gaussian function**	**Lorentzian function**
$I = I_0(\eta L + (1-\eta)G)$	$G = I_0 \exp - \frac{\pi(2\Theta - 2\Theta_0)}{\beta_G^2}$	$L = I_0 \frac{1}{1 + \frac{\pi(2\Theta - 2\Theta_0)^2}{\beta_L^2}}$

The observed FWHM (in the following H) values H^{obs} were corrected for the instrumental broadening H^{inst} to determine intrinsic contribution of the sample H^{sample}:

$$H_G^{sample} = \sqrt{(H_G^{obs})^2 - (H_G^{inst})^2} \tag{2.7}$$

for Gausian component, and

$$H_L^{sample} = H_L^{obs} - H_L^{inst} \tag{2.8}$$

for Lorentzian component.

The integral breadth of the Gaussian and Lorentzian functions are $\beta_G^{sample} = \frac{H}{2}\sqrt{\frac{H_G^{sample}}{\ln 2}}$ and $\beta_L^{sample} = \frac{\pi H_L^{sample}}{2}$, respectively. In our analysis, the instrumental resolution function was deduced from the $SrTiO_3$ substrate XRD reflections measured in the same conditions.

Crystalline materials which do not contain lattice strain and consist of particle sizes larger than 500 nm, show sharp lines in a powder diffractogram. Imperfections in the structure of the crystallites result in broadening of the diffraction line profiles. Large crystallites give rise to sharp peaks; as the crystallite size reduces, the peak width increases and the intensity decreases. Peak broadening can also originate from variations in lattice spacings, caused by lattice strain. Several analysis methods exist to calculate crystallite sizes and lattice strain separately from diffraction line broadening for example Williamson-Hall and Halder-Wagner methods.

Williamson-Hall analysis The classical Williamson-Hall representation (8) was used to separate the broadening caused by crystallite size from that arising from local strain (microstrains). This method is applicable for reflections with Lorentzian profiles. The integral breadth can be expressed as the summation of integral breadths resulting from size effect (β_D) and microstrains (β_e)

$$\beta^{sample} = \beta_D + \beta_e \quad . \tag{2.9}$$

In this representation, the reciprocal integral breadth

$$\beta^*_{sample} = \frac{\beta_{sample}\cos\Theta}{\lambda} \quad , \tag{2.10}$$

expressed in $Å^{-1}$, is plotted as a function of the reciprocal-lattice spacing

$$d^* = \frac{2\sin\Theta}{\lambda} \quad . \tag{2.11}$$

According to the Williamson-Hall relation

$$\beta^*_{sample} = \frac{1}{D} + ed^* \quad , \tag{2.12}$$

the slope of the graph depends linearly on the lattice strain *e* and the intercept varies as the inverse of the average grain size *D*. The average grain size and microstrains are estimated in the direction perpendicular to the *(hkl)* planes.

Halder-Wagner approximation Halder-Wagner approximation (9) can be applied for pseudo-Voigt profiles. In this method, the integral breadth is

$$\beta_{sample}^{2} = \beta_{L}\beta_{sample} + \beta_{G}^{2} \quad . \tag{2.13}$$

The Gausian and Lorentzian integral breadth can be expressed as follows

$$\beta_{L} = \frac{1}{D} \quad and \quad \beta_{G} = e\frac{d*}{2} \quad . \tag{2.14}$$

Thus, the Eq. 2-13 can be expressed as

$$\left(\frac{\beta_{sample}^{*}}{d^{*}}\right)^{2} = \frac{1}{D}\left(\frac{\beta_{sample}^{*}}{d^{*2}}\right) + \left(\frac{e}{2}\right)^{2} \tag{2.15}$$

The slope of the $\left(\frac{\beta_{sample}^{*}}{d^{*}}\right)^{2} = f\left(\frac{\beta_{sample}^{*}}{d^{*2}}\right)$ curve gives 1/D and the value of microstrains can be estimated from the intercept. The average grain size and microstrains are estimated in the direction perpendicular to the *(hkl)* planes.

2.3 Raman spectroscopy

Raman spectroscopy is a useful technique for the characterization of ferroelectrics. The Raman signal is sensitive to internal as well as external perturbation of lattice vibrations. This may affect the position, line width, line shape and intensity of the signal. Examples of such perturbations are symmetry breakdown due to phase transition, temperature, strain or lattice disorder. A careful analysis of Raman spectra can provide information about different material properties related to these perturbations.

2.3.1 Theoretical considerations

The principle of Raman effect is based on the inelastic scattering of light in matter. Considering a monochromatic electromagnetic field in a dielectric mater, a weak intensity can be detected at different frequencies due to scattering with the creation (stokes) or annihilation of vibrations (antistokes) (Figure 2-9). The scattering intensity of Stokes Raman process assuming a harmonic oscillator approximation is given by

$$I = C\sum_{\Gamma}\left|\vec{e}_{i}.R(\Gamma).\vec{e}_{d}\right|^{2} \tag{2.16}$$

where C is a constant, $\vec{e}_{i}$ and $\vec{e}_{d}$ are the polarizations of incident and scattered lights, and R(Γ) is the polarization tensor of phonons at Γ-point (the center of the Brillouin zone).

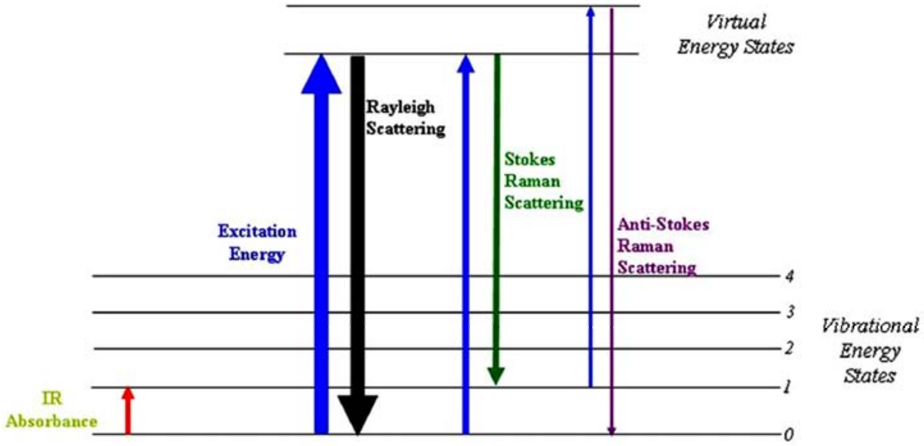

Figure 2-9: Raman effect - the inelastic scattering of light in matter with the creation (stokes) or annihilation of vibrations (antistokes).

In practical use, Raman scattering is revealed by exciting a material with a monochromatic light (laser) of well known energy $\hbar\upsilon_i$, momentum $\vec{k}_i$ and polarization $\vec{e}_i$ and collecting scattered photons of different energy $\hbar\upsilon_d$, momentum $\vec{k}_d$ and polarization $\vec{e}_d$. In the first order Raman scattering, the one-phonon process must fulfill the energy and momentum conservation:

$$\hbar\upsilon_i - \hbar\upsilon_d = \pm\hbar\upsilon_q \tag{2.17}$$

$$\vec{k}_i - \vec{k}_d = \vec{q} \tag{2.18}$$

Where $\hbar\upsilon_q$ and $\vec{q}$ are the energy and momentum of phonon. From the above relations, one can see that the phonons correspond to a momentum q~0 (long wavelength), i.e. belonging to the Γ-point of the Brillouin zone.

2.3.2 Spectrometer

Raman spectra were collected using a Jobin-Yvon/Horiba LabRam spectrometer. Experiments were conducted in the micro-Raman mode at room temperature in a backscattering geometry i.e., the wave vectors of incident photons $\vec{k}_i$ and scattered photons $\vec{k}_d$ are antiparallel (Figure 2– 10).

The incident source is provided by an air cooled multimode Ion Argon Laser (Melles Griot 35-LAP-431). We used in all experiments the 514.532 nm wavelength. In this region $PbTiO_3$ is transparent and we didn’t observe other sources of radiations such as fluorescence. The output power measured at the objective was about ~7 mW. No heating effect has been detected.

The excited beam is focused and the scattered light is collected through an Olympus BX41 microscope with the objective. We used two different Olympus objectives a x100 (N.A.=0.9) and x50 Long Working Distance (N.A.=0.5) their characteristics are given in Table 2-3.

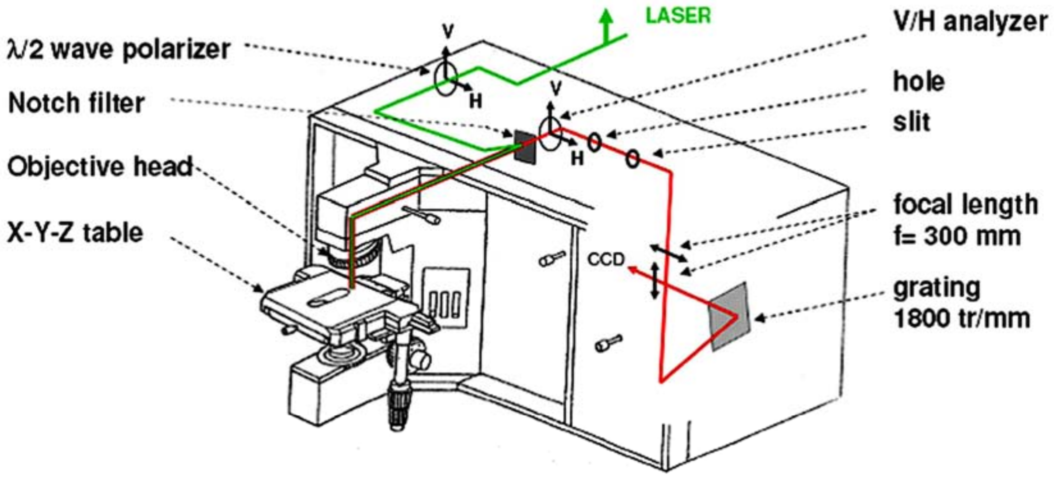
λ/2 wave polarizer
Notch filter
Objective head
X-Y-Z table
LASER
V
H
V
H
V/H analyzer
hole
slit
focal length
f= 300 mm
CCD
grating
1800 tr/mm

Figure 2-10: Raman spectra collection in backscattering geometry with Jobin-Yvon/Horiba LabRam spectrometer. The incident (green line) and scattered (red line) beams are represented and some optical component has been omitted for better reading.

The system is equipped with a notch filter rejecting the laser line. Figure 2–10 shows that the notch filter is used to send the laser beam to the microscope and to separate the Raman signal from sample reflection and Rayleigh scattering. In our investigation we study optical phonons above 70 cm^{-1} due to the limitation of the notch.

Table 2-3: x50 LWD and x100 objective characteristics.

Olympus objective	N.A. (sinφ)	Half angle (φ)	Lateral resolution D (Diffraction limit)* $D = \frac{1.22\lambda}{NA}$	Depth of focus d_f * $d_f = \frac{4n\lambda}{\pi(NA)^2}$
X100 MPlan	0.9	64^{o}	0.7 µm	1.3 µm
X50 LMPlanFi Long Working distance (~1 cm)	0.5	30^{o}	2 µm	7 µm

**n-refraction coefficient, λ-wavelength*

A 300 mm monochromator and nitrogen cooled 1024 x 256 spectra-one CCD disperse and collect the signal in a single shot from about 0 to 1500 cm^{-1} (Stokes side) with a spectral resolution of 1.7 cm^{-1}.

The polarization of the incident beam is controlled by a l/2 wave plat. Two positions are used in reference to spectrometer: vertical position (V) or horizontal position (H) (Figure 2–10). Also, the output polarization is selected before entering into the spectrometer by a two-position analyzer in vertical (V) or horizontal (H). For the analyzer in H position, the spectrometer intensity response is about a third of that in V position. As a consequence, the counting time should be adapted.

The system was calibrated using Si spectra at ambient temperature. The integration times were adjusted in order to have a high signal-to-noise ratio.

Dark field Raman spectroscopy measurements were performed with the same type of spectrometer in LMOPS (Metz, France).

The temperature measurements in the range from room temperature to 600 °C have been carried out by using a commercial LINKAM heating stage placed under the Raman microscope.

The fitting procedure of Raman spectra was performed with program PeakFit of Jandel using Lorentzian profiles. The background was adjusted by a line subtraction from spectra.

2.4. Other characterization techniques

2.4.1 Atomic force microscopy

Our sample surface morphology and roughness Ra (Ra - roughness average) were characterized using AFM - Digital instruments Multimode Scanning Probe Microscope in tapping mode.

2.4.2 Determination of film thickness

PTO film thicknesses were determined by two methods:

i) PTO films on Si were etched with concentrated HF in order to form a step for thickness determination by profilometry.

ii) Thickness of the films on other substrates was determined from the film cross-section images obtained by SEM (Philips XL30).

2.4.3 Wavelength dispersive X-ray spectroscopy

Wavelength dispersive X-ray spectroscopy (WDS) analysis was used for the evaluation of the film composition.

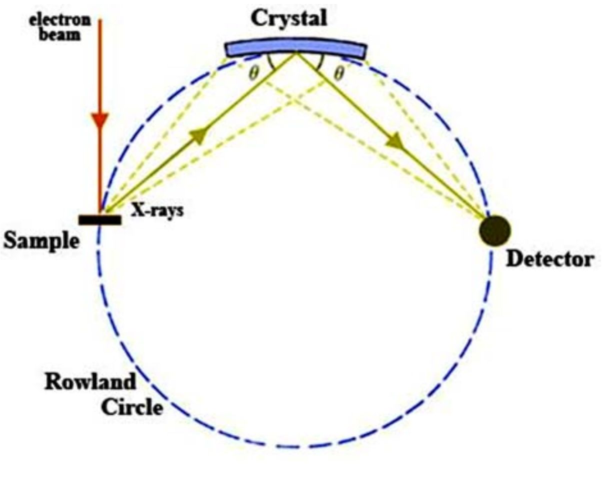

Figure 2-11: Principle of WDS analysis.

Principle A wavelength-dispersive spectrometer uses the characteristic X-rays generated by individual elements to enable quantitative analyses (down to trace element levels) to be performed at spot sizes as small as a few micrometers. When an electron beam of sufficient energy interacts with a sample target it generates x-rays, which are selected using an analytical crystal(s) with specific lattice spacing(s) (Figure 2- 11). The geometry of the X-ray generating sample and the analytical crystal is such that they maintain a constant take-off angle. When X-rays encounter the analytical crystal at a specific angle Θ, only those X-rays that satisfy Bragg's Law are reflected and a single wavelength is passed on to the detector. The wavelength of the X-rays reflected into the detector may be varied by changing the position of the analyzing crystal relative to the sample i.e. the X-ray source-crystal distance is a linear function of the wavelength. Consequently, X-rays from only one element at a time can be measured on the spectrometer and the position of a given analytical crystal must be changed in order to adjust to a wavelength characteristic of another element.

Measurements at different acceleration voltages (10, 15 and 20 kV for our samples) were performed in order to take into account that the film thickness is usually higher than penetration depth of electrons. Results were analyzed by specific program for thin films Strata, which allows estimating the film composition. The accuracy of composition determination by WDS is 5 %.

2.4.4 Transmission electron microscopy

PTO film domain structure, epitaxial quality and defect density were studied by transmission electron microscopy (TEM) in cross section. The samples were prepared by mechanical polishing (tripode technique) perpendicular to the film. The final thinning was performed by ion beam polishing (beam +8°-8° at 3,5KeV during 30 – 60 min). The observations on the film cross sections were carried out with TEM JEOL 2011.

Bibliography

1. **J.P. Senateur, F. Weiss, O. Thomas, R. Madar, and A. Abrutis.** s.l. : Patent 93/08838 PCT FR94/00858 (Europe, USA).

2. *Advances in Inorganic Films and Coatings.* **J.P. Senateur, A. Abrutis, F. Felten, F. Weiss, O. Thomas, and R. Madar.** s.l. : Ed. Vincenzin P, Italy:Techna srl., 1995.

3. *Innovative processing of films and nanocrystalline powders.* **J.P. Senateur, C. Dubourdieu, V. Galindo, F. Weiss, and A. Abrutis.** s.l. : Ed. K.-L. Choy, London: Imperial College Press, 2002.

4. **K.S. Lee and S. Baik.** s.l. : Annu. Rev. Mater. Res., 2006, Vol. 36, p. 81.

5. **http://www.crystec.de/daten/.**

6. **http://www.ioffe.rssi.ru/SVA/NSM/Semicond/Si/thermal.html.**

7. **T. Roisnel and J. Rodriguez-Carvajal.** s.l. : Mat. Sc. Forum, Proc. 7th Eur. Powder Diffraction Conference (EPDIC 7) Ed. R. Delhez and E.J. Mittenmeijer., 2000, p. 118.

8. **G.K. Williamson and W.H. Hall.** s.l. : Acta Metall., 1953, Vol. 1, p. 22.

9. **N.C. Halder and C.N.J. Wagner.** s.l. : Acta Cryst., 1966, Vol. 20, p. 312.

Chapter 3:

$PbTiO_3$ thin film deposition by PI MOCVD, process optimization

Chapter 3

3 PbTiO$_3$ thin film deposition by PI MOCVD, process optimization ______ *51*

3.1 Partial oxygen pressure effect on the film composition ______55

3.2 Deposition temperature influence on film composition and morphology______56

3.3 PbO desorption control with film growth rate ______59

3.4 Deposition pressure influence on growth rate______60

3.5 Deposition temperature influence on the film microstructure _60

Conclusions ______63

Bibliography ______65

3. $PbTiO_3$ thin film deposition by PI MOCVD, process optimization

High-quality epitaxial ferroelectric films are needed in prospect of new devices (1, 2) as ferroelectric properties originate from the structural anisotropy. Epitaxial PTO films have been grown by metalorganic chemical vapor deposition (MOCVD) (3–7), pulsed laser deposition (PLD) (8, 9) and rf-magnetron sputtering (10). Among various preparation methods, MOCVD has been recognized as the most promising technique due to the possibility to grow films on large area with high growth rate and good conformal step coverage.

In the literature, mainly liquid $PbEt_4$ and $Ti(O^iPr)_4$ compounds were used as precursors for MOCVD growth of PTO films by bubbling of carrier gas through containers of liquid precursors (4, 5, 11–15). However, some other pairs of Pb and Ti precursors have been also studied: $Pb(thd)_2$ (thd = 2,2,6,6-tetramethyl-3,5-heptanedionate) and $Ti(O^iPr)_4$ (16–19), $(C_2H_5)_3PbOCH_2C(CH_3)_3$ and $Ti(O^iPr)_4$ (20), $Pb(OAc)_2$ and $Ti(OnBu)_4$ (21), $PbEt_4$ and Ti-n-propoxyde (22) or $PbEt_4$ and $TiCl_4$ (23). Only several works (24, 25) can be found on the use of solid $Pb(thd)_2$ and $Ti(O^iPr)_2(thd)_2$ or $TiO(thd)_2$ precursors for PTO depositions. In these works, the vapor phase was generated by flash evaporation of a mixture of solid Pb and Ti precursors supplied into an evaporator. Solid metalorganic precursors are often preferred because they are non-toxic and more stable at room temperature as compared with liquid and extremely toxic tetraethyl lead precursor. In the last years single source liquid injection MOCVD techniques have been more and more used for the growth of multi-component oxide layers. These techniques additionally offer easier control of multi-component film composition and better process reproducibility than conventional CVD.

Most of PTO film studies are related to structural properties; some papers deal with ferroelectric and dielectric properties (26-30) and a few ones about piezoelectric properties are available (29, 30). In our study, $Pt/PbTiO_3/La_{1-x}Sr_xMnO_3/LaAlO_3$ (Pt/PTO/LSMO/LAO) heterostructures were grown and their microstructure, morphology and electrical properties were studied and given in Annex 2, as it is out of scope of this thesis.

In the present chapter we report on the role of oxygen partial pressure, deposition temperature and solution composition in the growth of $PbTiO_3$ films by pulsed liquid injection MOCVD using $Pb(thd)_2$ and $Ti(O^iPr)_2(thd)_2$ precursors dissolved in toluene. The influence of such parameters on film microstucture, composition and morphology was studied. Also it will be discussed on the role of system pressure, solution concentration and injection frequency on the growth rate and composition of $PbTiO_3$ films. The used deposition conditions of PTO films are summarized in Table 3- 1.

Table 3-1: Deposition conditions for $PbTiO_3$ layers grown by PI-MOCVD.

Substrates	$SrTiO_3$ (100), $LaAlO_3$ (001 – in a pseudo-cubic setting), sapphire (R-plane), Si (001)
Substrate temperature (T_{Dep}), °C	550 - 750
Evaporation temperature, °C	280
Transport gas	Ar + O_2
Total gas flow rate, l/h	60
Oxygen fraction (F_{ox}), %	7 - 50
Total pressure (P_T), Torr	2 - 10
Precursors	$Pb(thd)_2$, $Ti(thd)_2(O^iPr)_2$
Solvent	Toluene
Solution concentration (total, c_T), mol/l	0.02 - 0.08
Injection frequency (ν_{inj}), Hz	1 or 2
Thickness, nm	100-300

3.1 Partial oxygen pressure effect on the film composition

In order to test the oxygen effect on Pb content of the film, PTO films were grown (at T_{Dep}=650 °C, P_T = 5 Torr, c_T = 0.04 M, ν_{inj} = 2 Hz, and $Pb(thd)_2$:$Ti(thd)_2$ $(O^iPr)_2$=44:56) at four different oxygen partial pressures. Composition analysis showed that the maximum Pb content in films was obtained using 37.5 % oxygen in the gas flow (Figure 3-1a). The maximum growth rate (1.03 μm/h) of the films was obtained also at 37.5 % O_2. L.S. Hong et al. (12) established that an increase of O_2 concentration in gas promotes the PbO formation resulting in higher growth rate. However, too high oxygen concentration resulted in Pb deficient films, that was explained by stabilization of high valency Pb_3O_4 and PbO_2 at higher O_2 partial pressures (12). The optimum percentage of oxygen in the gas flow is highly dependent on the precursor type and its thermal stability. For example, in case of $Pb(C_2H_5)_4$ only 1 % of O_2 in gas flow was sufficient (12), while in our case it was necessary to use much more of oxygen. In further depositions we used 37.5 % oxygen in the gas flow.

Pb may be lost from PTO film during post-deposition treatment at higher temperatures or during the slow cooling after deposition at high deposition temperature. To get more information about the lead loss at high temperatures, several series of rapid thermal annealing (RTA) for 10 min at different temperatures and oxygen partial pressures were carried out. The composition of annealed films was analyzed by WDS and results are given in Figure 3– 1b. The films started to lose Pb at 700 °C and the Pb loss rate rapidly increased with the further increase of annealing temperature. The lead content did not change after annealing at lower temperatures. One can see in Figure 3-1 b that the Pb desorption rate can be reduced by increasing oxygen partial pressure. It means that during cooling high oxygen pressure stabilizes the $PbTiO_3$ phase in our films. In order to minimize the Pb loss, we used 0.4 atm O_2 pressure during film cooling from high deposition temperature.

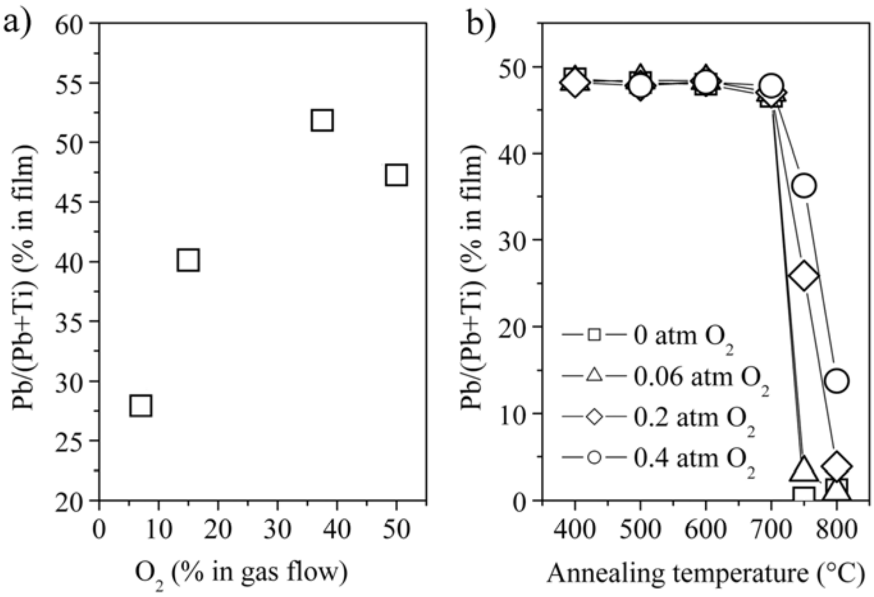

Figure 3-1: Pb content in PTO/LAO films: a) influence of oxygen percentage in gas flow during deposition, b) influence of annealing temperature and oxygen partial pressure.

3.2 Deposition temperature influence on film composition and morphology

Series of films were deposited at different temperatures in varying the composition of the solution (P_T = 5 Torr, c_T = 0.04 M, F_{ox} = 37.5 % and v_{inj} = 2 Hz). The composition of films deposited on $LaAlO_3$ was analyzed by WDS. The results are given in Figure 3-2. It is evident, that higher deposition temperatures require higher Pb precursor content in solution for achieving of the right cationic proportion in film. This may be related to higher lead oxide desorption at higher temperatures. At low T_{dep} = 550 °C the Pb content in film increases continuously with increasing the Pb content in solution. At higher deposition temperatures the Pb fraction in film increases until near stoichiometric value and after remains almost stable during further increase of the Pb content in solution. The minimum Pb content in solution necessary for achieving right Pb:Ti ratio in film may be named as “stoichiometric“. Although films grown from solution with Pb precursor excess may have right cationic ratio, they consist not only of tetragonal $PbTiO_3$ phase but also have some additional phases ($PbTi_{0.8}O_{2.6}$, PbO).

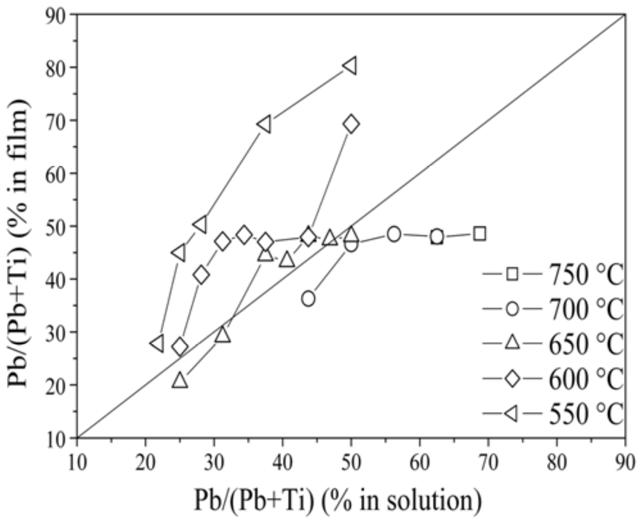

Figure 3-2: Composition of PTO/LAO films in relation with film composition.

The morphology of PTO films is very dependent on the solution composition especially for epitaxial films on LAO and SrTiO$_3$ substrates (Figure 3-3). Films grown from Pb deficient or “stoichiometric” solutions on both substrates have similar surface morphologies. On the other hand, the morphology of PTO films on sapphire is fully determined by island growth at all deposition temperatures resulting in rather rough film surface (Ra = 3–7 nm). Layers grown from solution with Pb deficit are made up of two zones, which become better separated in films deposited at higher temperatures (Figure 3-3). XRD showed that these films consisted of PTO tetragonal and pyrochlore phases (Figure 3-4). One zone is very smooth and the second one consist of small crystallites. As these different zones are clearly visible by using the optic microscope, Raman spectra in each zone have been measured (Figure 3-5). One can see that the smooth zone consists only of tetragonal PTO phase. The other zone presents a phase with lower symmetry than tetragonal PTO—it can be considered as monoclinic pyrochlore phase. Such film morphology (called “rosette-shaped”) was also observed by other authors (31 –33) and was considered as perovskite islands in a pyrochlore matrix. With the increase of Pb content in solution, smooth PTO zones increase in size and all the surface become smooth at Pb/Ti = 1 in film. The morphology of PTO films is defined by two factors: island growth and twinning (this aspect will be discussed in detail in next section). The twinning results in a film morphology with perpendicular line shaped zones (34). At higher temperatures, the twinning becomes the leading factor for surface morphology of PTO films. For example, the morphology of films grown at 650 °C and higher temperatures is mainly determined by twinning. Less twinned zones are observed in films grown at 600 °C. The morphology of films deposited at 550 °C is completely determined by island growth resulting in a rather rough surface compared to that of the twinned layers. Thus, the roughness of the films grown from “stoichiometric” solutions decreases with the increase of deposition temperature (Figure 3-6), and Ra reaches a very low value, 0.6 nm for films grown at 750 °C.

PTO films grown on STO substrates from solutions with Pb excess consist of spherical grains forming the structure of lines (Figure 3-3). Such structure becomes more ordered with increasing growth temperature and at 700 °C the lines are quasi parallel. In contrast, films on LAO substrates consist also of spherical grains but the line shaped structure is not observed.

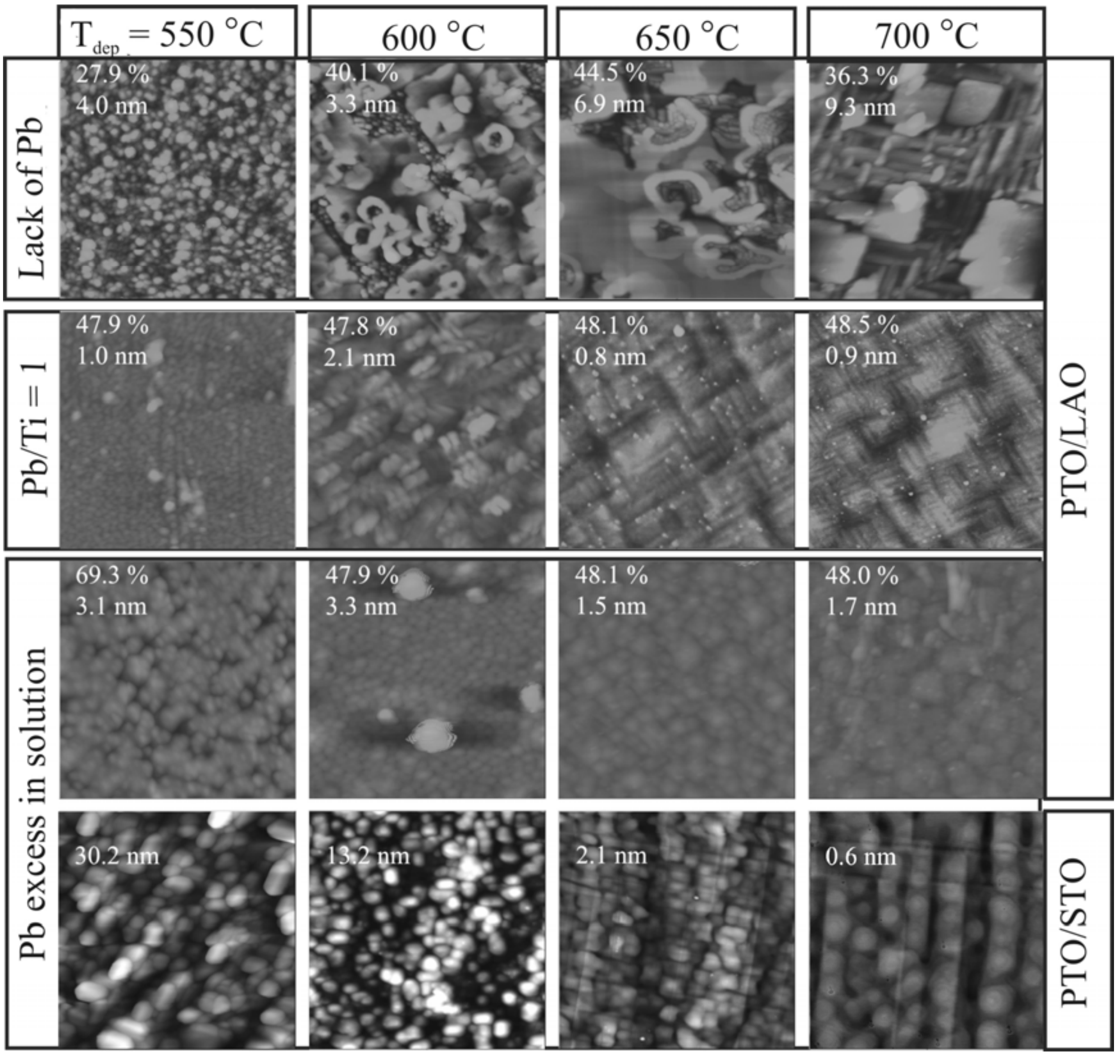
T_dep = 550 °C
600 °C
650 °C
700 °C
Lack of Pb
27.9 %
4.0 nm
40.1 %
3.3 nm
44.5 %
6.9 nm
36.3 %
9.3 nm
Pb/Ti = 1
47.9 %
1.0 nm
47.8 %
2.1 nm
48.1 %
0.8 nm
48.5 %
0.9 nm
Pb excess in solution
69.3 %
3.1 nm
47.9 %
3.3 nm
48.1 %
1.5 nm
48.0 %
1.7 nm
30.2 nm
13.2 nm
2.1 nm
0.6 nm
PTO/LAO
PTO/STO

Figure 3-3: AFM images (2 × 2 μm^2) of various compositions PTO/LAO and PTO/STO films deposited at different temperatures. The average roughness Ra and Pb/(Pb+Ti) (% in film) are given on photos.

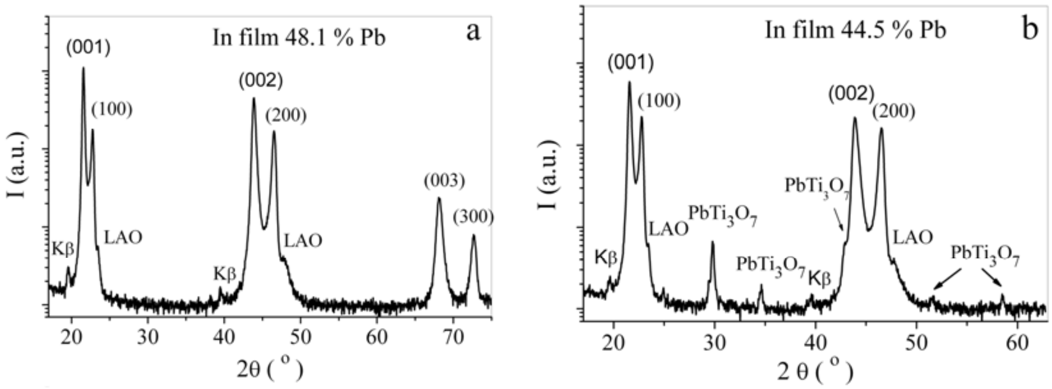

Figure 3-4: XRD patterns of (a) stoichiometric and (b) Pb deficient PTO/LAO films grown at 650 °C.

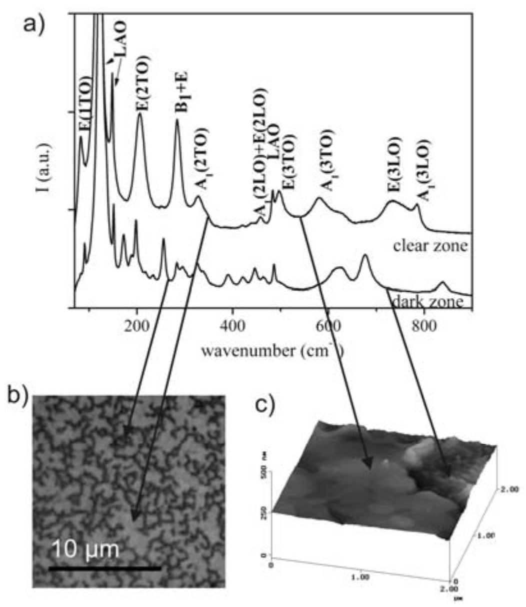

Figure 3-5: Identification of two zones with different morphology in Pb deficient PTO/ LAO film: a) Raman spectra of two zones, b) image of optic microscope and c) AFM image.

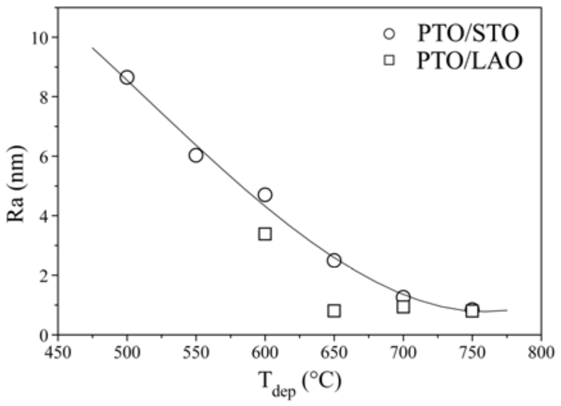

Figure 3-6: Roughness average (Ra) of PTO films versus deposition temperature (Pb/ Ti=1).

3.3 PbO desorption control with film growth rate

As shown above, Pb fraction in the film grown at higher temperatures ($T_{Dep}\geq 600$ °C) increases until near stoichiometric value and after remains almost stable with further increase of the Pb content in the solution. Thus, Pb excess cannot be reached in the film. In order to observe the maximum Pb/Ti ratio in the film which can be reached by varying the growth rate, lead deficient films were studied. Series of PTO films were deposited at 600 ˚C by varying the total solution concentration (0.02 M, 0.04 M or 0.08 M) and injection frequency (1 Hz or 2 Hz) while the precursors' ratio in solution (Pb/(Pb+Ti) = 28.1 %) and other deposition conditions were kept constant (P_T = 5 Torr, F_{ox} = 37.5 %, c_T = 0.04 M (varying ν_{inj}) and 2 Hz (varying c_T)). The variation of film composition

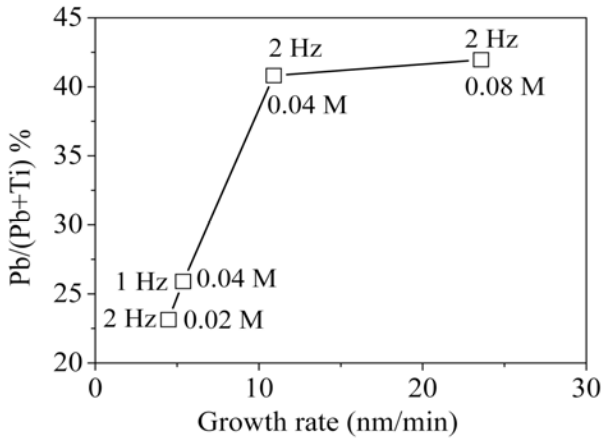

Figure 3-7: PTO/LAO film composition evolution as a function of growth rate.

with growth rate is shown in Figure 3-7. Pb content in the film increases with increasing growth rate from 4.9 to 10.9 nm/min and saturates when sufficiently high growth rates (> 10.9 nm/min) are reached. Deposition with low growth rate results in high Pb desorption from the film. For high growth rates, Pb loss highly decreases and film composition becomes defined mainly by Pb/Ti ratio in solution and precursors' decomposition rates at deposition temperature. In order to obtain Pb/Ti = 1 in the films grown with rates > 10.9 nm/min, Pb/(Pb+Ti) ratio in the precursor solution should be increased from 28.1 % to 31.3 % or more. The 0.04 M total concentration and 2 Hz injection frequency were chosen as optimal conditions for further deposition investigation.

3.4 Deposition pressure influence on growth rate

In order to test the influence of deposition pressure on PTO film growth, films were grown (at T_{Dep}=650 °C, c_T = 0.04 M, F_{ox} = 37.5 % and ν_{inj} = 2 Hz) at three different pressures (2, 5 and 10 torr). The surface of layers deposited at 2 torr of pressure was completely covered by spherical particles, probably due to precursor decomposition in the reactor volume, thus this pressure was discarded from further investigation. Stoichiometric film was reached using 0.020 M and 0.023 M $Pb(thd)_2$ concentrations (at c_T=0.04 M) for depositions carried at 5 torr and 10 torr pressure, respectively. The growth rates of stoichiometric PTO films at 5 torr and 10 torr were 20.6 nm/min and 18.8 nm/min, respectively. P. Lu et al.(35) also reported a growth rate decrease of PZT films with increasing pressure. As lower growth rate enhances Pb desorption, higher concentration of lead precursor was needed to obtain stoichiometric PTO at higher pressures.

The results of our studies on PTO deposition suggest the possibility to control accurately the film growth rate and film composition is important for reproducing stoichiometric PTO films. Therefore, PI-MOCVD is a promising method as it offers an easy control of precursor feeding rate, vapour and film composition.

3.5 Deposition temperature influence on the film microstructure

XRD spectra of PTO films on LAO and STO substrates grown from "stoichiometric" solutions consist only of *(00l)* and *(h00)* reflections (Figure 3-8a) corresponding to *c*-axis and *a*-axis oriented crystallites, respectively (further they will be called as *c*-domains and *a*-domains). The best crystallinity was obtained for films deposited at 650 °C. PTO/SAPH films are polycrystalline with a slightly *(101)* preferred orientation (Figure 3-8b).

PTO films on both STO and LAO substrates have very good in-plane orientation, as seen from pole figure for *(102)* reflection given in Figure 3-9. Double peaks (splitted in χ angle) appear in pole figure of *a*-domains due to domains twinning (for more details about twinning see in section 1.5.2).

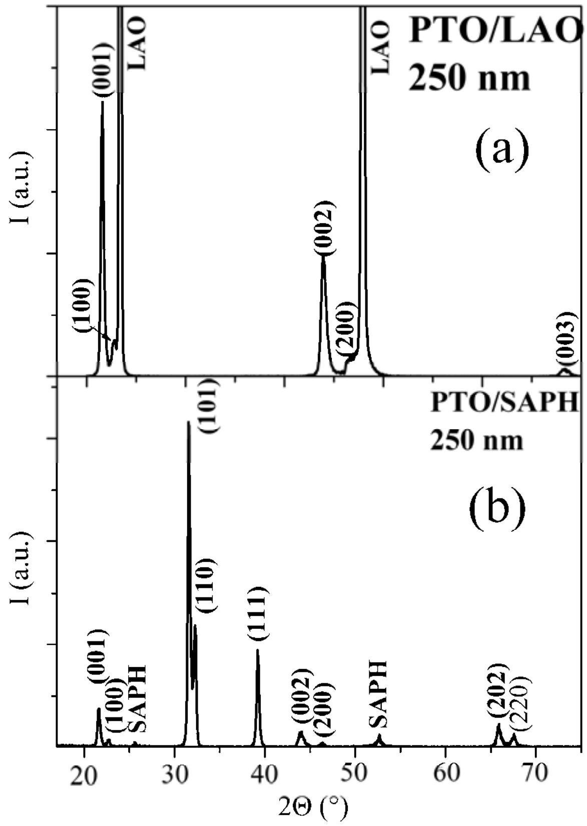

Figure 3-8: θ/2θ X-ray diffraction pattern of 250 nm thick PTO/LAO (a) and PTO/SAPH (b) films.

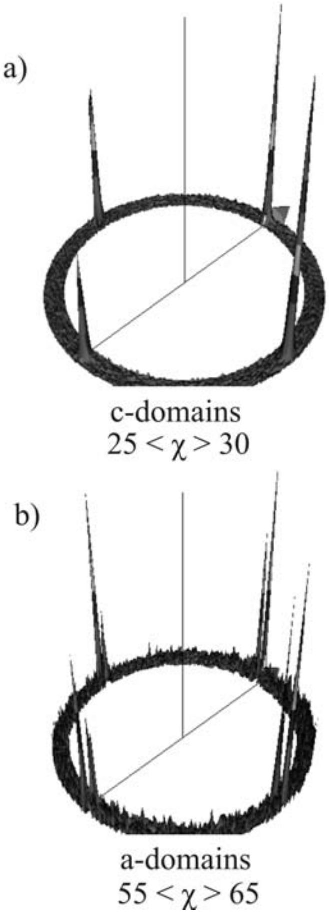

Figure 3-9: Pole figure of (102) reflection of PTO/LAO film grown at 650 °C.

As it is known, *a*-domains and *c*-domains in epitaxial ferroelectric films are tilted by a small angle from the substrate plane normal due to the twinning phenomenon (3). The *a*-domains and *c*-domains are bounded by the *(101)* twin plane, and this results in a tilt of [100] axis in *a*-domains, the tilt angle depending on the tetragonality of the cell (for c/a = 1.065 the tilt angle is 3.7 °) (3) (section 1.5.2). The tilt angle also depends on the domain volume fraction (36). For films with a high fraction of *c*-domains, the *c*-domain tilt angle is very small (37). Twinning is responsible for double rocking curves of *(00l)* and *(h00)* reflections and for the split in χ angle of peaks in pole figures (Figure 3-9) of *a*-domains. Rocking curves of *(001)* reflection of PTO/LAO films deposited at different temperatures are given in Figure 3-10. As mentioned about the surface morphology, twinning becomes a dominant factor when deposition is taken out at 650 °C or higher temperatures whereas the microstructure of layers deposited at lower temperatures is mainly determined by island growth. When layer is fully twinned (grown at $T_{Dep} \geq 650$ °C), the *(001)* rocking curve is double (Figure 3-10). The rocking curves for films

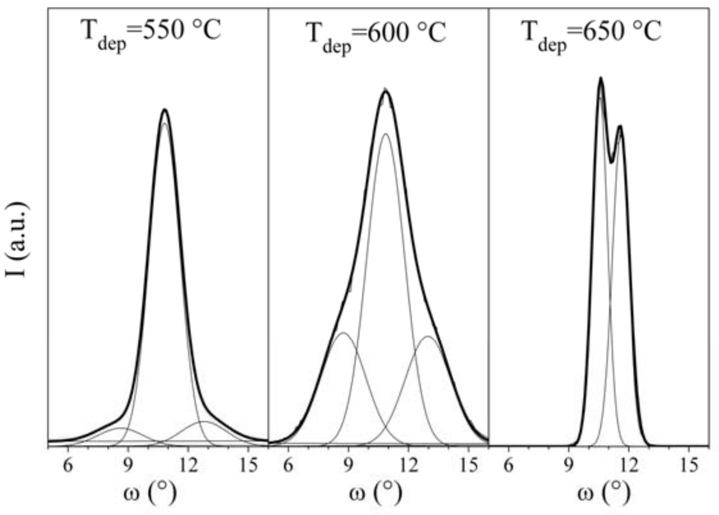

Figure 3-10: Evolution of (001) rocking curves in c-domains of PTO/LAO films with deposition temperature.

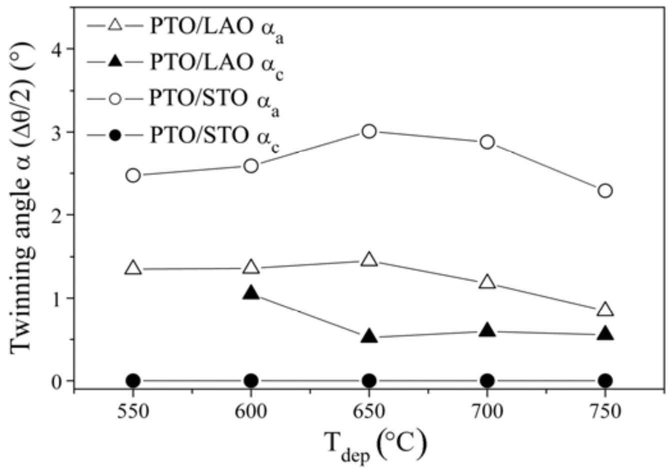

Figure 3-11: Evolution of twinning angles in a- and c-domains with deposition temperature.

deposited at lower temperatures are different. They become triple for films grown at 600 °C and lower temperatures: the peaks on both sides correspond to twinned zones and the central peak to non-twinned zones. This is in agreement with the fact that films grown at temperatures ≤ 600 °C are less or non-twinned and less textured than films obtained at higher temperatures. The twinning angles (tilt angles) for *a*- and *c*-domains (α_a and α_c respectively) in PTO films grown at various temperatures were estimated from rocking curves of *(001)* and *(100)* reflections and are given in Figure 3-11. PTO films on STO have highly dominant *c*-axis texture, so no split of rocking curve of *(001)* reflection in *c*-domains was observed. It is possible that the tilt angle of *c*-domains is too small to be detected.

PTO films grown at various temperatures on STO and LAO substrates consist of both *a*- and *c*-domains (Figure 3-12). However, the *c*-domain growth is dominant for all range of deposition temperatures because the *a*-parameter of PTO cell matches better the parameter of the substrate cell. The *a*-domain fraction was calculated by integration of peaks in φ-scans corresponding to *a*- and *c*-domains, as explained in section 2.2.1.The quantity of *a*-axis (A, %) textured crystallites in PTO films is clearly related to the deposition temperature and reaches minimum in highly crystalline films grown at 650 °C. As *a*-domains form only due to twinning, C.S. Ganpule et al. (34) proposed a relation between the twinning angles of *a*- and *c*-domains and the *a*-domain fraction (section 1.5.2). This relation perfectly works for our PTO films on STO and LAO substrates: $\tan\alpha_c/\tan\alpha_a$ linearly depends on A/(1-A) (Figure 3-13). The bigger the amount of *a*-domains, the bigger the tilt angle of *c*-domains and the smaller the twinning angle of *a*-domains.

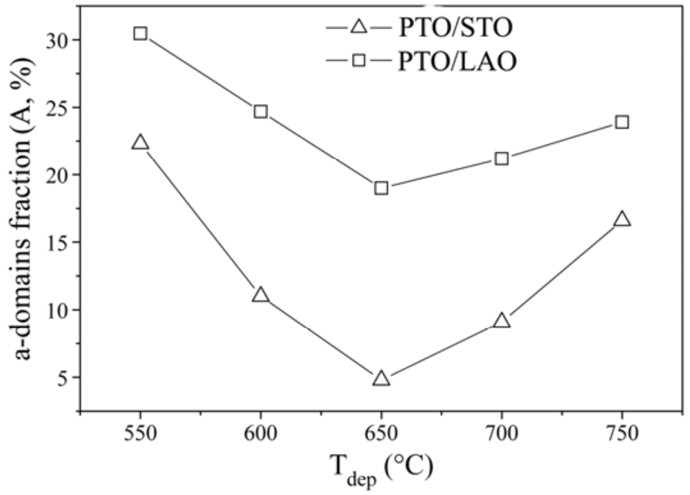

Figure 3-12: Evolution of a-domains percentage (A, %) in films with deposition temperature.

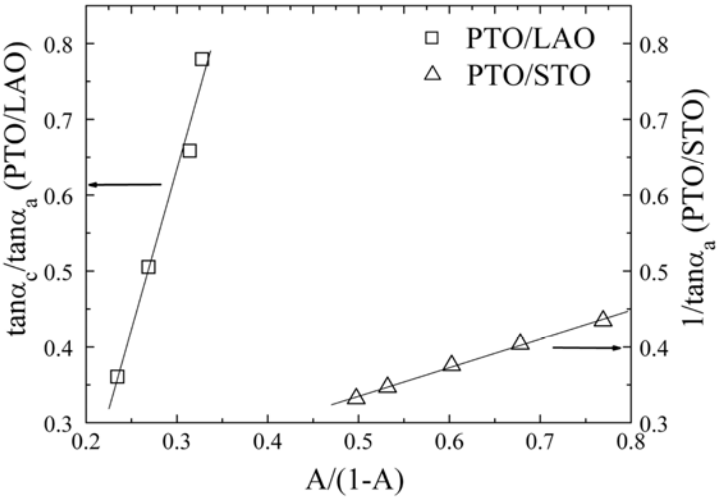

Figure 3-13: Relation between twinning angle and a-domain fraction (A/(1-A)) in PTO films.

Conclusions

The influence of various deposition conditions (deposition temperature, partial oxygen pressure, deposition pressure, injection frequency, solution concentration and solution composition) was examined for the growth of $PbTiO_3$ films on various substrates by pulsed liquid injection MOCVD.

The oxygen partial pressure influences the Pb loss during the film growth and post deposition thermal treatments. The maximum Pb/(Pb+Ti) ratio in the film was obtained using 37.5 % O_2 in the gas flow during the deposition. The Pb loss during the cooling from high growth temperature can be reduced using high O_2 pressure (0.4 atm).

The evolution of film composition, microstucture and morphology with solution composition at different deposition temperatures was investigated. Higher deposition temperatures require a higher concentration of Pb precursor in solution to achieve the right cationic proportion in the film. This may be related to higher Pb desorption at higher temperatures. The solution composition and growth temperature highly influence the film morphology and microstructure. Epitaxial films on perovskite substrates consist of dominant *c*-axis and minor *a*-axis textured zones (*c*-domains and *a*-domains). The surface morphology is mainly determined by island growth for films grown at $T_{Dep} \leq 600$ °C and by twinning phenomenon for films grown at $T_{Dep} \geq 650$ °C.

The growth rate and composition of PTO films were studied as a function of deposition pressure, solution concentration and injection frequency. It was shown, that Pb desorption can be governed by changing the film growth rate.

Fully twinned or partially twinned films can be obtained by varying deposition conditions. Twinning is observed in both *a*- and *c*-domains and twinning (tilt) angles depend on *a*-domain fraction. The best crystallinity and the lowest *a*-domain fraction were obtained in epitaxial films grown at 650 °C on $LaAlO_3$ *(001)* and $SrTiO_3$ *(001)* substrates.

The optimized deposition conditions are summarized in Table 3- 2.

Table 3-2: Optimized deposition conditions for $PbTiO_3$ layers grown by PI-MOCVD

Substrate temperature (T_{Dep}), °C	650
Evaporation temperature, °C	280
Transport gas	Ar + O_2
Total gas flow rate, l/h	60
Oxygen fraction (F_{ox}), %	37.5
Total pressure (P_T), Torr	5
Precursors	$Pb(thd)_2$, $Ti(thd)_2(O^iPr)_2$
Solvent	Toluene
Solution concentration (total, c_T), mol/l	0.04
Injection frequency (ν_{inj}), Hz	2

Bibliography

1. **C.H. Ahn, J.-M. Triscone, J. Mannhart**, Nature, 2003, Vol. 424, p. 1015.

2. **S.B. Desu**, Phys. Status Solidi A,1994, Vol. 141, p. 119.

3. **M. de Keijser, D.M. de Leeuw , P.J. van Veldhoven, A.E.M. De Veirman, D.G. Neerinck, G.J.M. Dormans,** Thin Solid Films, 1995, Vol. 266, p. 157.

4. **Y.-F. Chen, T. Yu, J.-X. Chen, L. Shun, P. Li, N.-B. Ming**, Appl. Phys. Lett., 1995, Vol. 66, No. 2, p. 148.

5. **C. Schmidt, E.P. Burte,** Microelectron. Reliab., 1999, Vol. 39, p. 257.

6. **H. Funakubo, K. Nagashima, K. Shinozaki, N. Mizutami,** Thin Solid Films, 2000, Vol. 368, p. 261.

7. **I.E. Korsakov, A.R. Kaul, L. Klippe, J. Korn, U. Krause, M. Pulver, G. Wahl,** Microelectron. Eng., 1995, Vol. 29, p. 205.

8. **Y.K. Kim, S.S. Kim, H. Shin, S. Baik,** Appl. Phys. Lett., 2004, Vol. 84, No. 25, p. 5085.

9. **Y.M. Kang, S.C. Bae, J.K. Ku, S. Baik**, Thin Solid Films,1998, Vol. 312, p. 40.

10. **K. Wasa, Y. Haneda, T. Sato, H. Adachi, K. Setsune,** Vacuum,1998, Vol. 51, No. 4, p. 591.

11. **C.-Y. Pan, D.-S. Tsai, L.-S. Hong,** Mat. Chem. Phys., 2001, Vol. 70, p. 223.

12. **L.S. Hong, C.C. Wei,** Mat. Lett., 2000, Vol. 46, p. 149.

13. **C. Byon, J.W. Jang, B.-W. Lee,** Mat. Lett, 1998,Vol. 34, p. 308.

14. **G.J.M. Dormans, P.J. van Veldhoven, M. de Kreiser,** J. Cryst. Growth,1992, Vol. 123, p. 537.

15. **M.U. Ramana Murty, S.K. Streiffer, G.B. Stephenson, J.A. Eastman, G.-R. Bai, A. Munkholm, O. Auciello, C. Thompson,** Appl. Phys. Lett.,2002, Vol. 80, No. 10, p. 1809.

16. **T.W. Kim, S.S. Youn,** J. Phys. Chem. Solids, 1999, Vol. 60, p. 935.

17. **S.-W. Chung, S.-O. Chung, K. No, W.-J. Lee,** Thin Solid Films,1997, Vol. 295, p. 299.

18. **K. Nishida, G. Matuoka, M. Osada, M. Kakihana, T. Katoda,** Appl. Surf. Sci., 2003, Vol. 216, p. 318.

19. **Y. Gao, G. Bai, L. Merkle, H.L.M. Chang, D.J. Lam,** Thin Solid Films, 1993, Vol. 235, p. 86.

20. **K. Tokita, F. Okada**, Nuc. Ins. Met. Phys. Res. B, 1997, Vol. 121, p. 408.

21. **B. Malic, M. Kosec, K. Smolej, S. Stauber**, J. Eur. Ceram. Soc., 1999, Vol. 19, p. 1345.

22. **A. Erbil, W. Braun, B.S. Kwak, B.J. Wilhens, L.A. Boatner, J.-P. Budai**, J. Cryst. Growth , 1992, Vol. 124, p. 684.

23. **M. Tong, G. Dai, D. Gao**, Mat. Lett., 2000, Vol. 46, p. 60.

24. **J.A. Rebane, O.Y. Gorbenko, S.G. Suslov, N.U. Yakovlev, I.E. Korsakov, V.A.**

Amelichev, Y.D. Tretyakov: Thin Solid Films,1997, Vol. 302, p. 140.

25. **P. Lu, H. Li, S. Sun, B. Tuttle,** J. Cryst. Growth, 1997, Vol. 171, p. 453.

26. **K. Nishida, T. Sugino, M.Osada, M. Kakihana, T. Katoda**, Appl. Surf. Sci., 2003, Vol. 216, p. 312.

27. **D. Bao, X. Yao, N. Wakiya, K. Shinozaki, N. Mizutani**, Mater. Sci. Eng. B, 2002, Vol. 94, p. 269.

28. **H. Huang, X. Yao, X. Wu, M. Wang, L. Zhang,** Microelectron. Eng., 2003, Vol. 66, p. 688.

29. **Z. Kighelman, D. Damjanovic, M. Cantoni, N. Setter,** J. Appl. Phys., 2002, Vol. 91, No. 3, p. 1495.

30. **B. Jaber, D. Remiens, E Cattan, P. Tronc, B. Thierry,** Sensors and Actuators A, 1997, Vol. 63, p. 91.

31. **S.Y. Chen, I.-W. Chen,** J. Am. Ceram. Soc,.1998, Vol. 81, p. 97.

32. S**.H. Kim, J.G. Hong, S.K. Streiffer, A.I. Kingon,** J. Mat. Res., 1999, Vol. 14, p. 1018.

33. **Y. Yao, S.G. Lu, H. Chen, K.H. Wong,** J. Appl. Phys., 2004, Vol. 96, No.10, p. 5830.

34. **C.S. Ganpule, V. Nagarajan, B.K. Hill, A.L. Roytburd, E.D. Williams, S.P. Alpay, A. Roelofs, R. Waser, L.M. Eng,** J. Appl. Phys., 2002, Vol. 91, p. 1477.

35. **P. Lu, H. Li, Y.-M. Wang, S. Sun, B. Tuttle,** J. Cryst. Growth, 1997, Vol. 181, p. 348.

36. **Y.M. Kang, J.K. Ku, S. Baik,** J. Appl. Phys., 1995, Vol. 78, p. 2601.

37. **C.M. Foster, Z. Li, M. Buchet, D. Miller, P.M. Baldo, L.E. Rehn, G.R. Bai, D. Guo, H. You, K.L. Merkle,** J. Appl. Phys., 1995, Vol. 78, p. 2607.

Chapter 4:

$PbTiO_3$ thin film structure evolution with misfit strain and film thickness

Chapter 4

4 $PbTiO_3$ thin film structure evolution with misfit strain and film thickness ____ *67*

4.1 Introduction ____ 70

4.2 Domain structure study by reciprocal space mapping ____ 71

4.3 Domain structure evolution with misfit strain and film thickness ____ 76

- 4.3.1 Domain fraction ____ 76
- 4.3.2 Twinned and non-twinned *a*- and *c*-domains ____ 79
- 4.3.3 Twinning angles ____ 81
- 4.3.4 Mosaicity ____ 86

4.4 HR TEM analysis of dislocations and twin defects ____ 87

4.5 Lattice parameters in *a*- and *c*-domains ____ 92

4.6 Residual stress ____ 95

- 4.6.1 Theoretical considerations ____ 95
- 4.6.2 Residual stress in $PbTiO_3$ films ____ 96

4.7 Heterogeneity of strains in $PbTiO_3$ films ____ 97

4.8 Microstrains and average grain size ____ 100

- 4.8.1 Average grain size ____ 100
- 4.8.2 Microstrains ____ 102

Conclusions ____ 102

Bibliography ____ 104

4. $PbTiO_3$ thin film structure evolution with misfit strain and film thickness

4.1 Introduction

Macroscopic strain is an important factor in determining the structure and behavior of ferroelectric films. Because of the strong coupling of strain with polarization, strains have a substantial impact on the structure, on ferroelectric transition temperatures, and on related properties such as dielectric and piezoelectric responses. Mechanical clamping by the substrate is of key importance for the formation of domain patterns in the film. A number of theoretical works on the effect of mechanical clamping on domain patterns can be found in the literature (1; 2; 3; 4; 5; 6).

Domain patterns in ferroelectric thin films have become an issue of interest over the last 15 years. Ferroelectric twin-domain structures have been investigated extensively in epitaxial $PbTiO_3$ thin films deposited on various single-crystal substrates, including MgO (7; 8; 9; 10; 11), $SrTiO_3$ (12; 7; 13), $KTaO_3$ (7) and $LaAlO_3$ (14; 8; 9) substrates using wide variety of deposition techniques. The domain patterns are studied using different techniques, such as scanning force microscopy (15), transmission electron microscopy (TEM) (16; 17; 7; 18; 19) and XRD (7; 8; 11; 17). An important domain structure parameter is domain fraction, which is usually determined by comparing intensities of XRD reflections corresponding to different domain states. For PTO and PZT films, the *a*-domain fraction has been evaluated as a function of film thickness by many authors. It has been found that it is sensitive to the substrate material and film composition (11; 20). However, the observed thickness dependence of domain fraction is often difficult to interpret in terms of existing theories due to the difficulty in the theoretical description of the thickness dependence of the stress release.

For instance, the investigation of the mechanical strain effect on ferroelectric film properties is studied using epitaxial films as the application of high stresses is possible by subjecting the film to the effect of the substrate (7; 8; 9). Since residual stress is a function of film thickness, the evolution of the film properties with thickness has been used as an experimental way to investigate the strain effect in ferroelectrics (21; 22; 23; 24). Some other ways to influence and to control the mechanical strain also used in literature have been: i) by selection of substrates, having different mismatch with the film (7; 9) or different thermal expansion coefficients (25), ii) by change the deposition conditions (8), iii) by post-annealing process, and iv) by insertion of a thin layer of a different chemical composition in between the film and the substrate (26).

Nevertheless, the control of the strain utilizing the relaxation process of the growing film is strongly related to misfit dislocation formation. Therefore it is difficult to purely separate the influence of mechanical stress in the film from other variables, such as domain structure, epitaxial quality, grain size, heterogeneous strain, defects and so on. Moreover, authors do not usually include any direct measurement of the residual

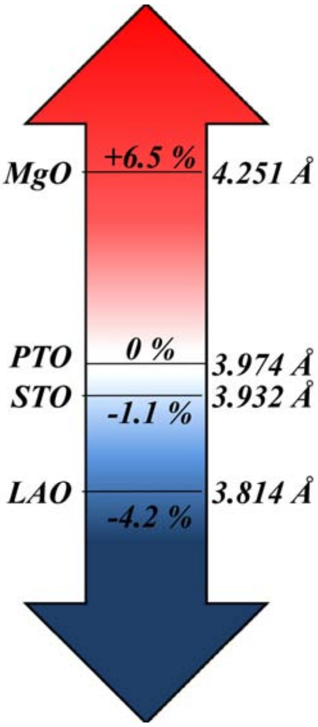

Figure 4-1: Scale of misfit strain in PTO films on STO, LAO and MgO substrates and lattice parameters of bulk PTO, STO, MgO and LAO at 650 °C.

stress in the film, but just give calculated values or expected trends. Therefore, the detailed experimental study of stresses and their influence on film properties is necessary.

Since technologically relevant films for ferroelectric memories are typically thicker than 120 nm, characterizations and analysis of film properties should be carried out at comparable length scales. Thus, in order to study the effects of stresses and their relaxation process in PTO films, 30-460 nm thick PTO films were deposited on LAO, STO and MgO substrates using optimized deposition conditions (Chapter 3, Table 3-2). The misfit strain in PTO films on these substrates varies from large compressive (LAO) and small compressive (STO) to large tensile (MgO) at deposition temperature Figure 4-1. To investigate the film relaxation and the origin of residual stress, a well understanding of film microstructure is needed. Therefore, in this chapter we present the detailed analysis of the film domain structure, epitaxial quality, defects, lattice parameters, strain homogeneity, microstrains and grain sizes. Moreover the residual stress values will be estimated from XRD data. However, the discussion on residual stress origin will be given in Chapter 7.

4.2 Domain structure study by reciprocal space mapping

The Θ/2Θ XRD patterns of the 30-460 nm PTO films on STO, LAO and MgO substrates are characteristic of the PTO tetragonal structure consisting only of *(00l)* or (*00l)*/ (*h00*) reflections. This indicates a pure *c*-domain or a *c/a/c/a* structure, respectively. Typical Θ/2Θ XRD patterns of epitaxial PTO films are given in section 3.5. The 2-D mappings of reciprocal space were used for more detailed analysis of our film structure. First, we will present the principles of the domain structure analysis and the measurement of the PTO thin film reciprocal space maps. The readers familiar with these 2-D mapping of PTO films may skip this section 4.2.

As explained in section 1.5.2, a *c/a/c/a* structure consists of twinned *a*- and *c*-domains bounded by a *(101)* plane (Figure 4‑2). The fourfold symmetry may be expected in both *a*- and *c*-domains due to twinning. The scheme in Figure 4‑2 is simplified, as only the tilts of *a*-domains are presented. The 460 nm thick PTO/STO film, consisting of non-tilted *c*-domains and *a*-domains having fourfold symmetry, will be analysed as an example. The corresponding two–dimensional (2-D) HL reciprocal space

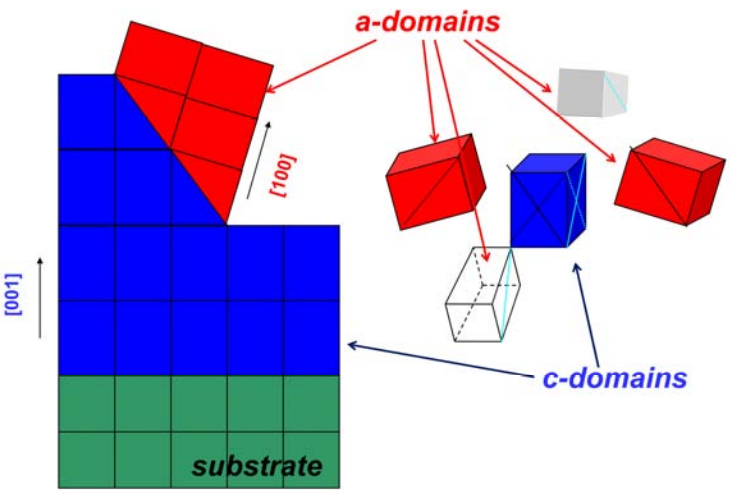

Figure 4-2: Scheme of twinning and tilt of a-domains in PTO films. The tilt angle is overestimated.

mapping at K=0 is given in Figure 4‑3. Six orientation matrices may describe the reciprocal space mapping for this film: a matrix of STO substrate, a *c*-domain matrix and four *a*-domain orientation matrices. In Figure 4‑3, there are presented the orientation matrices of STO, *c*-domain and only one *a*-domain. The film is epitaxial as *c*-domain orientation is highly related to that of substrate (ex. the *(h00)* planes superimposes). The *a*-domain reflections are deviated by a small angle from the principal axes of reciprocal space, indicating the *a*-domain tilt, which depends on the tetragonality of the cell (for more details see section 1.5.2). Thus, in the standar d Θ/2 Θ scans, corresponding to *(00l)* reciprocal space axis,

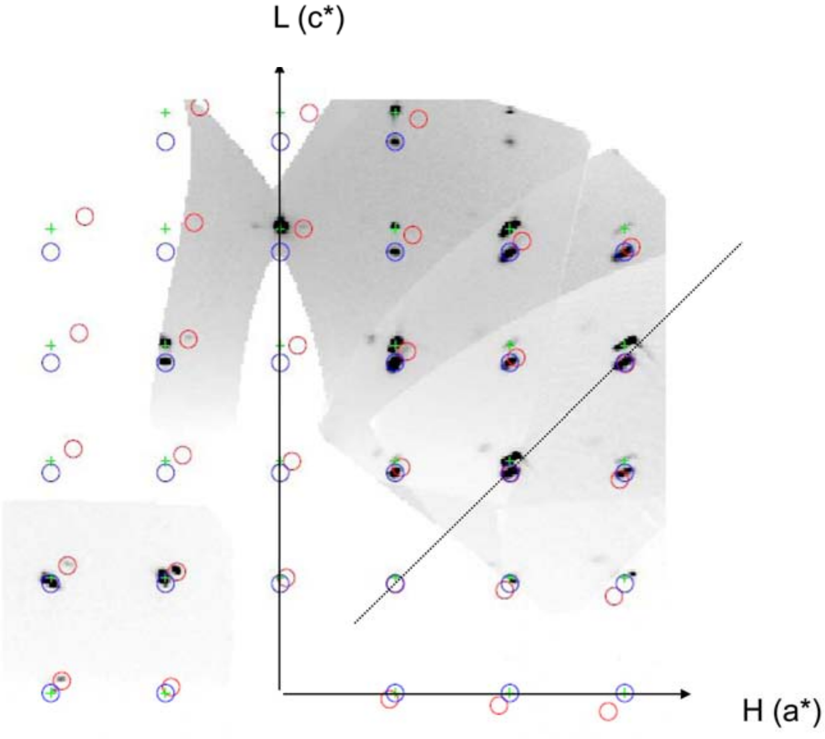

Figure 4-3: 2-D reciprocal space mapping (at K=0) of 460 nm thick PTO/STO film. Red and blue circles represent a- and c-domain orientation matrices, respectively. Green crosses represent the STO substrate orientation matrix. For more details see in the text.

c-domain and STO reflections should be observed. A fraction of the *a*-domain reflection, which does not correspond to the maximum of intensity, usually also appears in this scan. Moreover, the *(101)* planes of *a*- and *c*-domains superimpose, showing a bounding (twinning) plane between *a*- and *c*-domain.

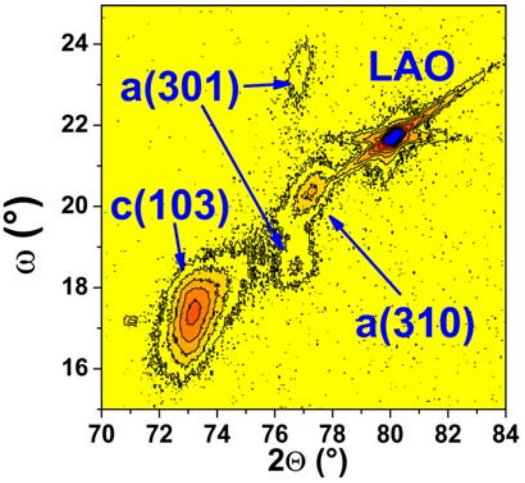

Figure 4-4: 2-D ω-2Θ contour map near (103) and (301)/(310) reflections of 125 nm thick PTO/LAO film. The spots corresponding to a- and c-domains are indicated by a and c, respectively.

The detailed analysis of our film structure is performed using not the general HKL reciprocal space mappings but the 2-D ω-2Θ mappings near the *(103)* and *(301)* PTO reflections. An example of ω-2Θ contour map is given in Figure 4‑4. The ω-2Θ mapping integrates the intensity from different φ-angles (± 5 °), making possible to observe together the *(301)* and the *(310)* reflections, which appear at different φ-values. As shown in Figure 4‑5, these reflections were found in the reciprocal space mappings collected at φ=0 and φ=+2 (φ=-2), where two spots and one spot correspond respectively to the *(301)* and the *(310)* *a*-domain reflections. In Figure 4‑4, the *(103)* and *(301)/(310)* reflections correspond to *c*- and *a*-domains, respectively. The coexistence of *(301)* and *(310)* reflections is the indication of the existence of a_1 - and a_2- domains: both types have their *c*-axis parallel to the substrate plane, but a_2-domains are rotated by 90 ° with respect to the a_1-domains (as already explained in section 1.5.2 and 3.5). The *(103)* spot elongation in ω-angle indicates that *c*-domains also are tilted by a small angle.

As mentioned in section 1.5.2 the fourfold tilt of domains is along $[h00]$, $[\bar{h}00]$, $[0k0]$ and $[0\bar{k}0]$ directions. Thus, two and four reflections corresponding to *a*-domains are observed in 2-D reciprocal space mappings at K=0 (or H=0) and L=3.9, respectively (Figure 4‑6). The *c*-domain fourfold tilt results in analogous reflection split. Therefore, depending on the measurement geometry, from one to four reflections of the fourfold symmetry may be observed in the different mappings and in the standard ω-, φ- and χ-scans. For example, the four spots corresponding to the fourfold split are indicated in the 2-D χ-ω mappings, corresponding to *a*-domain *(301)/(310)* reflections (Figure 4‑7). These contour maps are very similar to small pole figure and are used to study the *a*- and *c*-domain twinning and the tilt angles in our films. The centre corresponds to the direction of an asymmetric *(301)* (or *(103)* in the case of *c*-domains) reflection of cubic PTO. These maps show again a clear twinning of *a*-domains. The deviation of the spot from the centre in ω- and χ-angles indicates that unit cell is rotated by a small angle around *b*- and *c*-axis, respectively (Figure 4‑8). Two

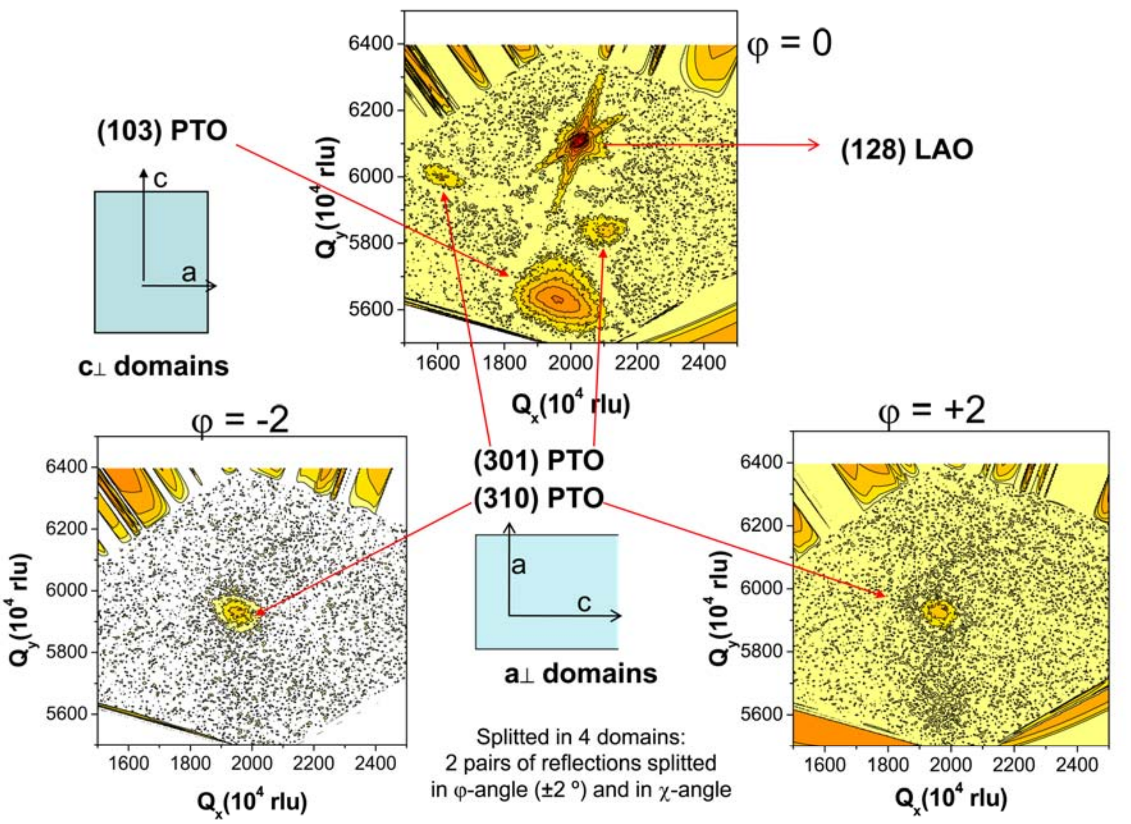

Figure 4-5: 2-D reciprocal space mappings near (103), (301) and (310) reflections of PTO at φ=0,φ=-2 and φ=+2.

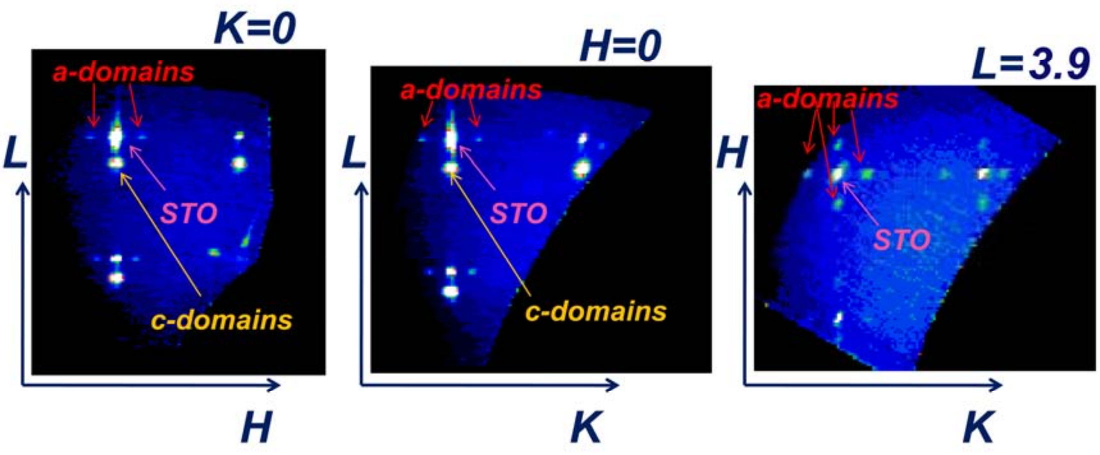

Figure 4-6: Detailed 2-D reciprocal space mapping at K=0, H=0 and L=3.9 of 460 nm thick PTO/STO film.

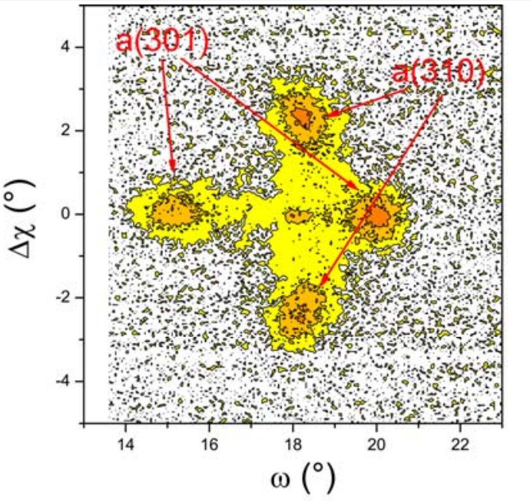

Figure 4-7: 2-D χ-ω contour map corresponding to the a-domain (301)/(310) reflections of 125 nm thick PTO/LAO films.

equivalents possibilities of rotation around each axis result in fourfold tilt of domains and consequently in four spots of 2-D χ-ω contour maps. The deviation in ω- and χ-angles is not symmetric, as the *c*- and *b*-lattice parameters of tetragonal PTO are different. In the case of *c*-domain fourfold symmetry, the split of the *(103)* reflection is similar to those of *a*-domain *(301)/(310)* reflections. However, in the case of the *(103)* reflection, the deviation in ω- and χ-angles is symmetric, as *a*- and *b*-lattice parameters are identical. If the domains are not tilted from the film-substrate normal, only one corresponding spot appears in these contour maps.

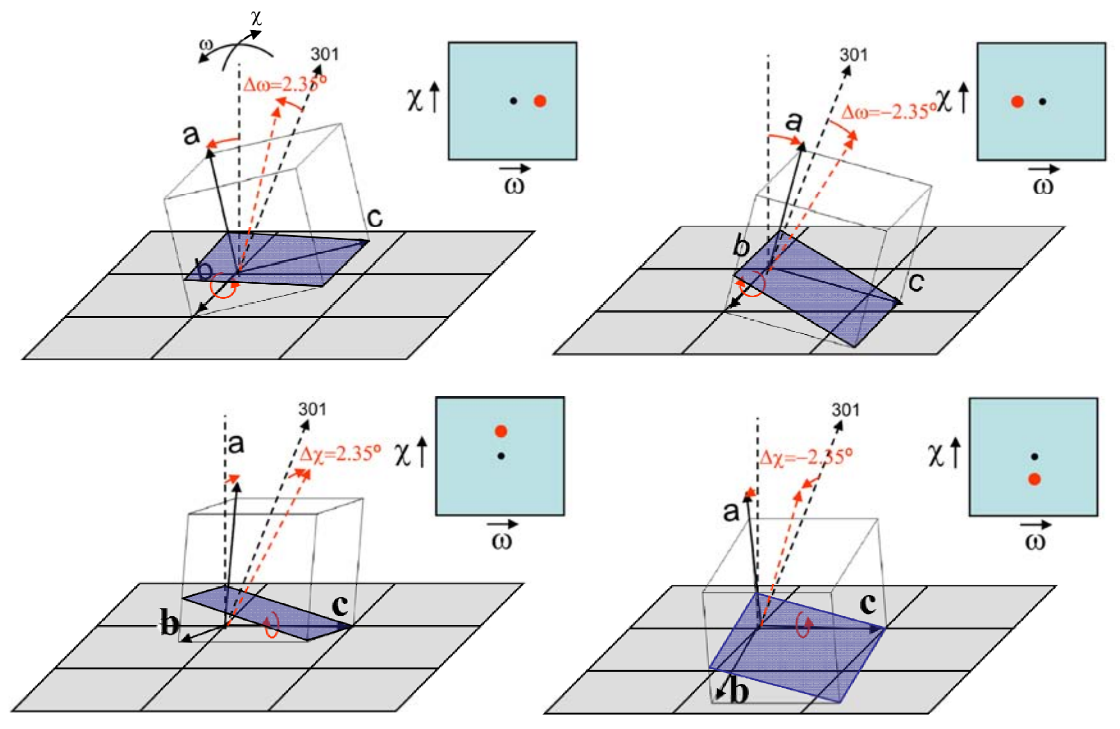

Figure 4-8: Schematic representation of a-domain tilts along the c- and b-axis and of resulting XRD reflection split.

4.3 Domain structure evolution with misfit strain and film thickness

In this section, we will discuss on the misfit strain, thermal stress and the film thickness influence on the domain structure: domain fraction, twinned and non-twinned domain formation, twinning angles and mosaicity.

The 2-D ω-2Θ contour maps near the *(103)* and *(301)/(310)* reflections are shown in Figure 4‑9 for PTO films on STO, LAO and MgO substrates with thickness varying between 30-460 nm. All the films consist of a *c/a/c/a* domain structure, except the 30-65 nm thick PTO/STO and the 30 nm thick PTO/LAO films, where only of *c*-domains were observed.

4.3.1 Domain fraction

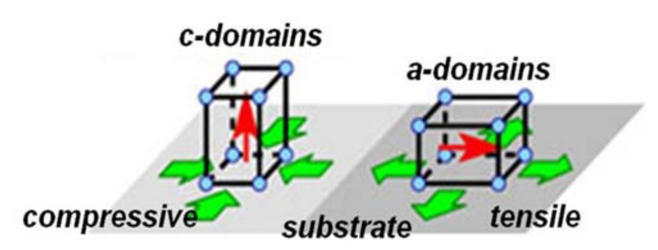

Figure 4-10: Misfit stress influence on domain formation.

The twinned *a*-domain fraction depends on the misfit and on the thermal stresses, as twinning is one of the main relaxation mechanisms in PTO films. Moreover, the *a*-domain and *c*-domain formations are favored by tensile and compressive stresses, respectively (Figure 4-10). The thermal expansion coefficients (TEC) of bulk PTO and the studied substrates (STO, MgO and LAO) are given in Table 4- 1. The calculated misfit stress at the deposition temperature (T_{Dep} = 650 °C) and thermal stress values accumulated during cooling from 650 °C to RT for each studied film/substrate system are also given in Table 4- 1. It is important to note that thermal stresses are independent of film thickness, while misfit stresses relax with the increase of the film thickness. Thus, the degree of misfit stress relaxation by dislocations generation plays a critical role in the final domain structures. The critical thickness for misfit dislocations formation is a good indicator of the film capability to relax the stresses (2). Lets us remind that the thickness of complete misfit stress relaxation is much bigger than critical thickness for dislocations generation, as our films were deposited at relatively low temperature, where the thermal energy needed for dislocations creation is low (see section 1.5). The critical thicknesses of PTO films deposited at 650 °C on STO, MgO and LAO substrates are given in Table 4- 1.

The *a*-domain fractions in all films were evaluated from the ratio of the integrated intensities corresponding to *the (301)/(310)* and *(103)* reflections, as explained in section 2.2.2. Evaluated volume fractions of *a*-domains as a function of film thickness are given in Figure 4‑11. One can see that the *c*-domain fraction is dominant in 30-460 nm PTO films on all three substrates. The thickness evolution of *a*-domain fraction in each film/substrate system will be separately discussed.

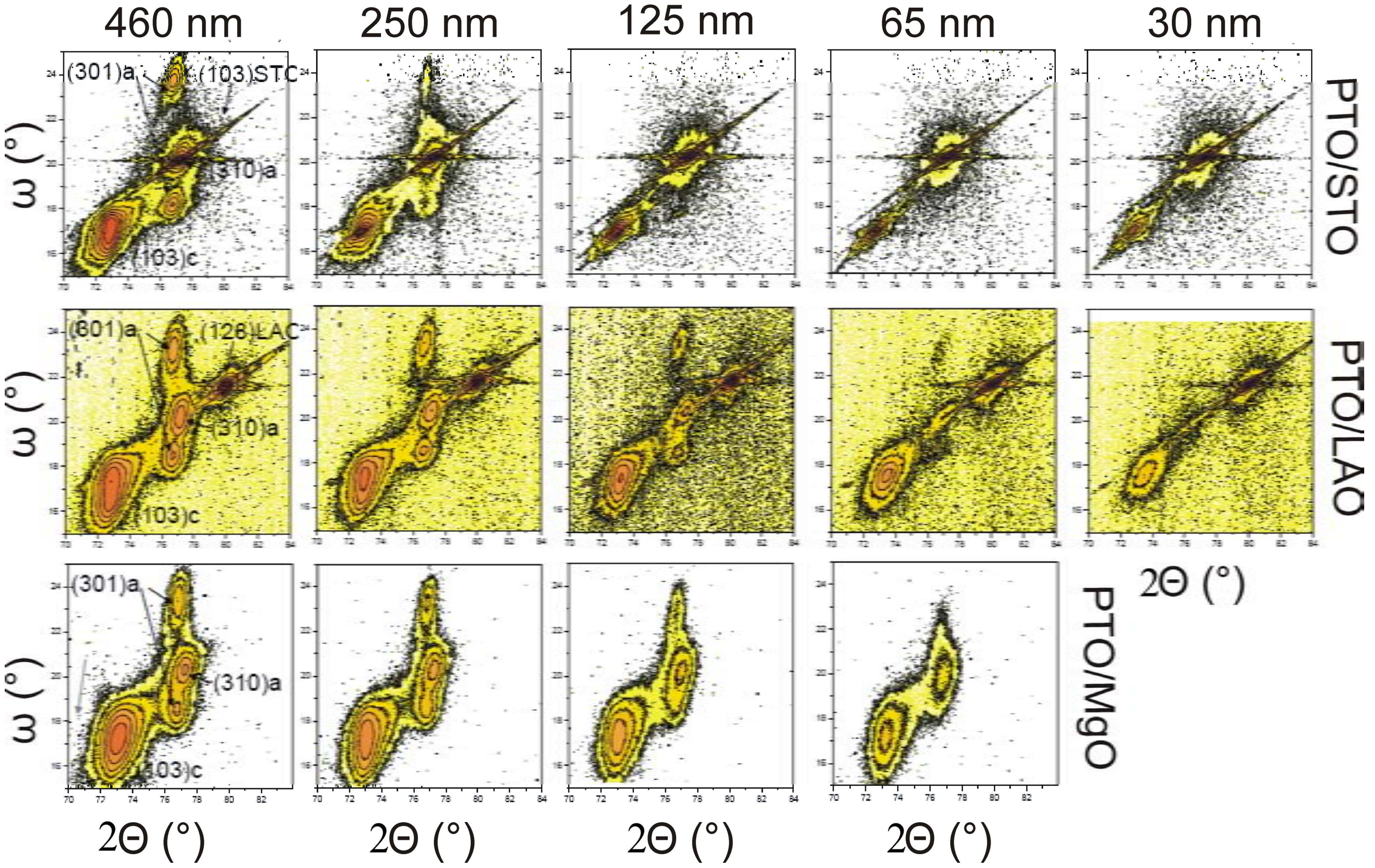

Figure 4-9: : 2-D ω-2Θ contour maps of 30-460 nm PTO film on STO, LAO and MgO substrates. (2θ scale: 70-84 °, ω scale: 15 -25 °)

Table 4-1: Structural parameters of bulk PTO and substrates, misfit and thermal stresses and critical thickness of PTO films deposited at 650 ºC (see section 1.5.1 for formula).

Material	Crystal structure	Lattice parameters (Å)		TEC (× 10^6 K^{-1})	Misfit strain at T$_{dep}$(%)	Misfit stress * at T$_{dep}$(GPa)	Thermal stress * (cooling 650 °C - RT)(GPa)	Critical thickness (nm) (11)
		RT	T$_{Dep}$ (°)					
PTO	tetragonal at RT cubic at T$_{Dep}$	a=3.899 c=4.153	3.974	12.6 (a-axis) (11)				
STO	cubic	3.905	3.932	11.5**	-1.1	-1.8	+0.11	7.1 (11)
LAO	pseudocubic	3.789	3.814	10.2**	-4.2	-7.0	+0.25	1.1 (11)
MgO	cubic	4.212	4.251	14.8 (11)	+6.5	+10.8	-0.23	0.4 (11)

**Initial values of misfit strain, the relaxation is not taken into account.*
*** Values estimated from our high-temperature XRD measurements.*

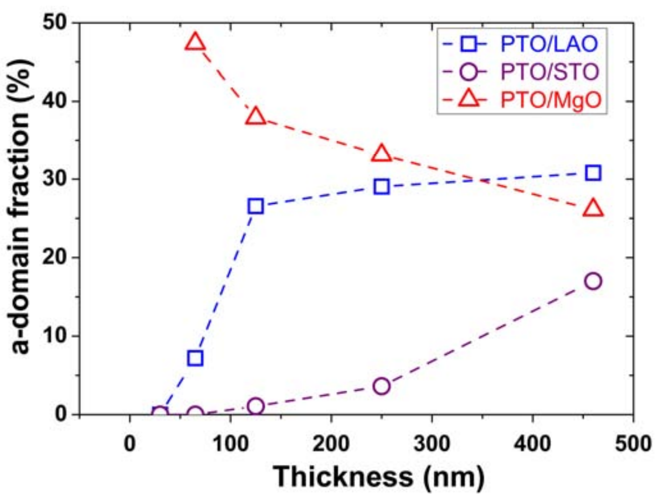

Figure 4-11: The a-domain fraction as a function of film thickness in PTO films on STO, LAO and MgO substrates.

PTO/STO films The 30-65 nm thick PTO/STO films consist only of *c*-domains, while at higher thicknesses *a*-domains start to form and their fraction increases from 1 % to 17 % with the increase of the thickness from 125 nm to 460 nm (Figure 4-11). In PTO films on STO substrate, the lattice mismatch between the *c*-domains and the substrate is very small (+ 0.1 % at RT) comparing to that of *a*-domains (-6.3 % at RT). Moreover the misfit stress is negative at 650°C (Table 4. 1). Thus, *c*-domain formation is energetically favoured. Moreover, the critical thickness for dislocation generation is relatively high (Table 4. 1). Therefore, the compressive misfit stress is not well relaxed by misfit dislocations at low thicknesses, up to ~100 nm, and determines the domain structure. In 125-460 nm films, the misfit stresses are more and more relaxed with the increase of the thickness, resulting in the appearance of *a*-domains in the film. The tensile thermal stress is very small and can influence the domain structure only when misfit stress is relaxed.

PTO/LAO films In PTO/LAO films, the misfit stress is also compressive and *c* -domain mismatch with substrate is lower than that of *a*-domains (at RT, -2,9 % and -9.6 %, respectively). Thus, the *c*-phase is favoured like in PTO/STO films. However, high misfit stresses are more released by misfit dislocations during the film growth, since critical thickness is much smaller than that of PTO/STO films (Table 4. 1)). Therefore, only the c-phase is observed for the 30 nm thick film, which is still under partially relaxed compressive misfit stresses. When increasing the film thickness from 30 nm to 125 nm, compressive misfit stress relaxes and *a*-domains may be formed. Thus, their fraction increases from 7 % to 27 % with increasing film thickness from 65 nm to 125 nm (Figure 4‑11). Moreover, tensile thermal stresses also favour the *a*-domain formation. However, the thermal stresses are small and can influence the domain structure only when misfit stress is almost relaxed. With the further increase of the thickness from 125 nm to 460 nm, the *a*-domain fraction increases less (from 27 % to 31 % (Figure 4‑-11)), as the main part of stresses are probably already relaxed.

PTO/MgO films The misfit strain at the deposition temperature in PTO/MgO films is positive and *c*- and *a*-domains have the same mismatch with MgO substrate at RT (+7.4 %). Therefore, equal *a*- and *c*-domain fractions may be expected. Nevertheless, the critical thickness for dislocation generation is very small (Table 4. 1) and thermal stresses are compressive. This results in a *c/a/c/a* polydomain state with dominant *c* -domain fraction. In the 65 nm thick PTO/MgO film, the *a*-domain fraction is big (47 %), as film is still under partially relaxed tensile misfit stress. Further increase of film thickness (from 65 nm to 460 nm) results in a complete misfit stress relaxation. Therefore, the final domain structure is mainly determined by compressive thermal stresses, resulting in the reduction of *a*-domain fraction from 47 % to 26 % (Figure 4‑11).

The literature reports on thickness evolution of a-domains are consistent with our results: *a*-domain fraction decreases with the increase of PTO/MgO film thickness (11), while in the case of STO and LAO substrates, the increase of *a*-domain fraction is observed with increasing the film thickness (12; 27). The thickness evolution of domain fractions in relation with stress relaxation will be discussed again in chapter 7, where we will explain the origin of residual stresses in PTO films.

4.3.2 Twinned and non-twinned a- and c-domains

In order to investigate the twin structure, ω-χ contour maps of the *c*-domain *(103)* reflection and the *a*-domain *(301)/(310)* reflections have been measured for the 30-460 nm thick PTO films on STO, LAO and MgO substrates (Figure 4‑12 and Figure 4‑13, respectively). The maps reveal twinning in *a*- and *c*-domains with fourfold symmetry. Twinning is usually very well pronounced in *a*-domains (Figure 4‑13), whereas it is less evident in *c*-domains despite the square shape of the spot (Figure 4‑12). As explained in sections 1.5 and 3.5, the *c*-domain tilt is observed only in films with relatively high *a*-domain fraction. However, it is not evident to indicate the spots corresponding to non-twinned (non-tilted) *a*- and *c*-domains, as they appear in the centre of these maps. The analysis of rocking curve profile is a commonly used method to identify the twinning in PTO films (9; 17). In order to get more information about the thickness evolution of twinned and non-twinned *c*- and *a*-domains, the corresponding standard rocking curves of *(001)* and *(100)* reflections were measured, respectively (Figure 4‑14 and Figure 4‑-15). The split of rocking curves indicates that domains are twinned. If the film consists of twinned and non-twinned *c*- or *a*-domains, the rocking curve consists of three components. The peak in the middle corresponds to the non-twinned domains and the other two peaks come from twinned domains. However, their contribution may overlap with the contribution of twinned domains, of which tilt is observed as split in χ-angle. The other two peaks (side peaks) come only from twinned domains. The fraction of domains tilted in χ and ω angles are identical, as can be seen from $\Delta\chi$-ω maps (Figure 4-12). Thus, the non-twinned domain can be identified from rocking curve if the middle component is more intense than sum of side peak intensities. Thickness evolution of twinned and non-twinned domain fraction will be discussed only qualitatively. However, in the case of *a*-domains in PTO/STO and PTO/LAO films, the substrate peak appears in the middle position in *a*-domain rocking curves. Thus, the non-twinned *a*-domains cannot be identified from these measurements.

PTO/STO films The *a*-domain fraction is small in PTO/STO films. The 30-65 nm thick films consist only of *c*-domains. Thus twinning is not observed. The *a*-domain fraction increases from 1 % to 17 % with the increase of the PTO/STO film thickness from 125 nm to 460 nm. The *a*-domains are twinned, as the *a*-domain peaks are clearly split in both *(301)/(310)* χ-ω map and *(100)* rocking curve (Figure 4‑13 and Figure 4‑-15). This shows that *a*-domain origin is the stress relaxation in PTO/STO films. Accordingly, the base of the *(001)* rocking curve enlarges with the increase of the thickness from 125 nm to 460 nm, indicating the increase of the twinned *c*-domain fraction (Figure 4‑12 and Figure 4‑14). The *c*-domain tilt is clearly observed only in 460 nm thick film, which has 17 % of *a*-domains. However, the majority of *c*-domains remain non-tilted in this film. The 250 thick film has only 4 % of *a*-domains, and the split of the rocking curve, corresponding to *c*-domains, is not observed. Nevertheless, the base of the peak is highly enlarged, what can be clearly seen in corresponding χ-ω map (Figure 4‑12). This indicates that a very small fraction of *c*-domains are tilted in the 250 nm thick film.

PTO/LAO films In the case of the 65 – 460 nm thick PTO/LAO films, the *c*-domain tilt is clearly observed in both *(001)* rocking curves and χ-ω maps (Figure 4‑12 and Figure 4‑14), as the *a*-domain fraction is higher (8 - 31 %) than in the PTO/STO films. It is not observable in the 30 nm thick film, consisting only of *c*-domains. The twinned *c*-domain fraction increases with the increase of the thickness and the *a*-domain fraction. In the 460 nm thick film, the twinned *c*-domain fraction is already higher than the non-twinned *c*-domain one or all *c*-domains are twinned. As it can be expected from the *c*- and *a*-domain mismatch with the LAO substrate, *a*-domains originate from relaxation process. Thus, all *a*-domains are twinned in PTO/LAO films (Figure 4‑13 and Figure 4‑15). Similar profile evolutions of rocking curves corresponding to *c*- and *a*-domains with the *a*-domain fraction increase were observed by Kim et al. (17).

PTO/MgO films The case of PTO/MgO films is different, as *a*- and *c*-domains have the same lattice mismatch with the MgO substrate. Unfortunately, we did not succeed to fit the *(001)* rocking curves, as no clear thickness evolution is observed (Figure 4‑14). Nevertheless, the *(103)* spots in χ-ω maps have a square form (Figure 4‑12), indicating the tilt of *c*-domains. The *a*-domains are also twinned, as rocking curves and *(301)* spots are split (Figure 4-13 and Figure 4-15). It is not possible to estimate if non-twinned *a*-domains fraction is dominant in these films, but it can be seen that it decreases with increasing film thickness. Non-twinned *a*-domains in PTO/MgO films were also observed by Lee et al. (28).

In conclusion, the non-twinned *a*- and *c*-domain appearance in the film depends on their mismatches with the substrate. If the *c*-domain mismatch with substrate is smaller than the *a*-domain one, only *c*-domains may be non-twinned (ex. PTO/STO and PTO/LAO films). During the stress relaxation, the twin structure forms in the film. Thus, twinned *a*- and *c*-domains indicates the stress relaxation in the film. In all the three film/substrate systems, the ratio of twinned domains with non-twinned ones increases with the increase of the film thickness. This indicates the film relaxation with film thickness. Furthermore, the twinning occurs between *a*- and *c*-domains, resulting in tilt from film-substrate normal in both types of domains (as explained in section 1.5). Thus, the presence of tilted *a*-domains indicates that some fraction of *c*-domains must be also tilted. Consequently, the twinned *c*-domain fraction increases with the increase of twinned *a*-domain fraction.

4.3.3 Twinning angles

The twinning angles of *a*- and *c*-domains were evaluated directly from the splitting of *(001)* and *(100)* reflections in the rocking curves, as shown in Figure 4‑14 and Figure 4‑15, respectively. The thickness evolution of *a*- and *c*-domain twinning angles in PTO films on STO, LAO and MgO substrates is presented in Figure 4‑16 a. The relation between *a*- and *c*-domain twinning angles are explained in sections 1.5 and 3.5. The twinning angle of *c*-domains (*a*-domains) increases (decreases) with the increase of *a*-domain fraction (29). This relation between *a*- and *c*-domain twinning angles and *a*-domain fraction is also observed in the 30-460 nm thick PTO films on STO, LAO and MgO films. The *a*-domain fraction increases with the increase of the film thickness in PTO films on STO and LAO substrates. Thus, the *a*-domain twinning angle decreases and the *c*-domain twinning angle increases with increasing film thickness. The same tendency was observed by Kim et al. (17). The exception is the 65 nm thick PTO/LAO

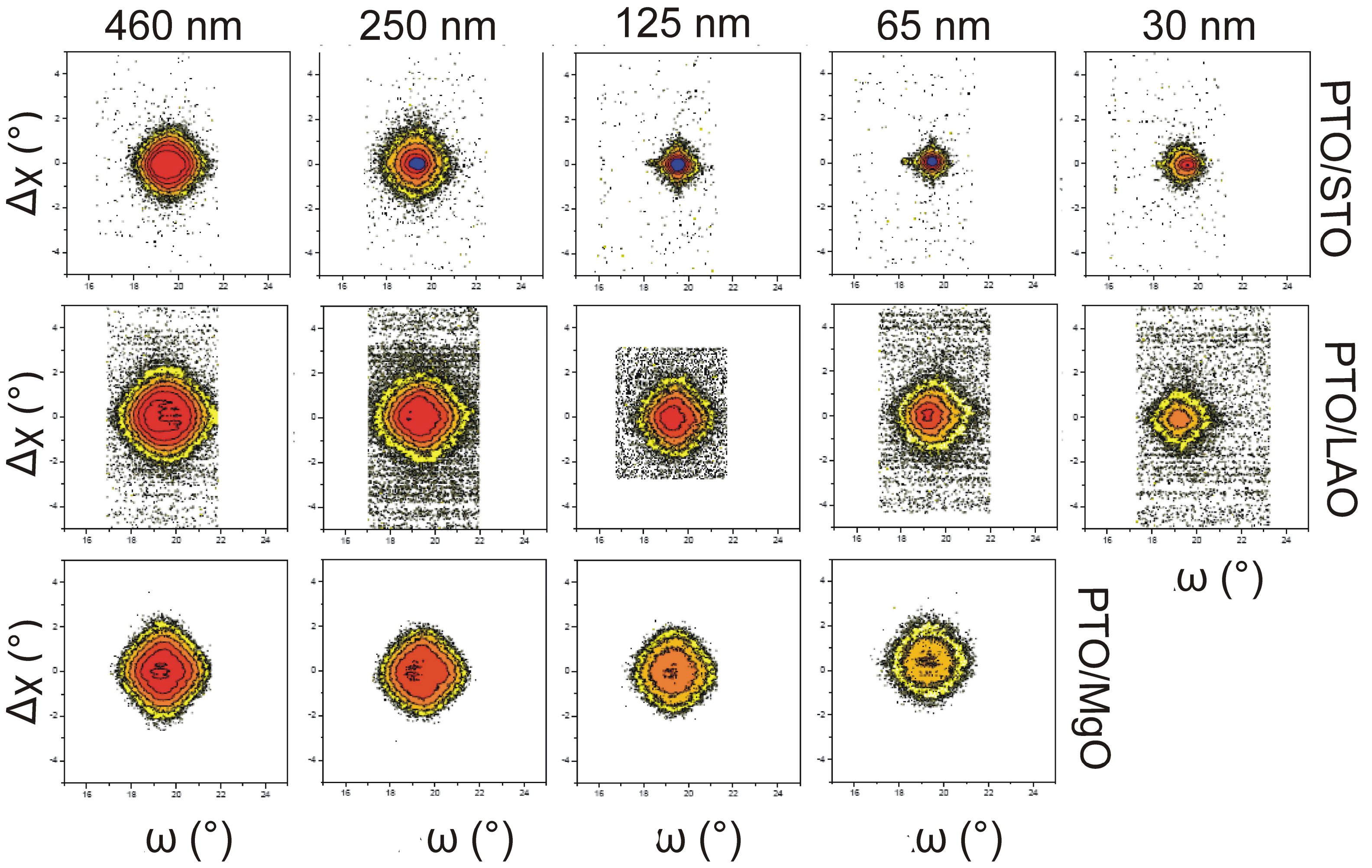

Figure 4-12: 2-D χ-ω contour maps of the (103) reflection corresponding to c-domains in the 30-460 nm thick PTO film on STO, LAO and MgO substrates. (ω scale: 15-25°, $\Delta\chi$ scale: -5—5 °)

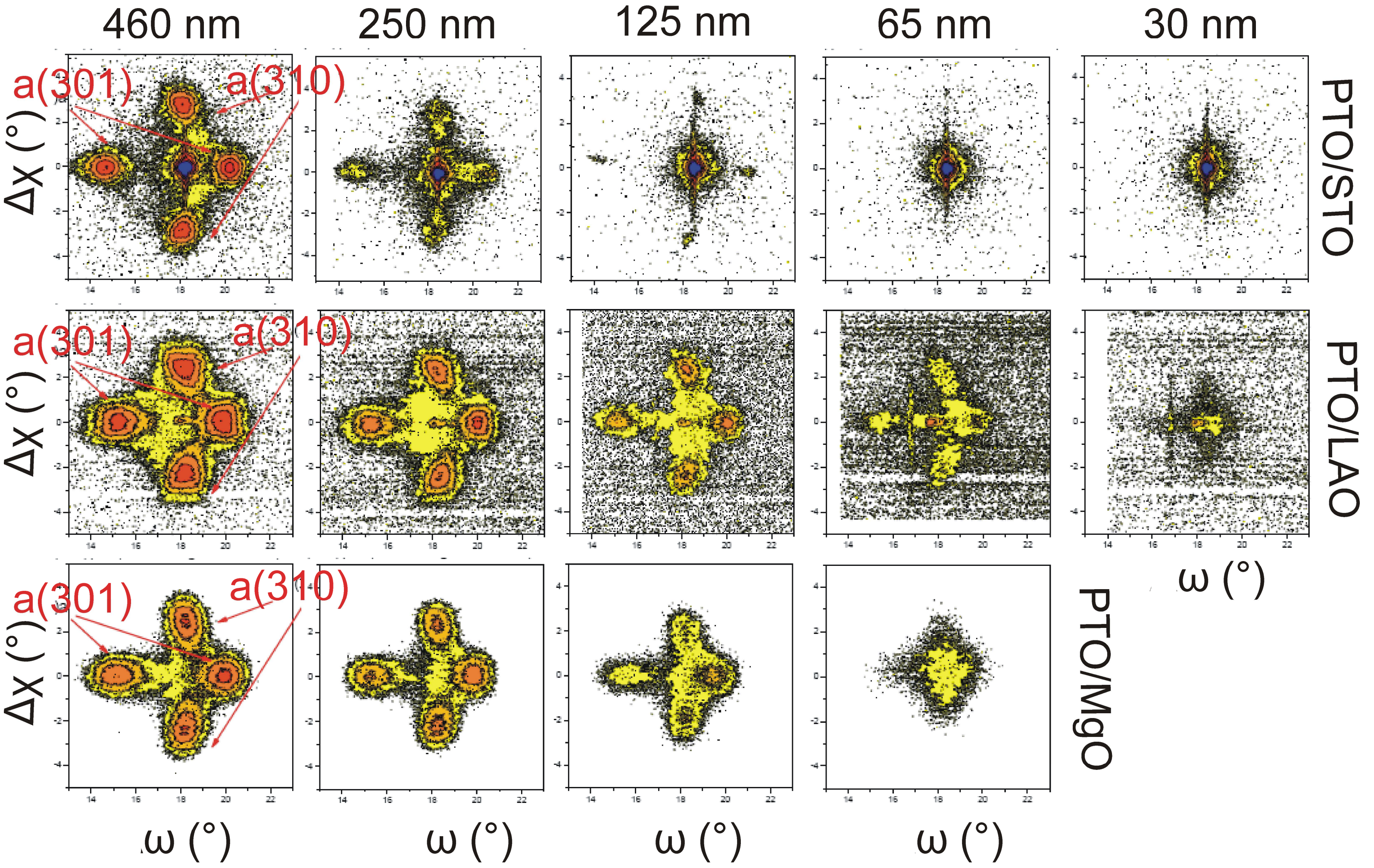

Figure 4-13: 2-D χ-ω contour maps of the (301)/(310) reflections corresponding to a-domains in the 30-460 nm thick PTO film on STO, LAO and MgO substrates. (ω scale: 15-25°, $\Delta\chi$ scale: -5—5 °)

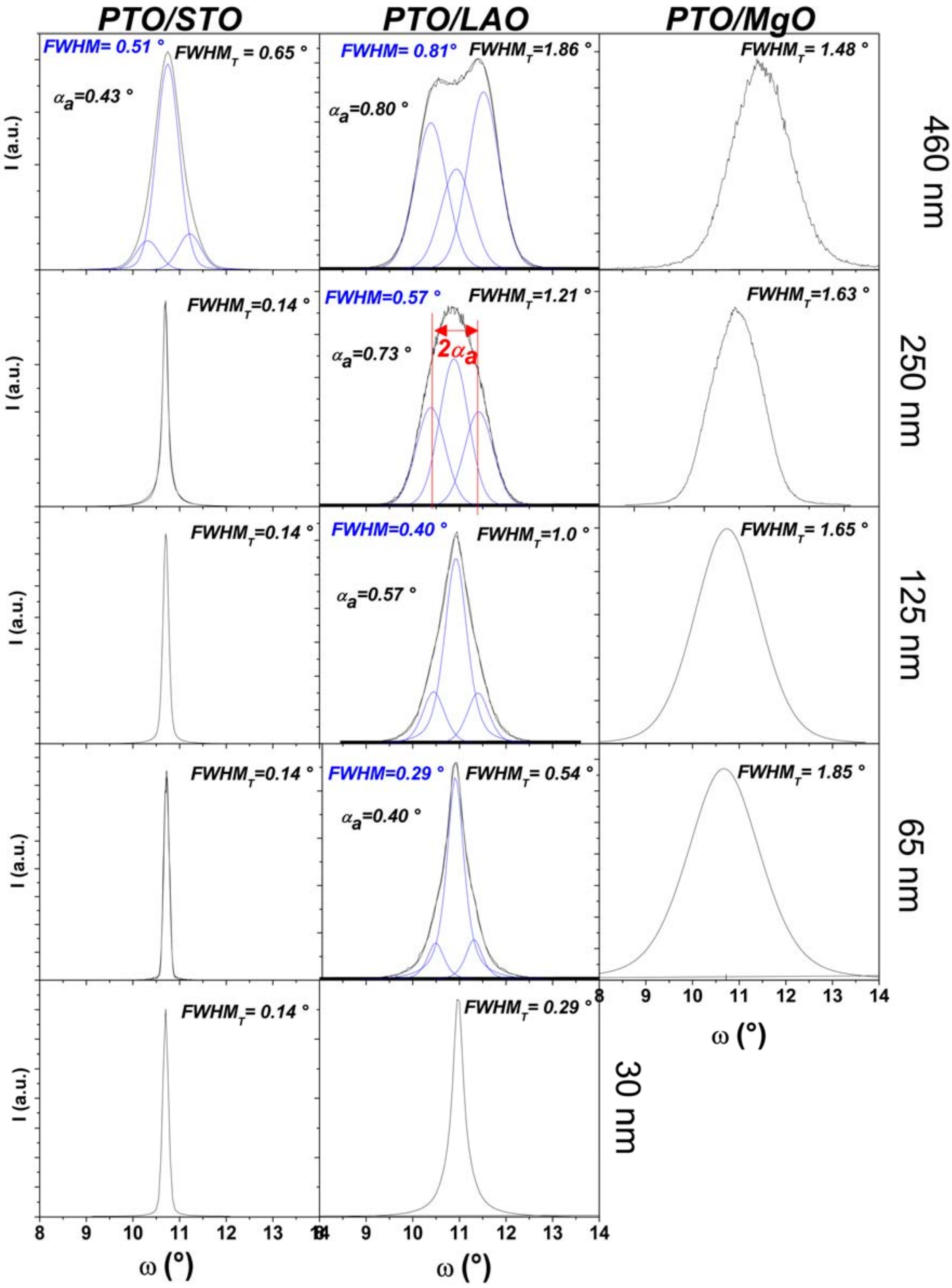

Figure 4-14: Rocking curves of the (001) reflection of c-domains in the30-460 nm thick PTO films on STO, LAO and MgO substrates. Estimation of c-domain twinning angle is shown on the rocking curve of 250 nm thick PTO/LAO film.

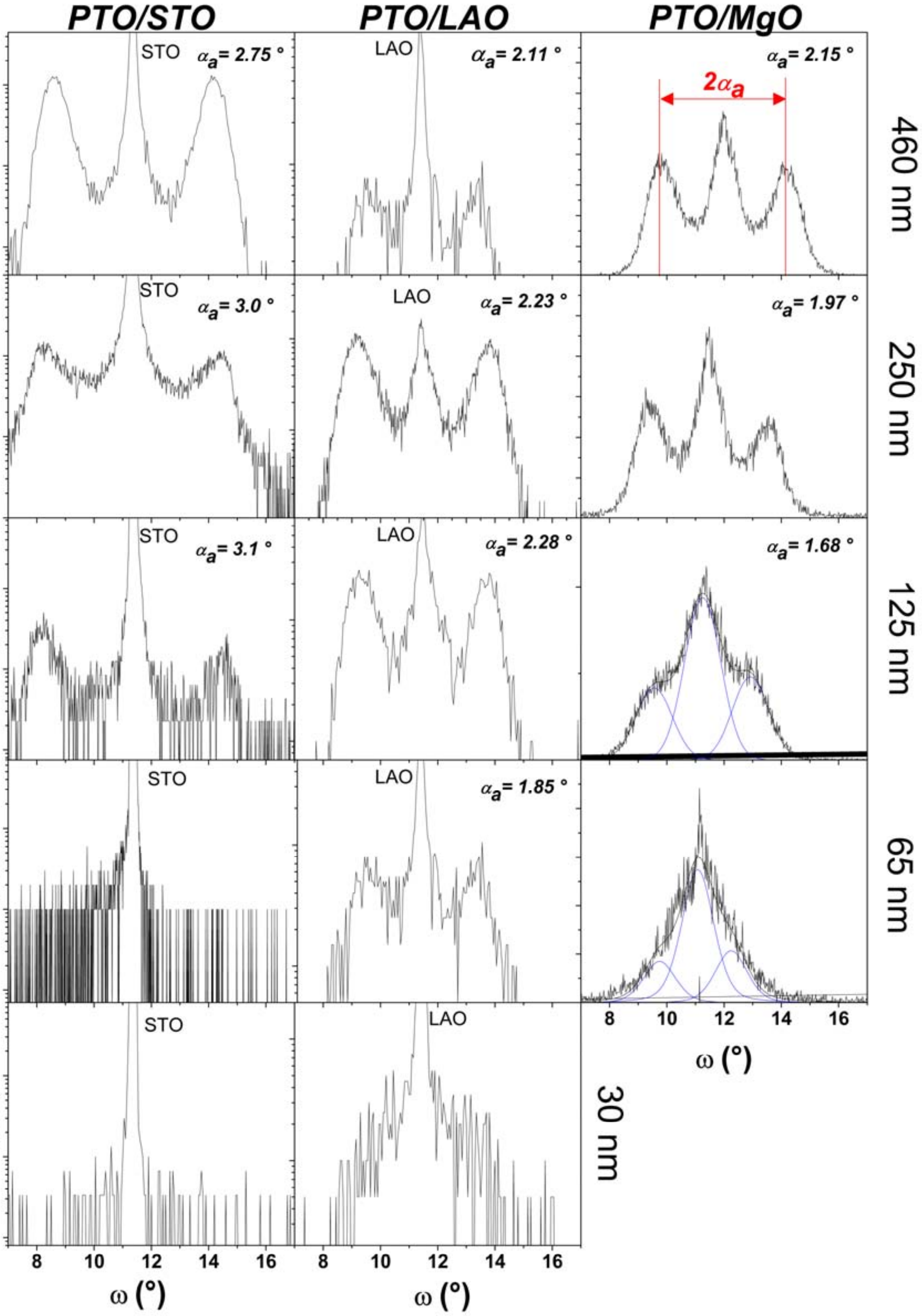

Figure 4-15: Rocking curves of the (100) reflection of a-domains in the30-460 nm thick PTO films on STO, LAO and MgO substrates. Estimation of a-domain twinning angle is shown on the rocking curve of 460 nm thick PTO/MgO film.

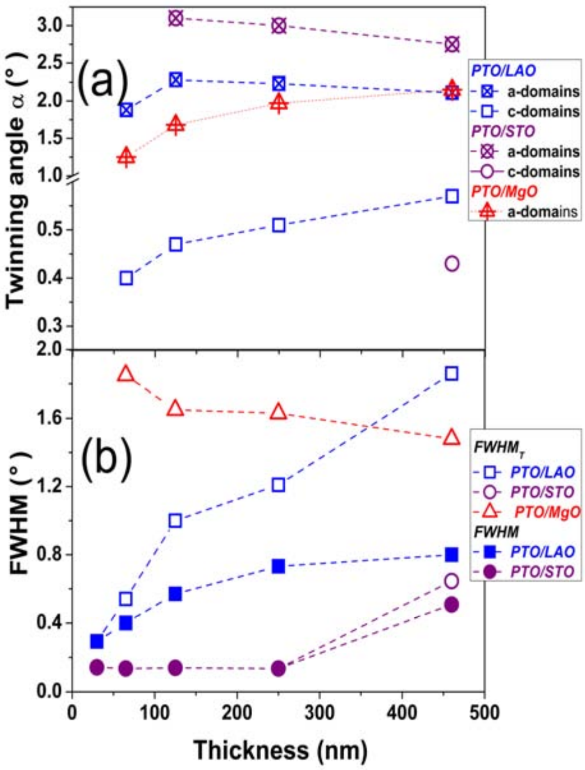

Figure 4-16: Thickness evolution of (a) twinning angles of a- and c-domains and (b) rocking curve FWHM (for more details see in the text) corresponding to the c-domain (001) reflection in PTO films on STO, LAO and MgO substrates.

film, where the *a*-domain twinning angle is lower than expected. In the case of PTO/MgO films, the *a*-domain fraction decreases when increasing film thickness, resulting in the increase of the *a*-domain tilt angle. We did not estimate the *c*-domain tilt angle in PTO/MgO films. However, the total FWHM of the rocking curve from the *(001)* reflection decreases with the increase of film thickness (Figure 4‑16b). This indicates that the *c*-domain tilt angle should decrease when increasing PTO/MgO film thickness.

4.3.4 Mosaicity

***c*-domains** The mosaicity of *c*-domains is evaluated from the FWHM of the *(001)* rocking curves. The FWHM of one profile component and the total FWHM$_T$ are presented in Figure 4‑16 b. One can see that FWHM$_T$ depends not only on the mosaicity but also on the *c*-domain twinning angle. Thus, in the case of triple rocking curves, mosaicity can be described only by FWHM of one component. In the case of PTO/MgO films, FWHM of one component was not estimated; thus, the thickness evolution of the mosaicity will not be discussed.

The *c*-domain mosaicity highly depends on the absolute value of the misfit strain: the bigger absolute misfit strain the bigger mosaicity. The big misfit strains result in low epitaxial quality and relatively high mosaicity. In the case of PTO/LAO films, the *c*-domain mosaicity gradually increases (from FWHM = 0.29° to 0.81°) with the increase of the film thickness. In the case of PTO/STO, the *c*-domain mosaicity is very low (FWHM = 0.14 °) and remains constant with the increase of film thickness from 30 nm to 250 nm, indicating a high epitaxial quality. The mosaicity of the 460 nm thick PTO/STO films is a few times higher (FWHM = 0.51 °) than in the thinner films. The mosaicity increase in the thick films can be explained by the increase of defects (such as twins and dislocations) concentration.

***a*-domains** It is difficult to evaluate the *a*-domain mosaicity from the *(100)* rocking curves, as peaks are usually asymmetric due to the twinning angle distribution.

However, the thickness evolution of twinned *a*-domain mosaicity can be estimated qualitatively from the χ-ω maps of *(301)/(310)* reflections (Figure 4-13). The 125 nm thick PTO/STO film and the 65-125 nm thick PTO/LAO films have a very small fraction of *a*-domains. Thus, *(301)/(310)* spots corresponding to *a*-domains have very low intensities and are not well defined. In PTO films with significant *a*-domain fraction (all PTO/MgO films and 250-460 nm PTO films on LAO and STO substrates), *the (301)/(310)* spot broadening is almost identical. This indicates that the thickness evolution of *a* -domain mosaicity is negligible. Moreover, the *a*-domain mosaicity is independent of misfit strain.

In conclusion, the *c*-domain mosaicity increases with increasing film thickness or with mismatch with the substrate due to the increase of defect concentration. Twinned *a* -domain mosaicity does not depend on substrate material nor on film thickness. This indicates that twinned *a*-domain mosaicity is determined by the film matrix. Taking into account the influence of twinning and instrumental resolution (0.1° in rocking curve) on FWHM values given in Figure 4-16, the epitaxial quality of PTO/STO is very good and PTO films on LAO and MgO substrates can be considered as rather well-oriented.

4.4 HR TEM analysis of dislocations and twin defects

In order to investigate the epitaxial quality of the film-substrate interface and the density of twins and dislocations, HR TEM analysis was performed on film cross sections. The effect of different mismatch between the film and the substrate was studied by comparison of the 250 nm thick PTO films on LAO and STO substrates. The effect of film thickness will be shown by comparing the 65 nm and the 250 nm thick PTO/LAO films.

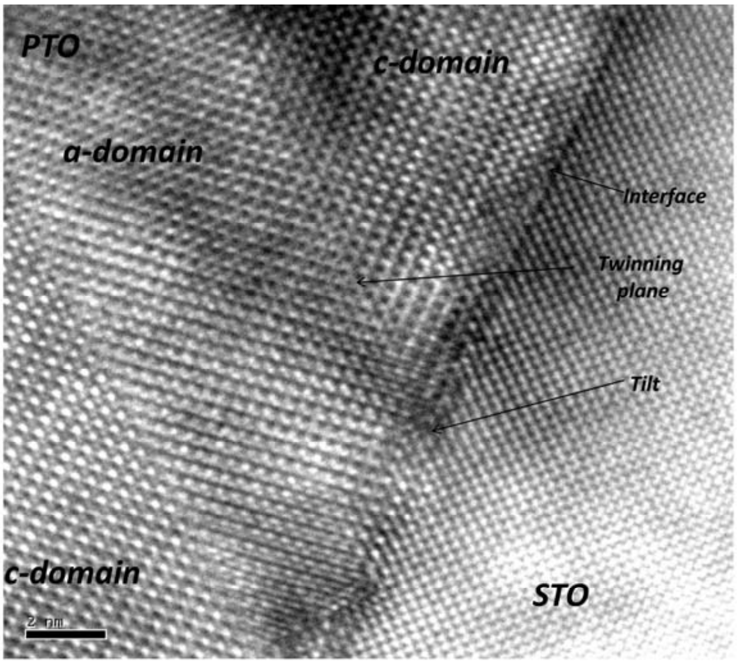

Figure 4-17: High resolution cross-sectional TEM micrograph of the 250 nm thick PTO/STO film.

PTO/STO films The high-resolution cross-section TEM image of the 250 nm thick PTO/STO film is given in Figure 4-17. It can be seen that the *c* -domain interface is congruent without any misfit dislocations in this region, indicating a high epitaxial quality of the film. Electron diffraction patterns taken at the interface, as seen in the Figure 4-18, confirmed the in-plane coherency, with no splitting

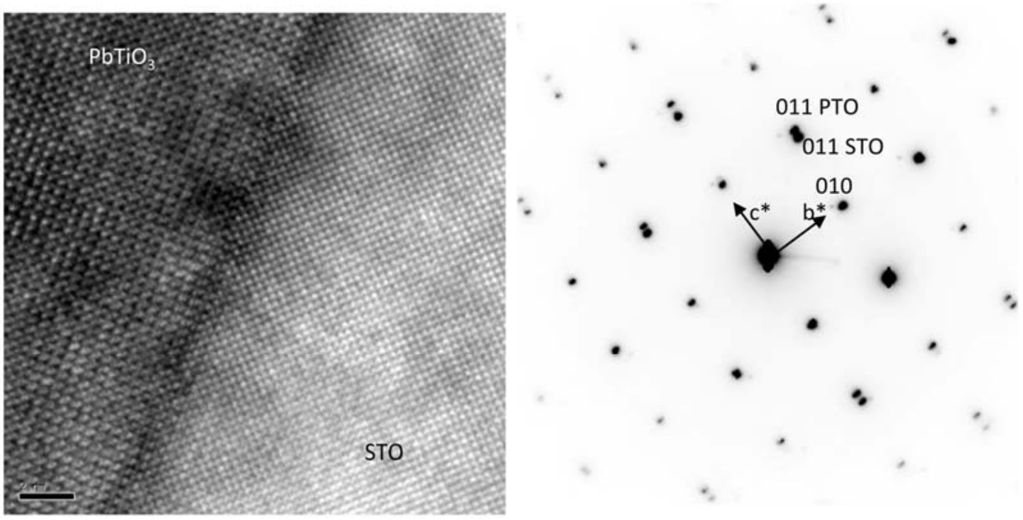

Figure 4-18: Electron diffraction patterns measured at the interface zone of the 250 nm thick PTO/STO film. The TEM micrograph corresponding to the analyzed zone is given in the left side of figure.

of the *(0k0)* PTO and STO reflections up to the third order. Such high quality interfaces were observed also by other authors (18). It is important to note that no splitting of the (*h00)* PTO and STO reflections was observed by XRD when probing all the film thickness, that indicates the high quality of the whole film and not only of the interface. The extra diffraction spots corresponding to *a*-domains were not observed in electron diffraction patterns, as they were obtained only at *c*-domain –substrate interface.

The cross-sectional TEM micrographs reveal the presence of *a*-domains which appear as wedge-shaped domains and twinned to the *c*-domain matrix (Figure 4-17). High resolution images of these twins confirmed the sharing of the *(101)* plane of both orientations. As explained in section 1.5, the consequence of this common *(101)* plane is the tilt of *a*- and *c*-domains from the surface normal. As shown above, the tilt angle is bigger in *a*-domains than in *c*-domains. In the case of the 250 nm thick PTO/STO film, *a*-domains are tilted by 3 ° from the surface normal (or from the substrate surface). Therefore, the tilt of *a*-domains can be observed in high resolution images: the basal plane of *a*-domains is slightly tilted from the substrate plane.

Furthermore, the interface between *a*-domain and substrate presents defects as can be seen in Figure 4-17. The *a*-domain formation is unfavourable on STO substrate due to the relatively big mismatch (-6.3 % at RT). In the 250 nm thick PTO/STO films, a part of the compressive misfit stress should be already relaxed by the formation of misfit dislocations, as proposed by Foster et al. (9) Thus, the formation of misfit dislocations at the interface may provide nucleation sites for *a*-domains during ferroelectric-paraelectric phase transition.

In the lower magnification cross-sectional TEM image of 250 nm PTO/STO film (Figure 4-19), only the primary twinned *a*-domains is observed, i.e., the twins which

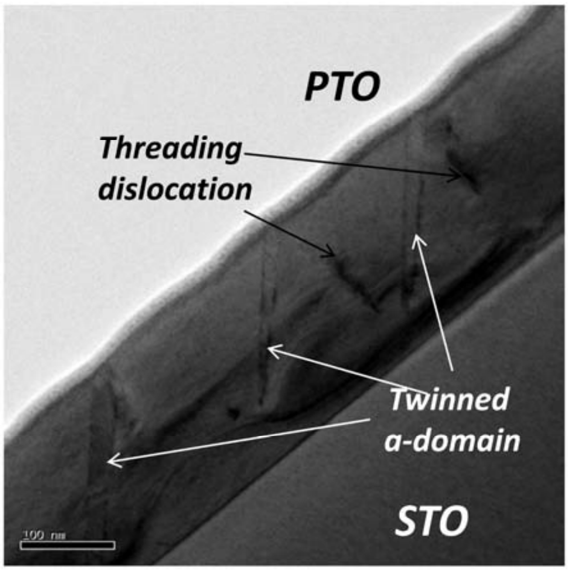

Figure 4-19: Cross-sectional TEM micrograph of the 250 nm PTO/STO film.

nucleate at film-substrate interface or in *c*-domain matrix. The secondary twins that nucleate on primary twins are also detected in other micrographs. However, the primary *a*-domains are dominant. The TEM micrograph with secondary *a*-domains in PTO/STO films is not presented here, as similar secondary *a*-domains are observed in PTO/LAO films and corresponding TEM image will be shown below. An average *a*-domain width and domain period W (or so called domain width, W, as defined in section 1.5) are ~ 25 nm and ~ 240 nm, respectively. Thus, polarization and strain fields should be highly heterogeneous, as W value is close to the film thickness (250 nm) (for more details see in section 1.5).

It can be seen that *a*-domains nucleate not only at the film-substrate interface, but also in the film volume. Generally, the defect density in the film volume and at the film interface increases with the increase of film thickness, providing the additional nucleation sites for *a*-domains. As seen in Figure 4‑19, the threading dislocations initiate not in the film interface, but also in the film volume. The *a*-domain volume fraction is only 4% in the 250 nm thick PTO/STO film. The threading dislocation density is ~ 10^{10} cm^{-2} and is consistent with literature data for PTO epitaxial films (9). Small *a*-domain fraction indicates a low defect density in the film volume and in the film-substrate interface. In conclusion, the misfit dislocation density decreases when decreasing the film thickness as the misfit stresses are less relaxed. Therefore, in the 30-125 nm thick PTO/STO films, where the misfit dislocations and volume defect density is much lower than in the 250 nm thick film, there are just a few or no nucleation sites for *a*-domains.

PTO/LAO films The high resolution cross-sectional TEM micrographs corresponding to the 65 nm and 250 nm thick PTO/LAO films are given in Figure 4‑20 and Figure 4‑21, respectively. One can see that the PTO/LAO film-substrate interface quality is lower than the PTO/STO one. This can be explained by a higher PTO lattice mismatch with LAO substrate (- 4.2 % at T_{Dep}) than with STO substrate (-1.1 % at T_{Dep}). The high mismatch with substrate results in low epitaxial quality and high misfit dislocation density. Furthermore, the 250 nm thick PTO/LAO film interface quality is lower than that of the 65 nm thick one: with increasing film thickness, the film relaxes stresses by generation of misfit dislocations and consequently the interface is of lower quality.

The electron diffraction pattern, measured at the interface zone of the 250 nm thick PTO/LAO film is presented in Figure 4‑22. Only the *(010)* reflections of PTO and LAO superimpose, while higher order reflections are split. This indicates that PTO films are not coherent in the plane with LAO substrate. Furthermore, extra diffraction spots corresponding to twinned *a*-domains are observed in electron diffraction pattern.

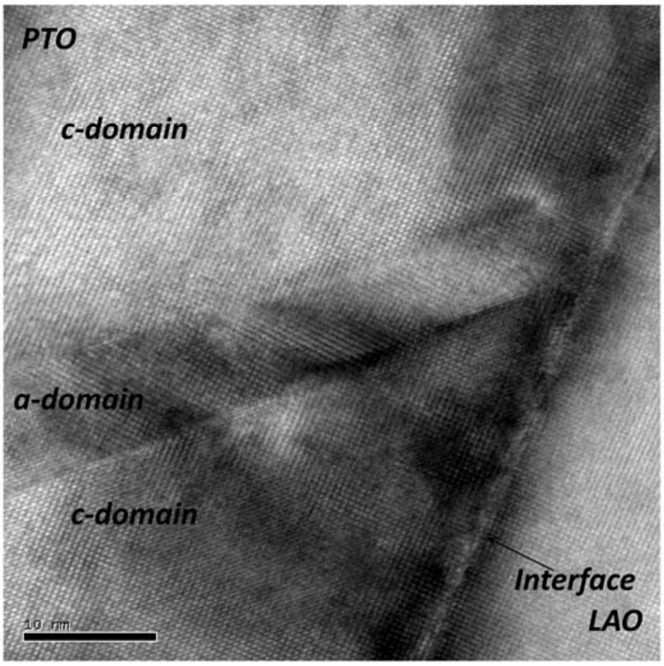

Figure 4-20: High resolution cross-sectional TEM micrograph of the 65 nm thick PTO/LAO film.

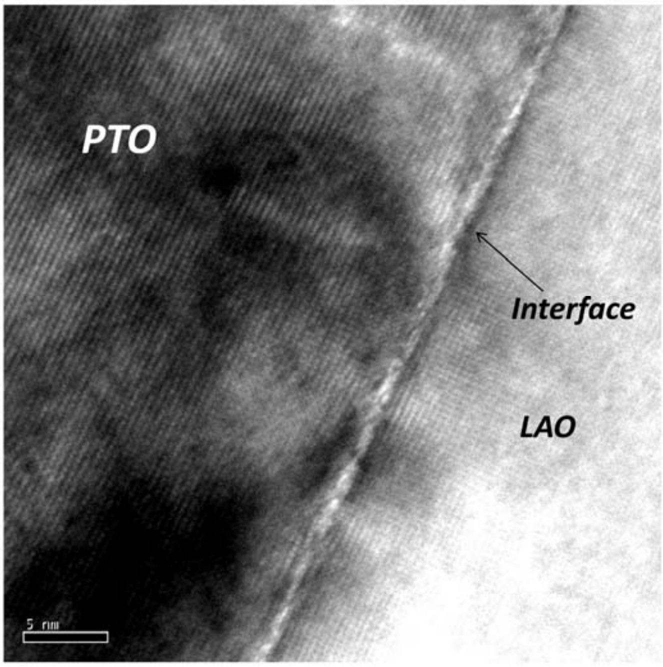

Figure 4-21: High resolution cross-sectional TEM micrograph of the 250 nm thick PTO/LAO film.

It can be seen in lower magnification TEM micrographs (Figure 4‑23) that primary *a*-domains are highly dominant in the 65 nm thick PTO/LAO film like in the 250 nm PTO/STO film. Nevertheless, both primary and secondary *a*-domains are observed in the 250 nm thick PTO/LAO film. Probably, the secondary *a*-domain formation is significant only in well-relaxed films. Furthermore, in the case of both 65 nm and 250 nm thick PTO/LAO films, the threading dislocations initiate at the film-substrate interface and cross the film thickness. Moreover twinned *a*-domains nucleate also mainly at the film-substrate interface, as misfit dislocation density is high enough. However, the twin and dislocation density in the 250 nm thick PTO/LAO film is considerably higher than in the 65 nm thick one. The threading dislocation density is ~ 10^{11} cm^{-2} in 250 and 65 nm thick films. The average domain period is 130 nm for the two thicknesses, which is smaller than in the 250 nm thick PTO/STO film. Nevertheless, the *a*-domain width is considerably smaller (8 nm) in 65 nm thick sample than in the 250 nm thick one (30 nm). Moreover, the non-twinned *a*-domains occur in the 250 nm thick film. The boundaries between non

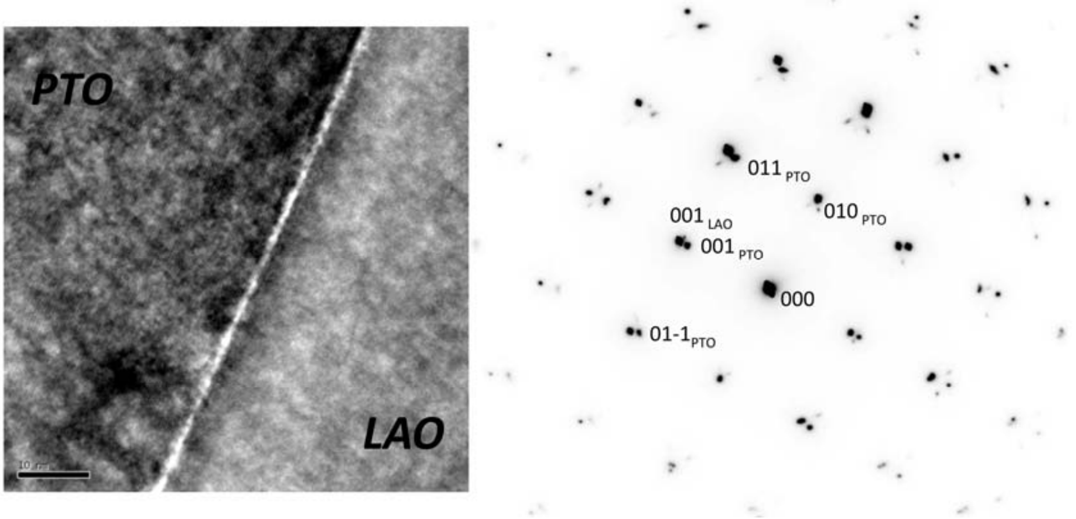
PTO
LAO
10 nm
011 PTO
010 PTO
001 LAO
001 PTO
000
01-1 PTO

Figure 4-22: Electron diffraction patterns measured at the interface zone of the 250 nm thick PTO/LAO film. The TEM micrograph corresponding to the analyzed zone is given in the left side of figure.

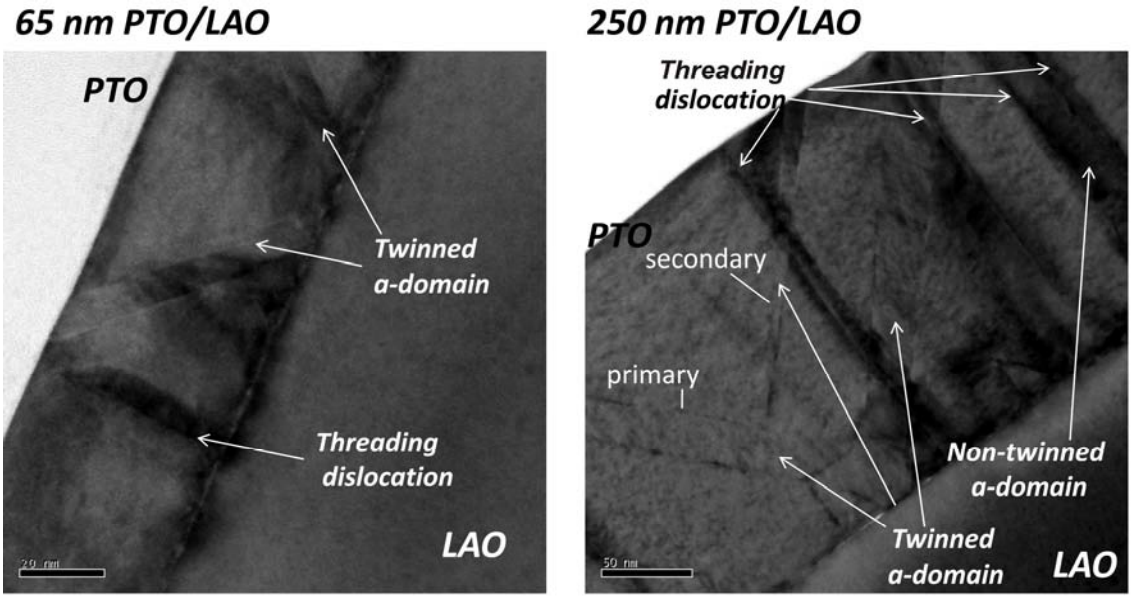
65 nm PTO/LAO
PTO
Twinned a-domain
Threading dislocation
LAO
20 nm
250 nm PTO/LAO
Threading dislocation
PTO
secondary
primary
Non-twinned a-domain
Twinned a-domain
LAO
50 nm

Figure 4-23: Cross-sectional TEM micrographs of the 65 nm and 250 nm thick PTO/LAO films.

-twinned *a*- and *c*-domains are defective: threading dislocation is observed on each boundary. A schematic representation of boundaries between twinned and non-twinned *a*- and *c*-domains is given in Figure 4‑24. The boundaries between non-twinned *a*- and *c* -domains are highly unfavoured, as the mismatch between *a*- and *c*-axis is 6.1 % (Figure 4-24). Therefore, non-twinned *a*-domains may form in *c*-domain matrix only in highly relaxed films, where the threading dislocation density is high. It is important to note that non-twinned *a*-domain fraction is very small as it is not observed by XRD.

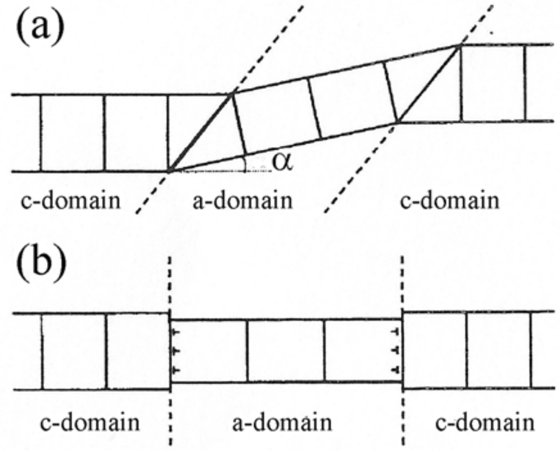

Figure 4-24: Schematic representation of boundaries between twinned (a) and non-twinned (b) a- and c-domains (28).

To conclude, the defect (dislocations and twins) density (or stress relaxation) increases with the increase of misfit strain and film thickness. The 250 nm thick PTO/STO films are coherent in-plane with substrate, while PTO/LAO films are epitaxial but not coherent in-plane with the substrate. The misfit dislocations are the main nucleation sites for *a*-domains in PTO films under compressive misfit stress. The secondary *a*-domains mainly form in relaxed films. The non-twinned *a*-domains are observed in films with high density of threading dislocations, as non-twinned *a*- and *c*-domain boundaries can be created only through defects.

4.5 Lattice parameters in a- and c-domains

The in-plane and out-of-plane lattice parameters of *a*- and *c*-domains were estimated from the *(103)* and *(301)/(310)* reflections in ω-2Θ area maps, as explained in section 2.2.2. The substrate peak positions were used as internal standard assuming that substrate is strain free. The thickness evolution of in- and out-of-plane lattice parameters of *a*- and *c*-domains is given in Figure 4‑25. We would like to note that in-plane and out of-plane *c*-domain lattice parameters of the 125-460 nm thick PTO/STO films were also estimated from 30 reflections in the reciprocal space maps, using orientation matrix. Moreover, *c*-lattice parameters of *c*-domains in the 30-460 nm PTO films on STO, LAO and MgO substrates were also checked from five *(00l)* reflections in standard Θ/2Θ scans. The values obtained by the three different methods were within the error bars. Therefore, the lattice parameters estimated from one reflection in ω-2Θ area maps are precise enough for our analysis. However, higher deviations between values of the in-plane parameters were observed. Therefore, in the case of in-plane parameters, error bars are bigger than these of *c*-axis of *c*-domain, as shown in Figure 4‑25. The lattice parameters of films on different substrates will be discussed separately.

4.5.1 PTO/STO films

***c*-domains** The *a* lattice parameters of *c*-domains in PTO/STO films remain constant in the limits of error bars with the change in film thickness from 30-460 nm. Their values are very close to those of STO and bulk PTO (Figure 4‑25). The out-of-plane lattice parameters of *c*-domains are smaller than *c*-parameter of bulk PTO whatever the film thickness. Compressive stress in the [00*l*] direction, dominant in the substrate/*c*-domains interface region, could explain such a difference with the bulk val-

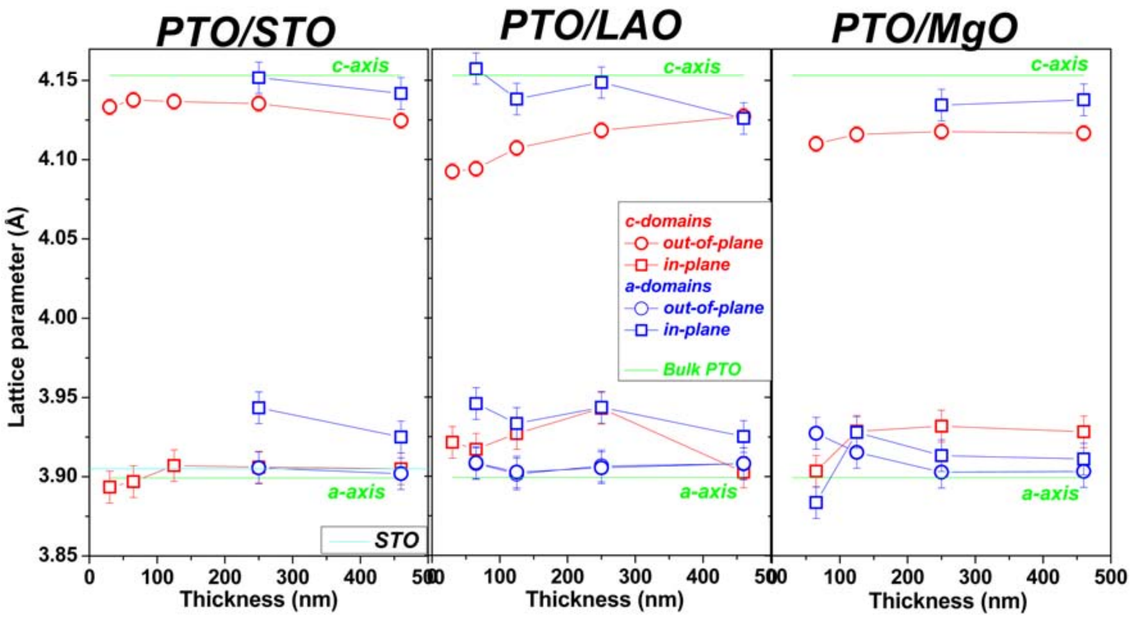

Figure 4-25: Thickness evolution of in-plane and out-of-plane lattice parameters of a- and c-domains in the 30-460 nm thick PTO films on STO, LAO and MgO substrates. Error bars of c-domain out-of-plane lattice parameters are within symbols. Bulk values are indicated by a

ues. However, thin films are usually considered as subjected to biaxial stresses in the film plane whereas the normal direction is stress free. Therefore, the *c* parameter decrease in *c*-domains should rather arise from biaxial tensile stress in the film plane. Furthermore, when increasing film thickness the *c*-lattice parameter decreases, indicating the increase of the biaxial tensile stress in the film.

a-domains In the case of *a*-domains, the out-of-plane lattice parameter (*a*-axis perpendicular to the substrate plane) is the same as the *a*-lattice parameter of *c*-domains in the 250-460 nm thick PTO/STO films. However, the in-plane *a*-lattice parameter is considerably increased comparing to the out-of-plane *a*-parameter. Moreover, the *c*-parameter of *a*-domains is also increased comparing to that of *c*-domains. The increase of in-plane lattice parameter in *a*-domains could not result from compressive misfit strain. He et al.(30) also observed significantly increased in-plane lattice parameters comparing to out-of-plane ones in cubic STO/LAO epitaxial films. Janolin et al. (31) reported on increased in-plane lattice parameters due to misfit dislocations as it is proposed by Speck et al. (2). As shown by TEM analysis of the 250 nm PTO/STO film, there is no defects in the *c*-domain/substrate interface, while some defects are observed in the *a*-domain/substrate interface. Therefore, the increase of in-plane lattice parameters of *a*-domains probably results from interfacial defects. The *c*-domains are coherent in the plane with the substrate. Thus, *c*-domain in-plane parameters show reasonable values. Furthermore, the out-of-plane *a*-parameters are the same as those of *c*-domains, as out-of –plane lattice parameters are not affected by interfacial defects.

4.5.2 PTO films on LAO and MgO substrates

In-plane lattice parameters

As shown by TEM analysis of PTO/LAO films, the *a*- and *c*-domain interfaces with substrate have defects. In the case of PTO/MgO films, TEM analysis was not performed but these films should have defective interfaces due to high mismatch with substrate. Moreover, XRD diffraction analysis showed that the PTO/MgO film crystalline quality is lower than that of PTO/STO and PTO/LAO films, indicating that films have a high concentration of defects. Therefore, the in-plane lattice parameters of *a*- and *c*-domains in PTO films on LAO and MgO substrates are highly affected by misfit dislocations or other interfacial defects. Thus, they do not show any clear evolution with film thickness and highly differ from out-of-plane lattice parameters, as seen in Figure 4‑25. Moreover, the in-plane lattice parameters depend more on the defects than on the applied stresses. Therefore, they cannot be used for stress relaxation study and for estimation of stress values .

Out-of-plane lattice parameters

c-axis of c-domains The evolution of the *c* lattice parameter in *c*-domains with film thickness in PTO films on LAO and MgO substrates is given in Figure 4‑25. Generally speaking, the *c* lattice parameter is lower in both PTO/LAO and PTO/MgO films whatever the film thickness comparing to the values reported in literature for bulk PTO. In the case of PTO films on LAO and MgO substrates, the lowest value of *c* lattice parameter of *c*-domains is observed in the thinnest films, and it gradually increases with the thickness without reaching the bulk *c* value even in the 460 nm thick film. However, this evolution is less pronounced in PTO/MgO films. This indicates that PTO films on both LAO and MgO substrates are under tensile stress in the film plane whatever the film thickness, although compressive and tensile misfit stresses are expected, respectively. Furthermore, the increase of *c* lattice parameter shows the relaxation of tensile stresses with the increase of film thickness. However, the strain relaxation is slow due to low thermal energy, as our films were deposited at relatively low temperature (650°C). Thus, the bulk PTO lattice parameter value is not reached even in the 460 nm thick films.

a-axis of a-domains In the 30-460 nm thick PTO/LAO and PTO/MgO films, the out-of-plane lattice parameters of *a*-domains are slightly higher than *a* lattice parameter of bulk PTO. In the case of PTO/LAO films, *a*-domain *a* parameter is very close to that of bulk PTO and is constant with the increase of film thickness in the limits of error bars. On the other hand, it decreases with the increase of the PTO/MgO film thickness, reaching the bulk PTO values in the 250-460 nm thick films.

In conclusion, the in-plane lattice parameters of *a*-domains are affected by interfacial defects, while the out-of-plane lattice parameters are more determined by the *c*-domain matrix. Our estimated a-parameters of c-domains are consistent with those reported in literature (24; 19; 32). According to Poisson law, tensile stress in the plane results in the increase of the in-plane lattice parameters and in the decrease of the out-of-plane lattice parameters. In the case of our films, the *c*-lattice parameter is smaller than the corresponding bulk value whatever the mismatch with the substrate. Other groups also reports on the decrease of *c*-axis on substrates inducing tensile or compressive misfit stress (19; 32; 24). However, the *c*-axis deformation with stresses is higher, as it is about four times more elastic than the *a*-axis (corresponding stiffness moduli will be given in section 4.6 (Table 4-2)). Furthermore, the in-plane lattice parameters usually are blocked by substrate and do not evolve with stress relaxation. Thus, we will use the *c* lattice parameter of *c*-domains to estimate the residual stress in the films.

4.6 Residual stress

In this section, first, we will shortly present the theoretical considerations on estimation of the residual biaxial (in-plane) stress from out-of-plane lattice parameters. In the following, we will present the residual stress values obtained for our films.

4.6.1 Theoretical considerations

Hooke's law for anisotropic materials is of the form

$$\varepsilon_{\mathrm{ij}} = \mathrm{S}_{\mathrm{ijkl}}\sigma_{\mathrm{kl}} \tag{4.1}$$

or, inverting the equation and expressing stresses in terms of strains:

$$\sigma_{ij} = C_{ijkl}\varepsilon_{kl} \quad . \tag{4.2}$$

Here $\varepsilon_{ij}(\varepsilon_{kl})$ is the strain, $\sigma_{kl}(\sigma_{ij})$ – the stress and S_{ijkl}, C_{ijkl} are the compliance and stiffness moduli of the crystal under consideration, and both are tensors of the fourth rank (33).

In the case of the tetragonal *c*-axis oriented thin film on cubic substrate, the film is under biaxial stress in the basal *xy* plane and z direction is stress free. Therefore, the principal stress components are equal $\sigma_b=\sigma_{xx}=\sigma_{yy}$ and we assume that there is no shear stress/strain component. For symmetry reasons, the basal strain is also biaxial $\varepsilon_{xx}=\varepsilon_{yy}=\varepsilon_b$ and we get in two index notation (Nye) the mechanical equilibrium relation:

$$\begin{pmatrix}\sigma_b\\ \sigma_b\\ 0\end{pmatrix} = \begin{pmatrix}C_{11} & C_{12} & C_{13}\\ C_{12} & C_{11} & C_{13}\\ C_{13} & C_{13} & C_{33}\end{pmatrix}\begin{pmatrix}\varepsilon_b\\ \varepsilon_b\\ \varepsilon_{zz}\end{pmatrix} \tag{4.3}$$

Developing line 3 in Eq. 4.3 and isolating the ε_b component, we get:

$$\varepsilon_b = -\frac{C_{33}\varepsilon_{zz}}{2C_{13}} \tag{4.4}$$

Lines 1 and 2 in Eq. 4.3 are identical:

$$\sigma_b = (C_{11} + C_{12})\varepsilon_b + C_{13}\varepsilon_{zz} \tag{4.5}$$

Substituting in Eq. 4.5, the ε_b component from Eq. 4.4, we obtain the result:

$$\sigma_b = \left(-\frac{(C_{11} + C_{12})C_{33}}{2C_{13}} + C_{13} \right)\varepsilon_{zz} \quad . \tag{4.6}$$

The elastic compliance and stiffness moduli are the same for both tension and compression (33). As it is only dependent on the variation of the interatomic forces with interatomic distance about the equilibrium position, the modulus is a basic material property and is not significantly affected by processes such as heat treatment or plastic deformation for most common engineering materials. Furthermore, since along various directions in the point lattices the spacing between the atoms is different, hence the elastic modulus will change the direction, causing anisotropy. The elastic modulus is constant along given direction through the crystal volume. The PTO stiffness moduli used in stress determination from Eq. 4.6 are given in Table 4- 2.

Table 4-2: $PbTiO_3$ stiffness moduli (34).

Stiffness modulus (GPa)	
C_{11}	237 ± 3
C_{33}	60 ± 10
C_{12}	90 ± 5
C_{13}	70 ± 10

The strain in *c*-domains of epitaxial $PbTiO_3$ thin films can be evaluated from the film *c*-lattice parameter, using equation:

$$\varepsilon_{zz} = -\frac{c_f - c_b}{c_f} \tag{4.7}$$

where c_b=4.1532 Å is the bulk PTO *c*-lattice parameter.

4.6.2 Residual stress in PTO films

The residual stress values in PTO films on STO, LAO and MgO subtrates were estimated from Eq. 4.6 and are given in Figure 4‑26. The positive stress values of σ_b suggest that all films are under tensile stress in the film plane whatever the mismatch with the substrate and the film thickness. The fact that we do not observe a compressive stress in PTO/LAO films at RT indicates that the films do not retain the strain induced by the mismatch with the substrate. A more important source of strains is probably produced by other types of stresses. We will address this apparent contradiction later in chapter 7.

Residual stress gradually relaxes from 1 GPa down to 0.4 GPa with increasing PTO/LAO film thickness from 30 to 460 nm. Residual stress remains almost constant within the error bars with the increase of PTO/MgO film thickness, while in PTO/STO films, the tensile stress increases with increasing the film thickness. In the case of the 30-125 nm thin films, the residual stress is highest (1.1-0.85 GPa) in PTO/LAO films, while it is as low as 0.3 GPa in PTO/STO films. The residual stress values are almost the same within error bars in the 460 nm thick films on STO, LAO and MgO substrates (0.48 GPa, 0.44 GPa and 0.62 GPa, respectively). An exhaustive discussion on residual stress evolution with film thickness, relaxation and residual tensile stress origin will be given in chapter 7.

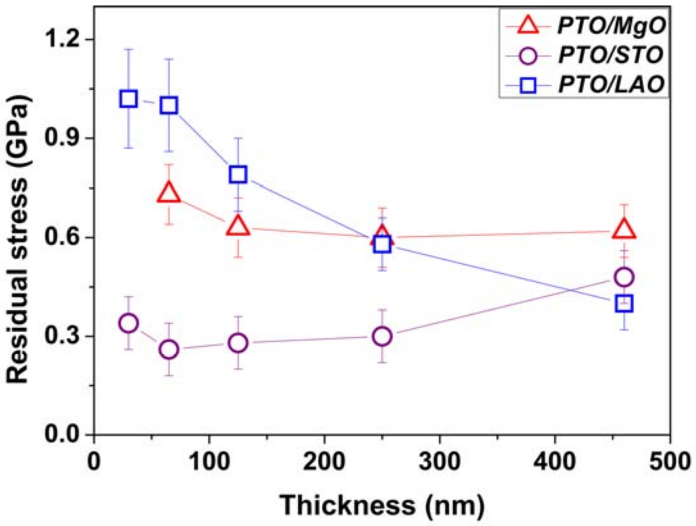

Figure 4-26: Thickness dependence of residual stress in PTO films on STO, LAO and MgO substrates.

4.7 Heterogeneity of strains in PTO films

The primary origin of homogeneous film strain is the stresses resulted from the substrate. In addition, defects can produce heterogeneous strains that can affect the technological relevance properties of thicker relaxed films (35). Furthermore, the heterogeneous strains couple strongly to the polarization and it has been shown by phenomenological theory that they significantly affect the phase transition temperature. Thus, it is of importance to study the heterogeneity of strains. In epitaxial films, the quantitative analysis of heterogeneous strain fields is based on modeling of the two-component XRD profiles (i.e. profiles made of the superposition of a narrow coherent Bragg peak and a broad diffuse scattering profile) (36; 37). Such analysis is out of scope of this study. Thus, our study of heterogeneous strain will be limited to qualitative analysis of XRD line profiles.

In order to study the strain distribution in the film, the diffraction peak profile analysis was performed. Figure 4‑27 shows the evolution of the *(003)* reflection line in Θ/2Θ scans as a function of PTO film thickness on STO, LAO and MgO substrates. The analysis of the line profile indicates an important line broadening in PTO films on LAO and MgO substrates. Reflection profiles of the 125-460 nm PTO films on LAO and MgO substrates present a marked asymmetry on the low *d* side which we attribute to an heterogeneous deformation of the *c* lattice parameter by defects. As shown above, these films have a higher defect density than 30-65 thick ones. Therefore, this asymmetry is not observed in very thin films. It is important to note that film volume heterogeneously strained is much smaller than that homogenously strained. In the case of PTO/STO

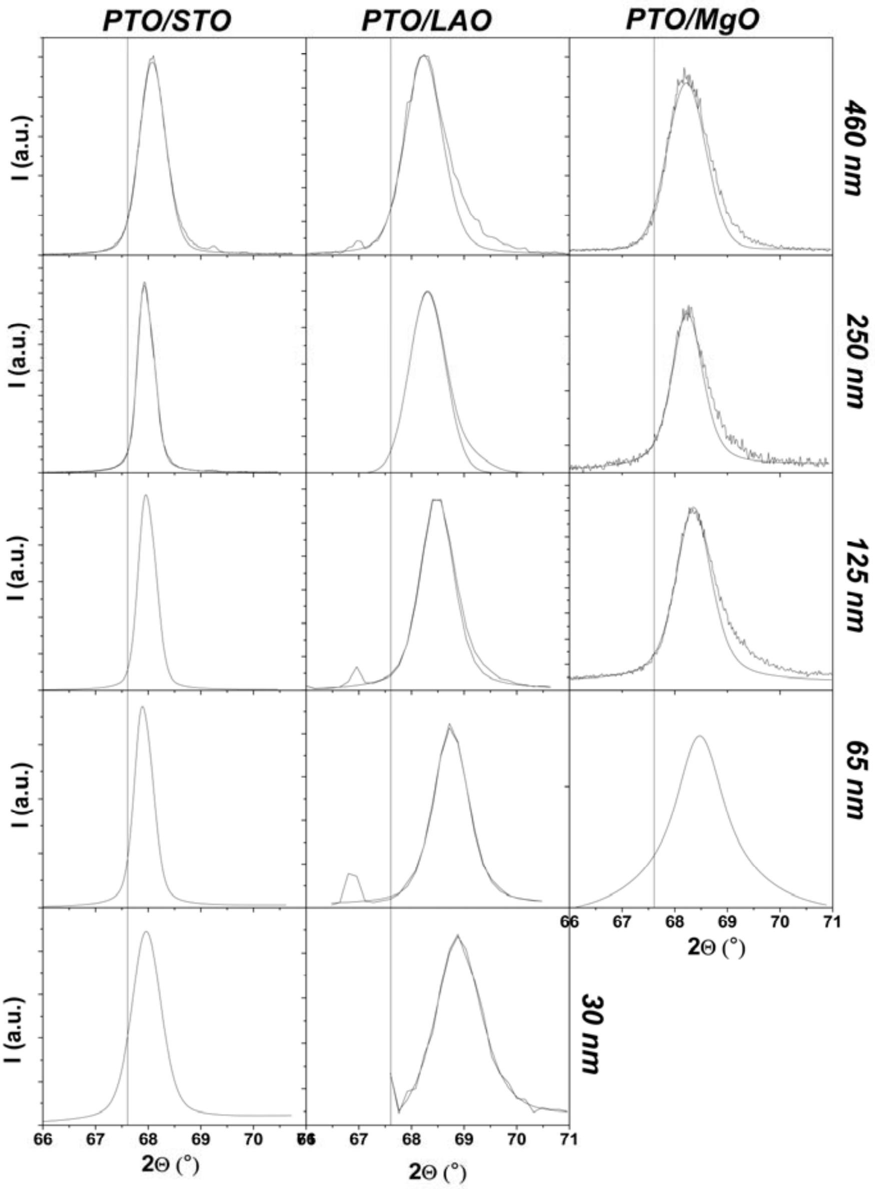

Figure 4-27: Evolution with thickness of the (003) XRD reflection profile corresponding to c-domains in PTO films on STO, LAO and MgO substrates.

films, the peaks are very thin for the 30-250 nm thin films, and a remarkable change in the peak profile is observed only for the 460 nm thick film. The epitaxial quality of PTO/STO films is high and the defect density is very low. Thus, defect effect on strains in the films is negligible.

In order to compare the strain homogeneity along the *c*- and *a*-axis, the *(113)* and *(131)* reflections corresponding to *c*-domains in the 460 nm PTO films on LAO and STO were studied and are given in Figure 4‑28. The *(113)* and *(131)* reflections have bigger contribution of *c*- and *a*-axis, respectively. This can be also seen qualitatively from the positions of the peaks:

$2\Theta(113)_{film} > 2\Theta(113)_{bulk}$ as $c_{film} < c_{bulk}$,

$2\Theta(131)_{PTO/LAO} < 2\Theta(131)_{bulk}$ as $a_{PTO/LAO} > a_{bulk}$,

$2\Theta(131)_{PTO/STO} = 2\Theta(131)_{bulk}$ as $a_{PTO/STO} = a_{bulk}$.

It is important to note, that the peak positions are not corrected and that a deviation from the real positions is possible.

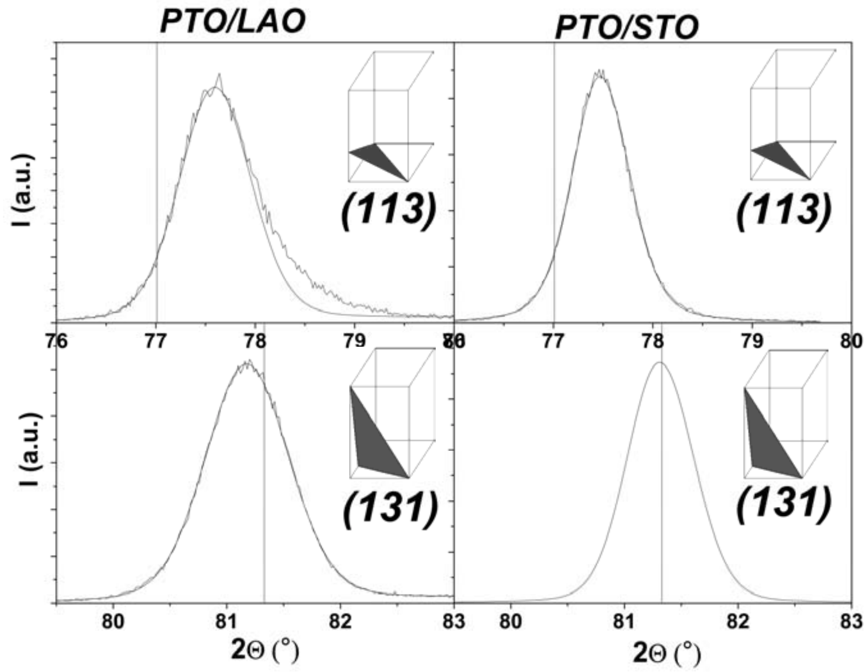

Figure 4-28: Profiles of the (113) and (131) reflections of c-domains in the 460 nm thick PTO films on STO and LAO substrates. The corresponding planes in the tetragonal cell are presented in the inset of each graph. The peak positions are not corrected and a deviation from the real positions is possible.

In the case of PTO/STO films, the strains along the *a*- and *c*-axis are homogeneous, as both *(113)* and *(131)* reflection profiles are symmetric. A significant asymmetry in the low *d* side is observed in the *(113)* reflection corresponding to *c*-domains in the 460 nm PTO/LAO film. As explained above, this indicates a strain heterogeneity. However, the *(131)* reflection profile of the PTO/LAO films is symmetric, indicating homogeneous strain of *a* lattice parameter.

To study the homogeneity of strains in *a*-domains, the *a*-domain reflections corresponding to the same planes as in c-domains were measured and are shown in Figure 4‑29. We denote these reflections as *(113)* and *(131)* by analogy with *c*-domains but they are the *(131)* and *(113)* reflections in *a*-domain coordinates, respectively. The *(113)* reflection profile is asymmetric in high-*d* side, while the *(131)* reflection profile is symmetric, indicating heterogeneous strain of *c*-axis, while *a*-axis is strained homogeneously. However, as shown above, *a*-axis deformation under stress is very small due to it small elasticity. Thus, if the *a* lattice parameter deformation gradients exist, they are too small to be observed. The *c*-axis is elastic, thus stresses or defects result in high deformations and in observable asymmetry in the case of heterogeneous strain. The asymmetry difference of peaks corresponding *a*– and *c*-domains results from out-of– and in-plane stress effects.

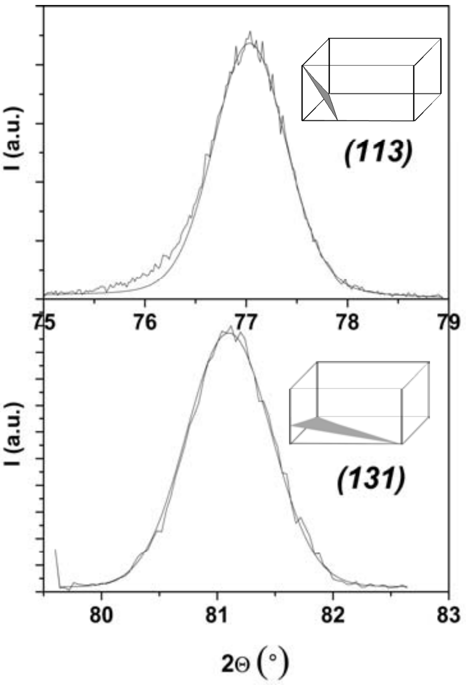

Figure 4-29: Profiles of the (113) and (131) reflections of a-domains in the460 nm thick PTO/LAO films. The corresponding planes in the tetragonal cell are presented in the inset of each graph. Note that planes are indicated in the coordinates of c-domains. The peak positions are not corrected and a deviation from the real positions is possible.

To conclude, heterogeneous strain can be observed by analyzing XRD reflections with high *c*-axis contribution, as *c*-axis is more elastic than *a*-axis. Strain relaxing defects, such as misfit or threading dislocations, reduce or eliminate the elastic energy associated with homogeneous strains. However, all the defects prevalent in the film do generate the heterogeneous strain. Thus, the strain is slightly heterogeneous in both *a*- and *c*-domains in the films with relatively high defect density. The heterogeneously strained volume is much smaller than the homogeneously strained one, indicating that homogeneous stress resulting from substrate is more important than heterogeneous one induced by defects.

4.8 Microstrains and average grain size

X-ray diffraction line broadening may come from strain and size effects. For example, the FWHM=0.40° observed for the *(001)* reflection in 125 nm PTO/LAO film is almost four times larger than the instrumental resolution (0.1˚ 2θ evaluated from the substrate line profile). The individual contributions from strain and size effects to the (00*l*) reflection line broadening were estimated using both the Williamson-Hall analysis (WH) and the Halder-Wagner approximation (HW) as explained in section 2.2.4. The deconvolution of the instrumental contribution and profile fitting using a pseudo-Voigt function approximation were carried out using the program *WinplotR*. Calculations were performed using the five (00*l*) reflections obtained for the 30-460 nm PTO films on STO, LAO and MgO substrates, and the results are given in Figure 4‑30. Both methods give the same tendencies in the average grain size and in microstrains in each case. Nevertheless, the absolute values obtained by WH and HW analysis differ but are of the same order.

4.8.1 Average grain size

As a general observation from the Figure 4‑30, the grain size increases with the film thickness. The only exception is the 460 nm thick PTO/STO film, whose grain size (118 nm in WH and 68 nm in HW analysis) is smaller than that of the 250 nm thick one

(250 nm in WH and HW analysis). Furthermore, the grain size decreases with the increase of the misfit strain. The average grain size is close to the thickness value in 30-250 nm thick PTO/STO films, indicating that films are almost single crystalline, i.e. there is no grains. In the 460 nm PTO/STO film, *a*-domain fraction is relatively high (~ 17 %). Thus, the domain size and consequently the average grain size decrease.

The grain size increases from 23 nm to 133 nm in WH analysis and from 18 nm to 76 nm in HW approximation with increasing the PTO/LAO film thickness. The grain sizes of the PTO/LAO film are smaller than film thickness and than those of PTO/STO films, except in the 30 nm thick PTO/LAO film, which consists only of *c*-domains. The grain sizes are relatively small (33-52 nm in WH and 22-37 nm in HW analysis for the 125-460 nm films) and the thickness dependence is smaller in PTO/MgO films than in PTO/LAO or PTO/STO films. In PTO films on LAO and on MgO the mismatch with the substrate is bigger than in PTO/STO films, resulting in lower crystalline quality. Moreover, domains are small due to high *a*-domain fraction. This results in a decrease of grain size comparing to PTO/STO films.

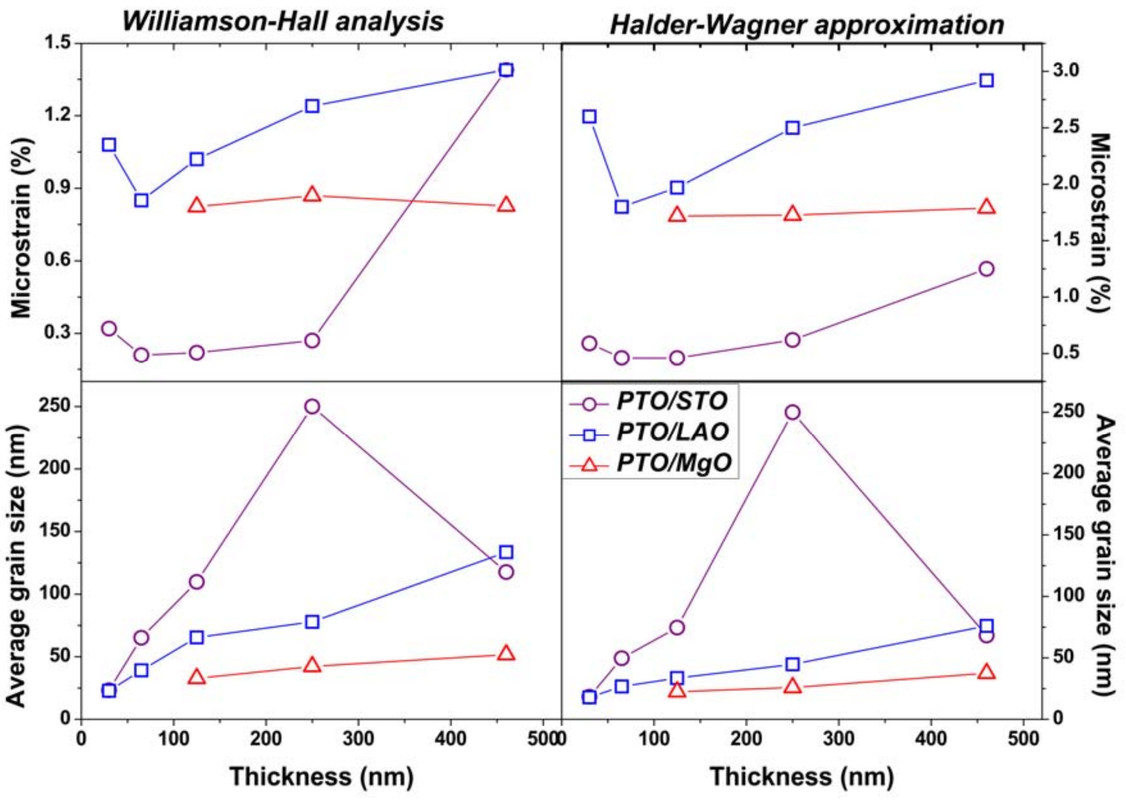

Figure 4-30: Evolution with thickness of microstrains and average grain sizes, estimated by using Williamson-Hall and Halder-Wagner analyses in PTO films on STO, LAO and MgO substrates.

4.8.2 Microstrains

Concerning microstrains, the lowest microstrain values (0.3 %) are estimated in PTO/STO films, where mismatch with the substrate is very small. PTO films have relatively big mismatch with MgO and LAO substrates, thus the microstrains are rather high. Moreover, they reach 3% in HW and 1.5 % in WH analysis in the 460 nm PTO/LAO films, where the misfit stress is already relaxed. This indicates that an other phenomenon than misfit stress may increase the microstrains in the film.

In the case of PTO/STO films, microstrains first decrease with film thickness reaching a minimum value (0.2 % in WH and 0.5 % in HW analysis) in between a thickness of 65 and 125 nm and then increase (up to 1.4 % (WH) and 1.2 % (HW)) in 460 nm thick film). The same behaviour was reported by de Keijser et al (38) in PTO/STO films. As the PTO/LAO film thickness increases from 30 nm to 65 nm, the misfit stresses relax, resulting in the decrease of microstrains from 1.1 % to 0.9 % (WH) and from 2.6 % to 1.8 % (HW). Further increase of the PTO/LAO film thickness up to 460 nm leads to the generation of defects, dislocations and twins, resulting in higher disorder and thus, in higher microstrains (up to 1.4 % (WH) and 2.9 % (HW)). However, the microstrain evolution with film thickness is more pronounced in PTO film on LAO substrate, than that on STO substrate. This can be explained by high stresses (section 4.6.2) in very thin films and by high defect concentration (section 4.4) in thicker PTO/LAO films.

In the case of the 125-460 nm thick PTO/MgO films, the microstrains are rather high and are independent (0.8 % (WH) and 1.8 % (HW)) of film thickness. As shown above, even thin PTO/MgO films consist of twinned and non-twinned *a*- and *c*-domains. This indicates, that PTO/MgO film structure has a high concentration of defects, such as twins and misfit and threading dislocations, resulting in high microstrains in films. Microstrains remain constant with the film thickness, as the defect concentration probably does not vary significantly in 125 -460 nm thick PTO/MgO films.

Both WH and HW analyses converge and give evidence that the line broadening is mainly due to strain effect but grain size effect cannot be neglected especially in the thinnest films. In conclusion, the high microstrains result from misfit stress in very thin films and from high defect concentration in thicker ones.

Conclusions

30 - 460 nm thick epitaxial PTO films were deposited on STO, LAO and MgO substrates by PI MOCVD. Epitaxial quality of PTO/STO films is very good and PTO films on LAO and MgO substrates can be considered as rather well oriented films. The *c*-domain mosaicity increases with the increase of film thickness and mismatch with the substrate, while it is thickness and substrate independent in the case of *a*-domains.

The *a*-domain fraction increases with increasing thickness in PTO films on STO and LAO substrates, inducing compressive misfit stresses, while in the case of tensile misfit stresses (PTO/MgO films) it decreases. In all three film/substrate systems, the twinned/non-twinned domain volume ratio increases with the increase of film thickness, indicating a stress relaxation. The twinning angle of twinned *a*-domains decreases with the increase of total (twinned and non-twinned) *a*-domain volume fraction and as a consequence, the tilt angle of *c*-domains increases.

TEM and XRD analysis revealed that high defect (dislocations and twins) density is observed in thick PTO films with high lattice mismatch with the substrate.

In-plane lattice parameters of *a*- and *c*-domains are affected by the presence of defects, while the out-of-plane parameters is stress dependent.

Residual stress values in c-domains were estimated from c-lattice parameters. The films are under tensile stress in the film plane whatever the substrate and the film thickness. With increasing film thickness, the residual stress decreases in PTO films on MgO and LAO, while it increases in PTO/STO films.

The analysis of XRD reflection profiles indicated a small volume fraction heterogeneously strained in the films with a high defect density. This shows that homogeneous stress resulting from substrate is more important than heterogeneous stress induced by defects.

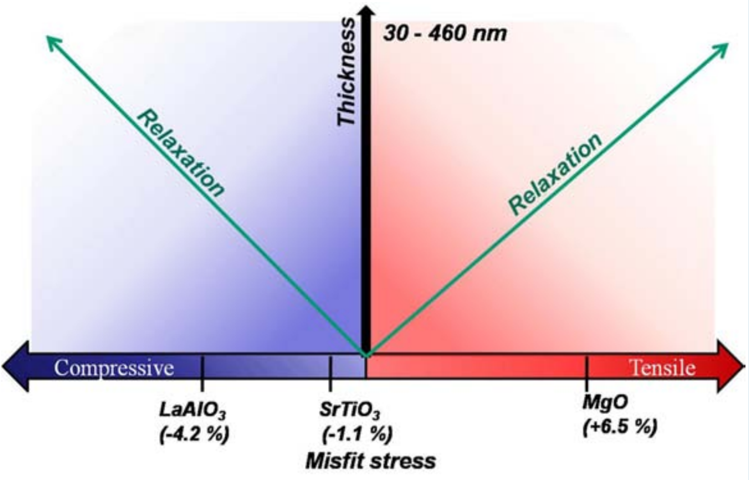

Figure 4-31: Schematic representation of stress relaxation with film thickness and misfit stress.

Both Williamson-Hall and Halder-Wagner analyses give evidence that XRD line broadening is mainly due to strain effects but grain size effect cannot be neglected especially in thinner PTO films on LAO and STO and in 125-460 nm PTO/MgO films. The high microstrains result from misfit stress in thin films and from defects in thicker ones.

To summarize, the stress relaxes by formation of defects such as twins and dislocations with the increase of the film thickness and the increase of lattice mismatch between the film and the substrate (Figure 4-31). Nevertheless, high defect density results in heterogeneous strains and microstrains.

Bibliography

1. **A.L. Roytburd.** s.l. : Phys. Status Solidi A, 1976, Vol. 37, p. 329.

2. **J.S. Speck and W. Pompe.** s.l. : J. Appl. Phys., 1994, Vol. 76, p. 466.

3. **W. Pompe, X. Gong, Z. Suo, and J.S. Speck.** s.l. : J. Appl. Phys., 1993, Vol. 74, p. 6012.

4. **Y.L. Li, S.Y. Hu, Z.K.Liu, L.Q. Chen.** s.l. : Appl. Phys. Lett., 2001, Vol. 78, p. 3878.

5. **V.G. Koukhar, N.A.Pertsev, and R. Waser.** s.l. : Phys. Rev. B, 2001, Vol. 64, p. 214103.

6. **N.A. Pertsev and A.G. Zembilgotov.** s.l. : J. Appl. Phys., 1995, Vol. 78, p. 6170.

7. **B.S. Kwak, A. Erbil, J.D. Budai, M.F. Chisholm, L.A. Boatner, and B.J. Wilkens.** 21, s.l. : Phys. Rev.B, 1994, Vol. 49, p. 14865.

8. **C.M. Foster, W. Pompe, A.C. Daykin, and J.S. Speck.** 3, s.l. : J. Appl. Phys., 1996, Vol. 79, p. 1405.

9. **C.M. Foster, Z. Li, M. Buckett, D. Miller, P.M. Baldo, L.E. Rehn, G.R. Bai, D. Guo, H. You, and K.L. Merkle.** 4, s.l. : J. Appl. Phys., 1995, Vol. 78, p. 2607.

10. **R.S. Batzer, B.M. Yen, D. Liu, H. Chen, H. Kubo, and G.R. Bai.** 11, s.l. : J. Appl. Phys., 1996, Vol. 80, p. 6325.

11. **K. Lee and S. Baik.** 81, s.l. : Annu. Rev. Mater. Res., 2006, Vol. 36, p. 81.

12. **W.-Y. Hsu and R. Raj.** 6, s.l. : Appl. Phys. Lett., 1995, Vol. 67, p. 792.

13. **Z. Li, C.M. Foster, D. Guo, H. Zhang, G.R. Bai et al.** s.l. : Appl. Phys. Lett., 1994, Vol. 65, p. 1106.

14. **B.M. Yen and H. Chen.** 2, s.l. : J. Appl. Phys., 1999, Vol. 85, p. 853.

15. **K. Franke, J. Besold, W. Haessler, and C. Seegebrath.** s.l. : Surf. Sci., 1994, Vol. 302, p. L283.

16. **S. Stemmer, S.K. Streiffer, F. Ernst, M. Ruhle, W.-Y. Hsu, and R. Raj.** s.l. : Solid State Ionics, 1995, Vol. 75, p. 43.

17. **Y.K. Kim, H. Morioka, R. Ueno, S. Yokoyama, H. Funakubo, K. Lee, and S. Baik.** s.l. : Appl. Phys. Lett., 2006, Vol. 88, p. 252904.

18. **A.T.J. van Helvoort, O. Dahl, B.G. Soleim, R. Holmestad, T. Tybell.** s.l. : Appl. Phys. Lett., 2005, Vol. 86, p. 092907.

19. **Y.K. Kim, H. Morioka, and H. Funakubo.** s.l. : J. Appl. Phys., 2007, Vol. 101, p. 064112.

20. **Y.K. Kim, H. Morioka, R. Ueno, S. Yokoyama, and H. Funakubo.** s.l. : Appl. Phys. Lett., 2005, Vol. 86, p. 212905.

.

21. **K.S. Lee and S. Baik.** s.l. : J. Appl. Phys., 2000, Vol. 87, p. 8035.

22. **D.D. Fong and C. Thompson.** s.l. : Annu. Rev. Mater. Res., 2006, Vol. 36, p. 431.

23. **M. Dawber, C. Lichtensteiger, P. Paruch and J.M. Triscone.** 12, s.l. : IEEE TUFC, 2006, Vol. 53, p. 2261.

24. **W.K. Choi, S.K. Choi, and H.M. Lee.** s.l. : J. Mater. Res., 1999, Vol. 14, p. 4677.

25. **S. Ito, H. Funakubo, I.P. Koutsaroff, M. Zelner and A. Cervin-Lawry.** s.l. : Appl. Phys. Lett., 2007, Vol. 90, p. 142910.

26. **B.H. Park, E.J. Peterson, Q.X. Jia, J.Lee, X. Zeng, W. Si, and X.X. Xi.** s.l. : Apl. Phys. Lett., 2001, Vol. 78, p. 533.

27. **R. Ahluwalia and W. Cao.** s.l. : J. Appl. Phys., 2001, Vol. 89, p. 8105.

28. **K. Lee, H. Yi, W.-H. Park, Y.K. Kim and S. Baik.** s.l. : J. Appl. Phys., 2006, Vol. 100, p. 05161529. **C.S. Ganpule, V. Nagarajan, B.K. Hill, A.L. Roytbard, E.D. Williams, S.P. Alpay, A. Roelops, R. Waser, and L.M. Eng.** s.l. : J. Appl. Phys., 2002, Vol. 76, p. 1477.

30. **F. He, B.O. Wells, Z.-G. Ban, S.P. Alpay, S. Grenier, S.M. Shapiro, W. Si, A. Clark, and X.X. Xi.** s.l. : Phys. Rev. B, 2004, Vol. 70, p. 235405.

31. **P.-E. Janolin, B. Fraisse, F. Le Marrec, and B. Dkhil.** s.l. : Appl. Phys. Lett., 2007, Vol. 90, p. 212904.

32. **Wenhui, M. Zhang, L. Sun, Y. Chen, N. Ming, Y. Jin, and Q. Huang.** s.l. : Ferroelectrics, 1998, Vol. 23, p. 153.

33. *Residual stress, Measurement by diffraction and Interpretation.* **I.C. Noyan and J.B. Cohen.** s.l. : Springer-Verlag/New York, 1987.

34. **A.G.Kalinichev, J.D. Bass, B.N. Sun and D.A. Payne.** s.l. : J. Mat. Res., 1997, Vol. 12, p. 2623.

35. **N. Setter, D. Damjanovic, L.Eng, G. Pax, S. Gevorgian, S. Hong et al.** s.l. : J. Appl. Phys., 2006, Vol. 100, p. 051606.

36. **A. Boulle, R. Guinebretiere and A Dauger.** s.l. : J. Phys. D: Appl. Phys., 2005, Vol. 38, p. 3907.

Chapter 5:

Raman modes and residual stress

Chapter 5

5 Raman modes and residual stress ______________________ *107*

5.1 Introduction ____110

5.2 General considerations: Raman modes and their activity in bulk $PbTiO_3$ ___________________________________111

5.2.1 Raman selection rules ______________________________111

5.2.2 Polarized Raman spectra _____________________________112

5.2.3 Origin of the so-called oblique modes (or “quasimodes)_________114

5.2.4 Polarized Raman spectra _____________________________112

5.3 Effect of polarization in $PbTiO_3$ films ______________________118

5.4 Estimation of residual stress by using the E(TO) modes ______120

5.4.1 Theoretical considerations ___________________________120

5.4.2 Relation between residual stress and misfit strain ____________121

5.4.3 Residual stress in *a*- and *c*-domains_____________________123

5.4.4 Effect of thickness on the residual stressing *c*-domains ________126

5.5 Analysis of the domain structure from A_1(TO) modes________127

5.5.1 A_1(1TO) soft mode_________________________________128

5.5.2 A_1(TO) hard modes and domain structure________________129

Conclusions ____130

Bibliography ____131

5. Raman modes and residual stress

5.1 Introduction

Physical properties of ferroelectrics in bulk material and in thin films can be substantially different due to stresses, grain size effect, domain structure, defects … (1,2) For instance, film stresses can significantly change mechanical, optical and electrical properties, ferroelectric domain structure and the nature of phase transition, which in turn has a potential influence on the reliability of devices. Ferroelectric properties such as dielectric, piezoelectric, and optical characteristics critically depend on the ferroelectric domain configuration (3,4) which in turn depends on the various stresses developed during film fabrication. Therefore, an experimental investigation of residual stress is useful for predicting and controlling physical properties for ferroelectric film-based devices.

Films are usually submitted to substantial stresses during growth and subsequent cooling process from deposition temperature to room temperature (RT). At the growth temperature, stresses are mainly misfit stresses (also called epitaxial stresses) and intrinsic stresses related to the growth technique, which are negligible in MOCVD. During the cooling process, additional thermal stresses and transformation stresses may develop in the film. Stresses in epitaxial ferroelectric films are mainly relaxed by the formation of dislocations and by twinning.

In the past, optical fluorescence (5), X-ray diffraction (XRD) (6), wafer curvature measurements (7), cantilever beam deflection (8), laser reflectance (9) and Raman spectroscopy (10; 11; 12; 13; 14; 15; 16; 17) have been used for stress analysis in ferroelectric materials. Among them, XRD and Raman spectroscopy are the most popular techniques, as they are powerful tools for non-destructive investigation of structure. Raman spectroscopy is complementary to XRD methods as it is a local probe and is sensitive to even subtle changes of symmetry. Moreover, ferroelectricity and, thus, Raman modes are strongly influenced by mechanical deformation of the sample resulting, for example, from hydrostatic pressure or stress (11; 12; 18; 19; 20; 21).

Even though epitaxial films often have physical properties superior to polycrystalline films (i.e. in terms of polarization), only few papers on stress evaluation by Raman spectroscopy are known in such epitaxial films (16; 17) and most reports concern stress evaluation in polycrystalline films on sapphire or Si substrates (10; 13; 14; 15). Different theoretical studies analyze the stress state (22) and the possible mechanisms for stress relaxation (23) in epitaxial PTO thin films.

This chapter reports on the Raman study of the residual stress evolution with film thickness in epitaxial PTO films. The depolarization effects due to polydomain structure and the influence of the numerical aperture of the objective on Raman modes were studied. In particular, Raman measurements have been performed in all attainable polarization configurations in the backscattering geometry, which allows to obtain information on both *a*- and *c*-domains.

5.2 General considerations: Raman modes and their activity in bulk $PbTiO_3$

We will see in the following that the analysis of the Raman spectra of PTO thin films is complex. It is for instance important to remind that our films consist of *a*- and *c*-domains and should have 180 º ferroelectric domains, as they are directly grown on dielectric substrates and are unpoled. Thus, Raman modes are not only affected by stresses in the film but also by depolarization effects of the laser beam resulting from 90 º and 180 º ferroelectric domain structure. Therefore, the various depolarization effects have to be taken into account before the evaluation of residual stress. In order to interpret in a meaningful manner the polydomain structure with its Raman modes and to eliminate residual stress effects, we present hereafter an analysis and discussion of the Raman signature of a PTO single crystal which contains 90 º and 180 º ferroelectric domains (just as our thin films).

5.2.1 Raman Selection Rules

Let us first discuss the Raman selection rules, which apply to a polydomain PTO single crystal. The crystallographic reference setting of the single crystal and of the films in our system (*a*- and *c*-domain structure) and the Raman selection rules, allow the assignment of the Raman modes as schematically illustrated in Figure 5‑1.

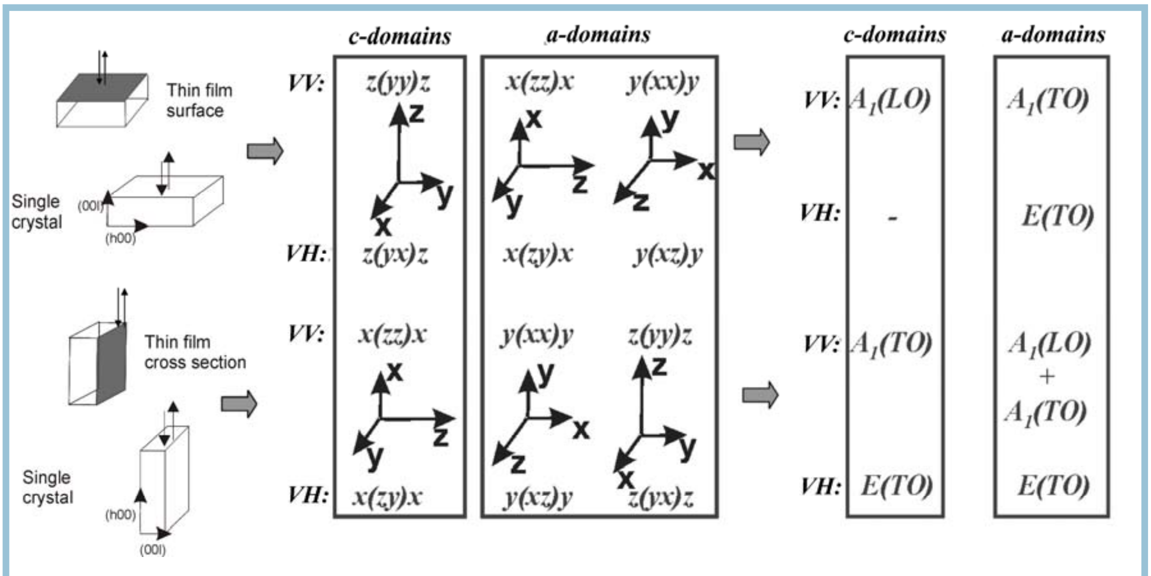
c-domains
a-domains
c-domains
a-domains
Thin film surface
Single crystal
(00l)
(h00)
Thin film cross section
Single crystal
(h00)
(00l)
VV:
z(yy)z
x(zz)x
y(xx)y
VH:
z(yx)z
x(zy)x
y(xz)y
VV:
x(zz)x
y(xx)y
z(yy)z
VH:
x(zy)x
y(xz)y
z(yx)z
x
y
z
VV: A1(LO)
A1(TO)
VH: -
E(TO)
VV: A1(TO)
A1(LO) + A1(TO)
VH: E(TO)
E(TO)

Figure 5-1: Raman scattering geometries and polarization configurations used for the Raman mode assignment in a- and c-domain PTO single crystals and thin films. In the case of the PTO single crystal the crystallographic axes are noted for c-domains.

When a spectrum is recorded on the film surface or in equivalent orientations when using a single crystal, *E(TO)* modes observed in *VH* configuration come from *a*-domains only whereas $A_1(TO)$ modes obtained in *VV* configuration originate in *a*-domains and A_1

(LO) in *c*-domains (Figure 5‑1). The spectrum recorded on the film cross section (or in equivalent orientations in single crystal) in *VH* configuration consists also of *E(TO)* modes, which come from *c*- and 50 % *a*-domains, according to Raman selection rules. *VV* spectra measured on cross section consist of $A_1(LO)$ modes related to *a*-domains and $A_1(TO)$ modes which come from *c*- and 50 % *a*-domains. Considering that the *c*-domain fraction is greater than the *a*-domain fraction in both single crystals and films, whatever the thickness, we can assume that *E(TO)* and $A_1(TO)$ modes come mainly from *c*-domains when spectra are collected on the cross section or in equivalent orientations in single crystals. As seen in Figure 5‑1, *E(LO)* modes cannot be observed in our measurement conditions if selection rules are strictly obeyed. In conclusion, modes relative to *a*- and *c*-domains can be clearly separated in polarized Raman spectra recorded on the cross section as well as on the surface.

5.2.2 Polarized Raman spectra

We now discuss experimental polarized Raman spectra of PTO. As expected from Raman selection rules (section 1.4, Figure 5‑1), *E(TO)* modes are observed in polydomain PTO single crystal spectra measured in *VH* configuration (Figure 5‑2). Peaks with low intensity related to $A_1(LO)$ and $A_1(TO)$ modes allowed in *VV* configuration can be considered as polarization leakage, their small intensity indicates the validity of the applied selection rules. The analysis of spectra recorded in *VV* configuration is more complex, as they consist not only of allowed $A_1(TO)$ and $A_1(LO)$ modes but also of forbidden *E(TO)* and *E(LO)* modes (Figure 5‑-2). Some depolarization effect of the laser beam due to the presence of domains can explain the presence of the *E(TO)* modes usually observed in *VH* configuration but not that of *E(LO)* modes which are forbidden in the backscattering geometry. Moreover, *E(TO)* modes observed in *VV* configuration are shifted towards higher wavenumbers in comparison with modes measured in *VH* configuration. Thus, such anomalies concerning *E(TO)* and *E(LO)* modes should result from another phenomenon. The A_1 and *E(LO)* (*E(TO)*) peak positions obtained from *VV* (*VH*) spectra are given in Table 5- 1. Observed *E(TO)* mode frequencies are rather close to those reported by Foster et al. (24), however some of other mode positions differ by more than 10 cm^{-1} (ex. *E(3LO)* and $A_1(1LO)$), as it will be discussed in the following section.

Table 5-1: $PbTiO_3$ Raman mode shifts at room temperature.

	Our work	Foster et al. (24)
E(TO)	89.5	87.5
	219.9	218.5
	506.2	505
B_1+E	289.7	289
E(LO)	123.2	128
	-	440.5
	718.4	687
$A_1(TO)$	150.5	148.5
	355.0	359.5
	640.7	647
$A_1(LO)$	184.3	194
	463.9	465
	795.4	795

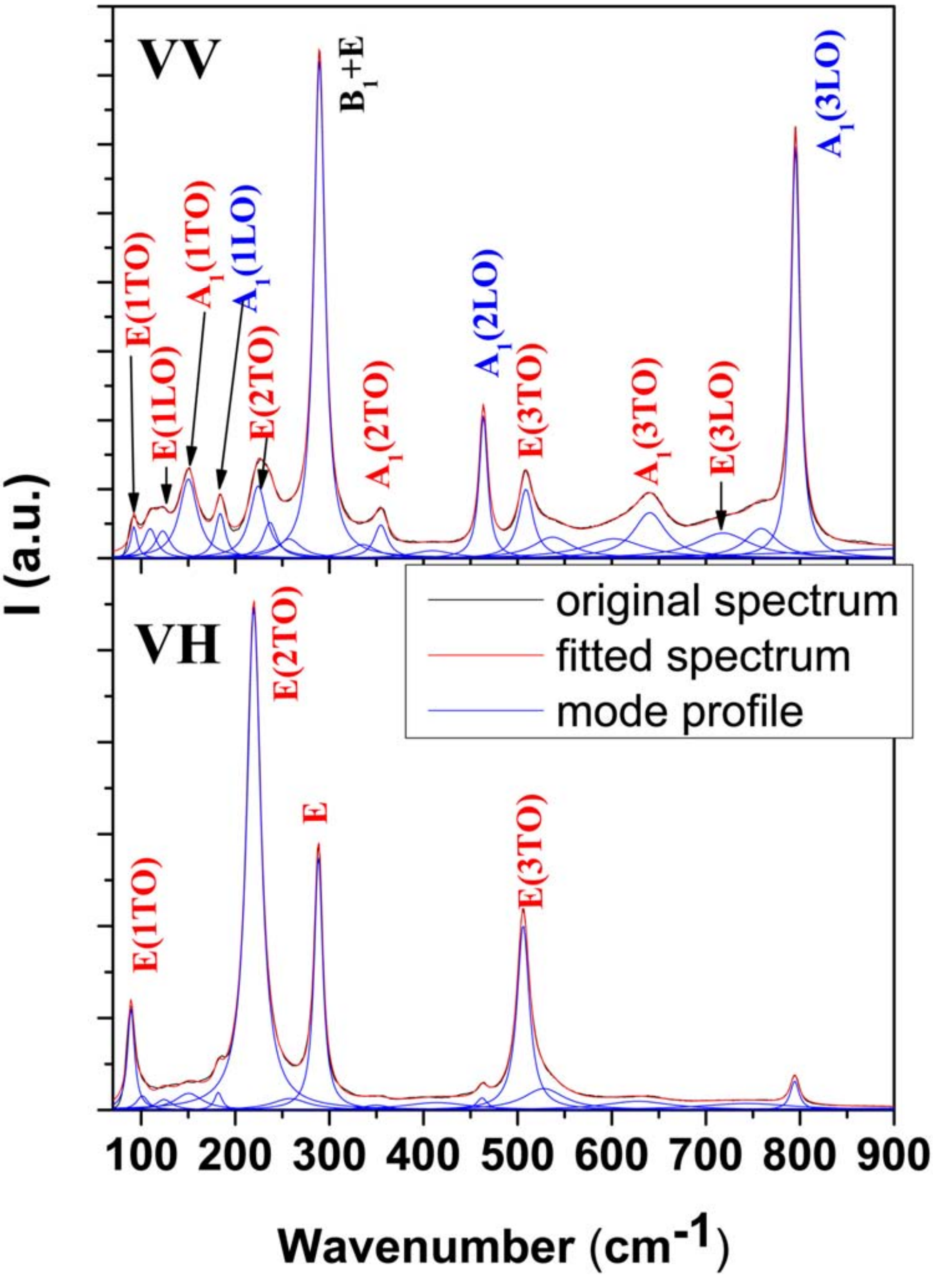

Figure 5-2: Polydomain PTO single crystal Raman spectra recorded in crossed (VH) and parallel (VV) polarization configurations. All modes come from a-domains, the exception is A_1(LO) modes of c-domains (blue indexations).

5.2.3 Origin of the so-called oblique modes (or "quasimodes")

We propose that the forbidden modes and the shift of the *E(TO)* modes can be related to "quasimodes" as defined in Section 1.4. "Quasimodes" are usually observed when $0<\Theta<\pi/2$ (with Θ being the angle between **k** and the direction of the spontaneous polarization) (24) and theoretically, they should not be observed in *c/a/c/a* PTO Raman spectra, as $\Theta = 0^o$ or 90^o.

The peak positions of all modes measured in *VV* polarization configuration agree rather well with Foster's PTO phonon positions as a function of Θ (Figure 5‑3). However, our experimental points appear at different angles on the corresponding curves,

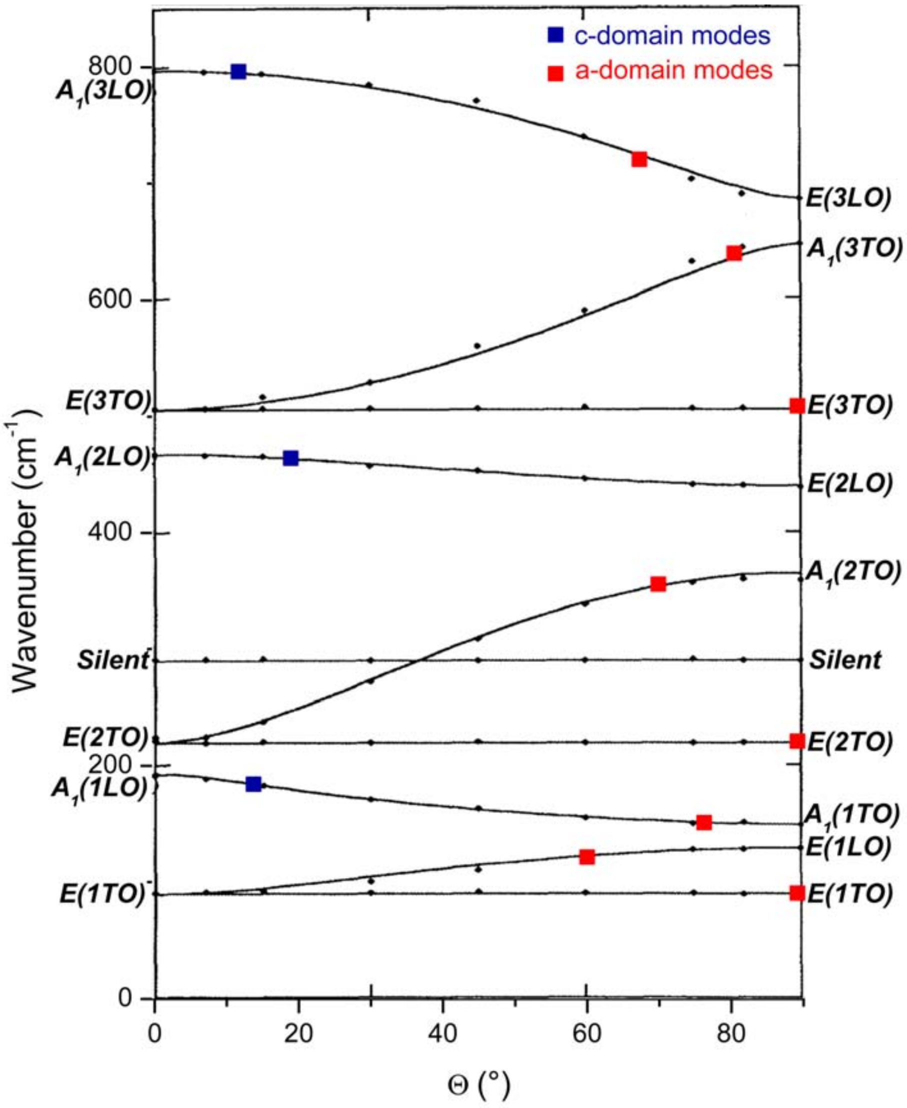

Figure 5-3: Comparison of the peak positions of our polydomain PTO single crystal Raman modes (large symbols on the curves) with PTO phonon frequency curves as a function of Θ as reported by Foster et al. (24).

depending on the type of modes: A_1 or *E*, *LO* or *TO*. As mentioned above, *E(TO)* modes are not affected by Θ. The deviation $\Delta\Theta$ from $\Theta = 0$ ° in *c*-domains and from $\Theta = 90$ ° in *a*-domains ranges from 20 to 30 ° in the case of *E(LO)* modes whereas it is smaller for all other modes (A_1(TO) and A_1(LO)) (10 – 20 °).

The deviation $\Delta\Theta$, which causes the presence of oblique modes in *c/a/c/a* PTO single crystal or film spectra, can be due to different intrinsic and extrinsic phenomena such as the ferroelectric domain structure, the sample misorientation, the numerical aperture and the misalignment in the system.

In agreement with literature we have experimentally observed that profiles of Raman modes in *VV* polarized spectra depend strongly on the sample orientation: a PTO sample exactly aligned with our crystallographic reference setting axes and turned from 20 ° in the base plane does not give identical Raman spectra as seen in Figure 5-4. Intensities and symmetry of A_1*(TO*) modes are especially affected in comparison with *E (TO)* modes. This observation can be understood by the consideration of quasimodes in the spectra.

All modes profiles are also sensitive to the numerical aperture (NA) of the objective as observed in Figure 5-4, where the *VV* polarized spectra were collected using long working distance (LWD) ×50 (NA = 0.5) and ×100 (NA = 0.9) objectives. The peaks are systematically shifted towards higher wavenumbers and A_1*(TO)* modes become more asymmetric and their intensities decrease in spectra collected with ×100 objective in comparison to LWD ×50 objective. From these observations, the effect of the numerical aperture of the objective on the incident and scattered laser beams has to be considered. In order to understand this observation we need to consider the angular dispersion φ_{air} of the incident laser beam: it is 64 ° or 30 ° when using ×100 or LWD ×50 objective, respectively (Figure 5-5). When the laser light reaches the crystal or film surface and due to the change in refraction index *n*, the angular dispersion of the incident light also changes. Calculations ($n_{air} sin\varphi_{air} = n_{PTO} sin\varphi_{PTO}$, where $n_{air} = 1$ and $n_{PTO} = 2.7$,) indicate that it varies from 64 ° to 20 ° with the ×100 objective and from 30 ° to 10 ° with the

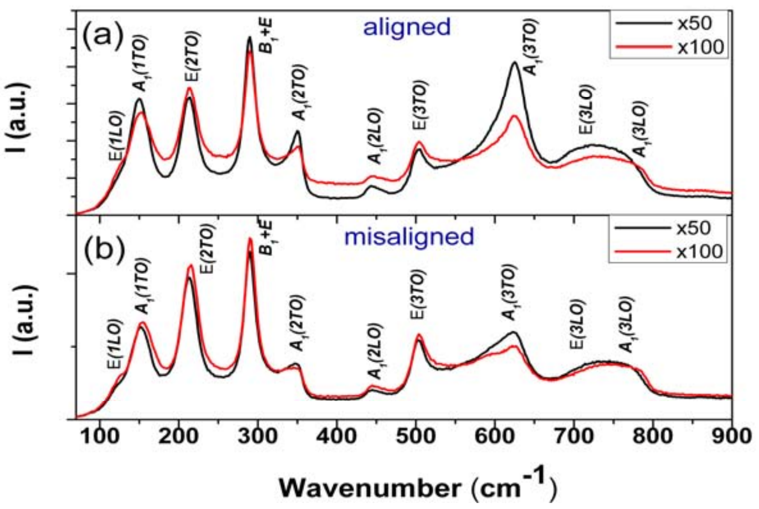

Figure 5-4: : VV polarized Raman spectra collected on the PTO/ MgO film aligned cross section (a) and on cross section turned

LWD ×50 objective. Such an angular dispersion results in the deviation ΔΘ = 20 ° or 10 ° and in the appearance of *A_1(TO), A_1(LO)* and *E(TO)* related oblique modes in VV spectra. In conclusion, quasimode appearance can be reduced but not eliminated by using LWD ×50 objective, having lower angular dispersion than ×100 objective. Because of this it would in principle be even more preferable to work with a x10 objective, but this would have the disadvantage of an enhanced optical depth, which in turn leads to a significant decrease of the signal coming from the thin film.

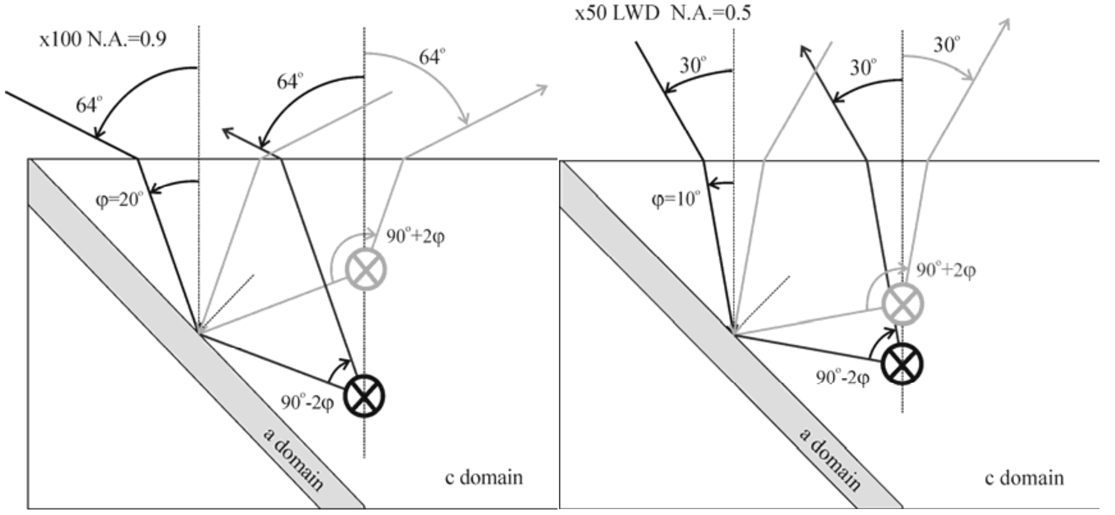

Figure 5-5: Schematic representation of maximum deviation from backscattering geometry and effects of laser light reflections from the a/c domain walls using x100(a) and x50 (b) objectives.

Next, both initial and scattered light can be scattered on a c/a domain wall before/ after being scattered by phonons resulting in a 90° scattering geometry (Figure 5‑5). Thus, the modes allowed in 90 ° scattering geometry can appear in the VV spectra collected in the backscattering geometry (Figure 5‑6). The *A_1(LO)* and *E(LO)* modes coming from *a*-domains can be observed in addition to the modes allowed in backscattering geometry. Furthermore, quasi-E and quasi-A (quasi-LO and quasi-TO) coming from *a*– and *c*-domains corresponding Θ = 45 ° at low wavenumbers < 200 cm^{-1} (at high wavenumbers > 200 cm^{-1}) can be also observed. The reflected and initial beams have the same angular dispersion resulting in oblique modes in the case of real modes and in deviation from 45 ° angle in the case of oblique modes. In the case of the *E(LO)*, the deviation ΔΘ = 20 – 30 ° from 90 ° (Figure 5‑3), indicates that these modes originated from *a*-domains as expected from Raman selection rules (Figure 5‑6). *3(TO)* oblique modes appear at lower wavenumbers than real modes of *a*-domains, as expected for ΔΘ = 45 ° in Foster's phonon curves (Figure 5‑3), and result in an asymmetry of *a*-domain *A_1(TO)* mode profile (Figure 5‑2) Finally, the *E(LO)* oblique modes are not observed in *VH* polarized spectra, where "quasimodes" are not allowed.

Angular resolved backscattering Raman spectroscopy experiments were performed in order to analyze the scattered light at different places in the scattering cone during the

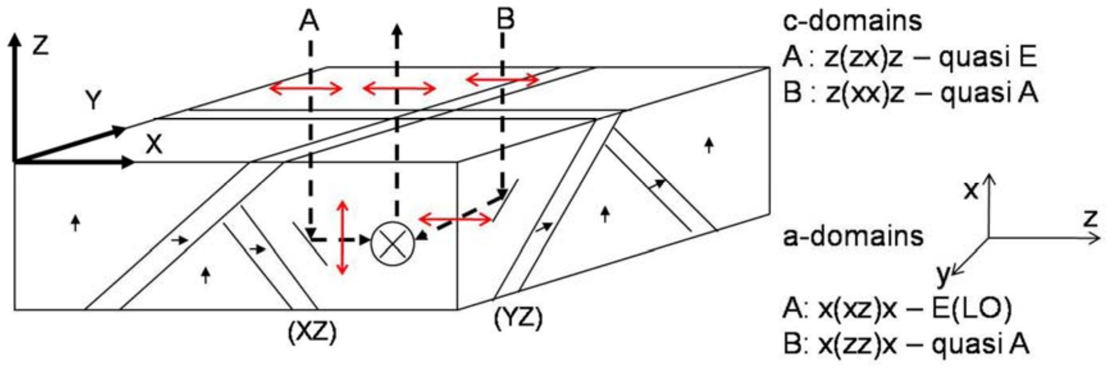

Figure 5-6: Raman 90 º scattering geometries resulting from light reflections on domain walls and a few examples of polarization configurations used for the Raman mode assignment in a- and c-domain PTO single crystals and thin films in the case of VV polarization configuration . The crystallographic axes in the film are presented for c-domains. Oblique modes are indicated for wavenumbers < 200 cm^{-1} where anisotropic forces dominate. In the case of high frequencies, electrostatic forces dominate and quasi-LO and quasi-TO modes will be observed.

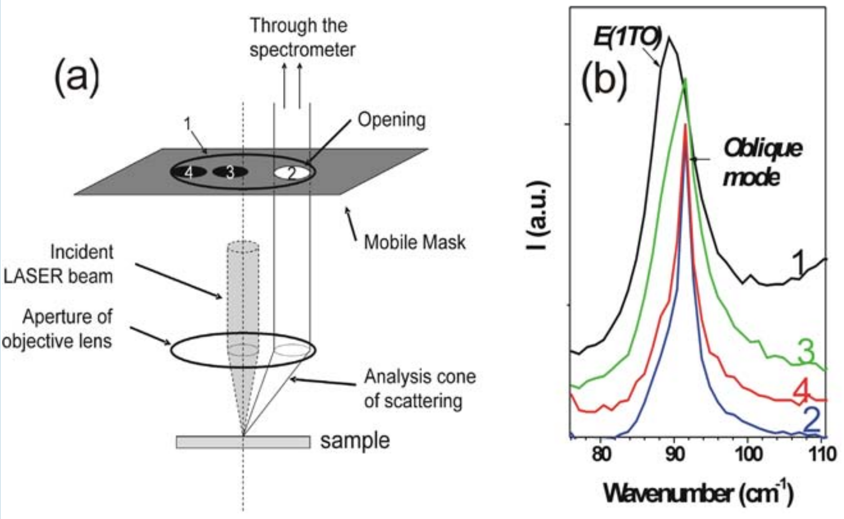

Figure 5-7: Angular resolved backscattering Raman spectroscopy experimental setup (a) and E(1TO) soft mode profiles collected for different selections of the scattered light in the scattering cone (b) (x100 objective, VV polarization configuration).

collection of *VV* spectra. To do this, a mobile mask with a hole was placed over the scattering cone (Figure 5‑7a) and was moved to select the light to analyze near the cone centre (position {3}) or on the sides (positions {2} and {4}). The evolution of *E (1TO)* mode profile for the different selections of the scattered light is shown in Figure 5‑7b. Position {1} corresponds to the normal scattered cone without mask. It appears that the position and shape of the *E (1TO)* mode vary inside the scattered cone. A thorough analysis of the *E(1TO)* line profile gives evidence of the presence of two components under the *E(1TO)* lineshape, more separated in situation {2} and {4}, i.e. in the light scattered in the cone sides. An intense sharp line centered near 91-92 cm^{-1} and a shoulder near 89 cm^{-1} corresponding to the *E(1TO)* peak position in the normal *VV* spectrum {1} are observed. The sharp line is the oblique mode related to *E(1TO)*. In the central zone of the scattering cone {3}, intensities of both modes are rather close which leads the whole peak to shift slightly towards lower wavenumbers. When the entire scattering cone is analyzed {1}, i.e. in the normal conditions to collect the *VV* sprectra, *E(1TO)* is the dominant mode but it is very asymmetric and slightly shifted towards higher wavenumbers in comparison with *VH* spectra, due to the oblique mode component on the right side. Therefore, it appears that *VH* polarization configuration is essential to measure *E(TO)* modes with accuracy since oblique modes are forbidden. This condition is fundamental for stress evaluation in PTO films based on *E(TO)* mode peak position. As mentioned above, $A_1(TO)$ and $A_1(LO)$ modes can be obtained only in *VV* spectra; accordingly, due to the presence of quasimode, their position cannot be accurately determined. Therefore, they can be used only for qualitative analysis. The same disadvantages related to quasimodes are observed in depolarized spectra.

5.3 Effect of polarization in $PbTiO_3$ films

Having set the framework of the interpretation of Raman scattering in polydomain PTO single crystals, we will now present and discuss polarized Raman spectra of PTO films on three different substrates (STO, LAO, MgO).

Raman spectra of PTO/LAO and PTO/MgO film have been measured in a crossed and parallel polarization configuration (*VH* and *VV*, respectively) on the film surface or on the film cross section. In the case of PTO/STO films, Raman spectra recorded on film surface were completely masked by the signal of STO substrate. Nevertheless, PTO modes were separated from STO modes in the spectra of 125-460 nm thick PTO film recorded on the film cross section.

As predicted by the C_{4v} point group selection rules and already mentioned for PTO single crystal, only *E(TO)* modes are observed in the PTO film spectrum recorded in *VH* configuration on the film surface and cross section (Figure 5‑8); this attests a good crystalline and epitaxial quality of the film. The spectrum measured in a parallel polarization configuration (*VV*) contains a mixture of $A_1(TO)$, $A_1(LO)$, *E(TO)* and *E(LO)* modes instead of the only allowed A_1 modes. Furthermore, when spectra are recorded on film surface, $A_1(TO)$ modes coming from both *c*- and *a*-domains are observed as seen in Figure 5‑8, although only *a*-domain modes should be allowed. The separation of both types of $A_1(TO)$ modes is not straightforward. Nevertheless, the higher intensity of *c*-domain modes in spectra recorded on cross section undoubtedly allows the identification of the different components (Figure 5‑9).

In the case of polycrystalline PTO/SAPH, A_1 and *E* modes are observed whatever the polarization configuration but the A_1 and *E(LO)* intensities decrease in *VH* geometry in comparison with *VV* configuration and they do not completely disappear (Figure 5‑-10). This indicates that films on SAPH are polycrystalline with only a minor preferred orientation, in agreement with results from XRD.

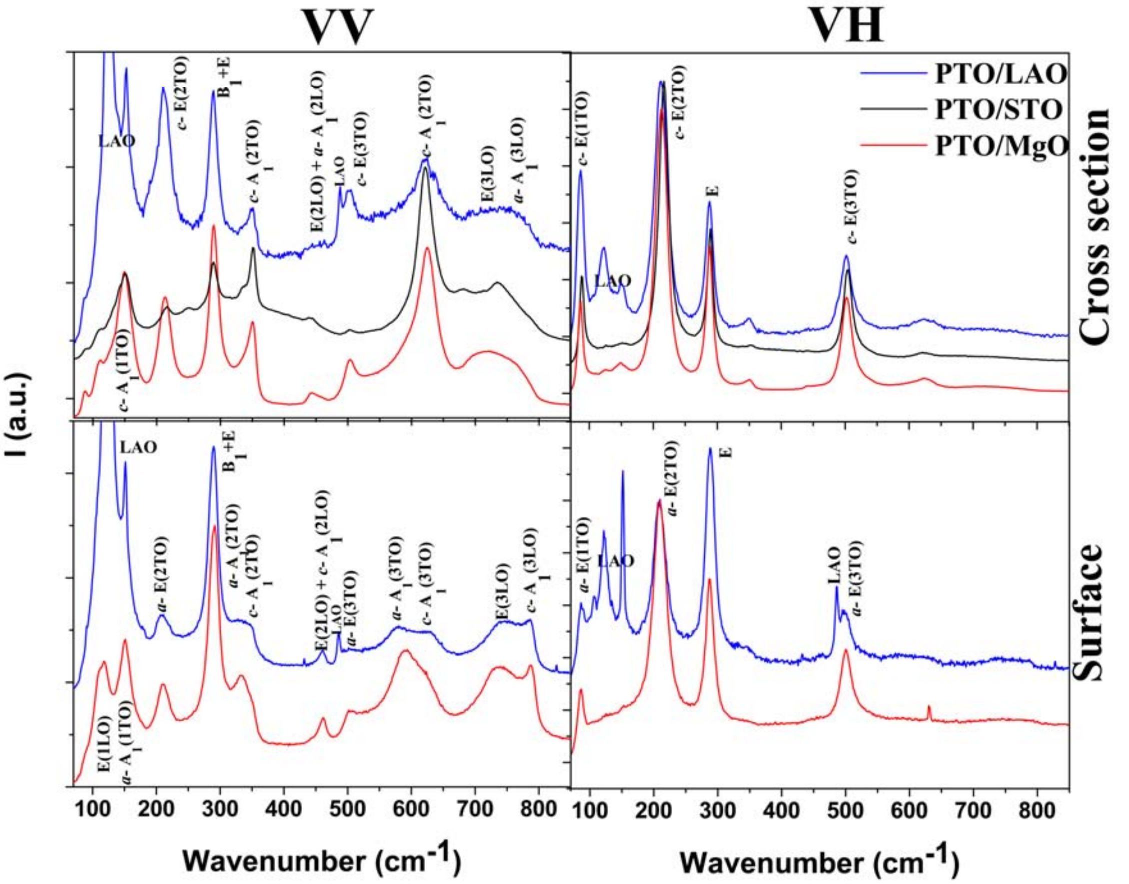

Figure 5-8: Polarized Raman spectra of 250 nm thick PTO/LAO, PTO/MgO and PTO/STO films recorded in a parallel and crossed polarization configuration on the film surface and on the film cross section.

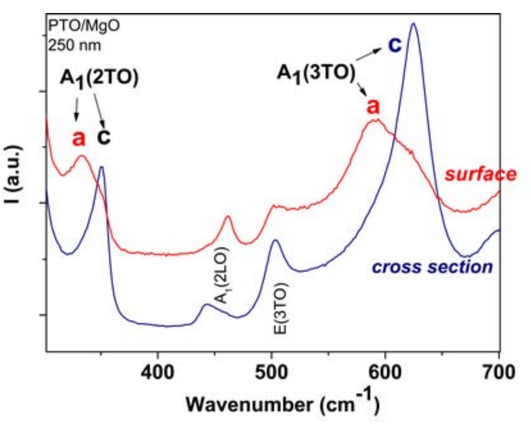

Figure 5-9: Comparison of A_1(2TO) and A_1 (3TO) modes coming from c- and a-domains in VV spectra collected on film surface and on film cross section.

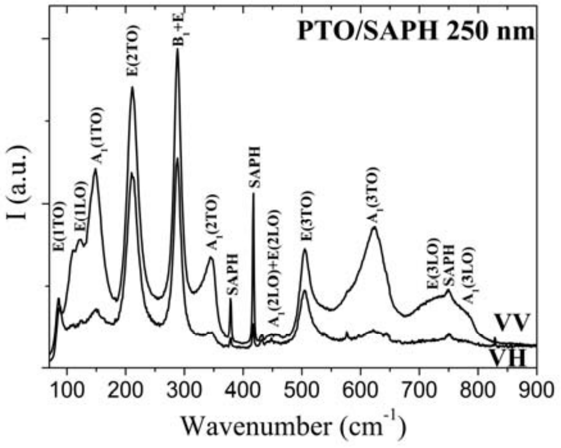

Figure 5-10: Polarized Raman spectra of 250 nm PTO/SAPH films recorded on film surface in parallel (VV) and crossed (VH) polarization configurations.

5.4 Estimation of residual stress by using the E(TO) mode

5.4.1 Theoretical considerations

It has been reported in earlier studies (11) that Raman modes are sensitive to pressure; their positions in wavenumber ω as a function of pressure can be described by an empirical law. If only *E(TO)* modes are considered

$$\omega_{E(TO)} = \omega_{0E(TO)} + (\partial\omega_{E(TO)} / \partial P)P \qquad (5.1)$$

where $\omega_{0E(TO)}$ is the mode wavenumber at ambient conditions (1 bar, 25 °C), and $\partial\omega_{E(TO)} / \partial P$ is the empirical pressure coefficient as determined from measurements under hydrostatic pressure (11; 12). However, stresses in thin films correspond to non-hydrostatic conditions, and we have thus to introduce the effect of anisotropy in phonon deformation potential. Supposing the E mode frequency under applied stresses can be described as follows (25)

$$\omega_{E(TO)} = a'_{E(TO)}\left(\sigma_{xx} + \sigma_{yy}\right) + b'_{E(TO)}\,\sigma_{zz} \pm \sqrt{c'_{E(TO)}\left(\sigma_{xx} - \sigma_{yy}\right)^2 + d'_{E(TO)}\left(\sigma_{xy}\right)^2} \qquad (5.2)$$

where $\Delta\omega_{E(TO)} = \omega_{E(TO)} - \omega_{0E(TO)}$ and $a^{'}_{E(TO)}$, $b^{'}_{E(TO)}$, $c^{'}_{E(TO)}$, $d^{'}_{E(TO)}$ are deformation potential constants expressed in terms of compliance and σ_{XX}, σ_{YY} and σ_{ZZ} are stresses along *a*-, *b*- and *c*-axes of the tetragonal PTO unit cell, respectively. $c^{'}_{E(TO)}$ is related to the split of double degenerate *E(TO)*. If a- and b-axis are affected by different stresses or ab-plane is under shear stresses, the *E(TO)* mode splits into two components. However, $c^{'}_{E(TO)}$ is usually quite small and the split of *E(TO)* modes is obscure. We assume that there is no shear stresses $\sigma_{XY} = 0$ in films. In the case of hydrostatic pressure P, $\sigma_{XX} = \sigma_{YY} = \sigma_{ZZ} = P$ and Eq. (5.2) can be written as

$$\Delta\omega_{E(TO)} = (2a^{'}_{E(TO)} + b^{'}_{E(TO)})P \qquad (5.3)$$

Epitaxial PTO films, grown on cubic substrates, are under biaxial stress σ_b in the substrate plane. Thus, $\sigma_{XX} = \sigma_{YY} = \sigma_b$ and the shift of *E(TO)* modes due to biaxial stress in *c*-domains can be expressed as

$$\Delta\omega_{E(TO)} = 2a^{'}_{E(TO)}\sigma_b \qquad (5.4)$$

In *a*-domains $\sigma_{XX} = \sigma_{ZZ} = \sigma_b$ thus,

$$\omega_{E(TO)} = a'_{E(TO)}\,\sigma_b + b'_{E(TO)}\,\sigma_b \pm \sqrt{c'_{E(TO)}}\sigma_b \qquad (5.5)$$

Although PTO films are strictly speaking not in hydrostatic conditions, it has been argued in the literature that hydrostatic pressure instabilities offer a guide how a material will react to an external stress as Raman modes also shift linearly under biaxial stress; only the relation coefficients differ. It is to be noted that, in literature works (10; 13; 15;

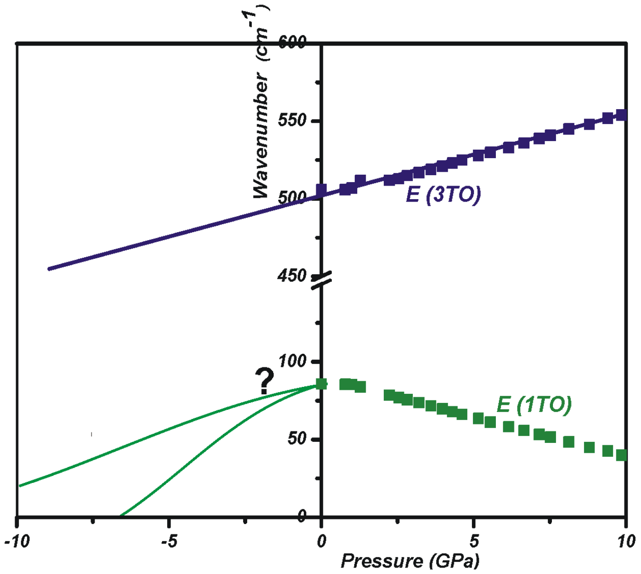

Figure 5-11: Soft E(1TO) and hard E(3TO) mode wavenumber evolution with hydrostatic pressure (P. Bouvier, personal communications) and their extrapolation to tensile stress side.

17), the stress values in tensile-strained PTO films were estimated from the shift of *E(1TO)* soft mode using Eq. 5.1. However, its pressure coefficient is experimentally only known for compression (hydrostatic pressure $\partial\omega_{E(1TO)}/\partial P = -5.8\pm0.2\,cm^{-1}GPa^{-1}$) and the soft mode is by definition anharmonic. Eq. 5.4 and 5.5 become more complex for anharmonic modes and its behavior under tensile stress cannot be predicted (Figure 5-11). In order to test the validity of such an approach, we performed stress value calculation not only from the shift of *E(1TO)*, but also from *E(3TO)* mode which is a real (harmonic) hard mode in the sense that its pressure coefficient is positive ($\partial\omega_{E(3TO)}/\partial P = +7.1\pm1.0\,cm^{-1}GPa^{-1}$). Thus, ω(P) can be linearly extrapolated to the tensile stress side.

The condition of conservation of wave vector has to be considered with some care in the case of nanostructures (for ex. nanocrystallites, *a*-domains, which are nano-sheats in the *c*-domain matrix, nano grain size in thin films). In nanostructures, a range of $\Delta\ k$ of phonon wave vectors can be excited. The range of phonon wave vectors that contribute to the Raman line shape is determined by the crystallite size *l* and is given by $\Delta k = 2\pi / l$. The spectra of nanomaterials give continua that probe modes of wave vectors that span some part of / whole Brillouin zone of the crystal. The soft mode profile should be more modified due to this confinement effect, as $\omega_{E(1TO)}$ varies more with k than wavenumbers of hard modes. This effect results in the asymmetry of profile or shift of soft mode to higher wavenumbers. Further, the decrease of size results in so called field effect— the decrease of tetragonality and T_c. As a consequence, the *E (1TO)* soft mode shifts to lower frequencies. In the case of hard modes, both effects usually results just in the increase of peak width.

In the following residual stress values estimated from *E(1TO)* will be used for comparison with the reported values of other groups.

5.4.2 Relation between residual stress and misfit strain

In 250 nm thick PTO films on SAPH, MgO, LAO and STO substrates, the *E(1TO)* soft mode is observed well below that observed in bulk PTO (89.5 cm^{-1}): it is located at roughly 83 , 86.2, 87 and 88.3 cm^{-1}, respectively. In order to determine the sign of residual stress in films, the position of the *E(3TO)* hard mode has been also considered. As for *E(1TO)* , *E(3TO)* mode wavenumber is always lower for PTO films 504.3, 502.4,

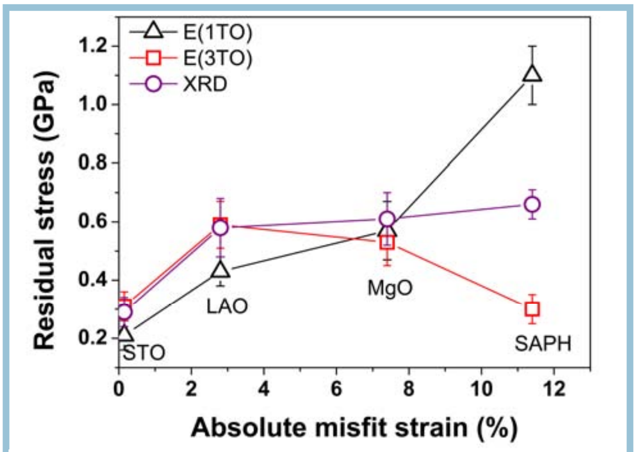

Figure 5-12: Residual stress evolution with absolute misfit strain in c-domains of 250 nm thick PTO films on different substrates.

502.0 and 504.0 cm^{-1} when the substrate is SAPH, MgO, LAO and STO respectively instead of 506.2 cm^{-1} for PTO single crystal. This fact suggests that PTO films are under tensile stress whatever the substrate, which is in agreement with XRD results (see section 4.6.2).

Stress values in 250 nm thick films on SAPH, MgO, LAO and STO substrates were calculated from *E(3TO)* and *E(1TO)* mode wavenumbers using Eq. 5.1 and reported as a function of the film misfit strain in Figure 5-12. For comparison, stress values obtained from lattice parameters measured by XRD are also given in Figure 5-12. In the epitaxial films, the values estimated from the shift of *E(3TO)* are in good agreement with XRD values while those obtained from *E(1TO)* are more different. The three estimations carried out for PTO/SAPH films give distinct stress values. The soft mode is anharmonic; therefore, the relation between the applied stress and the shift of the soft mode is nonlinear. Furthermore, the soft mode is also highly sensitive to the grain size (26). Thus, the anharmonic *E(1TO)* soft mode should not be used for an accurate evaluation of the residual stress in both epitaxial and polycrystalline $PbTiO_3$ thin films. In polycrystalline films, the grains have different crystallographic orientations, which results in dispersion of Θ angle and in the appearance of oblique modes. Furthermore, as mentioned above the Raman selection rules are not respected in polycrystalline films. Thus, the *E(3TO)* mode profile is modified by related quasimodes even in the VH spectra. Therefore, the *E(3TO)* hard mode position can be shifted upward and thus stress values estimated from this mode are lower than values obtained from lattice parameters. Accordingly, residual stress values cannot be estimated from *E(TO)* Raman modes in polycrystalline PTO films. The similarity between stress values estimated from *E(3TO)* mode and XRD data allows us to consider that Eq. 5.1 can be used for *E(3TO)* mode in the case of epitaxial PTO films and then, that Raman data obtained from hydrostatic pressure experiments can provide us an understanding and reasonable estimate of the stress state from *E(3TO)* hard mode in *c*-domains in PTO films.

It is at first sight surprising that residual stress does not depend directly on the sign of the misfit strain. Stress values as determined by XRD in PTO films on SAPH, MgO and LAO substrates are similar; they are lower in PTO/STO films, which have a very good epitaxy with the substrate. This indicates that residual stress is not only dominated by epitaxial stress in 250 thick PTO films; except in films having a very low mismatch with the substrate, thus other types of stresses contribute to the residual stress. The stress values related to 50-950 nm thick polycrystalline films were reported by different authors to be in the range of 2.6-0.9 GPa (10; 13; 15; 27; 28; 29). Dobal *et al.* (15) reported higher stress value (1.5 GPa) for the 250 nm PTO/SAPH film in comparison with our measured value (0.6 GPa). Stress values were measured as high as 2 GPa in epitaxial 250 nm thick PTO/MgO films (17), while it reaches only 0.6 GPa in our epitaxial PTO/MgO films. The hardening of soft mode (or shift towards highest wavenumbers) in PTO films on compressive $NdGaO_3$ substrates was reported by Sun et al. (16). The authors assume that the hardening of the soft mode is the result of compressive misfit stress. Let us remind that the *E(1TO)* soft mode shifts to lower wavenumbers under compressive hydrostatic pressure as well as under tensile stress. Furthermore, their study is based on non-polarized spectra only and they did not take the quasimodes into consideration and, last but not least, they used PTO single crystal wavenumbers coming from literature. Thus, the shift to higher wavenumbers of the soft mode probably results from quasimodes and not from soft mode hardening. Stress values estimated in our films are rather lower than literature values but it is to be noted that literature studies only use the disputable and non reliable *E(1TO)* soft mode (which we only used for comparison with literature values). However, we note that stresses are not only lattice mismatch dependent, but are highly sensitive to the deposition method and experimental conditions.

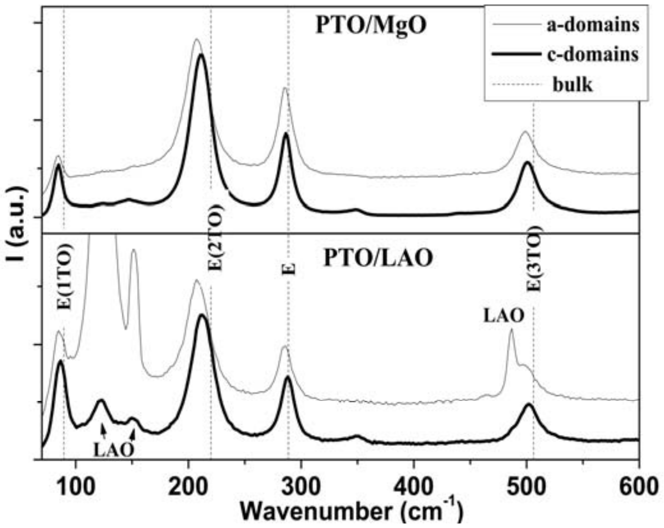

Figure 5-13: Comparison of Raman spectra measured on 250 nm thick PTO/MgO and PTO/LAO film surface (a-domains) and on cross section (c-domains) in VH polarization configuration. The wavenumbers of E modes in PTO single crystal are shown as dashed lines.

5.4.3 Residual stress in a– and c-domains

The Raman spectra of 250 nm thick PTO/LAO and PTO/MgO films recorded in *a*- and *c*-domains, using both scattering geometries, are given in *Figure 5‑13.* It appears that the deviation of the *E(TO)* mode wavenumbers from the values measured in single crystals is more important in *a*-domains than in *c*-domains. The Raman shifts of *E(1TO), E(2TO)* and *E (3TO)* are given in *Table 5- 2.* Unfortunately, the *E(3TO)* mode is partially masked by the intense LAO E_g mode in the thinner PTO/LAO films in the case of *a*-domains. From comparison of Eq. 5.1 and Eq. 5.3 , it results that $b'_{E(3TO)} << a'_{E(3TO)}$ and then from Eq. 5.4 and Eq. 5.5 , that the shift of the *E(3TO)* mode $\Delta\omega_{E(TO)}$ in *a*-domains should be half of that in *c*-domains for a given biaxial stress value, if $c'_{E(TO)}$ is very small. We observe that *E(3TO)* modes related to *a*-domains are more shifted to lower wavenumbers than modes coming from *c*-domains (Table 3), which indicates that *a*-domains are more stressed than *c*-domains.

E(TO) modes correspond to lattice vibration in the *ab*-plane of the tetragonal PTO unit cell, therefore *c*-domains are under biaxial stress in the film plane (Figure 5‑14). In

Table 5-2: E(1TO) phonon wavenumbers in PTO films of different thicknesses on LAO, MgO and STO substrates. The a- and c-domain values were obtained from film surface and cross section spectra recorded in VH polarization configuration, respectively.

		Mode	Bulk	460 nm	250 nm	125 nm	65 nm	30 nm
PTO/LAO	*a*-domains	*E(1TO)*	89.5	86.4	86	85.8	79.6	78.1
		E(2TO)	219.9	210.5	208.8	206.5	204.3	204.3
		E(3TO)	506.2	500.8	499.4	498	-	-
	c-domains	*E(1TO)*	89.5	87.4	87.0	-	84.8	83.1
		E(2TO)	219.9	214.6	212.4	210.8	208.6	204.3
		E(3TO)	506.2	503.0	502.0	501.2	499.9	496.9
PTO/MgO	*a*-domains	*E(1TO)*	89.5	88.1	85.8	84.8	84.2	-
		E(2TO)	219.9	215.6	209.8	206.6	205.7	-
		E(3TO)	506.2	504.1	500.4	499.7	499.5	-
	c-domains	*E(1TO)*	89.5	87.5	86.2	85.5	84.1	-
		E(2TO)	219.9	213.4	212.7	210.8	207.4	-
		E(3TO)	506.2	503.0	502.4	500.6	499.8	-
PTO/STO	*c*-domains	*E(1TO)*	89.5	87.2	88.3	89.1	-	-
		E(2TO)	219.9	215.1	216.5	217.0	-	-
		E(3TO)	506.2	503.1	504.0	-	-	-

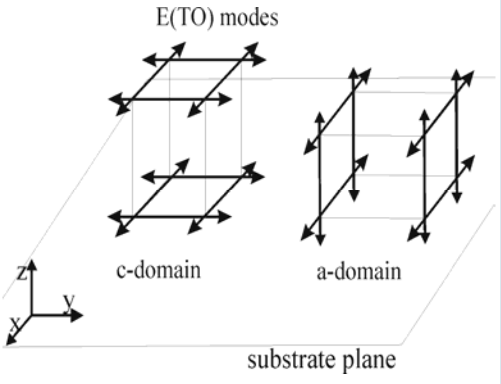

Figure 5-14: Schematic representation of the direction of vibration in E(TO) modes of PTO a- and c-domains.

the case of the *a*-domains, *ab*-plane is perpendicular to the substrate plane. Thus, one axis basal plane of tetragonal cell is under biaxial stress while second one is stress free.

Furthermore, *E(TO)* modes can be affected by stress generated by *c/a* domain interfaces (interfacial stress) in addition to the biaxial stress, as *a*-domains form thin sheet zones in a matrix of *c*-domains (30; 31, chapter 4.4). However, stresses along *a*- and *b*-axis of *a*-domains are different and the split of *E(TO)* modes can be expected.

The evolution of the *E(1TO)* soft mode as a function of film thickness in PTO/LAO films is reported in Figure 5-15. An *E(1TO)* mode splitting is systematically observed in a-domain whatever the film thickness, and similarly in 65 and 125 nm thick PTO/MgO films (Figure 5-16). However, no split occurs in *E(TO)* hard modes of a-domains nor in any *E(TO)* modes of c-domains. The *E (1TO)* component at higher wavenumber cannot be related to quasimodes, as they are

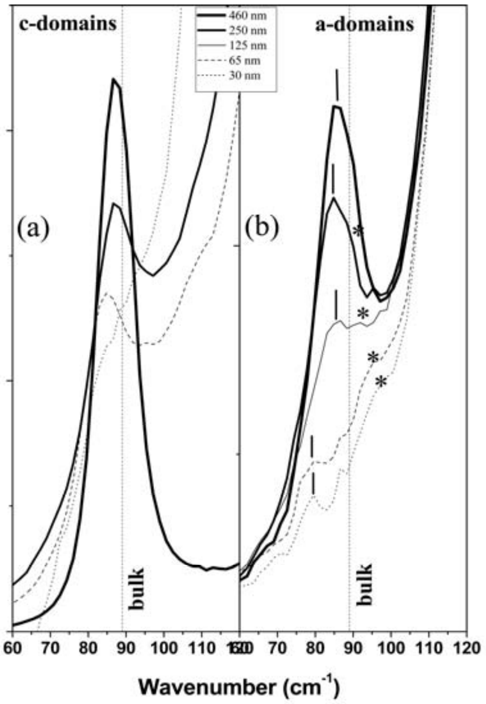

Figure 5-15: Film thickness evolution of the PTO/LAO E(1TO) soft mode recorded on cross section (a) and on film surface (b) in VH configuration. The E(1TO) wavenumber in PTO single crystal is shown as dashed line. The two components of the E(1TO) mode are marked by dashes and asterisks.

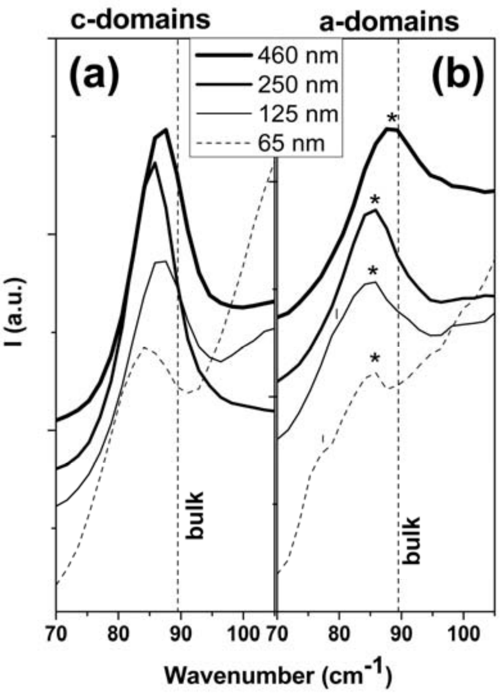

Figure 5-16: Film thickness evolution of the PTO/MgO E(1TO) soft mode recorded on cross section (a) and on film surface (b) in VH configuration. The E(1TO) wavenumber in PTO single crystal is shown as dashed line. The two components of the E(1TO) mode are marked by dashes and asterisks.

not observed in VH spectra. The following hypotheses can be considered to explain the *E(1TO)* splitting. First, as mentioned above, non biaxial stress in the ab-plane should result in the split of doubly degenerate *E(TO)* modes into two components; the fact that the split is only visible in the soft mode could be explained by its anharmonicity. The split in hard modes is probably too small to be observed. Second, the *E(1TO)* is close to the notch filter cutting. However, it is difficult to explain the behavior of the anharmonic soft mode. If interfacial stresses in a-domains are non negligible, the stress relation with $\Delta\omega_{E(3TO)}$ should be given by Eq. 5.2. Thus, residual stress values cannot be estimated from the shifts of Raman modes as far as the stress symmetry and $c'_{E(TO)}$ (constant) are unknown. The absence of *E(1TO)* splitting in c-domains indicate that they are under biaxial stress in ab-plane (Figure 5‑15a and Figure 5‑16a). Lee et al. also reported that *a*-domains are more stressed than *c*-domains in epitaxial 250 nm thick PTO/MgO films (17), but the given stress values (2.45 GPa and 2.11 GPa, respectively) are not exactly the right values since estimations were made from anharmonic *E(1TO)* mode using Eq. 5.1.

Qualitatively, one can see from the E(1TO) wavenumbers in Table 5-2 that the difference in residual stress in *a*- and *c*-domains is considerable, especially in PTO/LAO films. As *c/a/c/a* epitaxial PTO films have a dominant *c*-domain structure and because of the complexity of the spectra in *a*-domains, the residual stress values in such films have been only determined for *c*-domains, i.e. from *VH* polarized spectra measured on film cross section.

5.4.4 Effect of film thickness on the residual stress in c-domains

The *E(TO)* Raman shifts in *c*-domains of epitaxial PTO films on LAO, MgO and STO substrates are given in Table 5-2. The *E(2TO)* and *E(3TO*) hard modes follow the same behaviour in wavenumber with film thickness as *E(1TO)* soft mode. The *E(2TO)* mode is also anharmonic, thus it should not be used for the estimation of residual stress. The degenerate silent B_1+E (ω=290.1 cm^{-1}) mode remains almost constant in wavenumber whatever the film thickness or the misfit strain. However, the polarized Raman spectra in Figure 5‑8. indicate that the *E* mode can be entirely isolated from the B_1 mode in the *VH* geometry, as previously observed by Lee and Foster (17; 24).

Stress values in *c*-domains calculated from the shift of *E(*3TO) hard modes using Eq. 1 are given in Table 5-3 (the values estimated from the shift of *E(1TO)* are given for comparison with literature values) and in Figure 5‑17. In Table 5- 3 we compare stress values measured by XRD to values obtained by the hard E(3TO), it can be seen that there is a good agreement between both techniques, which further validates the reliability of the *E(3TO)* mode. Only a few papers report on residual stress values in c-domains in epitaxial PTO/MgO films (σ = 2.11 GPa (17)) and, as mentioned above, calculations are made using anharmonic *E(1TO)* soft mode.

Table 5-3: Residual stress values (GPa) in c-domains determined from E(1TO) and E(3TO) and from lattice parameters (XRD) in PTO films of different thicknesses on LAO, MgO and STO substrates.

Thickness (nm)		460	250	125	65	30
PTO/LAO	XRD	0.40 ± 0.08	0.58 ± 0.08	0.79 ± 0.11	1.00 ± 0.14	1.02 ± 0.15
	E(1TO)	0.36 ± 0.05	0.43 ± 0.09	-	0.81 ± 0.17	1.10 ± 0.35
	E(3TO)	0.45 ± 0.07	0.59 ± 0.10	0.70 ± 0.11	0.88 ± 0.14	1.30 ± 0.21
PTO/MgO	XRD	0.62 ± 0.08	0.60 ± 0.09	0.63 ± 0.09	0.73 ± 0.09	-
	E(1TO)	0.34 ± 0.05	0.57 ± 0.09	0.69 ± 0.12	0.93 ± 0.17	-
	E(3TO)	0.45 ± 0.07	0.53 ± 0.09	0.78 ± 0.13	0.90 ± 0.15	-
PTO/STO	XRD	0.48 ± 0.08	0.30 ± 0.08	0.28 ± 0.08	0.26 ± 0.08	0.34 ± 0.08
	E(1TO)	0.40 ± 0.05	0.21 ± 0.09	0.07 ± 0.12	-	-
	E(3TO)	0.43 ± 0.07	0.31 ± 0.05	-	-	-

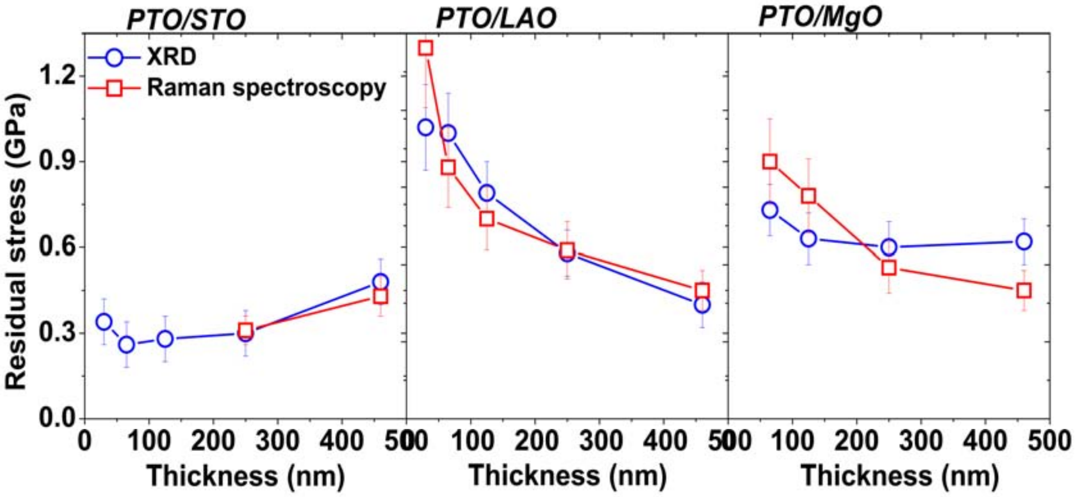

Figure 5-17: Residual stress evolution in c-domains with film thickness in PTO films on STO, LAO and MgO substrates. The residual stress was estimated from E(3TO) mode shift and XRD data.

5.4 Analysis of the domain structure from A_1(TO) modes

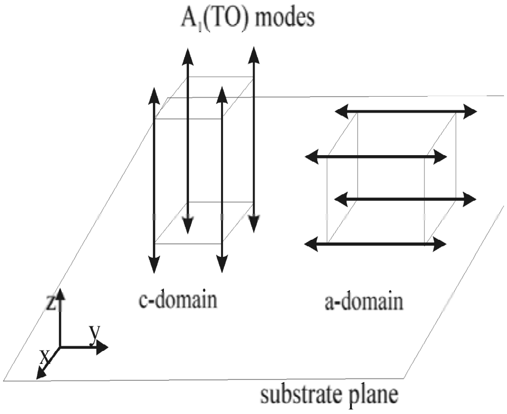

Figure 5-18: A_1(TO) modes of PTO lattice vibrations corresponding a- and c-domains. The arrows indicate the possible directions of atom vibrations.

A_1(TO) modes correspond to lattice vibrations along the *c*-axis of the tetragonal unit cell, i.e. along the spontaneous polarization axis (section 1.4 and Figure 5‑18). The relation between the shift of *A_1(TO)* mode and applied stresses can be written as

$$\Delta\omega_{A_1(TO)} = a'_{A_1(TO)}(\sigma_{XX}+\sigma_{YY}) + b'_{A_1(TO)}\sigma_{ZZ} \quad (5.6)$$

The *c*-axis is stress free in *c*-domains ($\sigma_{ZZ}=0$) as films are under biaxial stresses $\sigma_{XX}=\sigma_{YY}=\sigma_b$ in the film plane. Thus, the shift of *A_1(TO)* modes due to biaxial stress in *c*-domains can be expressed as

$$\Delta\omega_{A_1(TO)} = 2a'_{A_1(TO)}\sigma_b \quad (5.7)$$

In *a*-domains the *c*-axis lies in the film plane $\sigma_{XX}=\sigma_{ZZ}=\sigma_b$ and thus the effect of stresses can be expressed as follows

$$\Delta\omega_{A1(TO)} = (a'_{A1(TO)} + b'_{A1(TO)})\sigma_b \quad (5.8)$$

If stresses are not biaxial, Eq. 5.6 should be applied.

However, $A_1(TO)$ mode profiles are highly sensitive to the depolarization effects and numerical aperture, as discussed in section 5.2. As a consequence, their wavenumbers cannot be used for the estimation of residual stress due to appearance of oblique modes. Furthermore, the coefficients $a'_{A1(TO)}$ and $b'_{A1(TO)}$ are unknown, therefore we cannot assume from those mode shifts what type of domains is more stressed.

Table 5-4: $A_1(TO)$ phonon wavenumbers in PTO films of different thicknesses on LAO, MgO and STO substrates. The a- and c-domain values were obtained from film surface and cross section spectra recorded in VV polarization configuration, respectively.

		Mode	Bulk	460 nm	250 nm	125 nm	65 nm	30 nm
PTO/LAO	*a*-domains	$A_1(1TO)$	150.5	-	-	-	-	-
		$A_1(2TO)$	355.0	334.4	328.6	327.9	-	-
		$A_1(3TO)$	640.7	587.5	581.7	576.4	-	-
	c-domains	$A_1(1TO)$	150.5	-	-	-	-	-
		$A_1(2TO)$	355.0	352.9	349.8	-	-	-
		$A_1(3TO)$	640.7	632.9	622.6	-	-	-
PTO/MgO	*a*-domains	$A_1(1TO)$	150.5	151.4	150.8	149	148.7	-
		$A_1(2TO)$	355.0	329.0	332.7	323.5	320.8	-
		$A_1(3TO)$	640.7	592.0	586.8	579.4	575.2	-
	c-domains	$A_1(1TO)$	150.5	151.4	150.8	152.9	151.7	-
		$A_1(2TO)$	355.0	349.6	351.3	341.8	337.5	-
		$A_1(3TO)$	640.7	629.8	625.6	604.3	584.9	-
PTO/STO	*c*-domains	$A_1(1TO)$	150.5	148.2	150.5	-	-	-
		$A_1(2TO)$	355.0	353.4	351.2	-	-	-
		$A_1(3TO)$	640.7	631.7	621.9	-	-	-

5.4.1 $A_1(1TO)$ soft mode

The $A_1(1TO)$ soft mode shifts under hydrostatic pressure is not known, because $E(1LO)$ mode was analyzed as $A_1(1TO)$ mode in hydrostatic pressure studies. In PTO films on MgO and STO substrates, the $A_1(1TO)$ peak position is close too that in bulk PTO and it remains rather constant with varying film thickness (Table 5-4). A small variation in position can be explained by the appearance of oblique mode. It means that this mode is rather insensitive to stresses (or hydrostatic pressure) in the film (crystal). The $A_1(1TO)$ mode in PTO/LAO has not been accurately observed due to the too close LAO soft mode.

5.4.2 A_1(TO) hard modes and domain structure

$A_1(2TO)$ and $A_1(3TO)$ modes appear as broad bands split into two components corresponding to *a*- and *c*-domains in VV spectra recorded on epitaxial PTO/LAO film surface. The components are labelled *a* and *c* in Figure 5‑19; their intensity ratio varies with film thickness. As already mentioned in section 5.2, $A_1(TO)$ modes arise from a-domains in VV spectra collected on film surface, those coming from *c*-domains result from depolarization. In the case of PTO/MgO films, $A_1(TO)$ modes related to *a*-domains are mainly observed in VV spectra recorded on film surface due to the high *a*-domain fraction in the films; while in VV spectra recorded on the film cross section, $A_1(TO)$ modes mainly comes from *c*-domains, as *c*-domain fraction is dominant in the films. The $A_1(2TO)$ and $A_1(3TO)$ modes coming from *c*- and *a*-domains were separated as explained above and corresponding positions are given in Table 5-4 and Figure 5‑20. The $A_1(2TO)$ and $A_1(3TO)$ modes were observed at lower frequencies in a-domains than in *c*-domains whatever the film thickness and the mismatch with the substrate (Figure 5‑20). The $A_1(3TO)$ wavenumber increases with film thickness in both *a*- and *c*-domains indicating relaxation of stresses. The difference in wavenumbers between *a*- and *c*-domains remains almost constant in PTO/LAO films while in PTO/MgO, the *c*-domain $A_1(3TO)$ mode shifts quickly to lower frequencies with decrease of film thickness. 65 - 125 nm thick PTO/MgO films have significant non-twinned *a*-domain fraction (for more details see section 4.3). As was shown by TEM analysis (section 4.4), the interfaces between non-twinned *a*- and *c*-domains are highly unfavourable, resulting in higher stresses in *c*-domains.

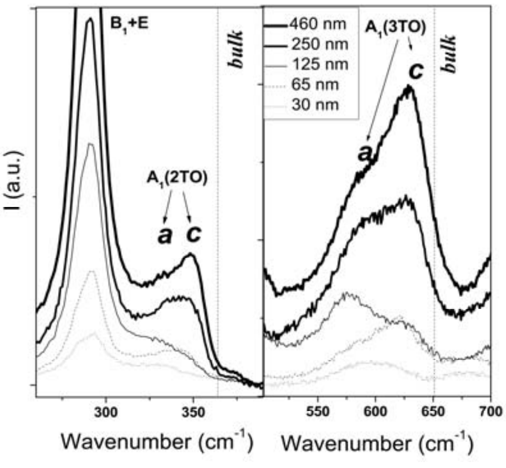

Figure 5-19: Evolution of the $A_1(2TO)$ and $A_1(3TO)$ modes as a function of PTO/LAO film thickness. a- and c-components of each $A_1(TO)$ mode refer to modes coming from a- and c-domains, respectively.

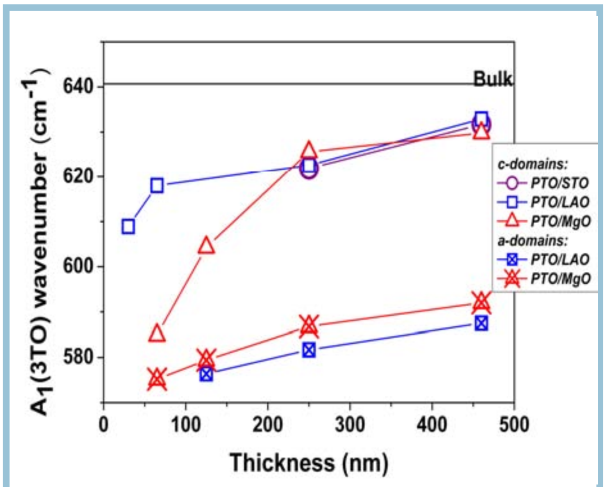

Figure 5-20: Evolution with film thickness of $A_1(3TO)$ mode wavenumber in a- and c-domains of epitaxial PTO films on MgO, LAO and STO substrates.

Conclusions

The polydomain PTO single crystal Raman spectra analysis revealed that:

Raman mode positions and peak profiles are modified due to the presence of oblique modes in *VV* polarized spectra. The oblique modes may result from different intrinsic and extrinsic phenomena such as the ferroelectric domain structure, the sample misorientation, numerical aperture and the misalignment in the system.

The analysis of the scattered light at different places in the scattering cone during collection of *VV* spectra was performed using angular resolved backscattering Raman spectroscopy. This study confirmed the presence and the importance of oblique modes in *VV* spectra and their influence on the asymmetry of peak profiles and positions.

VH polarization configuration is essential to measure *E(TO)* modes with accuracy since oblique modes are forbidden. This condition is fundamental for residual stress evaluation in PTO films based on *E(TO)* mode peak position.

From the PTO thin film Raman spectrum analysis we can conclude that:

The *E(1TO)* soft mode cannot be used for residual stress estimation, as it is anharmonic and thus, the relation between the applied stress and the shift of the soft mode is nonlinear and it is also sensitive to grain size effect.

Raman data obtained from hydrostatic pressure experiments can provide us an understanding and reasonable estimate of the tensile and compressive stress state from *E (3TO)* hard mode in *c*-domains in epitaxial PTO films.

30-460 nm PTO films are under tensile stress in the film plane whatever the tensile and compressive misfit stress and the film thickness. The *a*-domains are more stressed than *c*-domains. There is a good agreement between residual stress values in *c*-domains estimated from XRD and Raman spectroscopy data, which validates the reliability of the *E(3TO*) mode.

A_1*(TO)* hard modes corresponding to *a*- and *c*-domains were identified by comparison of the *VV* spectra recorded on the film surface and film cross section.

Bibliography

1. **M. Okuyama and Y. Hamakama.** s.l. : Sensor Mater., 1988, Vol. 1, p. 13.

2. **J.F. Scott and C.A. Paz de Araujo.** s.l. : Science, 1989, Vol. 246, p. 1400.

3 . **Damjanovic, D.** s.l. : Rep. Prog. Phys., 1998, Vol. 61, p. 1267.

4 . **R. Ramesh, T. Sands, and V.G. Keramidas.** 6, s.l. : Appl. Phys. Lett., 1993, Vol. 63, p. 731.

5. **Q. Ma and D.R. Clarke.** s.l. : J. Am. Ceram. Soc., 1993, Vol. 76, p. 1433

6 . **E. Ching-Prado, A. Reynes-Figueroa, R.S. Katiyar, S.B. Majimder, and D.C. Agrawal. s.l.** : J. Appl. Phys., 1995, Vol. 78, p. 1920.

7 . **C.C. Li and S.B. Desu.** s.l. : J. Vac. Sci. Technol., 1996, Vol. 14, p. 1.

8 . **J.H.L. Voncken, C. Lijzenga, K.P. Kumcer, K. Kiezer, A.J. Burggraaf, and B.C. Benekamp**. 2, 1992, J. Mater. sci., Vol. 27, p. 472.

9 . **S.S. Sengupta, S.M. Park, D.A. Payne, and L.H. Allen.** s.l. : J. Appl. Phys., 1998, Vol. 83, p. 2291

10**. D. Valim, A.G. Sauza Filho, P.T.C. Freire, J. Mendes Filho, C.A. Guavany, R.N. Reispaud, and E.B. Araujo. s.l.** : J. Phys. D:Appl. Phys., 2004, Vol. 37, p. 744.

11. **J.A. Sanjurjo, E. Lopez-Cruz, and G. Burns.** 12, s.l. : Phys. Rev. B, 1983, Vol. 28, p. 7260.

12 . **F. Cerdeira, W.B. Holzapfel, and D. Bauerle.** 3, s.l. : Phys. Rev. B, 1975, Vol. 11, p. 1188.

13 . **D. Fu, T. Ogawa, H. Suzuki, and K. Ishikawa.** s.l. : Appl. Phys. Lett., 2000, Vol. 77, p. 1532.

14 . **A.-D. Li, D. Wu, C.-Z. Ge, P. Lu, W.-H. Ma, M.-S. Zhang, C.-Y. Xu, J. Zuo, and N.-B. Ming.** s.l. : J. Appl. Phys., 1999, Vol. 85, p. 2146.

15. **P.S. Dobal, S. Bhaskar, S.B. Majamder, and R.S. Katiyar.** s.l. : J. Appl. Phys., 1999, Vol. 86, p. 828

6 . **L. Sun, Y.F. Chen, L.He, C.Z. Ge, D.S. Ding, T. Yu, M.-S. Zhang, and N.B. Ming. 18**, s.l. : Phys. Rev. B, 1997, Vol. 55, p. 12218.

7 . **S.-H. Lee, H.M. Jang, S.M. Cho, and G.-C. Yi.** s.l. : Appl. Phys. Lett., 2002, Vol. 80, p. 3165.

8 . **H. Zheng, J. Kreisel, Y.H. Chu, R. Ramesh, and L. Salamanca-Riba.** s.l. : Appl. Phys. Lett., 2007, Vol. 90, p. 113113.

9 **. I.A. Kornev, L. Bellaiche, P. Bouvier, P.E. Janolin, B. Dkhil, and J. Kreisel.** s.l. : Phys. Rev. Lett., 2005, Vol. 95, p. 196804.

20 . **I.A. Kornev and L. Bellaiche.** 4, s.l. : Phase Transitions, 2007, Vol. 80, p. 385.

21 . **G.A. Samara and E.L. Venturini.** 1-2, s.l. : Phase Transitions, 2006, Vol. 79, p. 21.

22 . **W.K. Choi, S.K. Choi, and H.M. Lee.** s.l. : J. Mater. Res., 1999, Vol. 14, p. 4677.

23 . **J.S. Speck and W. Pompe.** s.l. : J. Appl. Phys., 1994, Vol. 76, p. 466.

24 . **C.M. Foster, Z. Li, M. Grimsditch, S.-K. Chan, and D.J.Lam.** 14, s.l. : Phys. Rev. B, 1993, Vol. 48, p. 10160.

25 . **R.J. Briggs and A.K. Ramdas.** 12, s.l. : Phys. Rev. B, 1976, Vol. 13, p. 5518.

26 . **W. Ma, M. Zhang, and Z. Lu.** s.l. : Phys. Status Solidi A, 1998, Vol. 166, p. 811.

7 . **T. Ohno, D. Fu, H. Suzuki, H. Migazaki, and K. Ishikawa**, s. l. : J. Eur. Ceram. Soc., 2004, Vol 24, p. 1669.

28 . **W. Ma, M. Zhang, T. Yu, Y. Chen, and N. Ming**. s.l. : Appl. Phys. A, 1998, Vol 66, P. 345

29. **I. Taguchi, A. Pignolet, L. Wang, M. Proctor, F. Levy, and P.E. Schmid**. s.l. : .J Appl. Phys. 1993; Vol. 73, p. 394.

30**. C.S. Ganpule, V. Nagarajan, B.K. Hill, A.L. Roytbard, E.D. Williams, S.P. Alpay, A. Roelops, R. Waser, and L.M. Eng.** s.l. : J. Appl. Phys., 2002, Vol. 76, p. 1477.

31**. S. Stemmer, S.K. Streiffer, F. Ernst, M. Ruhle, W.-Y. Hsu, and R. Raj.** s.l. : Solid State Ionics, 1995, Vol. 75, p. 43

Chapter 6:

Effect of temperature on $PbTiO_3$ powder and thin films

Chapter 6

6 Effect of temperature on $PbTiO_3$ powder and thin films ___ *133*

6.1 Literature review____136

6.2 Temperature evolution of domain structure and lattice parameters in $PbTiO_3$ thin films________________________138

6.2.1 Domain structure ____139

6.2.2 Lattice parameters ____140

6.2.3 Domain fraction ____142

6.3 Domain transformations and phase transitions in $PbTiO_3$ ____143

6.3.1 High-temperature XRD study of epitaxial system PTO/STO films___143

6.3.2 Raman spectroscopy results___________________________________144

6.3.2.1 $PbTiO_3$ powder________________________________ 144

6.3.2.2 Polycrystalline $PbTiO_3$ films on sapphire substrate _____ 146

6.3.2.3 Strained epitaxial $PbTiO_3$ films on $SrTiO_3$ substrate_____ 147

6.3.2.4 Domain state transformations and structural phase transitions in partially or completely relaxed $PbTiO_3$ films on $LaAlO_3$ and MgO substrates ____ 149

Discussion____157

Bibliography ____160

6. Effect of temperature on $PbTiO_3$ powder and thin films

6.1 Literature review

Phase transitions in PTO single crystals have been well studied by several techniques (XRD (1; 2), Raman spectroscopy (3; 4; 5), XAFS (6; 7), neutron diffraction (8), birefringence (2) (see chapter 1) etc. On the other hand, they are less studied and understood in thin films. Epitaxial films are bound to the underlying substrate; therefore, the in-plane lattice parameters of the films are strained which prevents them to attain the bulk values. This is known as the substrate clamping effect, which forces the in-plane lattice parameters of films to vary as the substrate parameter with temperature. It has an important effect on phase transitions and domain formation in thin films (9; 10; 11; 12; 13). The out-of plane lattice parameters of the films must adapt to accommodate the volume change necessary for the phase transition by means of stresses which can modify the phase transition order, the transition temperature and the phase sequence (9).

Generally speaking, the primary and the secondary order parameters indicate the occurrence of a phase transition in bulk materials. However, a decoupling of these parameters has been recently observed in epitaxial thin films. For instance, He et al. (9) showed that only the internal order parameter, the TiO_6 octahedron rotational angle, drives the phase transition in STO films. The secondary order parameter, the c/a ratio or tetragonality, didn't show any change during the phase transition. In the case of BTO films, several authors observed the decoupling between the polarization and the tetragonality (10; 14). Moreover, the phase transition in BTO films becomes a second order phase transition while in bulk BTO, all the phase transitions are of first order (10). Recently, Janolin et al. reported a partial decoupling between the strain and the polarization in monodomain epitaxial PZT/STO films (13).

In recent years, theoretical efforts were made to understand the effects of strain on phase transitions in epitaxial PTO (PZT) films. Pertsev et al. (15; 16; 17) developed the misfit strain-temperature phase diagrams in PTO films, using the Landau-Ginzburg-Devonshire-type nonlinear phenomenological theory. These diagrams calculate the stability range of the various polydomain and single-domain states. Chen et al. (18; 19; 20) revisited the stability diagrams by adopting a phase-field approach, which does not give any priority to the possible domain structures that may appear for a given temperature and a given strain.

It was found that the Curie transition temperature (T_c) increases in monodomain epitaxial PTO and PZT films whatever the strain state. This result is consistent with the Pertsev diagrams (13; 12). In fact, a similar increase of T_c is reported for other perovskite oxide epitaxial films (9; 10; 21; 11; 14) in agreement with the phenomenological theory. In theory, the phase transition temperature increases when films are submitted to tensile or compressive stresses. Fong et al. reported the decrease of the ferroelectric-to-paraelectric phase transition temperature due to a size effect in ultrathin PTO/STO films (22).

According to the theoretical phase diagrams, T_c can be infinitely enhanced by increasing strain. In fact, the driving force for film relaxation increases with strain and film thickness. The critical thickness at which dislocations begin to form varies approximately in a reverse order to the lattice mismatch (23). When films are grown to attain thicknesses greatly exceeding critical values, the relaxation toward a zero-strain state starts by the formation of dislocations. The thickness allowing complete relaxation of misfit stresses is much higher than the critical thickness for dislocation generation and highly depends on deposition temperature (24) (more details are given in section 1.5). Therefore, in order to study the influence of stress on the phase transition, it is important to grow films with thicknesses lower than the thickness corresponding to complete relaxation.

Moreover, stresses can be relaxed by the formation of periodic domain structures (of the type *c/a/c/a*, *c*- or $a_1/a_2/a_1/a_2$). The domain structure results from the competition of polarization, electric field and strain effect. The temperature and related stress effects can then induce changes in the domain structure. In the case of PTO (PZT) films, a transformation of *c/a/c/a* to $a_1/a_2/a_1/a_2$ and *c*-phase was observed by XRD for films grown on tensile MgO (25; 26; 27; 28) and on compressive Pt/MgO substrates (26), respectively. In addition, a small decrease of the transition temperature associated to the polydomain structure was observed by XRD in films on MgO and LAO substrates (29; 30; 31) but the authors misinterpreted the disappearance of domain structure as a ferroelectric-to-paraelectric phase transition. Moreover, their films were completely relaxed.

Furthermore, little progress has been made in the understanding of Raman mode behaviour associated to phase transitions and domain transformations in epitaxial PTO films. A number of papers can be found on Raman studies of phase transitions in polycrystalline PTO films (32; 33; 34; 35; 36), but to our knowledge, only few papers report on a Raman study of phase transitions in PTO/MgO epitaxial films (37,38,39). In this study, the PTO/MgO film under investigation, 1 mm of thickness, was completely relaxed. Some of the authors in references (34; 33; 37) have observed a Raman signature of PTO single crystal and thin films above the phase transition temperature. Yuzyuk et al. (37) interpreted it as an effect of precursor contamination, while Fu et al. believed that the high-temperature phase was still ferroelectric (34; 33). Thus, the persistence of the Raman signature above the phase transition temperature requires further investigation to clarify its origin and its nature.

In order to investigate the influence of misfit stresses on the phase transition in polydomain epitaxial PTO films, partially relaxed PTO films have been studied by using high-temperature XRD and Raman spectroscopy. Our results are compared to those obtained with completely relaxed epitaxial and polycrystalline PTO films and with bulk PTO. Moreover, the phase transition in bulk PTO has been re-examined by Raman spectroscopy in order to have our own reference spectra of the high-temperature phase and thus, to determine accurately the phase transition temperature T_c.

6.2 Temperature evolution of domain structure and lattice parameters in PbTiO$_3$ thin films

High-temperature XRD measurements have been performed on PTO films deposited on LAO, MgO and STO substrates in order to investigate the effects of misfit and thermal stresses on the domain structure. Films of 460 and 65 nm of thickness were analyzed. Unfortunately, measurements stopped at 250 ºC due to a furnace break. Nevertheless, it appears that structural data differ as a function of the substrate and film thickness.

In order to determine the twinning angles in *a*- and *c*-domains, the in-plane and out-of-plane lattice parameters and to quantify the domain fractions, two-dimensional (2-D) ω-2Θ area scan maps near the (*103*) and (*301*) reflections have been collected. STO, LAO and MgO reflections were used as internal standards, assuming that the substrate is unstrained. The 2-D mappings of 460 and 65 nm thick films on different substrates measured at RT, 150 ºC and 250 ºC are given in Figure 6-1 and Figure 6-2, respectively. The reciprocal space mapping integrates the intensity from different φ-angles (± 5°), making possible to observe together the *(301)* and *(310)* reflections which are found at different φ-values. As explained in section 4.2, the coexistence of (*301*) and (*310*) re-

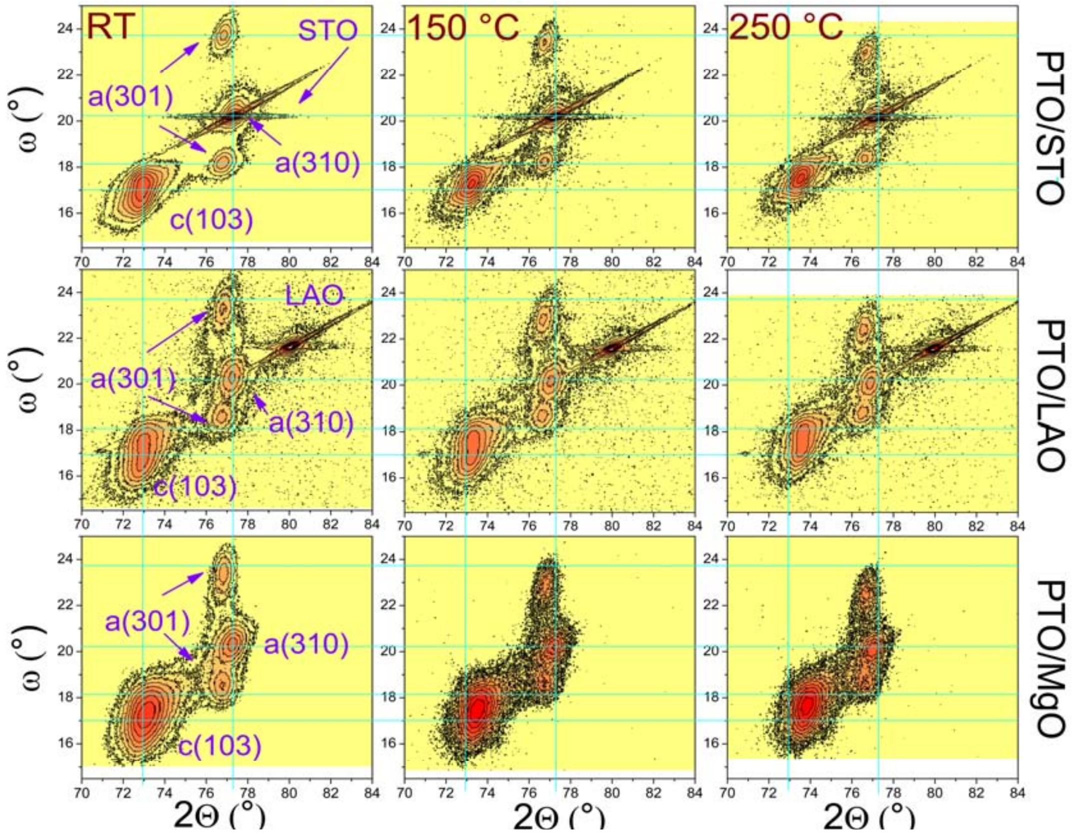

Figure 6-1: 2-D mapping of 460 nm thick PTO films on STO, LAO and MgO substrates at RT, 150 ºC and 250 ºC (see details in the text).

flections indicates that there exist two types of *a*-domains, a_1 and a_2. (*301*) reflection is split into two spots indicating a twinning of the corresponding *a*-domains. As it was mentioned before, the elongation along the ω-axis of the (*103*) spot corresponding to *c*-domains indicates that some twinning also appears in *c*-domains.

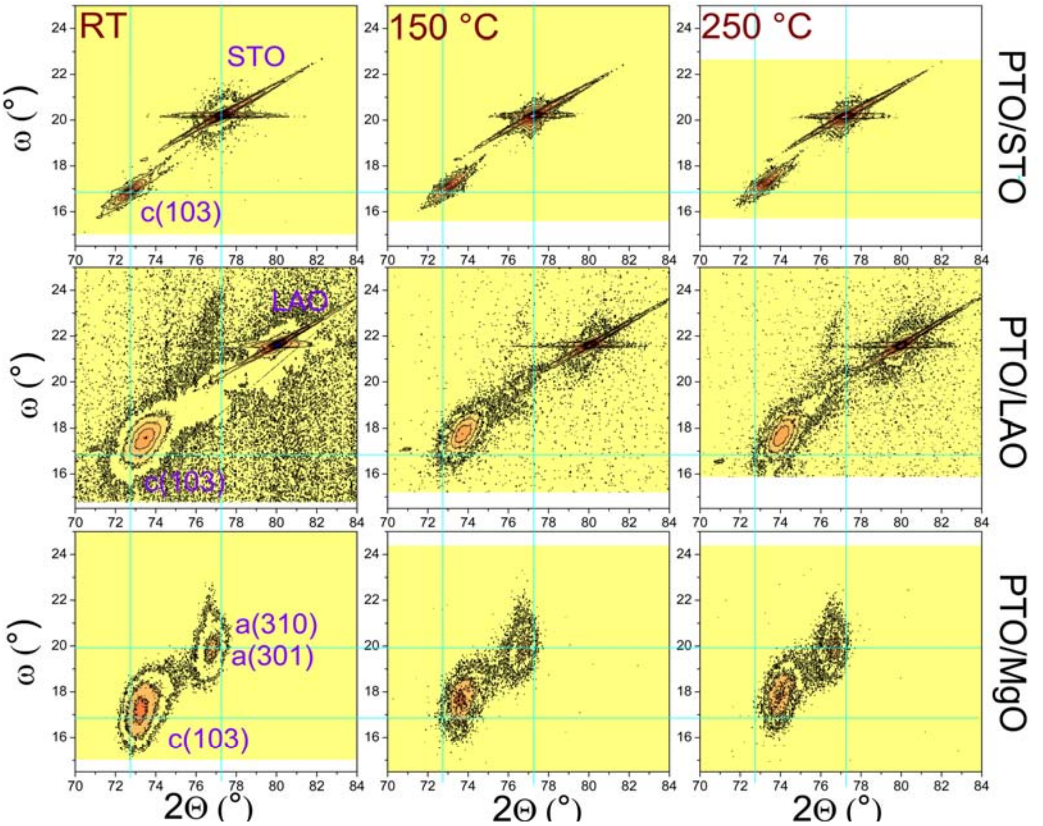

Figure 6-2: 2-D mapping of 65 nm thick PTO films on STO, LAO and MgO substrates at RT, 150 ºC and 250 ºC (see details in the text).

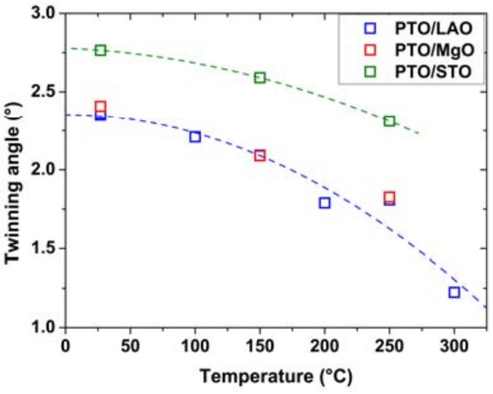

Figure 6-3: Evolution of twinning angles with the temperature in a-domains in 460 nm thick PTO films on STO, LAO and MgO substrates.

6.2.1 Domain structure

PTO films, 460 nm of thickness, have the *c/a/c/a* polydomain structure whatever the STO, LAO and MgO substrate (section 4.3). Figure 6‑1 shows that the distance between spots corresponding to *a*- and *c*-domains gets closer as temperature increases from RT to 250 ºC which indicates a decrease of the tetragonality. Exhaustive results concerning the evolution of lattice parameters with temperature will be given further. The twinning angle in *a*-domains has been evaluated from the distance in ω between both *(301)* reflections and their evolution with increasing temperature is given in Figure 6‑3 in the case of the 460 nm thick

PTO films. The twinning angle evolution is similar for films on the three substrates despite different angle values at RT: it decreases with increasing temperature, as reported by other groups in PTO/MgO films (26; 40). Similarly, the elongation of the *(103)* reflection in *c*-domains also decreases with increasing temperature which indicates a smaller tilt angle of *c*-domains from the substrate plane.

PTO films, 65 nm of thickness, have a fully *c*-domain structure on STO, consist of *c*-domains with a very small fraction of *a*-domains on LAO and have almost equal fractions of *c*- and *a*-domains on MgO. Corresponding 2-D mappings are given in Figure 6‑2. Qualitatively, the spot positions are less ω and 2Θ shifted with temperature than in the 460 nm thick films, except for PTO/MgO where the evolution is similar.

6.2.2 Lattice parameters

Epitaxial films In-plane and out-of-plane lattice parameters in *a*- and *c*-domains were determined from the positions of *(301)*/*(310)* and *(103)* reflections, respectively (see in section 2.2.2). Their temperature dependence in 65 nm and 460 nm thick PTO films on STO, LAO and MgO substrates as well as the substrate thermal expansion are shown in Figure 6‑4. The values of the thermal stresses developed during cooling down from T$_{Dep}$ are given in Section 4.3. Note that during the heating up, the sign of the thermal stress has opposite sign. It appears in the Figure 6-4, that lattice parameters are quite similar in *c*- and *a*-domains whatever the temperature. Therefore, they will be labeled with *a* and *c* without distinguishing domains in the following. The films on STO present a similar thermal expansion whatever the 65 or 460 nm film thickness,

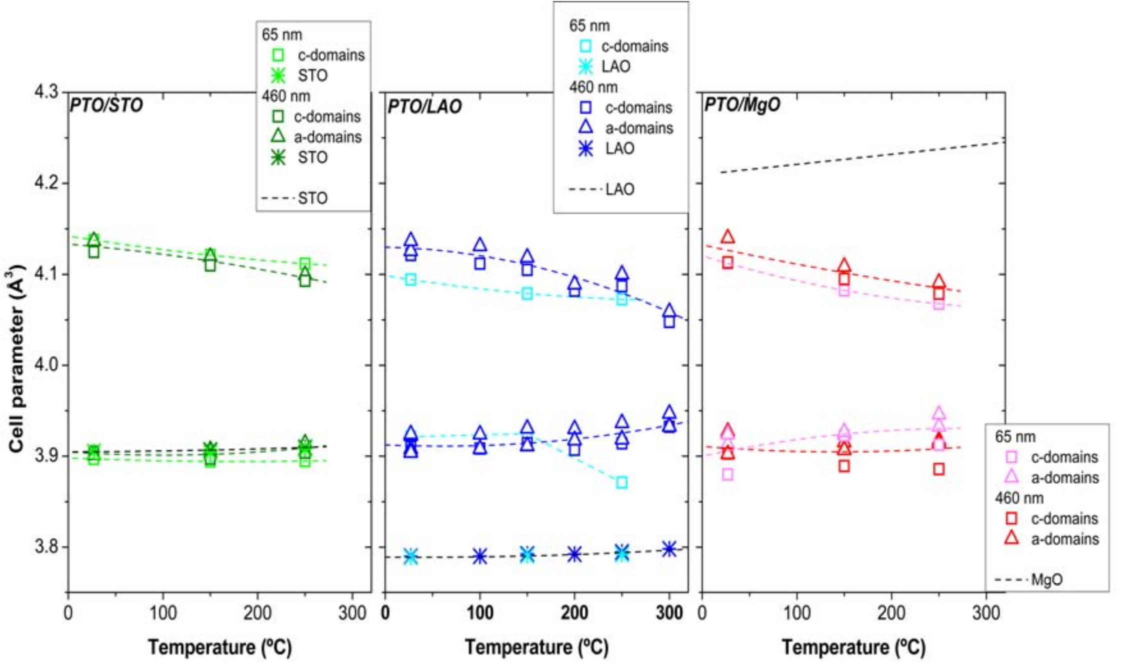

Figure 6-4: Temperature evolution of c- and a-domain lattice parameters in 460 nm and 65 nm thick PTO films on STO, LAO and MgO substrates. The thermal expansion of the three substrates is shown as black dashed lines.

and the expansion along the *a*-axis is the same as that of the substrate. This indicates that both PTO/STO films are highly substrate-dependent. In the case of PTO/LAO films, the film and substrate thermal expansions are slightly different which indicates that films are less substrate dependent than PTO/STO films. The *c*-axis evolution is thickness dependent and is almost the same for the thinner films on LAO and on STO which indicates that the 65 nm thick PTO/LAO film is more substrate dependent than the thickest one. Concerning PTO/MgO films, the thermal expansion along the *c*-axis is the same whatever the film thickness; it is higher in the thinner film along the *a*-axis. This can result from higher tensile thermal stresses in thinner films.

The thermal expansion along *a*- and *c*-axes in films of both thicknesses and in bulk PTO is shown in Figure 6‑5. Along the *a*-axis, it is always higher in bulk PTO than in the thickest films whatever the substrate; as for the *c*-parameter, its decrease is similar in films on LAO and MgO and in bulk PTO and is much smaller in films on STO. This means that the PTO thermal expansion along the *a*-axis is governed by the STO substrate whereas PTO films on LAO and MgO are almost “free” from the substrate influence. In 65 nm films on STO and LAO, the *c*-axis decrease with temperature is similar; it is slower than that in PTO single-crystal, indicating the substrate dependence of the film. Therefore, the *a*-axis expansion in these films is expected to be also highly dependent on substrate thermal expansion as see in Figure 6-4. The thermal expansion in 65 nm films on MgO is almost the same than that in bulk PTO, and then it is higher than that in the other films, as it is greatly affected by positive thermal stresses.

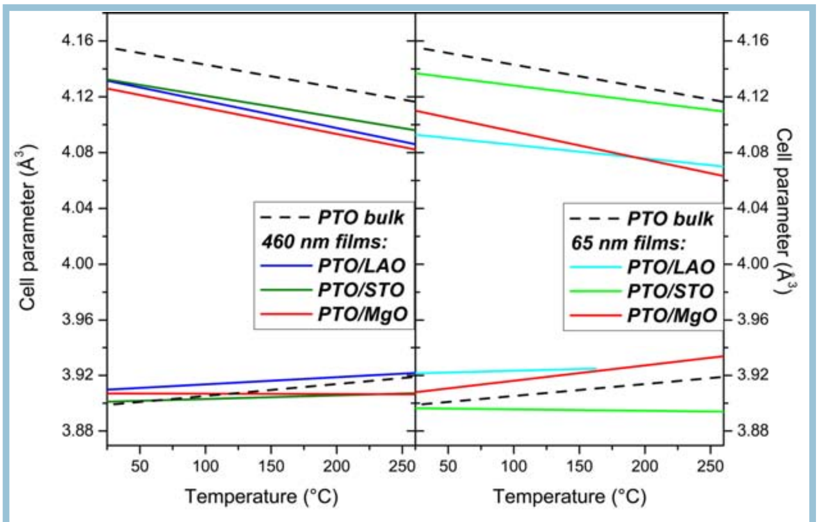

Figure 6-5: Comparison of thermal expansion in bulk PTO (9) and in 460 nm and 65 nm thick PTO films on STO, LAO and MgO substrates.

In conclusion, 65 – 460 nm PTO/STO films and 65 nm films on LAO and MgO are highly substrate dependent. Thus, the *c*-parameter decrease with temperature is smaller than that in bulk PTO and thermal expansion of *a*-axis is mainly governed by the thermal expansion of the substrate. The 460 nm films on LAO and MgO are almost “free” from the substrate influence.

Polycrystalline films In polycrystalline films, misfit stresses do not exist and films are only affected by internal and external thermal stresses. External thermal stresses result from the difference in thermal expansion between the substrate and the film whereas internal thermal stresses result from the difference in thermal expansion

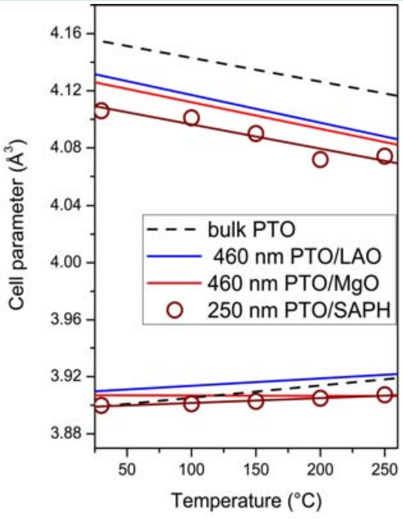

Figure 6-6: Temperature evolution of lattice parameters in a 250 nm PTO/SAPH film and comparison to bulk PTO and to 460 nm thick PTO films on MgO and LAO. Error bars are within the symbols.

between each grain and its surrounding. In order to compare the evolution of lattice parameters with temperature in epitaxial and polycrystalline films, 250 nm thick PTO/SAPH films have been also studied by using high-temperature XRD. SAPH has a much smaller thermal expansion coefficient (~5x10^{-6} K^{-1} (41)) than PTO (12.6x10^{-6} K^{-1} (1)) which alters the lattice parameters and the PTO thermal expansion. Lattice parameters of PTO films on SAPH films have been calculated by fitting with the least square method, assuming the same lattice parameters for all grains (Section 2.2.2). The evolution of lattice parameters with temperature is shown in Figure 6‑6 and compared to that of bulk PTO and of PTO films on LAO and MgO. The evolution along the *c*-axis is quite similar to that of bulk PTO and 460 nm films on LAO and MgO. The *a*-axis expansion is similar to that in PTO/LAO film and then, smaller than that in bulk PTO.

6.2.3 Domain fraction

The proportion of *a*-domains was estimated from the ratio of integrated intensities of *(301)*/*(310)* and *(103)* reflections as explained in section 2.2.2. The evolution of *a*-domain fraction with temperature is given in Figure 6‑7. It greatly increases with increasing temperature in the 65 nm film on MgO, as the formation of *a*-domains is favoured by tensile thermal stresses. In the 460 nm film on MgO, the *a*-domain fraction increases more slowly since the film is less substrate-dependent than the 65 nm one. These observations are in agreement with reported results on PTO/MgO films (26, 27, 28). Furthermore, a transformation from the *c/a/c/a* polydomain structure to the $a_1/a_2/a_1/a_2$ structure has been observed with increasing temperature in PTO/MgO films by Janolin et al. (25). PTO/STO films are submitted to compressive thermal stress, therefore the

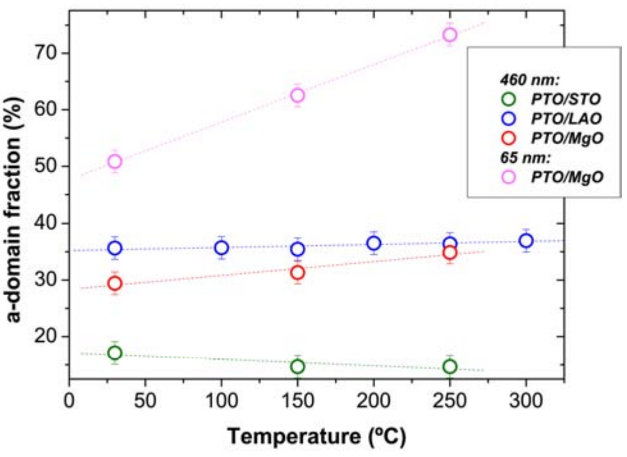

Figure 6-7: Temperature evolution of a-domain fraction in PTO films on STO, LAO and MgO substrates. The a-domain fraction in 65 nm PTO films on STO and LAO was not possible to measure, as a -domain XRD reflection intensities were very weak.

c-domain fraction increases with increasing temperature. In the 460 nm film on LAO, the *a*-domain fraction is almost constant with the increase of the temperature. As mentioned above, the *c*-domain fraction increase with increasing temperature is expected to be due to compressive stress in PTO/LAO films. Indeed, Lee et al. have observed significant changes in domain fractions only at temperatures higher than 400 ºC in PTO/Pt/MgO films (26).

To conclude, we expect that 460 nm thick epitaxial PTO films on LAO and MgO substrates should have similar high-temperature phase transition to that of the polycrystalline PTO/SAPH films and the bulk PTO. Different behaviour at high-temperature is expected for 65-460 nm thick PTO/STO and 65 nm thick PTO films on LAO and MgO substrates, as they are highly substrate dependent. Transformation from the *c/a/c/a* polydomain state to the *c*-phase may be expected in PTO/STO and PTO/LAO, while in PTO/MgO case the *c/a/c/a* state should be replaced by the $a_1/a_2/a_1/a_2$ state at high-temperature.

6.3 Domain transformations and phase transitions in $PbTiO_3$

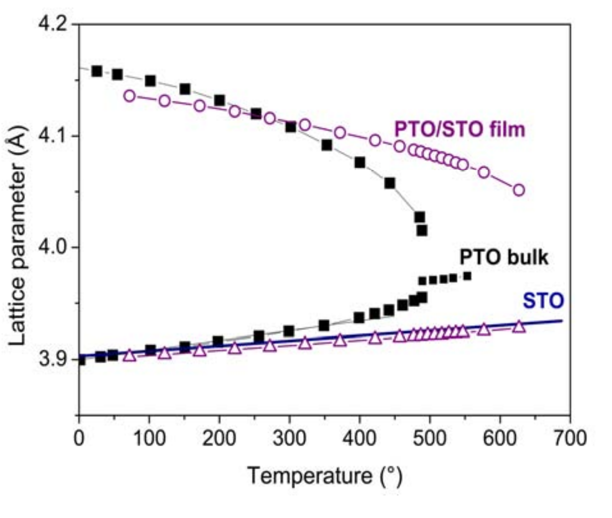

Figure 6-8: Temperature evolution of lattice parameters in 250 nm thick PTO/STO film and in bulk PTO. The solid line shows the thermal expansion of STO substrate.

6.3.1 High-temperature XRD study of epitaxial system PTO/STO films

In order to investigate the misfit stress influence on the phase transition in PTO films, a coherent epitaxial 250 nm thick PTO/STO film was studied by high-temperature XRD in Θ/2Θ standard scans. The *a*-domain fraction is very small (~ 4 %) in this film, indicating that misfit stress governs the domain structure and the transformations.

The *a*- and *c*-lattice parameters were calculated from the *(004)* and *(400)* reflections (for more details see in section 2.2.2), respectively, stress governs the domain structure and the transformations. The *a*- and *c*-lattice parameters assuming that out-of-plane *a*-parameter of *a*-domains is the same as in-plane *a*- parameter of *c*-domains. The XRD measurements were carried out from RT up to 650 ºC. The temperature evolution of *a*- and *c*-lattice parameters of the PTO film is given in Figure 6‑8 for comparison with bulk PTO. In the whole temperature range (RT to 650 ºC), the PTO/STO film has a *c/a/c/a* polydomain structure and no phase transition is evidenced. Recently, similar observations were reported for monodomain PZT and PTO films on STO substrate by Janolin et al. (12, 13). High-temperature phase transition was no more observed in PTO/BTO superlattices

(42). Furthermore, a ferroelectric-to-paraelectric phase transition in 50 nm thick PZT film was evidenced by piezoforce microscopy measurements at temperature as high as 787 ºC (43). The main difference between our films and the reported ones is the existence of the *c/a/c/a* polydomain state at high-temperature. Indeed, theory predicts the stability of *c*- or $a_1/a_2/a_1/a_2$ phase at high-temperatures whereas the *c/a/c/a* domain structure should be stable only below the bulk PTO phase transition temperature. In our films, the film thickness H is almost the same as the domain width W (W = 240 nm) (see for more details section 1.6 and section 4.4). Therefore, the polarization and strain internal fields are highly inhomogeneous. This can explain the deviation observed from the theoretical phase diagrams developed for dense domain structures, where W<<H (section 1.6). However, comparable temperature shifts have been reported for the paraelectric-to-ferroelectric phase transition in other high-quality thin films of perovskite oxides such as STO and BTO (21, 11).

6.3.2 Raman spectroscopy results

In order to investigate phase transitions and domain state transformations in epitaxial PTO films, high-temperature Raman spectroscopy measurements have been performed. The evolution of the *E(1TO)* and $A_1(1TO)$ soft modes with temperature will not be studied because they shift towards low wavenumbers very quickly and out of our attainable spectral range and this long below the transition temperature (notch filter cutting at about 70 cm^{-1}). Therefore, our analysis of the phase transition in the different films will be based on the concept of hard mode spectroscopy (44, 45, 46).

In the first part, the tetragonal-to-cubic phase transition in PTO powder and in PTO polycrystalline films will be studied. On the basis of these results, phase transitions and domain state transformations will be investigated in epitaxial films of different thicknesses and mismatch with substrates.

6.3.2.1 PTO powder

Let us first discuss results on PTO powder samples which we will then consider in the later work as our own proper reference system for the understanding of thin films. The temperature evolution between RT and 600°C of depolarized Raman spectra of PTO powder is given in Figure 6‑9. A considerable change is observed in the spectrum at 520°C: the intensities decrease abruptly and the line widths greatly increase. It is known that the increase of Raman line widths results from a shortening of phonon lifetime at high temperature. The temperature dependence of the mode wavenumbers in Figure 6‑10 shows that all modes shift to lower wavenumbers and that hard *E(TO)* and $A_1(TO)$ modes merge. These results are consistent with the works of Burns et al. (3) and Idrissi (47). As shown in section 1.4.3 and 5.2, $A_1(TO)$ modes are highly sensitive to the crystal orientation. Crystallites in a powder have random orientations, thus, $A_1(TO)$ mode positions are an average of the positions of all oblique modes appearing between *a* - and *c*-axis orientations (Fig. 1-13). Therefore, we will discuss only the general trends of the evolution of $A_1(TO)$ modes. *E(TO)* mode profiles are less modified by quasimode appearance; accordingly their positions can be qualitatively compared to those obtained in our PTO films.

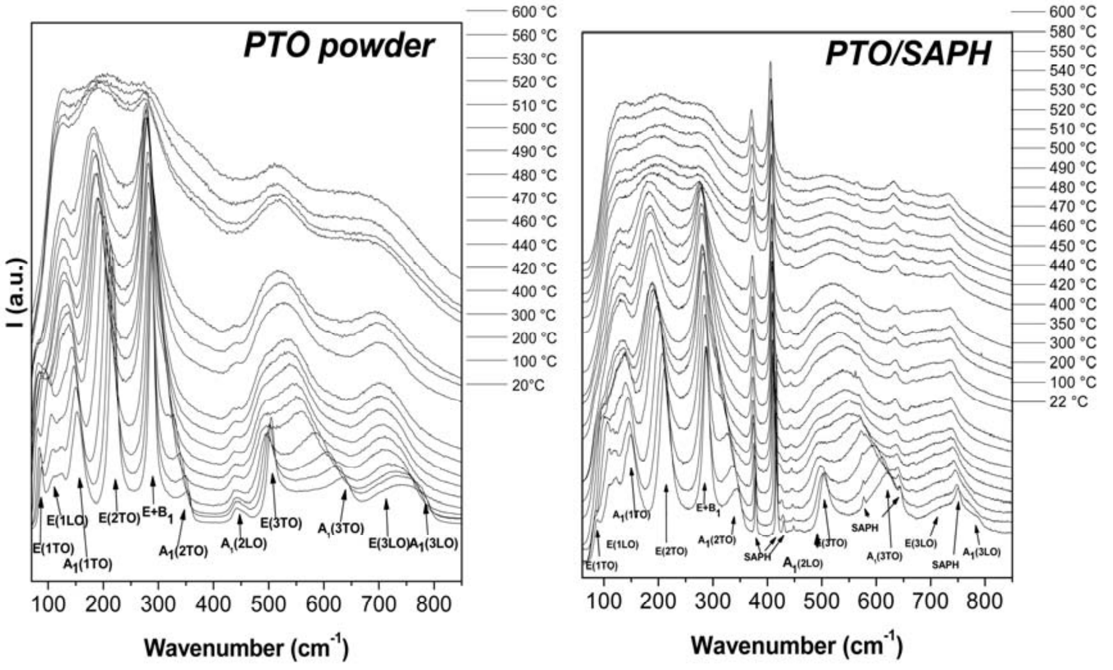

Figure 6-9: Temperature evolution of depolarized Raman spectra of PTO powder and of a 250 nm thick polycrystalline PTO/SAPH film. Intensities have been normalized for better reading.

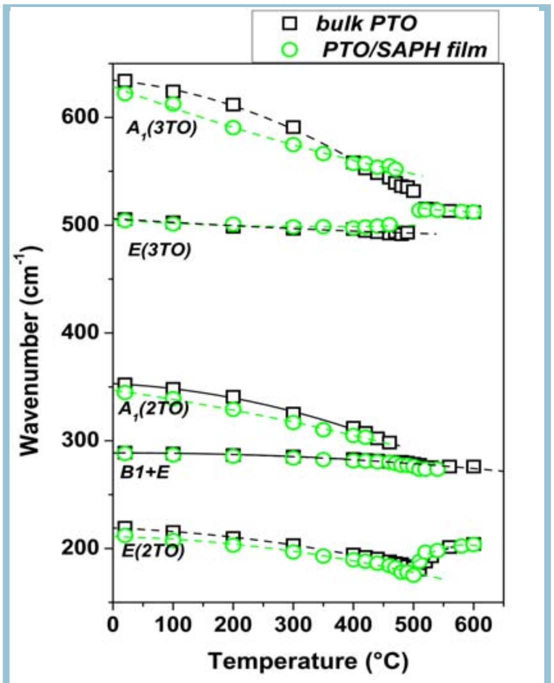

Figure 6-10: Temperature evolution of Raman mode wavenumbers in bulk PTO and in a 250 nm thick PTO/SAPH film.

The abrupt change observed at 520°C in the spectra of PTO powder give evidence of the expected structural phase transition. However, the Raman signature remains significant in the spectra above 520°C (Figure 6.9), while Burns et al. (3) reported the disappearance of the modes at 496°C. In the same high-temperature range, Fontana et al. (4) observed a quasi-elastic scattering in the Raman spectra of the high-temperature phase. The high brightness of the spectrometer has probably made possible the observations of the weak Raman signature of PTO at high temperature, unlike Burns and Fontana (3, 4).

As mentioned in Section 1.3, some XAFS measurements have given evidence of a local tetragonal structure of PTO even at high-temperature, whereas an average cubic structure is observed by XRD (section 1.3) (6, 7). Therefore, the PTO high-temperature phase can be considered as a disordered cubic structure, as observed in BTO or $KNbO_3$ and probably any other perovskite-type ferroelectric at high-temperature (48, 49). Indeed, this discrepancy between XAFS and XRD results can be explained by the fact that XAFS probes the direct atomic environment only while the coherence length of XRD provides information about long-range order (> several hundred Å). Raman scattering stand somehow in-between the two latter techniques and can probe short-range polar regions on the length scale of several 10 Å.

The abrupt change in the line intensities and widths indicates a significant increase of disorder in the tetragonal structure, i.e. a non negligible order-disorder character of the phase transition. This was also suggested by the occurrence of a central peak in PTO crystal Raman spectra above 600 K (4; 5). Therefore, the high-temperature ferroelectric-to-paraelectric phase transition can be interpreted as a transition from a tetragonal to a disordered cubic structure. It is to be noticed that the difference in T_c values could be ascribed to the way temperature is measured; in our heating stage, the thermocouple was placed under the sample holder and a slight temperature difference may appear between the sample and the thermocouple. Nevertheless, the temperature of 520°C measured as the phase transition temperature in bulk PTO will be used for comparison with temperature determined in our thin films, as the measurements were carried out in the same experimental conditions. The increase of the line widths during further increase of temperature up to 600 ºC may come from an increased thermal disorder.

6.3.2.2 Polycrystalline PTO films on sapphire substrate

To investigate the influence of thermal stresses on phase transitions in PTO films without any contribution of misfit stresses, Raman measurements have been performed on polycrystalline films. Raman spectra of 250 nm thick PTO/SAPH films were collected in the temperature range from RT to 600 ºC and reported in Figure 6‑9. Their evolution with temperature is rather similar to that of PTO powder spectra, and the Raman modes also shift to lower wavenumbers. However, the positions of the different Raman lines differ in wavenumbers for a given temperature, especially the $A_1(TO)$ and the *E(2TO)* modes (Figure 6‑10). PTO/SAPH films are polycrystalline with some preferred orientations and differences between peak positions can be explained by the existence of oblique modes. Unlike PTO powder, only certain oblique modes are collected in the polycrystalline film in addition to the real *TO* and *LO* modes, depending of the preferred orientation of the film. The tetragonal-to-disordered cubic phase transition in PTO/SAPH films was observed at 510 ºC; T_c is thus slightly lower than in PTO powder.

Finally let us shortly recall and discuss previous literature results of similar films. Fu et al. reported an increase of more than 40° C of the tetragonal-to-cubic transition temperature of PTO/SAPH films in comparison with bulk PTO (33; 34). Unfortunately, the authors have considered the high-temperature phase Raman spectra as spectra of the ferroelectric tetragonal phase. They have observed an anomaly in the soft mode evolution at 480 ºC but did not interpret this change as a ferroelectric-to-paraelectric transition. Dobal et al. have reported a T_c decrease with decreasing thickness in PTO/SAPH films (35) and interpreted the temperature shift of T_c as the result of hydrostatic pressure related to the clamping of each grain by its neighbours. However, spectra in Ref.35 show that the *E(3TO)* mode is shifted to lower wavenumber while it should be shifted upward under hydrostatic pressure. This suggests the existence of tensile stresses in their films and throws questions on their model. They have also reported a *c* parameter decrease with decreasing the film thickness that clearly indicates an increase of tensile stresses in the films. Taguchi et al. have observed the tetragonal-to-cubic phase transition at 476 ºC in PTO/Pt/Si films, which were under tensile stress, as the authors reported a shift of the *E(3TO)* mode to lower wavenumbers (36). Therefore, the downshift of the transition temperature reported in different previous papers probably result from tensile stresses which originate from thermal stresses in polycrystalline PTO films on SAPH and Si. It is important to note that in the case of polycrystalline films the tensile stress is probably non-biaxial but 3-D.

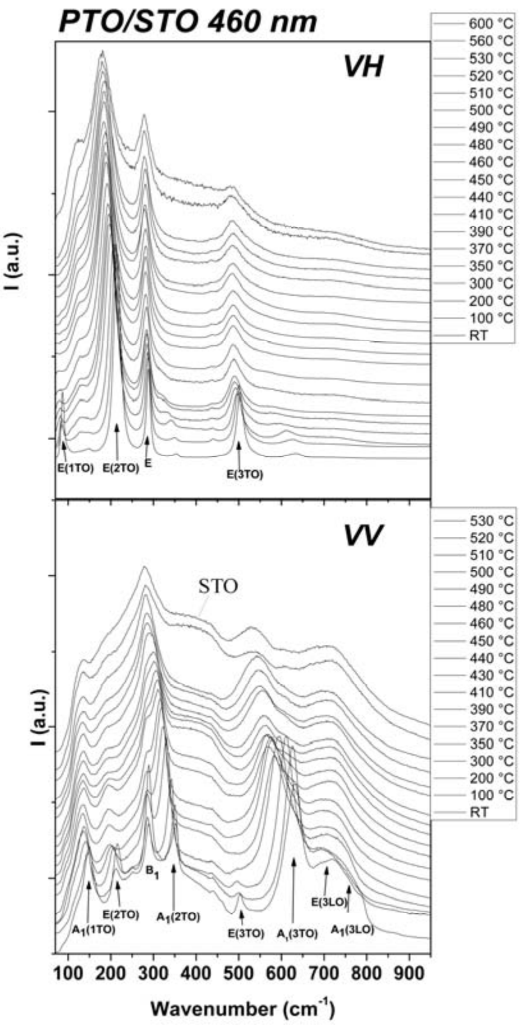

Figure 6-11: Temperature evolution of 460 nm PTO/STO film spectra recorded on film cross section in VH and VV polarization configurations. At 520-530 °C STO Raman mode intensities relatively increase in VV spectra.

6.3.2.3 Strained epitaxial PTO films on STO substrate

Although no structural phase transition should be observed in 250 nm thick PTO/ STO films by XRD (section 6.3.1), we have undertaken a Raman study of these films as a function of temperature because this technique can reveal even subtle changes in symmetry. To our knowledge, no report exists in literature about such a Raman study of PTO (PZT) films on STO substrates. Unfortunately, in normal measurement conditions (film surface), the PTO Raman signature is masked by a huge scattering signal coming from the STO substrate, this probably explains the absence of literature data. A way of decreasing the STO signal in our work has been to collect the spectra on the film cross section, which also increases the intensities of PTO Raman lines as PTO/STO films consist mainly of *c*-domains (section 5.3). Polarized Raman spectra of 250 and 460 nm PTO/STO films were recorded on the film cross section in the temperature range from RT to 600 ºC (Figure 6‑11 and Figure 6‑-12, respectively). *VV* polarized spectra of 250 nm films are not presented as the PTO lines are completely masked by the intense Raman lines from the STO substrate. The figures show that the hard modes remain well defined and intense up to 600°C in both films without any visible anomaly in their evolution.

As explained in section 5.2, *E(TO)* and *A$_1$(TO)* wavenumbers have been determined the wavenumbers of each mode from *VH* and *VV* polarized spectra, respectively, and their temperature evolution is shown in Figure 6‑13. Unlike powder and polycrystalline PTO, the decrease in wavenumbers in both 460 nm and 250 nm PTO/STO films is continuous up to 600°C without any significant anomaly in the fitting curves and this evolution attests the absence of a phase transition in this temperature range. The modes shift to lower wavenumbers with a slight increase in line width and decrease in intensity. The decrease in wavenumbers is slightly smaller than in bulk PTO (Figure 6‑13).

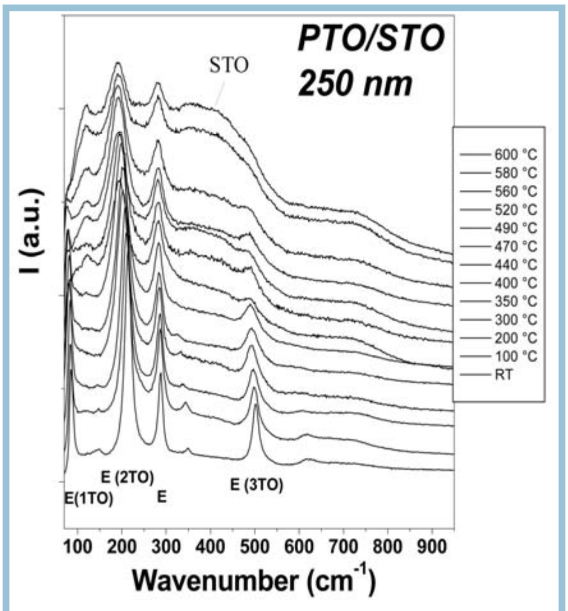

Figure 6-12: Temperature evolution of 250 nm PTO/STO film spectra recorded on film cross section in VH polarization configuration. At high-temperature PTO Raman modes are partially masked by STO modes.

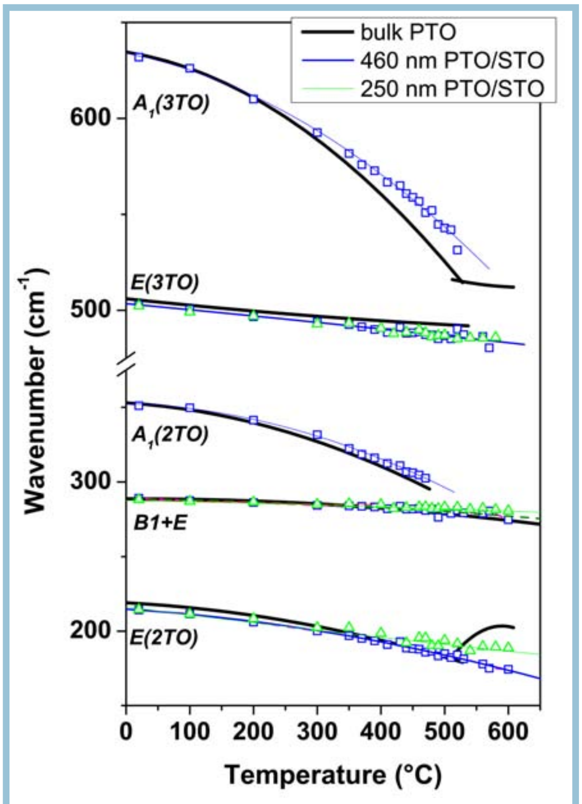

Figure 6-13: Temperature evolution of Raman mode wavenumbers in 460 nm and 250 nm thick PTO/STO films.

In the case of the 250 nm thick film, the downshift of the E modes is slightly slowed down in comparison with the 460 nm film. As a consequence, we can expect that T$_c$ should be higher in the 250 nm film than in the 460 nm film. While the *E(1TO)* soft mode shifts quickly to lower wavenumbers with increasing temperature in bulk PTO (3),it is still well observed at ~ 74 cm^{-1} at 600 ºC in the case of the 250 nm PTO/STO film (Figure 6‑14). However, the soft mode position is not easily determined at high-temperature due to the close cutting of the notch filter. These results are in agreement with those obtained in the high-temperature XRD analysis of PTO/STO films.

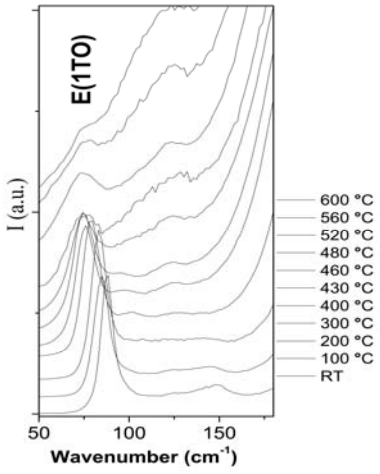

Figure 6-14: Temperature evolution of the E(1TO) soft mode profile in the 250 nm thick PTO/STO film.

As a conclusion, the Raman study of epitaxial PTO/STO films has revealed that 250 and 460 nm thick films remain tetragonal and do not undergo a phase transition up to 600 ºC. Therefore, these films are expected to be ferroelectric at temperatures as high as 600 ºC. The comparison of the Raman spectrum evolution of both films with temperature favours a higher transition temperature in the 250 nm thick film due to higher compressive stresses.

6.3.2.4 Domain state transformations and structural phase transitions in partially or completely relaxed PTO/LAO and PTO/MgO films

Transformations between domain states

The epitaxial property of PTO films on LAO and MgO is of lower quality when compared to films on STO. As discussed in section 6.2, a transformation from the *c/a/c/a* polydomain structure to a *c*-phase or a $a_1/a_2/a_1/a_2$ state may occur before the ferroelectric-to-paraelectric phase transition (15). It has been reported in Section 5.3 that Raman lines related to a-domains and *a*- & *c*-domains are obtained from polarized spectra recorded on film surface and on film cross section, respectively. A possible change in the domain structure can be easily observed in comparing the temperature evolution of *VH* spectra measured on film surface and on film cross section. A detailed report on such domain transformations in 460 nm thick PTO/MgO and PTO/LAO films will be presented in the following as well as a short discussion about transformations in thinner films.

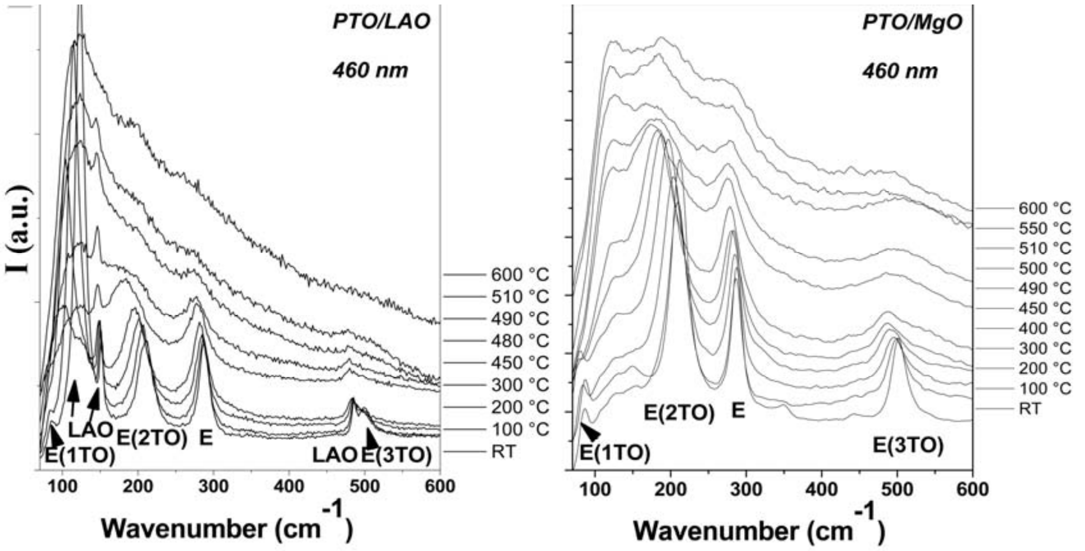

Figure 6-15: Temperature evolution of VH polarized spectra recorded on the surface of 460 nm thick PTO/LAO and PTO/MgO films.

The temperature evolution of *VH* polarized spectra related to *a*- and *c*-domains in 460 nm PTO films on MgO and LAO is presented in Figure 6‑15 and Figure 6‑16, respectively. It appears that the Raman signature of *a*-domains vanishes at 490 °C in PTO/LAO films while it is observed up to 600 ºC in PTO/MgO films (Figure 6‑15). Spectra recorded on the film cross section reveal that the Raman signature is retained in the whole temperature range up to 600°C in PTO films on both substrates (Figure 6‑16). This indicates a transformation from the *c/a/c/a* polydomain structure to the *c*-phase in PTO/LAO. On the other hand, the domain transformations in PTO/MgO films remain unclear.

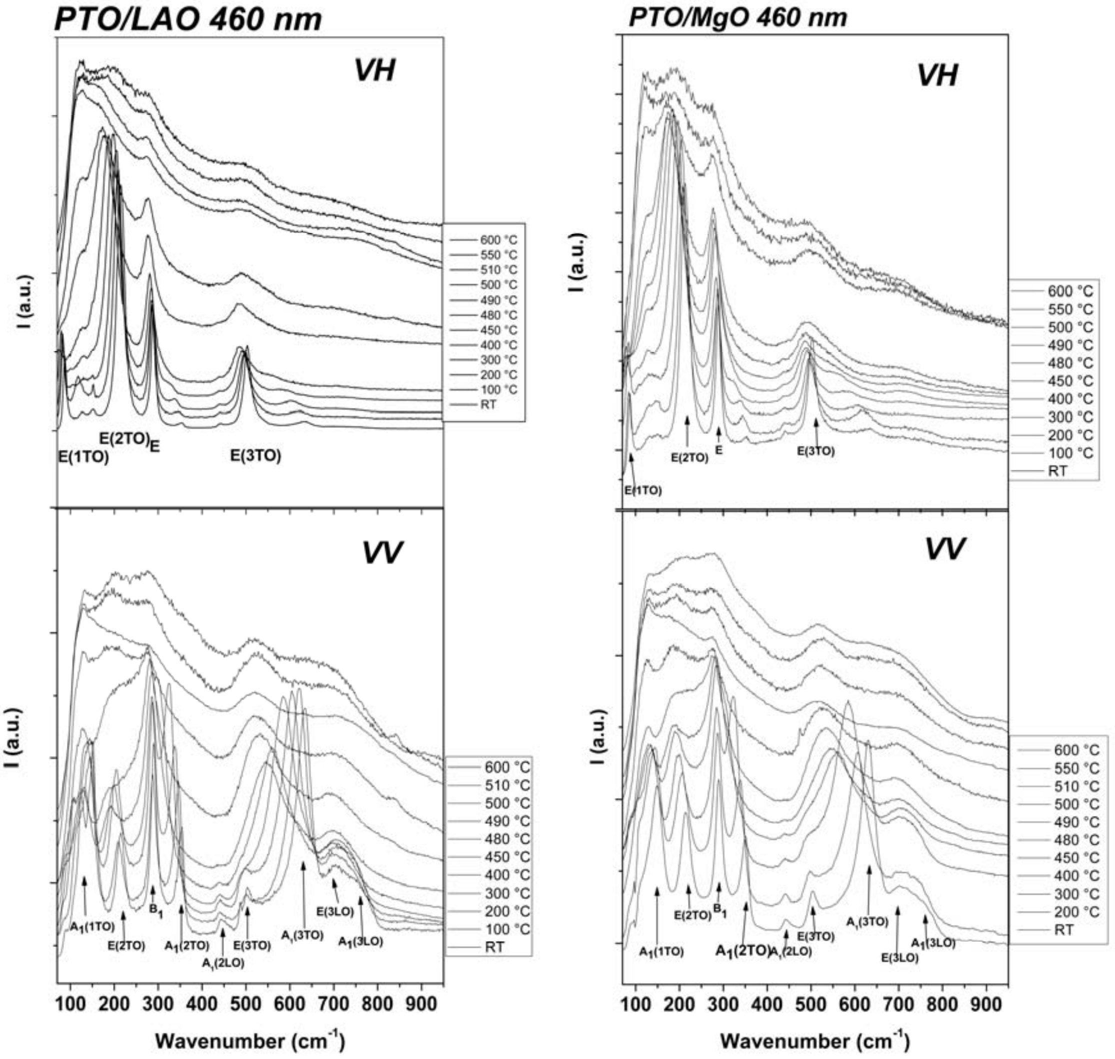

Figure 6-16: Temperature evolution of VV and VH polarized spectra measured on the cross section of 460 nm thick PTO films on LAO and MgO substrates. The intensities were normalized to the most intense mode.

The temperature evolution of band positions in *a*- and *c*-domains is shown in Figure 6‑17. It is to be noted that *E(TO)* modes observed in spectra collected on the film cross section come from both types of domains in *c/a/c/a* phase and only from *a*-domains in

$a_1/a_2/a_1/a_2$ state. As a consequence, the interpretation of *E(TO)* evolution curves in Figure 6‑17 is much easier for PTO/LAO films than in PTO/MgO films. The temperature evolution of *E(TO)* modes in *a*- and *c*-domains is similar for PTO films on both substrates. As shown in Figure 6‑17, an anomaly is observed at 500°C in the evolution of *E (TO)* wavenumbers in 460 nm PTO/MgO films. This anomaly occurs in *VH* spectra recorded on the film cross section as well as on the film surface. It is not related to domain transformation and will be discussed in the following section. The *E(TO)* wavenumbers plotted in Figure 6‑17 for *a*- and *c*-domains are very close each other.

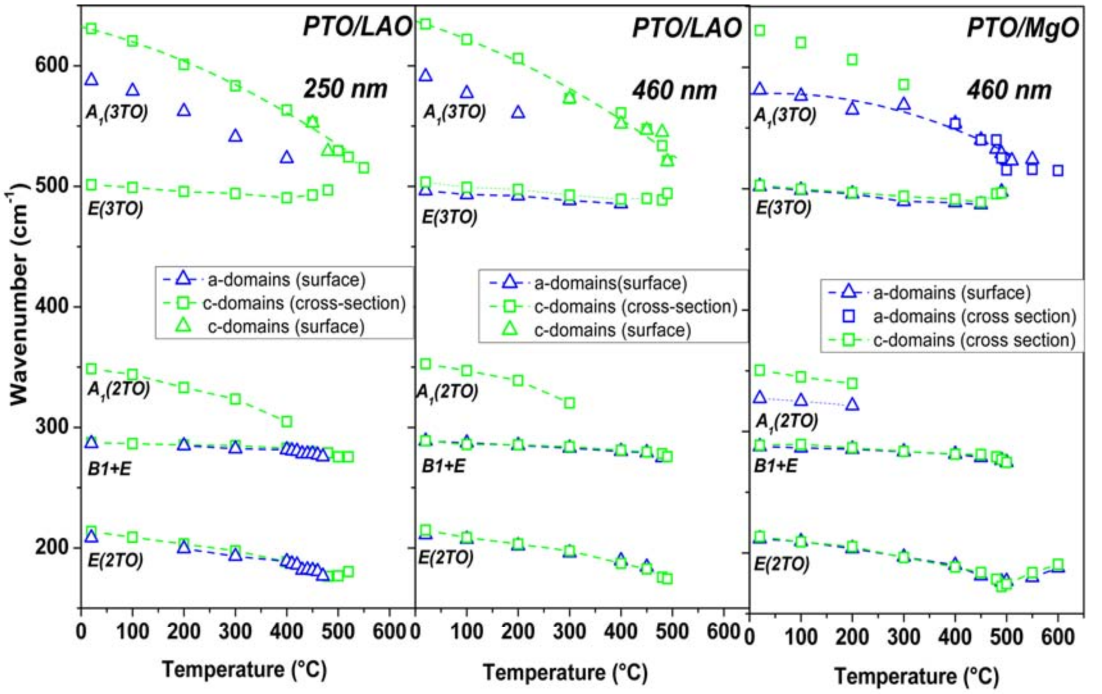

Figure 6-17: The a- and c-domain Raman mode evolution with the temperature in 250 nm and 460 nm thick PTO/LAO and 460 nm thick PTO/MgO films (more details are given in the text).

The *A_1(2TO)* (MgO) and *A_1(3TO)* (MgO and LAO) mode wavenumbers are significantly different in *a*- and *c*-domains which allow them to be easily identified in comparing *VV* spectra recorded on the film surface and on the film cross section (section 5.2). Unfortunately, *A_1(2TO)* modes are very close to the intense B_1+E mode. Thus, the mode separation is possible only at low temperatures. The downshift of *A_1(3TO)* modes in PTO films on both substrates is similar in *a*- and *c*-domains up to 200°C despite lower wavenumbers in *a*-domains. At 300 – 400 °C *A_1(3TO)* double modes become a single one, i.e. the intensity of one of the two components, corresponding to *a*- or *c*-domains, vanishes. This indicates that an abrupt change in domain proportions occurs in both films. This observation is consistent with reported XRD results on PTO/MgO films (26). With a further increase of temperature, the *A_1(3TO)* mode continuously follows the temperature evolution of *c*-domain mode in PTO/LAO film and of *a*-domain mode in PTO/ MgO film. This shows that PTO films on LAO and MgO become mainly *c*- and *a*-

domain oriented, respectively. However, in the case of PTO/LAO films, *a*-domains completely disappear only at 490 °C. Unfortunately, we cannot estimate the *c/a/c/a* to $a_1/a_2/a_1/a_2$ transformation temperature in PTO/MgO films, as the *E(TO)* modes are observed for both *a*- and *c*-domains in the spectra collected on the film cross section. The transformation from the *c/a/c/a* to the $a_1/a_2/a_1/a_2$ domain structure can be expected from Pertsevs' diagram ((15) and section 1.6) at temperatures lower than the phase transition temperature in bulk PTO phase transition. This transformation was observed by XRD in 200 nm PTO/MgO films at 460°C which is close to the phase transition temperature in bulk PTO (26). It is to be noted that during the transformation of the domain structure, no anomaly was observed in the temperature evolution of the Raman modes.

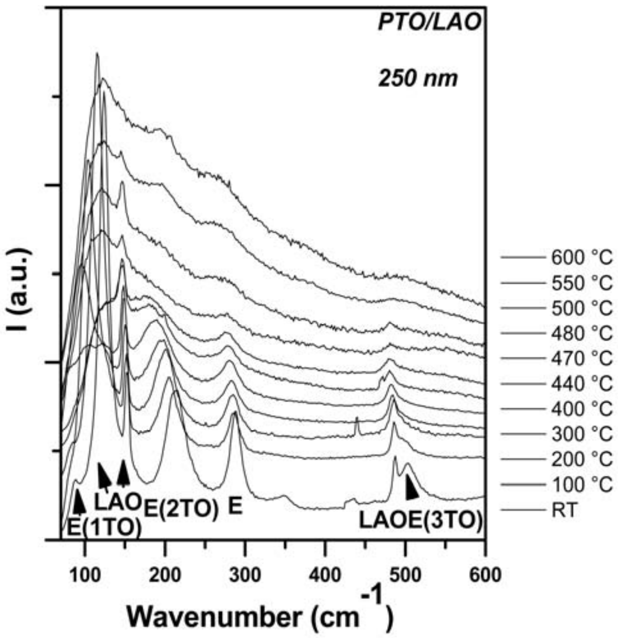

Figure 6-18: Temperature evolution of VH polarized spectra recorded on the surface of 250 nm thick PTO/LAO and PTO/MgO films.

The temperature evolution of *VH* polarized spectra recorded on 250 nm thick PTO/LAO film surface and cross section are presented in Figure 6-18 and Figure 6-19. The Raman signature of *a*-domains vanishes at 480 °C which indicates the *c/a/c/a* to *c*-phase domain structure transformation. It takes place at a lower temperature than in the 460 nm thick PTO/LAO film. As shown above and expected intuitively, thin films are more stressed by the substrate than thick ones and compressive thermal stresses in PTO/LAO films increase with increasing temperature. Therefore, 250 nm films should be under higher compressive stresses than the 460 nm ones. As expected from Pertsevs' diagram (15), higher compressive stresses stabilize the *c* -phase and as a consequence the temperature of the *c/a/c/a* to the *c*-phase transformation decreases. As shown in Figure 6-17, the temperature evolution of the Raman modes in *a* - and *c*-domains is similar in 250 nm and 460 nm PTO/LAO films.

The *a*-domain fraction is very small (7.8 %) in 65 nm thick PTO/LAO films. Thus, the *a*-domain Raman signal in *VH* spectra has a rather low intensity and is masked by the LAO Raman signature (Figure 6-20). No increase in intensity is observed during the temperature increase from RT to 600 °C which indicates that *c/a/c/a* to c-phase transformation may be expected in these thin films. On the contrary, a well-defined Raman signature is observed in *VH* spectra of 65 nm thick PTO/MgO films recorded on film surface and cross section up to 600 °C (Figure 6-20). In this film the *a*-domain fraction quickly increases with the increase in temperature, as was shown by high-temperature XRD analysis. Thus, a transformation from the *c/a/c/a* to the $a_1/a_2/a_1/a_2$ domain state should take place. The *a*-domain fraction increases slower in the 460 nm PTO/MgO film than in the 65 nm thick one. Therefore, the transformation temperature can be expected to be lower in the thinner film.

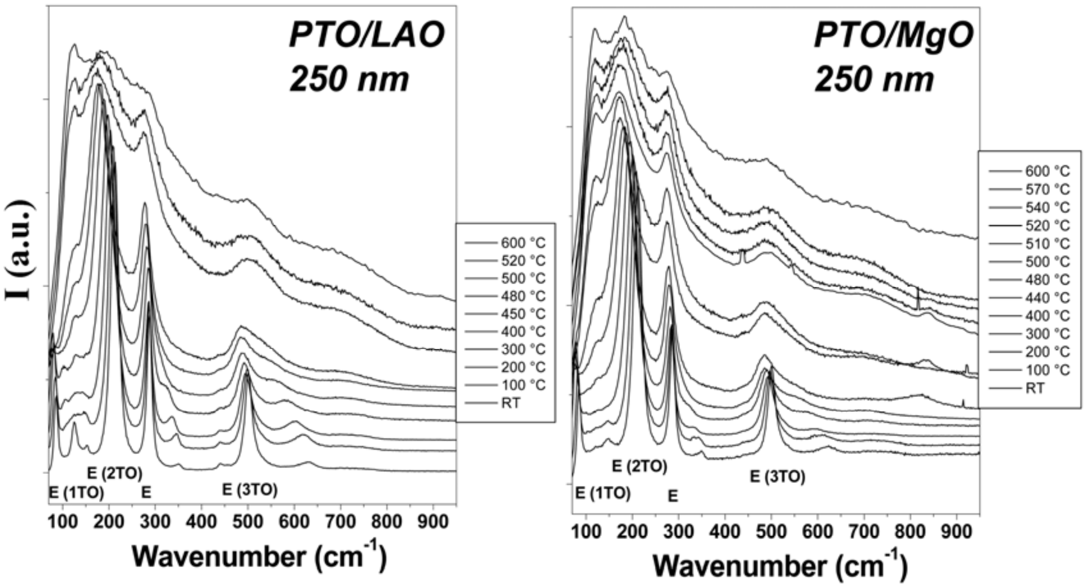

Figure 6-19: Temperature evolution of VH polarized spectra collected on the cross section of 250 nm thick PTO films on LAO and MgO substrates. The intensities were normalized to the most intense mode.

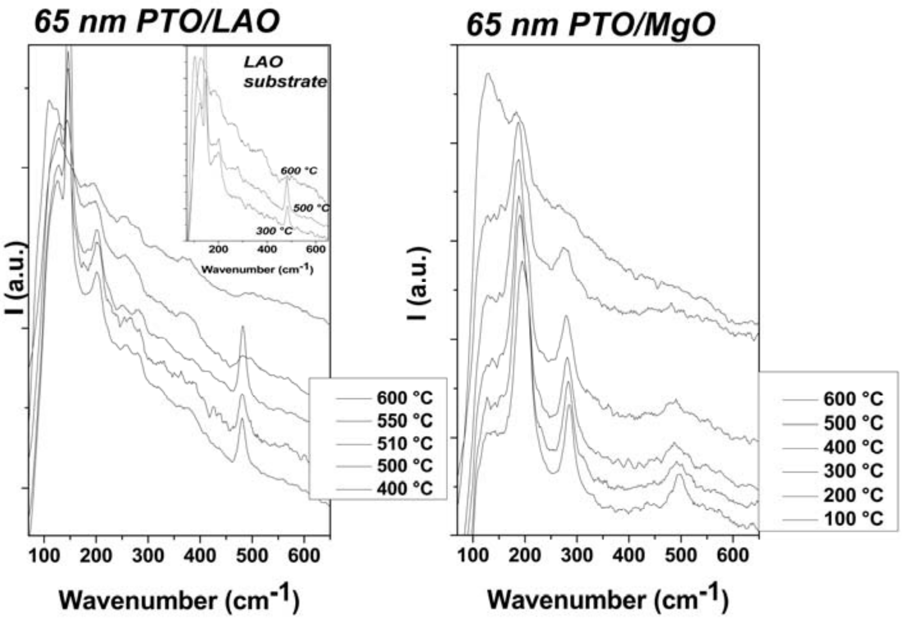

Figure 6-20: Temperature evolution of VH polarized spectra recorded on the surface of 65 nm thick PTO/LAO and PTO/MgO films. The VH polarized spectra of LAO substrate is given in the inset.

In conclusion, we have observed transformations from the *c/a/c/a* polydomain state to the *c*-phase and to the $a_1/a_2/a_1/a_2$ state take place in PTO/LAO and PTO/MgO films, respectively. The transformation temperature decreases with decreasing film thickness due to increased tensile/compressive stresses. No anomaly is observed in the temperature evolution of the mode wavenumbers during domain state transformations. The mode downshift is continuous and only line intensities of *a*-domains (PTO/LAO) or of *c* -domains (PTO/MgO) vanish. It is important to note that Raman investigations on the high-temperature phase transition in PTO/LAO films must be performed by using only spectra recorded on the film cross section whereas both types of spectra (film surface and film cross section) can be used in PTO/MgO films.

Structural phase transitions

A further investigation of phase transitions in epitaxial films will be based on the analysis of Raman spectra recorded on the film cross section, where Raman modes related to *a*- and *c*-domains are allowed by Raman selection rules. In this section we will discuss anomalies observed in the temperature evolution of the mode wavenumbers which are not related to transformations between domain states. As expected from XRD results, the structural phase transition in 460 nm thick PTO films on LAO and MgO substrates should be similar to that in bulk PTO while the 65 nm films should behave differently. In order to present the influence of film thickness on phonon high-temperature behaviour, the PTO films of different thicknesses will be discussed in the following order: 460 nm, 250 nm and 65 nm on LAO and MgO substrates.

The temperature evolution of *VV* and *VH* polarized spectra in 460 nm thick PTO/ MgO and PTO/ LAO films is presented in Figure 6‑16. A similar temperature-dependent spectral signature is observed in PTO films on LAO and MgO. The *E(TO)* and $A_1(TO)$ modes shift continuously to lower wavenumbers and line widths increase with increasing temperature up to 490 °C. An abrupt change in *VV* and *VH* polarized spectra is observed at 500 °C which suggests a first order phase transition. The high-temperature phase spectra are similar to those observed for bulk PTO (Figure 6‑9). A further increase of temperature up to 600 °C results in an increase of the line broadening. Furthermore, the temperature evolution of the mode wavenumbers is alike in the 460 nm films on MgO and LAO substrates and in the PTO powder (Figure 6‑21). Therefore, this change can be identified as a tetragonal-to-disordered cubic phase transition, which corresponds also to the ferroelectric-to-paraelectric phase transition.

The temperature evolution of *VH* polarized spectra of 250 nm thick PTO/LAO and PTO/MgO films is shown in Figure 6‑19. The spectra are similar to those observed in 460 nm thick PTO films on LAO and MgO substrates (Figure 6‑19 and Figure 6‑16). The temperature evolution of the mode wavenumbers in both film thicknesses is also quite similar, as shown in Figure 6‑21. The first order phase transition takes place at 500 °C and at 510 °C in PTO/LAO and PTO/MgO films, respectively. However, the profile of the high-temperature mode is less broadened than those in 460 nm thick PTO/ LAO and PTO/MgO films or in a PTO powder. This suggests a smaller disorder in dipole orientations or an increase in the ferroelectric cluster size (ferroelectric correlation) in the 250 nm PTO films on LAO and MgO.

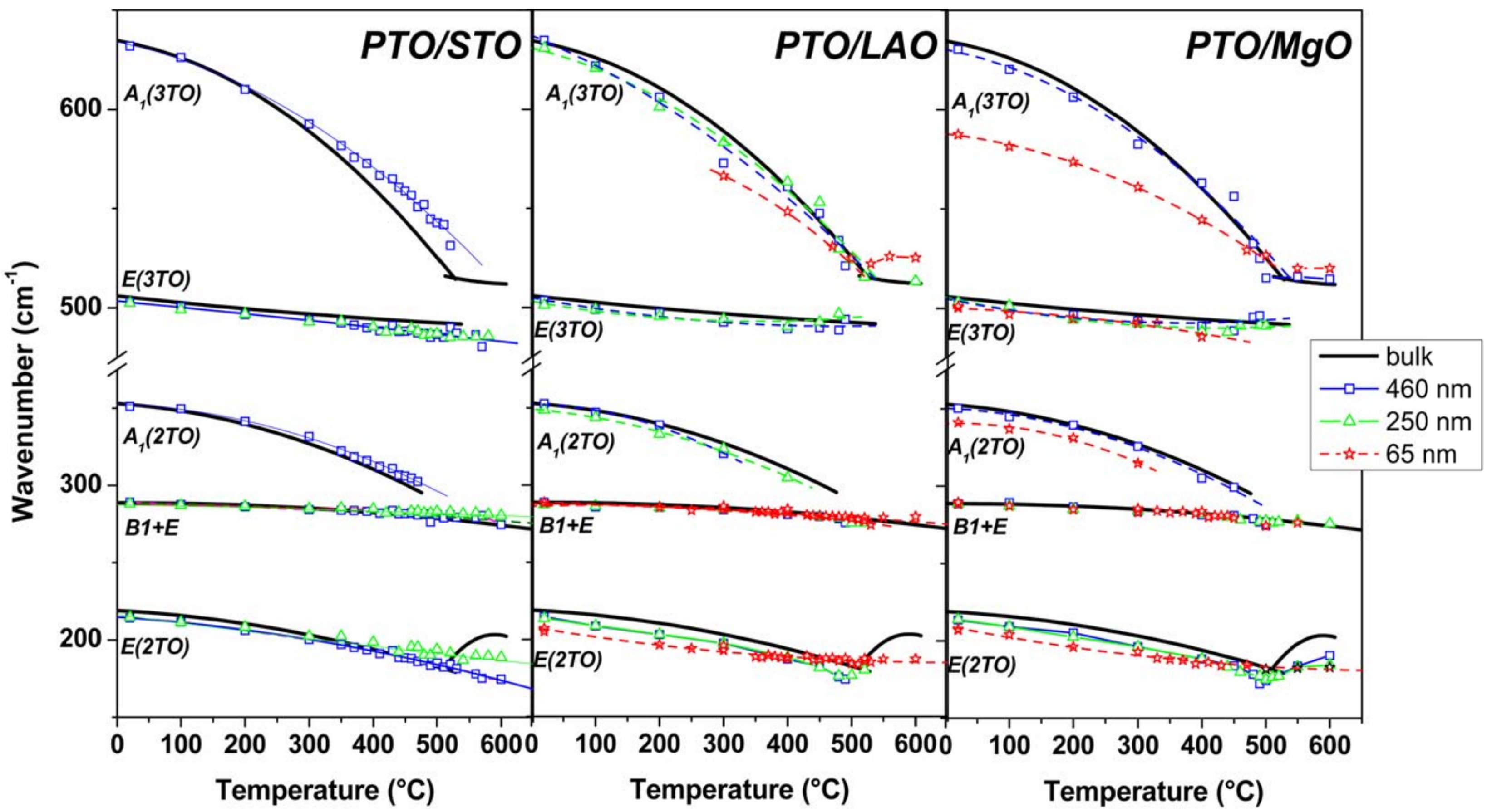

Figure 6-21: Temperature evolution of A_1(TO) and E(TO) mode wavenumbers in 460nm, 250 nm and 65 nm thick PTO films on STO, LAO and MgO substrates. Black lines refer to the PTO reference powder.

It is important to note that above T_c, the PTO Raman signature is still dependent on the used configuration of polarization: *VV* and *VH* polarized spectra are different (Figure 6‑16) which we can understand by considering that the local structure of PTO remains tetragonal.

The temperature evolution of *VV* and *VH* polarized spectra in 65 nm thick PTO/LAO and PTO/MgO films is reported in Figure 6‑22. It is significantly different from that in 250 and 460 nm thick PTO films on LAO and MgO substrates:

All the downshift, line width increase and intensity decrease with temperature are smaller than in thicker films;

At temperatures higher than 430 °C, the *E(2TO)* mode does no more shift significantly;

The *E(TO)* mode profiles remain well-defined in the whole temperature range (20-600°C) which indicates a limited disorder.

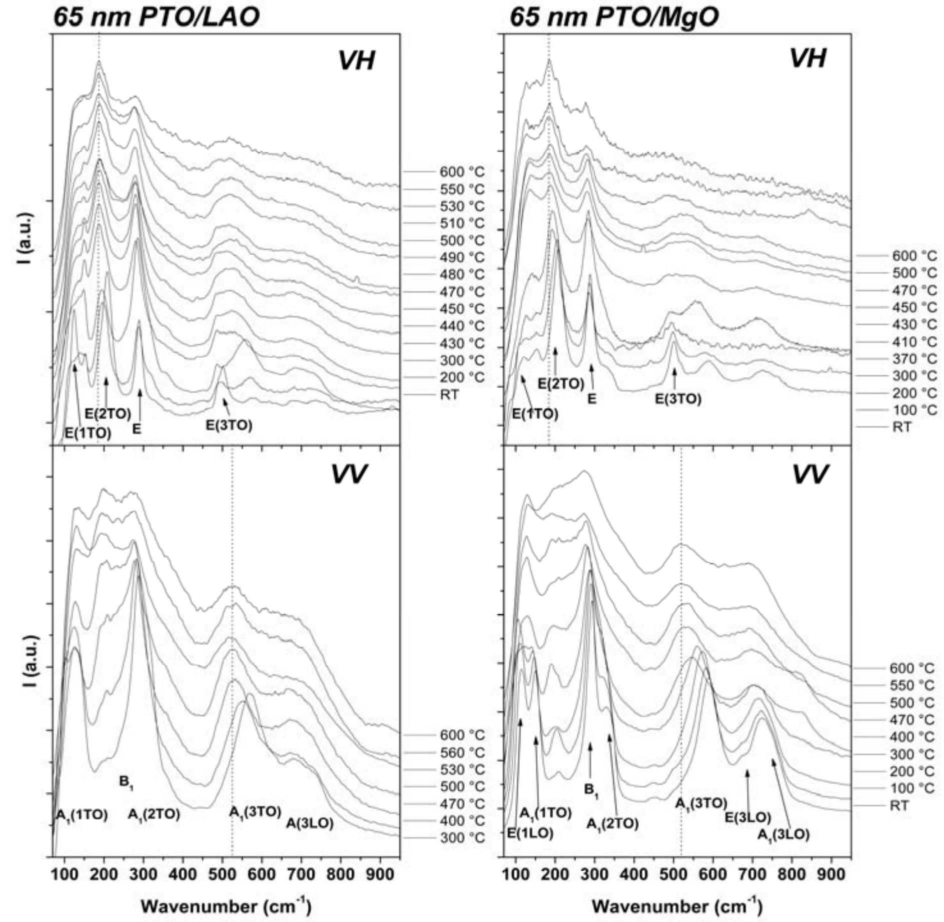

Figure 6-22: Temperature evolution of VV and VH polarized spectra in 65 nm thick PTO/LAO and PTO/MgO films . Spectra were recorded on film cross section. The dotted lines correspond to E(2TO) and A_1(3TO) positions at 600 °C in VH and VV polarized spectra, respectively.

The temperature evolution of the mode wavenumbers is presented in Figure 6‑21. One can see that the decrease in wavenumber of the *E(2TO)* mode in 65 nm films is rather continuous in the whole temperature range just as in PTO/STO films (Figure 6‑-21) unlike PTO powder and thicker films on LAO and MgO for which an anomaly is observed in the curves at 520, 500 and 510°C, respectively. The downshift of the A_1 *(3TO)* mode is lower in the 65 nm film than in the thicker films but above ~ 500 °C this mode wavenumber remains constant like in thicker PTO/MgO and PTO/LAO films. This indicates that a structural rearrangement occurs at this temperature. The modes are less broadened above 500 °C in the 65 nm films than in thicker films which indicates that the structure is more ordered compared to the 250 and 460 nm PTO/LAO and PTO/MgO films. The 65 nm PTO/LAO and PTO/MgO films are likely to be an intermediate case between the substrate-dependent PTO/STO films and the almost “free” from substrate influence 250 and 460 nm thick PTO/LAO and PTO/MgO films. However, Raman spectroscopy results do not allow to judge if the films are macroscopically paraelectric above 500 °C. Moreover, spectra of the high-temperature phase also follow Raman selection rules as in thick films and the Raman signature of 65 nm films is considerably different in *VV* and *VH* polarized spectra (Figure 6‑22) due to local tetragonality.

The fact that *E(TO)* and A_1*(TO)* are two distinct modes is a direct indication of tetragonality. The merger of these modes in the high-temperature phase indicates that local tetragonality is identical in the PTO powder, polycrystalline PTO/SAPH and partially/ completely relaxed PTO/LAO and PTO/MgO films.

Discussion

To summarize our results on phase transitions in PTO powder, polycrystalline and epitaxial films, we propose an hypothetical model for phase transitions developed in PTO films. It is presented in Figure 6‑23. Bulk PTO passes from a tetragonal to a disordered cubic structure at 520 °C. This high-temperature phase has a local tetragonal structure and Ti atoms displacements along the three possible directions (6 sites) have equal probabilities; this results in an average cubic structure. Moreover, very small ferroelectric clusters (below the diffraction limit) may exist. The polarization of clusters is macroscopically disordered, resulting in the paraelectric phase. The high-temperature behaviour of the polycrystalline film is similar to that of bulk PTO except the phase transition temperature T_c which is slightly lower due to tensile thermal stresses.

The phase transition in epitaxial films is considerably different from that in a PTO powder or polycrystalline films. The orientation of completely and partially relaxed films is governed by the substrate. Thus, transformations from the *c/a/c/a* polydomain state to the *c*-phase and the $a_1/a_2/a_1/a_2$ state are observed whatever the thickness of films on compressive and tensile substrates, respectively. XRD and Raman spectroscopy results have shown that the temperature at which domain transformations take place decreases with decreasing film thickness.

In the case of completely relaxed films such as the 250 and 460 nm thick PTO/LAO and PTO/MgO films, the high-temperature phase transition is quite similar to that observed in PTO powder and polycrystalline films. Above T_c, the Raman line widths of 460 nm thick films are significantly broadened which indicates disorder and that any size of ferroelectric clusters has to be very small and comparable as in the high-temperature phase of bulk PTO. In the case of 250 nm thick films, the mode widths are slightly decreased compared to those of 460 nm films, indicating the increase of ferroelectric correlation. However, the epitaxial relation with substrate prevents the film to be completely disordered. This favours an elastic distortion and thus a Ti displacements along the normal to the substrate plane or along both directions in the substrate plane in PTO films on LAO and MgO substrates, respectively.

In the partially relaxed films as in the 65 nm thick PTO/LAO and PTO/MgO films, the temperature evolution of the film orientation and structure is highly substrate-dependent and some structural rearrangement takes place at 500 °C. The high-temperature phase is highly *c*- and *a*-axis oriented in PTO/LAO and PTO/MgO substrates, respectively. Raman line widths are less broadened which indicates an increase of the cluster size as compared with the relaxed films. The possibility of Ti atom displacement is higher along one or two directions in films on compressive and tensile substrates, respectively. The tetragonality of the average structure should be increased in comparison with that in completely relaxed films. However, we cannot judge if this phase is macroscopically ferroelectric or not.

It is important to note that local tetragonality is the same in PTO powder, polycrystalline and partially/completely relaxed epitaxial films, as the $A_1(TO)$ and $E(TO)$ modes merge at ~ 500 °C. However, the tetragonal cell orientations are highly limited by the substrate in epitaxial thin films. Thus, the possibilities of Ti displacement in some directions are reduced, resulting in slightly tetragonal average structure. It is possible that this tetragonality is no more coupled to the primary order parameter (polarization) as it was observed in other perovskite films (9; 13). Therefore, partially/completely relaxed films may be/are paraelectric in the high-temperature phase.

Finally, in strained coherent epitaxial films (PTO/STO), no phase transition is observed in the temperature range from RT to 600 °C. The average structure is identical to the local tetragonal structure. The Ti displacements are possible only along one direction. Moreover, the ferroelectric correlation should be large, even at high temperature, resulting in the ferroelectric phase. However, even though the Raman signature is similar at low and high-temperature, strictly speaking, our Raman data does not allow to confirm this hypothetical model. This needs precise measurements of the in-plane and out-of-plane lattice parameters as well as electrical characterizations at high-temperatures.

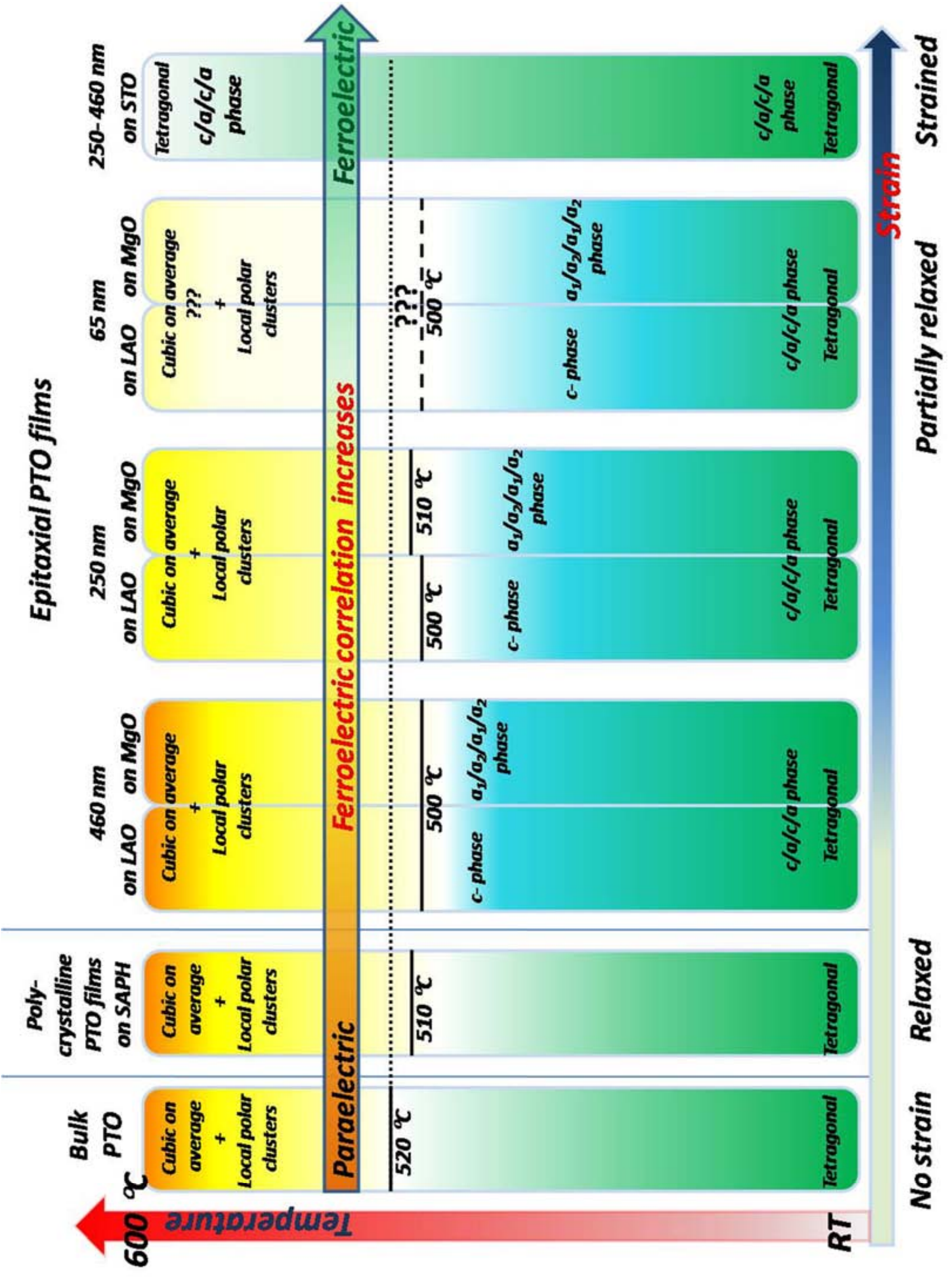
Bulk PTO
Poly-crystalline PTO films on SAPH
Epitaxial PTO films
460 nm
on LAO
on MgO
250 nm
on LAO
on MgO
65 nm
on LAO
on MgO
250–460 nm
on STO
600 °C
Temperature
RT
Cubic on average + Local polar clusters
Cubic on average ??? + Local polar clusters
Tetragonal
c/a/c/a phase
Paraelectric
Ferroelectric correlation increases
Ferroelectric
520 °C
510 °C
500 °C
510 °C
500 °C
500 °C
???
c- phase
a1/a2/a1/a2 phase
c/a/c/a phase
Tetragonal
Strain
No strain
Relaxed
Partially relaxed
Strained

Figure 6-23: Summarized results on phase transitions in PTO powder, polycrystalline and epitaxial films.

Bibliography

1. **G. Shirane and S. Hoshino.** 4, s.l. : J. Phys. Soc. Jap., 1951, Vol. 6, p. 265.

2. **S.A. Mabud and A.M. Glazer.** s.l. : J. Appl. Cryst., 1979, Vol. 12, p. 49.

3. **G. Burns and B.A. Scott.** 3, s.l. : Phys. Rev. Lett., 1970, Vol. 25, p. 167.

4. **M.D. Fontana, H. Idrissi, G.E. Kugel, and K. Wojcik.** s.l. : J. Phys.: Condens. Matter, 1991, Vol. 3, p. 8695.

5. **M.D. Fontana, H. Idrissi, G.E. Kugel, and K. Wojcik.** s.l. : Ferroelectrics, 1988, Vol. 80, p. 117.

6. **Y. Yacoby, Y. Girshberg and E.A. Stern.** s.l. : Z. Phys. B, 1997, Vol. 104, p. 725.

7. **N. Sicron, B. Ravel, Y. Yacoby, E.A. Stern, F. Dogan, and J.J. Rehr.** 18, s.l. : Phys. Rev. B, 1994, Vol. 50, p. 13168.

8. **R.J. Nelmes and W.F. Kuhs.** s.l. : Solid State Commun., 1985, Vol. 54, p. 721.

9. **F. He, B.O. Wells, Z.-G. Ban, S.P. Alpay, S. Grenier, S.M. Shapiro, W. Si, A. Clark, and X.X. Xi.** s.l. : Phys. Rev. B, 2004, Vol. 70, p. 235405.

10. **F. He and B.O. Wells.** s.l. : Appl. Phys. Lett, 2006, Vol. 88, p. 152908.

11. **K.J. Choi, M. Biegalski, Y.L. Li, A. Sharan, J. Shubert, R. Uecker, P. Reiche, Y.B. Chen, X.Q. Pan, V. Gopalan, L.-Q. Chen, D.G. Schlom, C.B. Eom.** s.l. : Science, 2004, Vol. 306, p. 1005.

12. **P.-E. Janolin, F. Le Marrec, J. Chevreul, and B. Dkhil.** s.l. : Appl. Phys. Lett, 2007, Vol. 90, p. 192910.

13. **P.-E. Janolin, B. Fraisse, F. Le Marrec, and B. Dkhil.** s.l. : Appl. Phys. Lett., 2007, Vol. 90, p. 212904.

14. **Yu. I. Yuzyuk, P. Simon, I.N. Zakharchenko, V.A. Alyoshin, and E.V. Sviridov.** s.l. : Phys. Rev. B, 2002, Vol. 66, p. 052103.

15. **V.G. Koukhar, N.A.Pertsev, and R. Waser.** s.l. : Phys. Rev. B, 2001, Vol. 64, p. 214103.

16. **N. Pertsev, V. Khukar, H. Kohlstedt, and R. Waser.** s.l. : Phys. Rev. B, 2003, Vol. 67, p. 054107.

17. **N. Pertsev, A. Zembilgotov, and A. Tagantsev.** s.l. : Phys. Rev. Lett, 1998, Vol. 80, p. 1988.

18. **Y.L. Li, S.Y. Hu, Z.K.Liu, L.Q. Chen.** s.l. : Appl. Phys. Lett., 2001, Vol. 78, p. 3878.

19. **Y.L. Li, S.Y. Hu, Z.K. Liu, L.Q. Chen.** s.l. : Acta Mater., 2002, Vol. 50, p. 395.

20. **L.Q. Chen.** s.l. : Annu. Rev. Mater. Res., 2002, Vol. 32, p. 113.

21. **J.H. Haeni, P. Irvin, W. Chang, R. Uecker, P. Reiche, Y.L. Li, S. Choudhury, W. Tian, M.E. Hawley, B. Craigo, A. K. Tagantsev, X.Q. Pan, S.K. Streiffer, L.Q. Chen, S.W. Kirchoefer, J. Levy, D.G. Schlom.** s.l. : Nature, 2004, Vol. 430, p. 758.

22. **D.D. Fong, A.M. Kolpak, J.A. Eastman, S.K. Streiffer, P.H. Fuoss, G.B. Stephenson, C. Thompson, D.M. Kim, K.J. Choi, C.B. Eorn, I. Grinberg, and A.M. Rappe.** s.l. : Phys. Rev. Lett., 2006, Vol. 96, p. 127601.

23. **J.S. Speck and W. Pompe.** s.l. : J. Appl. Phys., 1994, Vol. 76, p. 466.

24. **L.S.-J. Peng, X.X. Xi, B.H. Moeckly, and S.P. Alpay.** 22, s.l. : Appl. Phys. Lett., 2003, Vol. 83, p. 4592.

25. **P.-E. Janolin, F. Le Marrec, E. Ringgaard, B. Fraisse, and B. Dkhil.** s.l. : Appl. Phys. Lett., 2007, Vol. 90, p. 162906.

26. **K. Lee and S. Baik.** 81, s.l. : Annu. Rev. Mater. Res., 2006, Vol. 36, p. 81.

27. **S.P. Alpay, A.S. Prakash, S. Aggarwal, P. Shuk, M. Greenblatt, R. Ramesh, and A.L. Roytburd.** 10, s.l. : Scripta Materialia, 1998, Vol. 39, p. 1435.

28. **M. Y. El-Naggar, D.A. Boyd, D.G. Goodwin.** 11, s.l. : J. Mater. Res., 2005, Vol. 20, p. 2969.

29. **Y.-F. Chen, T. Yu, J.-X.Chen, L. Shun, P.Li, and N.-B. Ming.** 2, s.l. : Appl. Phys. Lett., 1995, Vol. 66, p. 148.

30. **R.S. Batzer, B.M. Yen, D. Liu, H. Chen, H. Kubo, G.R. Bai.** 11, s.l. : J. Appl. Phys., 1996, Vol. 80, p. 6235.

31. **B.M. Yen and H. Chen.** 2, s.l. : J. Appl. Phys., 1999, Vol. 85, p. 853.

32. **P.S. Dobal and R.S. Katiyar.** s.l. : J. Raman Spectrosc., 2002, Vol. 33, p. 405.

33. **D.S. Fu, H. Suzuki, and K. Ishikawa.** s.l. : Ferroelectrics, 2001, Vol. 259, p. 79.

34. **D.S. Fu, H. Iwazaki, H. Suzuki, and K. Ishikawa.** s.l. : J. Phys.: Condens. Matter, 2000, Vol. 12, p. 399.

35. **P.S. Dobal, S. Bhaskar, S.B. Majumder, and R.S. Katiyar.** s.l. : J. Appl. Phys., 1999, Vol. 86, p. 828.

36. **I. Taguchi, A. Pignolet, L. Wang, M. Proctor, F. Levy, and P.E. Schmid.** s.l. : J. Appl. Phys., 1993, Vol. 73, p. 394.

37. **Yu. I. Yuzyuk, R. Farhi, V.L. Lorman, L.M. Rabkin, L.A. Sapozhnikov, E.V. Svidorov, and I.N. Zakharchenko.** 1, s.l. : J. Appl. Phys., 1998, Vol. 84, p. 452.

38. **S. Srinivas, S. Bhaskar and R.S. Katiyar.** s.l. : Ferroelectrics, 1999, Vol. 232, p. 141.

39. **E.V. Sviridov, I.N. Zakharchenko, V.A. Alyoshin, L.A. Sapozhnikov, Yu. I. Yuzyuk, R. Farhi, V.L. Lorman.** s.l. : Ferroelectrics, 1999, Vol. 235, p. 131.

40. **R.S. Batzer, B.M. Yen, D. Liu, H. Chen, H. Kubo, and G.R. Bai.** 11, s.l. : J. Appl. Phys., 1996, Vol. 80, p. 6325.

41. **http://www.crystec.de/daten/al2o3.pdf.**

42. **F. Le Marrec, R. Farhi, B. Dkhil, J. Chevreul, M.G. Karkut.** s.l. : J. Eur. Ceram. Soc., 2001, Vol. 21, p. 1615.

43. **P. Paruch and J.M. Triscone.** s.l. : Appl. Phys. Lett., 2006, Vol. 88, p. 162907.

44. **E.K.H Salje and U. Bismayer.** s.l. : Phase transitions, 1997, Vol. 63, p. 1.

45. **E.K.H. Salje and Y. Yogal.** 10, s.l. : J. Phys. Chem. Solids, 1996, Vol. 57, p. 1413.

46. **U. Bismayer.** s.l. : Phase transitions, 1990, Vol. 27, p. 211.

47. *Etude par spectroscopie Raman des transitions structurales de PbTiO3.* **E.H. Idrissi raport DEA.** s.l. : Universite de Metz, 1986.

48. **Ph. Pruzan, D. Gourdain and J.C. Chervin.** 10-12, s.l. : Phase transitions, 2007, Vol. 80, p. 1103.

49. **C.H. Perry and D.B. Hall** s.l. : Phys. Rev. Lett., 1965, Vol. 15, p. 700.

Chapter 7:

Origin of residual stress

Chapter 7

7 Origin of residual stress 163

7.1 Misfit strain 166

7.2 Thermal stresses 168

7.3 Phase transformation stress 168

7.4 Stresses and a-domain fraction 169

Conclusions 170

Bibliography 170

7. Origin of residual stress

We have already discussed in section 1.5 that PTO films are submitted to substantial stresses during growth and subsequent cooling process from deposition temperature to RT. At the growth temperature, stresses are mainly misfit and intrinsic stresses. Usually, the intrinsic stresses are negligible in films deposited by MOCVD. During the cooling process, additional stresses may develop in the film either due to thermal stresses or to stresses related to the phase transformation. Heterogeneous stresses may also appear in the films due to defects such as dislocations, grain boundaries and vacancies. As shown in section 4.7, heterogeneous stresses are observed in the 125 and 460 nm thick PTO films on LAO and MgO, where the defect concentration is relatively high. However, the film volume fraction which contains heterogeneous strains seems to be much smaller than the volume fraction with homogeneous strains. Therefore, we assume that heterogeneous strain resulted from intrinsic stresses and relaxation process are negligible and do not influence residual stress values. The residual stress measured at RT is the sum of all stresses developed during the complex process of film preparation.

Both XRD and Raman techniques reveal that 30 – 460 nm PTO films are under tensile stress in the film plane whatever the tensile or compressive misfit stress (Figure 7-1b). The residual stress is strongly thickness-dependent. In the case of PTO/LAO and PTO/MgO films the thinner films are more stressed and residual stress is partially relaxed with increasing film thickness. The residual stress evolution in PTO/STO films is quite unexpected: tensile residual stress slightly increases with increasing thickness from 125 to 460 nm. Indeed, XRD and TEM analyses have shown (section 4.3 and 4.4) that twin and dislocation density increase with increasing film thickness in PTO films on STO, LAO and MgO substrates, which gives evidence of film relaxation during the thickness increase.

In the following, we will address the open questions related to the origin of residual stress and its thickness evolution in PTO/STO films. We will specifically discuss the contribution of misfit, thermal and transformation stress to the residual stress estimated at RT. Furthermore, residual stress and *a*-domain fraction will be considered.

7.1 Misfit strain

Calculations of misfit stress in PTO films on STO, LAO and MgO substrates at the deposition temperature lead to the following values: -1.8 GPa (compressive), -7 GPa (compressive) and +10.8 GPa (tensile), respectively. Of course, such high stress values are not observed in the films as misfit stresses are relaxed by the formation of misfit dislocations during the film deposition. The critical thickness for dislocation generation is a good indicator of the capacity of the film to relax stresses. It is 7.1 nm, 1.1 nm and 0.4 nm in PTO films deposited at 650 °C on STO, LAO and MgO substrates, respectively (1). However, the thickness for complete relaxation of films is much higher than that for dislocation generation. XRD and Raman spectroscopy results indicate that misfit stresses relax quickly with increasing thickness in PTO/LAO and PTO/MgO films and should be almost completely relaxed in 250 and 460 nm thick films (2). The film/ substrate interface is coherent in PTO/STO films, i.e. the alignment of atomic rows across the interface is perfect, as the mismatch is rather small. Thus, the relaxation is slow in these films, and even the 460 nm film is only partially relaxed. The thickness evolution of misfit stresses in the three PTO/substrate systems given in Figure 7-1a

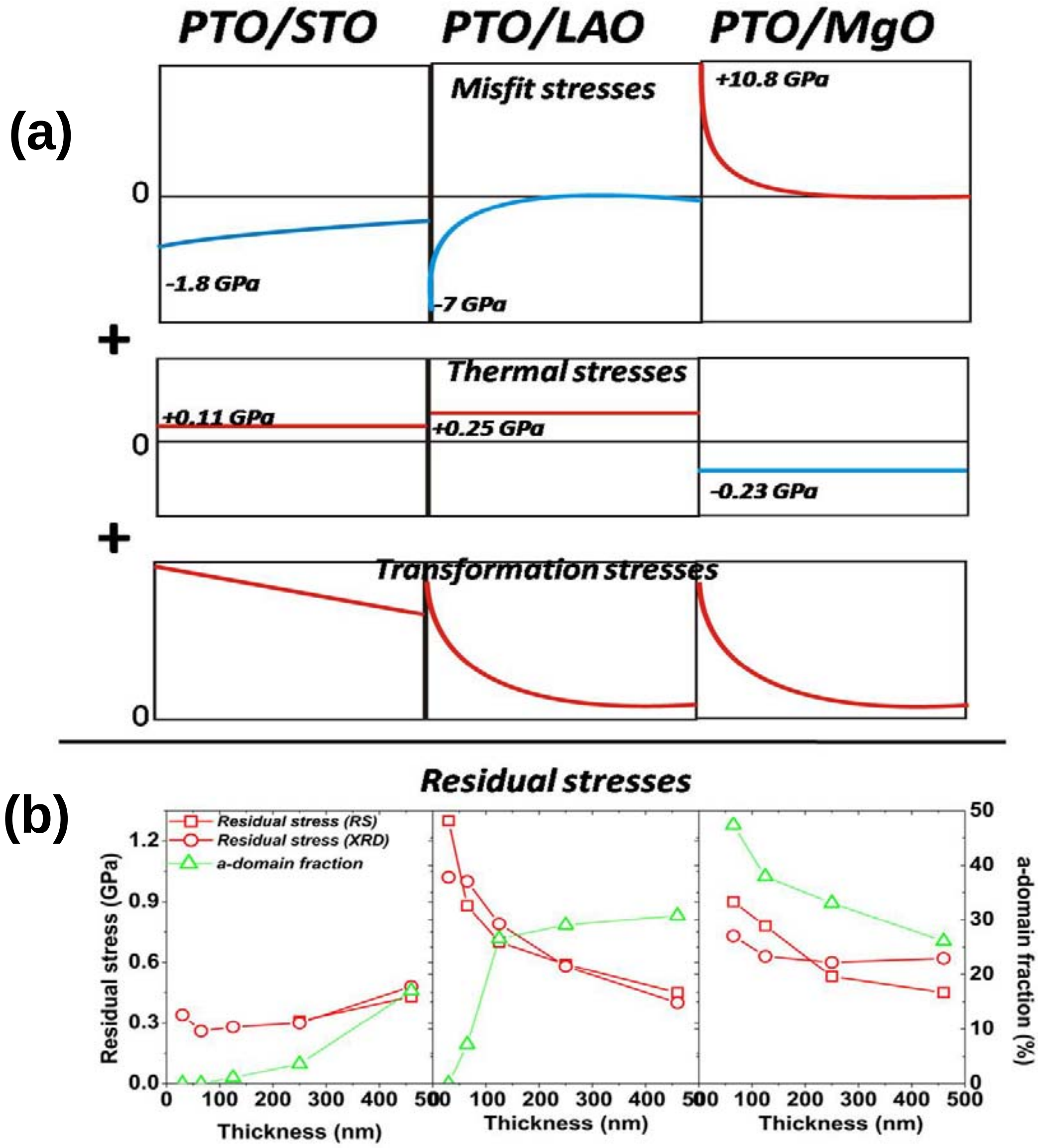

Figure 7-1: Diagram showing misfit, thermal and transformation stress evolution in PTO films on STO, LAO and MgO substrates as a function of film thickness (a). The figure presents only trends of the evolution with thickness, absolute values do not correspond to real ones. The misfit, thermal stresses are given only for c-domains. Film thickness evolution of residual stress, in c-domains and a-domain fraction in PTO films on LAO, STO and MgO substrates (b). Residual stress values have been evaluated from Raman spectroscopy results (RS) and XRD data, a-domain fraction from XRD data.

shows a strong disagreement with the evolution of residual stresses at RT, especially in films on substrates inducing compressive misfit stresses. This indicates that films are submitted to quite high additional stresses.

7.2 Thermal stresses

Thermal stresses are not thickness-dependent and are usually rather small in PTO films on perovskite substrates. Thermal stresses developed in our PTO films during the cooling down (from T_{Dep} = 650 °C down to RT) are evaluated to 0.11 GPa, 0.25 GPa and -0.23 GPa on STO, LAO and MgO substrates, respectively (Figure 7-1a). However, these small values cannot explain themselves tensile residual stresses as high as 0.4 to 1.2 GPa in PTO films on LAO and STO substrates. Moreover, both misfit and thermal stresses are more or less relaxed in the films. Therefore, the thermal stress contribution to residual stress should be smaller than values given above.

7.3 Phase transformation stress

As discussed above and especially in the thinnest films on substrates inducing compressive misfit stress, residual stress values cannot be explained if the stress related to the phase transition is neglected or to be completely relaxed. *In-situ* curvature measurements indicated that stresses are not completely relaxed during phase transition as it was expected (3, 4). As it was observed by high-temperature XRD and Raman spectroscopy, the nature of the phase transitions which take place in epitaxial PTO films depends on the film thickness and on the substrate nature. In order to illustrate the effect of thickness and mismatch on the transformation stress, we have plotted the deviation in wavenumbers of the *E(2TO)* mode position measured in PTO films, 65 to 460 nm of thickness, from its position in bulk PTO (Figure 7-2), which is linearly proportional to residual stress values.

One can see that an anomalous phonon behavior is observed in strained/partially relaxed films (250-460 nm PTO/STO and 65 nm PTO films on MgO and LAO substrates) in comparison with bulk PTO, especially at temperatures higher than 300°C. As shown by high-temperature XRD analysis, the thermal expansion in these films is governed by the substrates, i.e. the cell volume cannot expand freely. This creates an additional stress as temperature gets closer to the bulk PTO phase transition temperature. As seen in Figure 7-2, the film is reminiscent of its phase transition (the order parameter is still temperature-dependent) at temperatures a few hundred degrees lower than T_c. Thus, this stress cannot be neglected even in films deposited below bulk PTO phase transition temperature.

Completely relaxed films (250 and 460 nm PTO/LAO and PTO/MgO films) do not present this anomalous phonon behaviour up to T_c. However, above T_c, the phonon be-

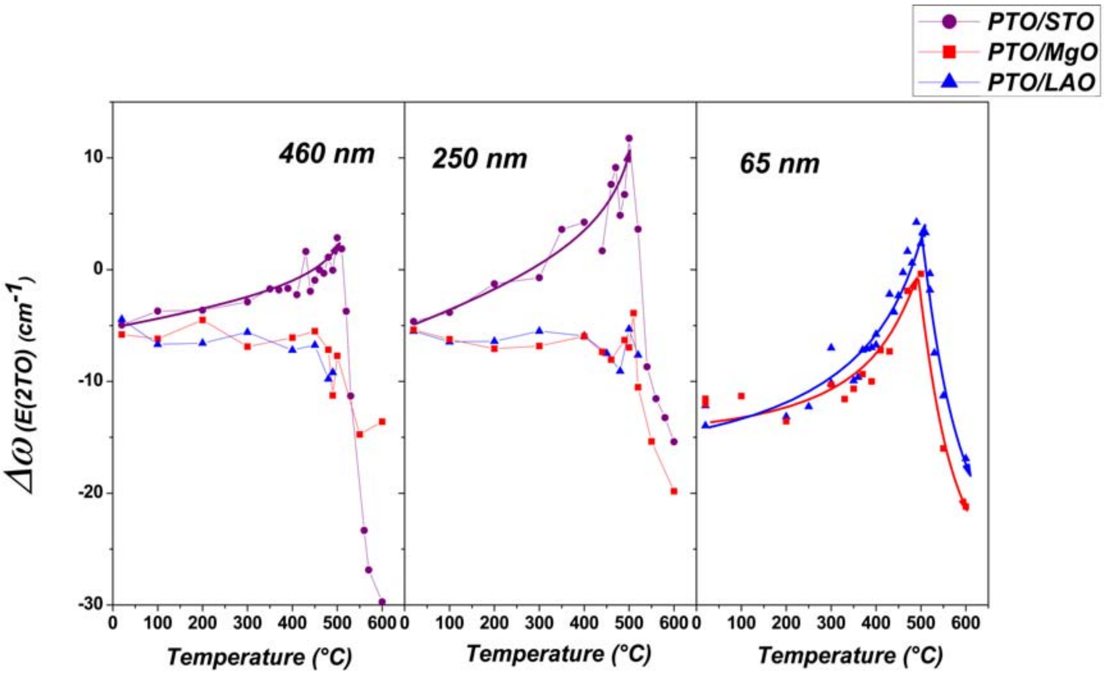

Figure 7-2: : Temperature evolution of the deviation in wavenumbers Δω of the E(2TO) mode position in PTO films on STO, LAO and MgO from its position in bulk PTO. 460 nm, 250 nm and 65 nm thick films are considered.

haviour is similar in completely and partially relaxed films: the *E(2TO)* mode downshift is slower in the films than in bulk PTO. This maybe understood as follows: in the high temperature phase, the epitaxy with substrate does not allow the creation of a disorder as in bulk PTO. Therefore, transformation stresses induced by the phase transition cannot be neglected even in relaxed films. These observations show the importance of transformation stresses in epitaxial films and especially in partially relaxed films, where the thermal expansion is governed by the substrate.

The film thickness dependence of the transformation stress evolution in PTO/LAO films is given in Figure 7-1a. It is consistent with the evolution of residual stress, indicating that residual stress mainly results from transformation stress in these films. Misfit stresses should be completely relaxed in 250 and 460 nm thick PTO/MgO films, thus the tensile stress of ~ 0.6 GPa mainly comes from the transformation stress. PTO/STO films, 30-460 nm of thickness, are submitted to both misfit and transformation stresses. Tensile residual stress indicates that the transformation stress is higher than the misfit stress. Furthermore, the misfit stress relaxes more quickly with increasing film thickness than the transformation stress. As a consequence, the tensile residual stress increases with increasing film thickness.

7.4 Stresses and *a*-domain fraction

One of the main stress relaxation mechanisms in PTO (and other ferroelectrics) thin films is twinning. As seen in Fig. 7-1b, the *a*-domain fraction increases with increasing film thickness in PTO films on substrates inducing compressive misfit stress, and it decreases on tensile substrates as MgO. Furthermore, the thickness-dependence of the *a*-

domain fraction is consistent with that of misfit stress (Figure 7-1a). Compressive misfit stresses prevent the formation of *a*-domains but during their relaxation, misfit dislocations are created at the interface and serve as nucleation sites for *a*-domains. Therefore, the relaxation of compressive misfit stress results in an increase of the *a*-domain fraction. Tensile thermal stresses can also contribute to the formation of *a*-domains, especially in thick films where compressive misfit stresses are almost relaxed.

The formation of *a*-domains is highly favored by tensile stress in the plane. As a consequence, the relaxation of tensile misfit stresses allows the increase of the *c*-domain fraction which is also favored by compressive thermal stresses.

During film cooling from T_{Dep}, twinning may occur through the formation of *a*- and *c*-domains in *c*- and $a_1/a_2/a_1/a_2$ domain states. Thus, transformation stress relaxation results in the increase of *a*- and *c*-domain fraction in films on substrates inducing compressive (STO, LAO) and tensile (MgO) misfit stresses. The transformation strain was systematically varied by a change in Zr concentration (x) in $PbZr_xTi_{1-x}O_3$ films, which induced corresponding tetragonality change (1). It was observed that the *a*-domain fraction decreases with decreasing the transformation strain.

Conclusions

To summarize the discussion about the origin of the tensile residual stress in PTO films, we can say that different types of stresses contribute to the residual stress. They are not only related to the mismatch between the film and the substrate but also to the difference in film and substrate thermal expansion coefficients and to the phase transition itself. The contribution of transformation stresses to the residual stress is dominant while that of misfit stresses is significant at low thicknesses and that of thermal stresses is small. Concerning the *a*-domain fraction, it depends on misfit, thermal and transformation stresses.

Bibliography

1. **K. Lee and S. Baik.** 81, s.l. : Annu. Rev. Mater. Res., 2006, Vol. 36, p. 81.

2. **L.S.-J. Peng, X.X. Xi, B.H. Moeckly, and S.P. Alpay.** 22, s.l. : Appl. Phys. Lett., 2003, Vol. 83, p. 4592.

3. **D.A. Boyd, M.Y. El-Naggar, D.G. Goodwin.** s.l. : Int. Ferroelectrics, 2006, Vol. 83, p. 155.

4. **D.A. Boyd, M.Y. El-Naggar, D.G. Goodwin.** s.l. : Int. Ferroelectrics, 2005, Vol. 71, p. 21.

General conclusions and perspectives

General conclusions and perspectives

This work has been done in the context of a collaboration between LMGP/CNRS-INPG (France) and Faculty of Chemistry at Vilnius University (Lithuania). The elaboration and characterization of perovskite films are the main research topics in both laboratories. The aim of this collaboration is to improve our understanding of the intrinsic properties underlying the electronic and magnetic functions of relaxor ferroelectric oxides, traditional ferroelectrics, multiferroics, giant magnetoresistant manganites, and nickelates. The physical properties of films are strongly influenced by their conditions of growth, their structure, and by the stresses and consequences of final size. This thesis has focused on the residual stress estimation methods and the stress origin and their effects on the nature of the phase transitions in ferroelectrics $PbTiO_3$ thin films.

General conclusions

In this study, Raman spectroscopy, XRD and TEM were used to investigate the origin of residual stress and stress effects on phase transitions in PTO epitaxial films deposited by MOCVD. In order to vary the stress level in the films a series of epitaxial PTO films with different thicknesses was elaborated on different substrates which induce either a compressive (STO and LAO) or a tensile (MgO) misfit stress.

Our Raman analysis of a stress-free polydomain $PbTiO_3$ single crystal and dark field Raman spectroscopy revealed that phonon mode profiles can be significantly modified by the existence of oblique modes in *VV* polarized and depolarized Raman spectra. We note that oblique modes exist in all ferroelectrics but surprisingly, they are almost never taken into account in the current literature for the analysis of Raman scattering in ferroelectric films reported in literature. Moreover, most works on residual stress in these films are based on Raman modes coming from depolarized spectra. On the other hand, our result illustrates that the use of a *VH* configuration of polarization and the consideration of oblique modes are essential to obtain spectra allowing an accurate estimation of residual stress values.

In the literature the residual stress in PTO films is mainly analyzed by considering the shift of the *E(1TO)* soft mode. We argue in our work that this choice is questionable because of the anharmonic nature of the soft mode and because the existing data cannot be extrapolated for the case of tensile strain. Other papers report on residual stress values determined from *E(LO)* or *A(3TO)* modes, which are highly modified by oblique modes. Moreover, residual stress values could not be estimated from Raman modes for polycrystalline PTO films. As a consequence we propose and apply an alternative analysis based on the behaviour of the *E(3TO)* mode which is a hard mode and possibly the unique reliable mode for such a determination. Residual stress values obtained from the *E(3TO)* mode are consistent with those calculated from lattice parameters issued from XRD data.

We note that hydrostatic pressure data, and specially the pressure coefficient of the *E(3TO)* mode, can be used in good approximation for the determination of residual stress in epitaxial PTO films in the case of *c*-domains because the stress is biaxial in the substrate plane and b‘(*E(3TO)) << a‘(E(3TO))* of PTO. In other cases where the stress is not biaxial (*a*-domains probably), the a‘, b‘ and c‘ deformation potential constants should be known to allow calculations of stress values from the shift of Raman modes.

Further to the choice of the right Raman mode for a meaningful analysis we argue, on the base of Raman selection rules, that Raman spectra should be collected on the film cross section to obtain information about *c*-domains which are dominant in the film. The measurements on the film surface give information about *a*-domains only.

XRD and Raman results reveal that PTO films are under tensile stress on STO, LAO and MgO substrates and that residual stress values are strongly thickness dependent. XRD and TEM analyses show that twin and dislocation density increase with increasing film thickness of PTO films, which gives evidence of film relaxation with film thickness.

The analysis of the evolution of residual stress with thickness and the analysis of film relaxation indicate that the residual stress originates from various types of stresses and not only from misfit stress as usually proposed in literature. We have shown that the dominant stress in our films is related to the phase transformation while it is usually assumed in literature that it does not exist or is completely relaxed by domain structure.

Our study illustrates that an investigation of the high-temperature behaviour, close to the phase transition, is instructive and allows to evidence and discuss the influence of the substrate on the film. It is important to note that the confusion between domain state transformations and the phase transition in epitaxial PTO films can be avoided by investigating the high temperature behaviour of both *a*- and *c*-domains using XRD and Raman spectroscopy.

As a general trend, we have observed the following tendency: The smaller the lattice-mismatch with substrate, the greater the influence of the substrate and the more stressed film. The influence of the substrate also increases with decreasing film thickness. High temperature XRD and Raman spectroscopy give evidence that residual stresses do not indicate the substrate dependence of the films, as they are the sum of all contributions of induced stresses. For example, residual stress values are lower in PTO/STO films which are more substrate dependent than PTO films on MgO and LAO substrates.

Finally, our observations show that phase transitions in epitaxial films are considerably different from that in PTO powder or polycrystalline films. Domain state transformations are observed at lower temperatures in thin epitaxial films than in thicker ones due to the stronger influence of ferroelectric correlation in the high temperature phase increases with decreasing film thickness. Furthermore, no thickness dependence of the phase transition temperature is observed in such films. A manifestation of the substrate effect is found in 250 nm PTO/STO strained films which remain ferroelectric and have a *c/a/c/a* domain structure up to 650 °C whereas theory predicts the stability of the *c/a/c/a* domain state only below the phase transition temperature in bulk PTO.

Perspectives

The high temperature XRD analysis of in-plane and out-of-plane lattice parameters in PTO films on different substrates should be completed in order to determine the average structure of the high-temperature phase in our films.

The next step to our study would be the analysis of stress effects on the electrical properties of thin films. For this purpose, PTO films should be deposited on an electrode/substrate system before proceeding to a similar study of residual stress in the different films.

It would be also interesting to investigate stress effects, using the same techniques, in other ferroelectric perovskite films in which several phase transitions take place. Thus, the relaxation of the transformation stress might be different for each phase transition due to the difference in the available thermal energy.

Résumé

Effet des contraintes et transition de phase dans des couches minces de $PbTiO_3$ obtenues par MOCVD

Résumé* ____ *177

Introduction____179

Dépôt de films de $PbTiO_3$ par PI MOCVD ____________________180

Evolution de la structure des films de $PbTiO_3$_________________182

Modes Raman et contraintes résiduelles _____________________187

Effet de température sur $PbTiO_3$ poudre et en films ___________190

Origine de contraintes résiduelles __________________________192

Conclusions générales et perspectives _______________________195

Introduction

Les oxydes de type pérovskite présentent une extraordinaire richesse de propriétés physiques et structurales. Ils sont bien connus pour leurs instabilités structurales qui peuvent être contrôlées par des paramètres extérieurs comme la température, le champ électrique, les contraintes,… Une méthode originale de varier ces instabilités structurales, et ainsi les propriétés associées, consiste à utiliser les contraintes interfaciales quand un film est déposé sur un substrat. Les propriétés physiques des films peuvent ainsi être considérablement différentes de celles des matériaux massifs, non seulement à cause de l'interaction film-substrat, mais à cause de la taille des grains, des défauts,… Les contraintes peuvent aussi altérer les propriétés mécaniques, optiques, structurales et électriques ainsi que la nature des transitions de phases de films minces ce qui peut jouer un rôle sur la fiabilité et performances.

Les oxydes pérovskites ferroélectriques ont reçu considérablement d'attention pour l'attractivité de leurs propriétés physiques. Ainsi, les études concernant les films épitaxiaux ferroélectriques sont de grand intérêt à cause de leur potentielle application comme composant dans les mémoires, les diélectriques hautes permittivités et des guides d'onde. Par le passé, les contraintes internes dans les films ferroélectriques ont été systématiquement étudiées en variant différents paramètres: l'épaisseur des films, le choix des substrats pour obtenir différent désaccord et différence de dilatation thermique, les variations des conditions de déposition et de traitements thermiques, l'insertion d'une fine couche intermédiaire de composition chimique intermédiaire entre le film et le substrat,…

Cependant, les différents films obtenus peuvent présenter des microstructures et taille de grains différentes qui peuvent affecter les caractérisations électriques. On peut ainsi noter que dans la littérature peu de travaux présentent une mesure directe des contraintes et ces dernières sont en général associées à une origine unique de contraintes (par exemple d'épitaxie ou thermique). Dans les systèmes où les contraintes résiduelles sont données, il est souvent supposé que les contraintes ont une unique origine, et ce, bien que les contraintes résiduelles à température ambiante sont la somme de toutes les contraintes se développant pendant le processus complexe de préparation des films. D'autant plus, les contraintes résiduelles sont le plus souvent estimées par une méthode unique dont la validité est rarement discutée. Ainsi, les méthodes simples pour estimer les contraintes résiduelles et étudier leur origine utilisant des techniques de caractérisations telle que la diffraction des rayons X et la spectroscopie Raman sont d'un intérêt particulier.

L'effet des contraintes sur les transitions de phase dans les films ferroélectriques a été déjà étudié dans la littérature. Il est connu que dans les films contraints de haute qualité épitaxiales, la transition de phase peut être décalée de plusieurs centaines de degrés, aussi, les paramètres de premier et de second ordre peuvent découplés. Cependant, l'effet des contraintes sur des films partiellement relaxé ne reste pas clair dû au manque d'études poussées basés sur l'influence du degré de relaxation sur la nature des transitions de phases.

Dans notre étude, nous avons choisi le ferroélectrique titanate de plomb $PbTiO_3$ (PTO) de structure pérovskite car il peut être considéré comme un prototype d'une large classe de matériaux ferroélectriques. Aussi, les propriétés physiques, structurales et spectroscopiques de PTO sont plutôt bien connues ce qui en fait un matériau de référence pour l'étude des films minces. Il se trouve que les films de PTO ont été intensivement étudiés ces 15 dernières années ce qui nous permet de comparer et discuter nos résultats avec ceux déjà rapportés dans la littérature.

L'objectif de notre étude était d'étudier l'origine des contraintes résiduelles et leur effet sur la nature des transitions de phase et de la transformation des structures de domaine dans les films epitaxial de PTO en utilisant la diffraction des rayons X et la spectroscopie Raman. Afin de varier le niveau de contraintes résiduelles dans les films, une série d'épaisseur de films de PTO ont été déposés sur des substrats très courants, induisant des contraintes de désaccord en compression ou en tension (Figure I.1, page 3).

Dépôt de films de $PbTiO_3$ par PI MOCVD. Procédure d'optimisation.

La croissance de films épitaxiaux de PTO a été effectuée par dépôt chimique des composés metal-organiques en phase vapeur (MOCVD) (Chap. 3, Ref. 3-7), dépôts par ablation laser pulsé (PLD) (Chap. 3, Ref. 8-9), rf-magnetron sputtering (Chap. 3, Ref. 10). Parmi les différentes méthodes de préparation, la MOCVD a été reconnue en tant que technique la plus prometteuse à cause de la possibilité de croître des films sur de larges aires avec un taux de croissance rapide.

Dans la littérature, les composés $PbEt_4$ et $Ti(O^iPr)_4$ ont principalement été utilisés comme précurseurs pour la croissance MOCVD en faisant buller le gaz vecteur à travers des fioles de précurseurs liquides (Chap. 3, Ref. 4, 5, 11-15). Dans ce travail, la phase vapeur est générée par évaporation flash du solution de $Pb(thd)_2$ et $Ti(thd)_2(O^iPr)_2$ dissouts dans du toluène. Les précurseurs sont solides à la température ambiante et ils sont souvent préférés car ils sont non toxiques et plus stables à température ambiante par rapport aux précurseurs liquides. Dans les années passées, les sources uniques ont été de plus en plus utilisées pour croître des composés multiples d'oxyde. Cette technique offre de plus un meilleur contrôle de la composition et une meilleure reproductibilité que la CVD conventionnelle.

L'influence de différentes conditions de dépôts (température, pression partielle d'oxygène, fréquence d'injection, concentration et la composition de la solution) a été examinée pour la croissance de films de PTO sur différents substrats par injection pulsée (PI) MOCVD.

La pression partielle d'oxygène influence la perte de plomb pendant la croissance et les traitements thermiques (Figure 3-1, page 56). Le maximum du ratio Pb/(Ti+Pb) dans les films a été obtenu en utilisant 37.5 % de O_2 dans le flux de gaz. La perte de plomb pendant l'étape de refroidissement peut être réduite en utilisant une haute pression d'oxygène (0.4atm).

Température de dépôt L'évolution de la composition des films, la microstructure et la morphologie a été étudiée pour différentes compositions injectées et températures de substrat. A haute température, il est nécessaire d'augmenter la concentration de précurseur de plomb pour avoir la bonne proportion de cations dans les films. Ceci peut être relié à une grande désorption du plomb à haute température (Figure 3-2, page 57). La composition de la solution et la température de croissance influence fortement la morphologie et la microstructure (Figure 3-3, page 58). Les films épitaxiaux sur les substrats de pérovskite consistent principalement en des domaines *c* et peu de domaines *a*. La morphologie de surface est principalement déterminée par la croissance d'îlots pour la croissance de films a $T<600^{o}C$ et par le phénomène de maclage pour la croissance de film $T_{dep}> 650^{o}C$.

Le taux de croissance et la composition des films de PTO ont été étudiés en fonction de la pression de dépôt, la concentration en solution et la fréquence d'injection. Il a été montré que la désorption en Pb peut être contrôlée par le changement du taux de croissance (Figure 3-7, page 59).

Maclage Les films totalement et partiellement maclés peuvent être obtenus en variant les conditions de dépôt (Figure 3-10, page 62). Les macles sont observées pour les domaines *a* et *c* (Figure 3-11, page 62). L'angle de tilt dépend de la fraction de macles (figure 3-13, page 63). La meilleur cristallinité et la plus basse fraction de domaine a été obtenue dans des films épitaxiaux obtenus à 650^{o}C sur des substrats de $LaAlO_3$ *(001)* (LAO) et $SrTiO_3$ *(001)* (STO).

Les conditions de dépôts sont résumées dans le Tableau 1.

Tableau 1: Conditions optimisées de dépôt pour la croissance de $PbTiO_3$ par PI MOCVD

Température du substrat (T_{Dep}), °C	650
Température d'évaporation , °C	280
Gaz de transport	$Ar + O_2$
Flux total de gaz, l/h	60
Fraction d'oxygène (F_{ox}), %	37.5
Pression totale (P_T), Torr	5
Précurseurs	$Pb(thd)_2$, $Ti(thd)_2(O^iPr)_2$
Solvant	Toluene
Concentration de la solution (total, c_T), mol/l	0.04
Fréquence d'injection (ν_{inj}), Hz	2

Evolution de la structure des films de $PbTiO_3$ avec le désaccord de maille et l'épaisseur des films

Puisque la technologie de films appropriées aux mémoires ferroélectriques est typiquement supérieure à 120 nm, les caractérisations et l'analyse des propriétés films doivent être menée sur des épaisseurs équivalentes. Ainsi, dans le but d'étudier les effets des contraintes et les procédés de croissance de films de PTO, des films d'épaisseur de 30-460 nm ont été déposé sur des substrats de LAO, STO et MgO utilisant des conditions optimisée de dépôt (Tableau 1). Le désaccord de maille dans les films de PTO sur ces substrats varie de fortement compression (LAO) et de faible compression (STO) à forte tension (MgO) aux conditions de dépôts (Figure 4-1, page 71). Pour étudier la relaxation de films et l'origine de contraintes résiduelles, une compréhension de la microstructure est nécessaire. Ainsi, dans ce chapitre nous présentons une résumé d'analyse détaillée de la structure de domaine, de la qualité d'épitaxie, des défauts, des paramètres de réseau, de l'homogénéité des contraintes et de la taille des grains. De plus, les valeurs des contraintes résiduelles seront estimée d'après les données de DRX.

Relaxation des contraintes par maclage et dislocations

Introduction Les films sont d'ordinaire soumis à une contrainte conséquente pendant la croissance et le refroidissement de la température de dépôt à la température ambiante. A la température de croissance, les contraintes proviennent essentiellement du désaccord (aussi appelées contraintes épitaxiales) et de la technique de dépôt (contraintes intrinsèques) ce qui est négligeable en MOCVD. Pendant le refroidissement, des contraintes additionnelles thermiques et de transformation peuvent se développer dans les films. Les contraintes de épitaxiales de films ferroélectriques sont principalement relaxées par la formation de dislocation et de macles (domaines).

La fraction de domaines a dépend du désaccord et des contraintes thermiques en tant que mécanisme de relaxation dans les films PTO. De plus, la formation des domaines *a* et *c* est favorisée par les contraintes de tension et compression, respectivement (Figure 4-10, page 76). Il est important de noter que les contraintes thermiques sont indépendantes de l'épaisseur des films, tandis que les contraintes de désaccord sont relaxées avec l'augmentation de l'épaisseur. Ainsi, le degré de relaxation des contraintes par la génération de dislocation de désaccord joue un rôle critique dans la structure finale de domaines. L'épaisseur critique pour la formation de dislocation de désaccord est un bon indicateur de la capacité des films de se relaxer des contraintes (Tableau 2). L'épaisseur de complète relaxation des contraintes est bien plus grande que l'épaisseur critique pour la génération de dislocations. Comme nos films ont été déposés à relativement basse température, l'énergie thermique nécessaire pour la création de dislocations est faible.

Fraction des domaines Les fractions de domaine *a* dans tous les films ont été évaluée d'après le rapport d'intensité intégrée correspondant aux réflexions *(301)/(310)* et *(103)* (section 2.2.2, page 41). Les fractions de volume évaluées de domaines *a* sont donnés en fonction de l'épaisseur des films dans la figure 4-11 (page 78). Les films d'épaisseur de 30 à 460 nm sur les substrats STO, LAO et MgO présentent une structure *c/a/c/a*, excepté pour les films d'épaisseur de 30 et 65 nm de PTO/STO et de 30 nm de PTO/LAO où seul les domaines *c* ont été observés. La littérature reporte l'évolution en épaisseur des domaines *a* conforme avec nos résultats : la fraction des domaines *a* décroît avec l'augmentation de l'épaisseur de PTO/MgO tandis que dans le cas des substrats de STO et LAO, l'augmentation de la fraction des domaines *a* est observée avec l'accroissement de l'épaisseur des films.

Maclage L’apparence des domaines *a* et *c* non maclés dans les films dépend du désaccord avec le substrat. Si le désaccord des domaines *c* avec le substrat est plus petit que celui des domaines *a*, seul les domaines les domaines *c* peuvent être non maclés (par exemple pour les films PTO/STO et PTO/LAO). Pendant, la relaxation des contraintes la structure de domaines se forme dans les films. Ainsi, le maclage des domaines *a* et *c* indique une relaxation dans les films. Dans les trois systèmes film/ substrat, la proportion de domaines maclés augmente avec l’épaisseur des films. Le maclage apparaît entre les domaines *a* et *c*, résultant en un en une inclinaison depuis la normale du film des deux types de domaines (l’explication est donnée en section 1.5, page 19). Ainsi, la présence d’une inclinaison des domaines *a* indique qu’une fraction des domaines *c* doit aussi être inclinée. Par conséquent, la fraction de domaines *c* macls s’accroît avec l’augmentation des domaines *a*. L’angle d’inclinaison des domaines *c* (domaines *a*) s’accroît (décroît) avec l’accroissement de la fraction de domaines *a* (Figure 4-16, page 86).

Tableau 2: Paramètres structuraux de PTO massif et des substrats : désaccord de maille, contraintes thermiques, épaisseur critique des films PTO déposés à 650 °C.

Matériaux	Structure cristalline	Paramètre de maille (Å)		Coefficient de dilatation thermique ($\times 10^{6}$ K^{-1})	Désaccord de maille à T_{dep} (%)	cContraintes d’épitaxie * à T_{dep}(GPa)	Contraintes thermiques *(650 –20 °C) (GPa)	Epaisseur critique (nm) (11)
		Température ambiante	T_{Dep} (°)					
PTO	quadratique à 20 °C, cubique à T_{Dep}	a=3.899 c=4.153	3.974	12.6 (a-axis) (11)				
STO	cubique	3.905	3.932	11.5**	-1.1	-1.8	+0.11	7.1 (11)
LAO	pseudocubique	3.789	3.814	10.2**	-4.2	-7.0	+0.25	1.1 (11)
MgO	cubique	4.212	4.251	14.8 (11)	+6.5	+10.8	-0.23	0.4 (11)

* **Valeurs initiales du désaccord de maille, la relaxation n’est pas prise en compte.*

*** Valeurs estimées depuis nos mesures de diffraction des rayons X à haute température.*

Densité des défauts Dans le but d'étudier la qualité épitaxiale de l'interface film substrat et la densité de macles et dislocations, une analyse HRTEM a été effectuée sur la section de la couche. L'effet des différent désaccord entre le film et le substrat a été étudié pour les couches de 250 nm d'épaisseur sur LAO et STO. L'effet de l'épaisseur est comparé entre les films de 65 nm et 250 nm d'épaisseur des films PTO/LAO.

La densité de défauts (dislocation et macles) ou de relaxation des contraintes augmente avec l'augmentation du désaccord et de l'épaisseur. Les films de 250 nm d'épaisseur PTO/STO sont cohérents et dans le plan avec le substrat (Figure 4-17, page 87), tandis que PTO/LAO est epitaxial mais n'est pas cohérent dans le plan avec le substrat (Figure 4-21, page 90) . Les dislocation de désaccord sont principalement des sites de nucléation pour les domaines *a* dans les films sous compression. Les domaines *a* secondaires se forment principalement dans les films relaxés (Figure 4-23, page 91). Les domaines *a* non maclés sont observés dans les films avec une grande densité de dislocation traversantes, alors que les domaines *a* et *c* non maclés ne peuvent être créé que par l'intermédiaire des défauts (Figures 4-23 et 4-24, pages 91 et 92).

La mosaïcité des domaines *c* augmente avec l'épaisseur des films ou le désaccord de maille du à l'augmentation de la concentration de défauts (Figure 4-16, page 86) . La mosaïcité des domaines *a* maclés ne dépend pas des matériaux de substrat ni de l'épaisseur des films. Ceci indique que la mosaïcité des macles est déterminée par la matrice du film. En prenant en compte l'influence des macles et la résolution instrumentale (0.1^{o} en rocking-curve) sur les valeurs de la largeur (Figure 4-16, page 86) la qualité épitaxiale de PTO/STO est très bonne alors que PTO/LAO et MgO peut être considérée comme bien orientée.

Les contraintes

Les contraintes résiduelles dans les couches minces peuvent être estimées à partir des déformations des paramètres de maille. Selon la loi de Poisson, les contraintes de tension dans le plan résultent par l'augmentation des paramètres hors du plan.

Paramètres de maille Les paramètres dans le plan et hors du plan des domaines *a* et *c* ont été étudiés par les réflexions *(103)* et *(301)/(310)* en images ω-2Θ (section 2.2.2, page 40). Dans le cas de nos films, le paramètre *c* est plus petit que celui d'un massif pour n'importe désaccord de maille (Figure 4-25, page 93). La relaxation thermique est négligeable car nos films ont été déposé à relativement basse température (650^{o}C). Ainsi, les valeurs du massif ne sont pas atteintes même pour des épaisseurs de 460 nm. D'autres groupes ont aussi rapporté que la diminution de l'axe *c* sur les substrat induisent des contraintes compressives ou de tension. Cependant, la déformation de l’axe *c* avec les contraintes est plus grande, plus de 4 fois plus élastique que l’axe *a* (correspondant au module élastique donné en section 4.6 Table 4-2, page 96). De plus, les paramètres dans le plan sont d’ordinaire bloqués par le substrat et n’évoluent pas avec l’évolution de la relaxation. L’évolution du paramètre *a* dépend plus des défauts que des contraintes appliquées. Ainsi, ils ne peuvent être utilisé pour une étude de la relaxation des contraintes et pour l’estimation de la valeur des contraintes. Nous utiliserons le paramètre *c* des domaines *c* pour mesurer les contraintes résiduelles dans les films.

Contraintes résiduelles Les contraintes résiduelles biaxiales dans les films PTO sur STO, LAO et MgO ont été estimes a partir de la formule (1).

$$\sigma_b = \left(-\frac{(C_{11} + C_{12})C_{33}}{2C_{13}} + C_{13} \right) \varepsilon_{zz} \qquad (1)$$

Ou, ε_{ji} est la déformation, σ_{ij} est la contrainte, $C_{ijkl}=(S_{ijkl})^{-1}$ est le tenseur de compliance (rigidité) du cristal considéré.

L’évolution des contraintes résiduelles avec l’épaisseur est donnée sur la figure 4-26 (page 97). La valeur positive de σ_b suggère que tous les films sont en tension pour tous les substrats et leur épaisseur. Les contraintes résiduelles se relaxent graduellement de 1 GPa à 0.4 GPa en augmentant l’épaisseur des films PTO/LAO de 30 à 460 nm. La contrainte résiduelle reste constante aux incertitudes expérimentales près sur les couches PTO/MgO tandis que sur les films PTO/STO, la contrainte de tension augmente en augmentant l’épaisseur. Pour les couches de 30 à 125 nm, les contraintes résiduelles sont les plus importantes (1.1 a 0.85 GPa) pour PTO/LAO, tandis qu’elle descendent jusqu'à 0.3 GPa sur PTO/STO. On retrouve environ les mêmes contraintes sur les films à 460 nm pour STO, LAO et MgO (respectivement : 0.48 , 0.44 et 0.62 GPa).

Contraintes hétérogènes La première cause de contraintes homogènes est la contrainte du substrat. S’ajoute les défauts qui produisent des contraintes hétérogènes ce qui peut affecter l’intérêt technique et les propriétés des films. D’autant plus que les déformations hétérogènes se couplent très fortement avec la polarisation comme il a été montré par des théories phénoménologiques où elles modifient la température de transition de phase. Ainsi, il est important d’étudier les déformations hétérogènes. Ces déformations peuvent être analysées par diffraction des rayons X de l’axe *c* car il est le plus élastique. La relaxation par les défauts des déformations comme les dislocations de désaccord et traversantes réduisent ou éliminent l'énergie associée aux contraintes homogènes. Cependant, tous défauts dans le film génèrent de déformation hétérogène. Ainsi la déformation est peu hétérogène dans les domaines *a* et *c* avec une forte densité de défauts. Le volume de déformation hétérogène est plus faible que celui homogène, ceci indiquant que les contraintes du substrat restent très importantes par rapport à celle induite par les défauts (Figures 4-27, page 98).

Effet de taille et microdéformations L'élargissement des pics de la diffraction des rayons X peut venir des déformations et de l'effet de taille. La contribution individuelle des contraintes et de l'effet de taille sur la réflexion *(00l)* ont été estimés en utilisant l'analyse de Williamson-Hall et l'approximation de Halder-Wagner. Les deux analyses convergent et donnent une preuve que la contribution principalement est l'effet des déformations bien qu'à faibles épaisseurs, l'effet de taille ne puisse être aussi négligé (Figure 4-30, page 101). En conclusion, de fortes microdéformations résultent du désaccord de maille dans les films très minces et de la concentration de défauts dans les films épais.

Modes Raman et contraintes résiduelles

La spectroscopie Raman est complémentaire de la diffraction des rayons X car c'est une sonde locale et sensible à de petits changements de symétrie. De plus, la ferroélectricité et ainsi les modes Raman sont fortement influencés par la déformation mécanique résultant de la pression hydrostatique ou des contraintes (Chap. 5, Ref. 11; 12; 18; 19; 20; 21).

Nous verrons par la suite que l'analyse des spectres Raman de PTO est très complexe. Il est par exemple très importante de se rappeler que nos films consistent dans des domaines *a* et *c* et peuvent présenter des domaines à 180° puisqu'ils sont obtenus sur des substrats diélectriques et sont non polarisés. Ainsi, les modes Raman ne sont pas seulement affectés par les contraintes dans les films mais aussi par la dépolarisation du laser résultante des domaines à 90 et 180°. Par conséquent, les causes de dépolarisation doivent être prisent en compte avant l'évaluation des contraintes. Pour interpréter d'une manière utile la structure polydomaine, nous présentons par la suite une analyse et une discussion de la signature des modes Raman de monocristal de PTO présentant des domaines à 90 et 180° comme dans nos films.

Les modes Raman relatifs aux domaines *a* et *c* peuvent être clairement discernés par l'enregistrement de spectres polarisé en surface et en section (Figure 5-1, page 111). Quand un spectre est enregistré sur la surface, ou sur un monocristal, les modes *E(TO)* sont observés en *VH* alors que les modes $A_1(TO)$ proviennent des domaines *a* et les modes $A_1(LO)$ des domaines *c*. Les spectres obtenus sur la section en *VH* montrent des modes *E(TO)* qui proviennent des 50% des domaines *a* et domaines *c*. En *VV*, les modes $A_1(LO)$ sont relatifs aux domaines *a* et $A_1(TO)$ proviennent de 50% des domaines *a* et domaines *c*. Les modes durs $A_1(TO)$ correspondant aux domaines *a* et *c* ont été identifié par comparaison des spectres *VV* en surface et sur la tranche (Figure 5-9, page 119).

Monocristaux polydomaines de PTO

L'analyse des spectres Raman révèle que :

La position des modes Raman et le profile des pics sont modifiés par la présence de modes obliques en configuration *VV* (Figures 5-2 et 5-3, pages 113-114). Les modes obliques peuvent résulter d'une origine intrinsèque et extrinsèque comme la structure de domaines ferroélectriques, la mauvaise orientation des échantillons, l'ouverture numérique et le mauvais alignement du système Raman.

L'analyse de la lumière diffusée à différent endroit du cône de lumière pendant une acquisition en *VV* a été effectuée en utilisant une modification du Raman en champ sombre (Figure 5-7, page 117). Cette étude confirme la présence et l'importance de modes oblique en spectres *VV* et leur influence sur l'asymétrie des profiles et des positions.

Les spectres en polarisation *VH* sont essentiels pour mesurer les modes *E(TO)* avec précision puisque les modes obliques ne sont pas possibles. Cette condition fondamentale pour l'évaluation des contraintes résiduelles dans les films de PTO basée sur la position des pics *E(TO)*.

Détermination des contraintes résiduelles

La fréquence des modes *E(TO)* $\omega_{E(TO)}$ en fonction des contraintes hydrostatiques P peuvent être décrite de la manière suivante :

$$\Delta\omega_{E(TO)} = (2a'_{E(TO)} + b'_{E(TO)})P \qquad (2)$$

ou a' et b' sont les constante du potentiels de déformation exprimés en terme de compliance. Dans le cas des domaines *c* sous contraintes biaxiales σ_b, ω(E(TO)) peut s'écrire :

$$\Delta\omega_{E(TO)} = 2a'_{E(TO)}\sigma_b \qquad (3)$$

Bien que les conditions dans les films ne soient strictement pas hydrostatiques, il a été supposé que les instabilités des contraintes hydrostatiques offrent un guide sur comment un matériau va réagir à une contraintes extérieure. Comme les modes Raman varient linéairement avec les contraintes biaxiales, seules les coefficients sont différents. Il peut être noter que dans la littérature (Chap. 5, Ref. 10; 13; 15; 17), la valeur des contraintes en tension de PTO ont été estimées par le décalage du mode mou *E(1TO)*. Cependant, les coefficients en pression ont été déterminé uniquement en compression (pression hydrostatique $\partial\omega_{E(1TO)}/\partial P = -5.8 \pm 0.2 cm^{-1}GPa^{-1}$) et le mode mou est par définition anharmonique. Ainsi, la relation entre la contrainte appliquée et le décalage Raman est non linéaire et sensible à l'effet de taille. Ce mode ne peut donc pas être utilisé précisément pour déterminer les contraintes résiduelles sur les films epitaxiales et polycristallins. Nous avons donc utiliser le mode *E(3TO)* qui est un mode dur (harmonique) dans le sens ou sa dépendance en pression montre un décalage positif et linéaire ($\partial\omega_{E(3TO)}/\partial P = +7.1 \pm 1.0 cm^{-1}GPa^{-1}$). Dans les films polycristallins, les grains ont différentes orientations cristallographiques ce qui résulte en l'apparition de modes obliques. D'autre part, comme mentionné plus haut, les règles de sélection ne sont pas respectée dans les films polycristallins. Ainsi, même le profile du mode *E(3TO)* est modifié par les modes obliques dans les films polycristallins. Le mode dur *E(3TO)* peut ainsi être décalé vers les hautes fréquences et ainsi déterminer des contraintes apparemment plus faibles que déterminées par diffraction des rayons X. Il s'en suit que les valeurs des contraintes résiduelles ne peuvent pas être estimée à partir des modes E(TO) en milieu dans les films polycristallins de PTO. La similarité des contraintes estimées par DRX et la spectroscopie Raman du mode *E(3TO)* (Figure 5-12, page 122) nous permet de considérer l'equation 2 valide puisque b'<<a' pour ce mode. Les données obtenues par pression hydrostatiques peuvent donc nous fournir une compréhension et une estimation correct de l'état de contraintes à partir du mode dur des domaines *c* dans les films de PTO.

Les films de 30 à 460 nm sont en tension dans le plan du film lorsqu'ils sont en désaccord de maille compressif ou de tension (Figure 5-17, page 127) . Les domaines *a* sont plus contraints que les domaines *c*. Cependant, nous ne pouvons pas estimer les valeurs des contraintes dans les domaines *a* tant que la symétrie des contraintes et le potentiel de déformation n'est pas connu. Il y a toutefois un très bon accord entre les valeurs des contraintes estimées par DRX et par la spectroscopie Raman, ce qui justifie bien l'emploi du mode *E(3TO)*.

Effect de la température sur $PbTiO_3$ poudre et en films

Dans le but d'étudier l'influence du désaccord de maille sur la transition de phase dans les films de PTO polydomaines, les films partiellement relaxés en utilisant DRX et la spectroscopie Raman en température. Nos résultats sont comparés à ceux complètement relaxés des films épitaxiaux et polycristallins ainsi qu'avec un échantillon massif (poudre). De plus, la transition de phase dans le massif PTO a été à nouveau étudiée par spectroscopie Raman dans le but d'avoir une référence connue des spectres à haute température et ainsi d'étudier précisément la transition de phase à la température T_c.

Pour résumer nos résultats sur la transition de phase sur poudre (massif), films polycristallins et epitaxial, nous avons proposé un model hypothétique de la transition de phase développée dans les transitions cubiques désordonnées. Ceci est présenté sur la figure 6-23 (page 159). Le PTO massif traverse la phase quadratique à la phase cubique désordonnée à 520 ^{o}C (Figures 6-9 et 6-10, page 145). Cette phase haute température a une symétrie local quadratique avec les ions de Ti suivant les trois directions possibles (6 sites) ont une probabilité équiprobable. Ainsi la structure est en moyenne cubique. De plus, des petits domaines ferroélectriques peuvent exister (inférieure à la limite de diffraction). La polarisation des domaines est macroscopiquement désordonnée, résultant en une phase paraélectrique. Le comportement haute température des films polycristallins de PTO est similaire (Figures 6-9 et 6-10, page 145) au massif excepté que la transition de phase est plus basse à cause des contraintes thermiques de tensions.

La transition de phase dans les films épitaxiaux est considérablement différente de celle du massif. L'orientation des films complément et partiellement relaxé est gouvernée par le substrat. Ainsi, les transformations de phase des polydomaines *c/a/c/a* en domaines *c* ou domaines $a_1/a_2/a_1/a_2$ sont observés pour toutes les épaisseurs sur substrats en compression et en tension respectivement. Les résultats de DRX (Figure 6-7, page 142) et la spectroscopie Raman (Figures 6-15 (page 149), 6-17 (page 151) et 6-18 (page 152)) montrent que la température, à la quelle les transformations de domaine ont lieu, diminuent avec l'épaisseur.

Dans le cas des films complètement relaxés tels que les films PTO/LAO ou PTO/MgO de 250 et 460 nm, la température de transition est similaire à celle du massif (Figures 6-16 (page 150), 6-19 (page 153) et 6-21 (page 155)). Au dessus de T_c, la largeur des raies Raman de l'échantillon à 460 nm est nettement plus grande ce qui indique un désordre plus important avec des clusters ferroélectriques plus petits et comparable au massif. Dans les films de 250 nm, la largeur est légèrement plus faible indiquant une augmentation de la corrélation ferroélectrique. Ceci permet une distorsion élastique et ainsi un déplacement du titane suivant la normale au plan du substrat ou dans les deux directions du plan du substrat pour LAO ou MgO respectivement.

Dans les films partiellement relaxés de LAO et MgO de 65 nm d'épaisseur, l'évolution de la température de l'orientation des films et de leur structure dépendant fortement du substrat. Un réarrangement structurale se produit à 500^{o}C. La phase haute température est fortement orienté suivant *c* ou *a* dans les films sur LAO et MgO respectivement. Les raies Raman sont plus fines ce qui indique encore un déplacement préférentiel des ions titanes dans les clusters suivant la normale au plan (Figure 6-20 (page 153) et 6-22 (page 156)). La structure doit être en moyenne plus quadratique mais nous ne pouvons pas juger si la phase est ferroélectrique ou pas.

Il est important de noter que la distorsion quadratique est la même dans les poudres et les films polycristallins, partiellement et complètement relaxés puisque les modes *A* et *E* se confondent à environ 500^{o}C (Figure 6-21, page 155). Cependant, les orientations quadratiques sont fortement limitées par le substrat dans les films épitaxiés. Ainsi, les possibilités du déplacement du titane dans certaines directions sont réduites, résultant en une structure en moyenne quadratique. Il est possible que cette distorsion quadratique ne soit plus couplée au premier paramètre d'ordre (polarisation) comme il a été observé sur d'autres films de structure pérovskite. Ainsi, les films partiellement et complètement relaxés peuvent/sont paraélectriques à haute température.

Finalement, dans les films épitaxiaux cohérents (PTO/STO), aucune transition de phase n'est observée entre la température ambiante et 600^{o}C (Figures 6-8 (page 143), 6-11 (page 147), 6-12 et 6-13 (page 148). La structure moyenne est identique à la structure locale quadratique. Les déplacements du titane ne sont possibles que dans une direction. De plus, la corrélation ferroélectrique est plus grande résultant en une phase ferroélectrique à haute température. Cependant, bien que la signature Raman est similaire à basse et haute température, nos données Raman ne peuvent à proprement parler confirmer cette hypothèse. Ceci nécessite des mesures dans le plan et hors du plan plus précises ainsi que des caractérisations électriques à haute température.

Origine des contraintes résiduelles

Nous avons discuté dans la section 1.5 (page 19) que les films de PTO sont soumis à des contraintes importantes pendant la croissance et le refroidissement. A la température de dépôt, les contraintes ont principalement du au désaccord de maille et des contraintes intrinsèques. D'ordinaire, les contraintes intrinsèques sont négligées dans les dépôts MOCVD. Pendant le refroidissement des contraintes supplémentaires peuvent se développer dans les films soi par les contraintes thermiques soi par les contraintes associées à la transition de phase. Les contraintes hétérogènes peuvent aussi apparaître dans les films à cause des défauts telles que les dislocations, les joints de grains et les lacunes. Comme montré dans la section 4.7 (page 97). Les contraintes hétérogènes ont été observées dans les films de 125 et 460 nm déposé sur LAO et MgO, où la concentration en défaut est relativement élevée. Cependant, la fraction volumique qui contient des contraintes hétérogènes semble être nettement plus faibles que le volume homogène. Ainsi, nous avons supposé que les contraintes résultant des contraintes hétérogènes sont négligeables et n'influence pas la mesure des contraintes résiduelles.

Les deux techniques spectroscopie de Raman et DRX montrent que les films de 30 à 460 nm sont sous tension dans le plan des films pour tous les substrat étudiés. Elles dépendent très de l'épaisseur des substrats. Dans le cas de PTO/LAO et PTO/MgO, les films les plus fins sont les plus contraints et les contraintes se relaxent en augmentant l'épaisseur. L'évolution des contraintes résiduelles dans PTO/STO est cependant inattendue, les contraintes de tension augmentent avec l'épaisseur entre 125 et 460 nm. En effet, les études TEM et DRX montrent que les macles et la densité de dislocation en augmentant l'épaisseur. Ceci confirme une augmentation de la relaxation avec l'épaisseur.

Dans la suite, nous allons ouvrir le débat sur l'origine des contraintes résiduelles et leur évolution avec l'épaisseur sur les films de PTO/STO. Nous discuterons spécifiquement de la contribution des contrqintes du désaccord, des contraintes thermiques et des contraintes de transformation sur les contraintes résiduelles mesurée à température ambiante. De plus, les contraintes résiduelles seront discutées au vu des fractions de domaines.

Contrainte de désaccord de maille

Les calculs des contraintes de désaccord dans PTO sur les substrats de STO, LAO et MgO à la température de dépôt a conduit aux valeurs de -1.8 GPa, -7 GPa et +10.8 GPa respectivement. Bien sur, des contraintes aussi importantes ne sont pas observées dans les films car les contraintes sont relaxées par la formation de dislocations pendant le dépôt. L'épaisseur critique pour la génération des dislocations est un bon indicateur de la possibilité des films de se relaxer. Elle est de 7.1, 1.1, 0.4 nm pour les films déposés a 650^{o}C sur STO, LAO, MgO respectivement. Cependant, l'épaisseur pour la relaxation complète est plus grande que celle pour la génération de dislocation. Les résultats de DRX et spectroscopie Raman indiquent que le désaccord se relaxe rapidement avec l'augmentation de l'épaisseur dans les films de PTO/LAO et PTO/MgO (Figure 4-31, page 103). Les contraintes sont presque complément relaxé dans les films de 250 et 460 nm d'épaisseur. L'interface film/substrat est cohérente dans les films de PTO/STO, c'est-à-dire, que l'alignement des colonnes atomiques à travers de l'interface est parfait, en effet le désaccord est faible. Ainsi, la relaxation est lente dans ces films, même le film à 460 nm, elle est seulement partiellement relaxée. L'évolution de l'épaisseur avec les contraintes de désaccord dans les trois substrats est donnée sur la figure 7.1a (page 167). Cette dernière montre un désaccord avec l'évolution des contraintes résiduelles à température ambiante. Spécialement dans les films sur substrats qui induisent des contraintes de compression. Ceci indique que les films sont soumis à de fortes contraintes additionnelles.

Contraintes thermiques

Les contraintes thermiques ne dépendent pas de l'épaisseur et sont d'ordinaire plutôt faibles dans les films de PTO sur les substrats pérovskites. Ces contraintes se développent dans nos films de PTO pendant le refroidissement depuis la température de dépôt. Elles sont évaluées à 0.11, 0.25 et -0.23 GPa sur STO, LAO et MgO respectivement. Cependant, ces petites valeurs ne peuvent pas expliquer elles-mêmes les contraintes résiduelles de tension. De plus, des contraintes thermiques sont aussi relaxées. Elles sont donc plut petites que celles estimées.

Contraintes de transformation.

Comme discuté plus haut, et spécialement dans les films les plus fins sur substrat induisant de fortes contraintes de compression, les contraintes résiduelles ne peuvent pas être expliquées si l'on néglige les contraintes de transition de phase. Les mesures de courbure indiquent que les contraintes ne sont pas complètement relaxées pendant la transition de phase comme attendue (Chap. 7; Ref. 3, 4). Comme il a été montré par DR X et spectroscopie Raman, la nature de la transition qui prend place dans les films épitaxiaux dépendant de l'épaisseur des films et la nature du substrat. Dans le but d'illustrer cela, nous avons tracé sur la figure 7.2 (page 169) la déviation de la position des modes

E(2TO) des films PTO de 65 a 460 nm d'épaisseur et sur la poudre. Cette séparation est alors supposée proportionnelle aux contraintes résiduelles.

Les films complètement relaxés (250 et 460 nm sur LAO et MgO) ne présentent pas cette anomalie jusqu'à la transition. Cependant, au delà de T_c, le comportement est similaire que dans les films complètement et partiellement relaxés : Le mode *E(2TO)* se décalent plus lentement vers les basses fréquences que la poudre. Ceci peut être compris comme si dans la phase haute température, les contraintes épitaxiales avec le substrat ne peuvent permettre la création d'un désordre. Ainsi, les contraintes de transformation induites par la transformation de phase ne peuvent être négligée, même dans les films relaxés. Ces observations montrent l'importance des contraintes de transformation dans les films épitaxiaux et spécialement dans les films partiellement relaxés, ou l'expansion thermique est gouvernée par le substrat.

La dépendance en épaisseur des films de la contrainte de transformation dans les films PTO/LAO est donnée sur la figure 7-1a (page 167). Celle-ci est compatible avec l'évolution des contraintes résiduelles, indiquant que les contraintes résiduelles résultent principalement des contraintes de transformation dans ces films. Les contraintes de désaccord doivent être complément relaxées dans les films de PTO/MgO de 250 et 460 nm d'épaisseur, ainsi la contrainte de 0.6 GPa doit provenir essentiellement des contraintes de transformation. Les films de PTO/STO de 30 à 460 nm d'épaisseur sont soumis à la fois à des contraintes de désaccord et de transformation. Les contraintes de tension mesures dans les films indiquent que la contrainte de transformation est plus importante que celle du désaccord. De plus, les contraintes de désaccord se relaxent plus rapidement avec l'épaisseur que la contrainte de transformation. En conséquence, les contraintes de tension augmentent lorsque l'épaisseur des films augmente.

Contraintes et fraction de domaine a

L'une des plus importantes sources de relaxation dans les films de PTO (et les autres ferroélectriques pérovskites) est le maclage. Comme montré sur la figure 7-1b (page 167), la fraction de domaine *a* augmente avec l'épaisseur quand les films sont déposés sur des substrats de désaccord de compression (LAO, STO) et décroît sur des substrats en tension (MgO). De plus, la dépendant en épaisseur de la fraction de domaine *a* est en accord avec celle des contraintes de désaccord (figure 7-1a, page 167). Les contraintes de compression empêchent la formation de domaines *a* mais pendant la relaxation, des dislocations de désaccord sont générées à l'interface ce qui sert à la nucléation de domaines *a*. Ainsi la relaxation des contraintes de compression résulte en l'apparition de domaines *a*. Les contraintes thermiques en tension peuvent aussi contribuer à la formation de domaines *a*, spécialement dans les films épais ou les contraintes de désaccord sont presque totalement relaxées.

La formation de domaines a est fortement favorisée par les contraintes de tension dans le plan. En conséquence, la relaxation du désaccord de maille en tension permet l'augmentation de la fraction de domaines *a*, ce qui est favorisé par les contraintes thermiques de compression.

Pendant le refroidissement de la température de dépôt T_{dep}, les macles peuvent apparaître à travers la formation de domaines *a* et *c* dans les domaines *c* et $a_1/a_2/a_1/a_2$. Ainsi, la relaxation des contraintes de transformation résulte dans l'augmentation des fractions de domaines *a* et *c* dans les films sur substrat induisant des contraintes compressives (STO, LAO) et en tension (MgO). Les contraintes de transformation ont été étudiées en variant la concentration en zirconium dans le système $PbZr_{1-x}Ti_xO_3$. Ce qui a conduit a un changement de la quadracité. Il a ainsi été aussi observé une décroissance de la fraction de domaine *a* en diminuant les contraintes de transformation (Chap. 7, Ref. 1)

Conclusions générales et perspectives

Dans cette étude, les techniques de DRX, microscopie électronique en transmission haute résolution (HRTEM) et spectroscopie Raman ont été utilisées pour étudier l'origine des contraintes résiduelles et l'effet des contraintes sur la transition de phase des films épitaxiaux de PTO déposés par MOCVD. Dans le but de varier le niveau de contraintes dans les films une série de films avec différentes épaisseurs a été élaborée sur différents substrats. STO et LAO présentent un désaccord de maille en compression et MgO un désaccord en tension.

Notre analyse sur un monocristal de $PbTiO_3$ polydomaine sans contrainte par spectroscopie Raman a révélé que le profile des phonons peut être singulièrement modifié par l'existence des modes obliques en polarisation VV et sans polarisation. Nous avons noté que les modes obliques existent toujours dans les ferroélectriques mais qu'à notre surprise ils sont la plupart du temps pas pris en compte dans la littérature pour l'analyse Raman de ferroélectriques. De plus, la plupart des travaux sur les contraintes résiduelles dans ces films sont basés sur les modes Raman issus de spectres non polarisés. D'un autre coté, nos résultats montre que l'utilisation de la configuration de polarisation VH et la considération des modes obliques permet d'obtenir des spectres qui permettent une estimation des contraintes résiduelles.

Dans la littérature, l'analyse des contraintes résiduelles est principalement basée sur l'analyse du décalage du mode mou *E(1TO).* Nous avons montré dans notre travail que ce choix est questionnable car l'anharmonicité du mode mou et les données existantes ne peuvent être utilisées pour mesurer des contraintes en tension. D'autre travaux rapportent des contraintes mesurée par les modes *E(LO)* et *A(3TO)* ceux mêmes qui sont très sensibles aux modes obliques. De plus, les contraintes résiduelles ne peuvent être estimées à partir des modes Raman de poudre de PTO. Par conséquent nous avons proposé et utilisé une analyse alternative basée sur le comportement du mode *E(3TO)* qui est un mode dur et possiblement le seul mode pour une détermination des contraintes résiduelles. Ces mesures ont montré un très bon accord avec les données issues des paramètres de maille de DRX.

Nous avons montré que les données de pression sur le mode *E(3TO)* peuvent être utilisées pour une estimation des contraintes résiduelles biaxiales dans les films épitaxiaux de PTO des domaines *c*. Effet, le potentiel de déformation donne $b'_{E(3TO)} << a'_{E(3TO)}$. Dans les autres cas où les contraintes résiduelles ne sont pas biaxiales (probablement dans les domaines *a*), le seul décalage ne suffit pas pour calculer la valeur des contraintes.

D'autant plus, le choix du bon mode Raman *E(3TO)* pour une analyse précise est basée sur une analyse en polarisation respectant les règles de sélection. Les spectres collectés en section apportent des informations à propos domaines *c* qui sont prédominant. Les mesures sur la surface ne donnent accès qu'aux domaines *a*.

DRX et la spectroscopie Raman révèlent que les films sont sous tension sur les substrats STO, LAO et MgO et que les contraintes dépendent de l'épaisseur des films. Les analyses de diffraction des rayons X et HRTEM montrent que les macles et la densité de dislocation s'accroissent avec l'épaisseur des films de PTO, ce qui met en évidence la relaxation des films.

L'analyse de l'évolution des contraintes résiduelles avec l'épaisseur et l'analyse de la relaxation indique que les contraintes ont plusieurs origines et pas seulement le désaccord de maille comme proposé dans la littérature. Nous avons montré que les contraintes dominantes dans nos films sont reliée à la transformation de phase alors que la littérature indique que celle-ci n'existent pas ou sont complètement relaxées par la structure de domaine.

Notre étude illustre que le comportement à haute température, proche de la transition de phase est très instructif et permet de mettre en évidence et discuter de l’influence du substrat sur les films. Il est important de noter que la confusion entre la transformation de domaine et la transition de phase dans les films épitaxiaux peut être évitée par une étude du comportement à haute température des domaines *a* et *c* par DRX et spectroscopie Raman.

La tendance générale que nous avons observée est la suivante : plus le désaccord de maille est faible avec le substrat, plus grand est l’influence du substrat et plus les films sont contraints. L’influence du substrat est aussi accrue quand l’épaisseur du substrat diminue. DRX et la spectroscopie Raman à haute température donne une preuve que les contraintes résiduelles ne déterminent pas la dépendance avec le substrat car elles sont la somme de toutes les contributions des contraintes induites. Par exemple, les valeurs des contraintes résiduelles sont plus basses dans les films sur STO qui dépendent très fortement du substrat que dans les films sur MgO et LAO.

Finalement, nos observations montrent que les transitions de phase dans les films épitaxiaux sont considérablement différentes que dans les poudres et dans les monocristaux polydomaines. Les transformations de domaines sont observées à plus basse température dans les films minces épitaxiés que dans les plus épais à cause de la forte dépendance de la corrélation ferroélectrique dans la phase à haute température. De plus, pas de dépendance de température de la transition de phase n’a été observée dans de tels films. Une manifestation de l’effet du substrat est trouvée dans les films de 250 nm PTO/STO ce qui montre une ferroélectricité et des domaines *c/a/c/a* jusqu'à 650^{o}C. Ceci contredit la théorie qui prédit que les domaines *c/a/c/a* ne sont stables que sous la température de transition du PTO massif.

Perspectives

La structure à haute température par DRX devrait être poursuivie sur les paramètres de maille dans le plan et hors du plan dans le but de déterminer la structure moyenne dans les films à haute température.

L’étape suivante de notre étude devrait être l’analyse de l’effet des contraintes sur les propriétés électriques des films. Dans ce but, les films devraient être déposés sur des systèmes électrodes/substrat avant de procéder à des études similaires sur les contraintes résiduelles.

Il serait aussi intéressant d'étudier l'effet des contraintes en utilisant les mêmes techniques sur d'autres ferroélectriques pérovskites dans lesquels plusieurs transitions de phase se produisent. Ainsi, la relaxation des contraintes de transformation devrait être différente pour chaque transition de phase à cause de la différence d'énergie thermique accessible.

Annex 1:

ICDD 00-006-0452

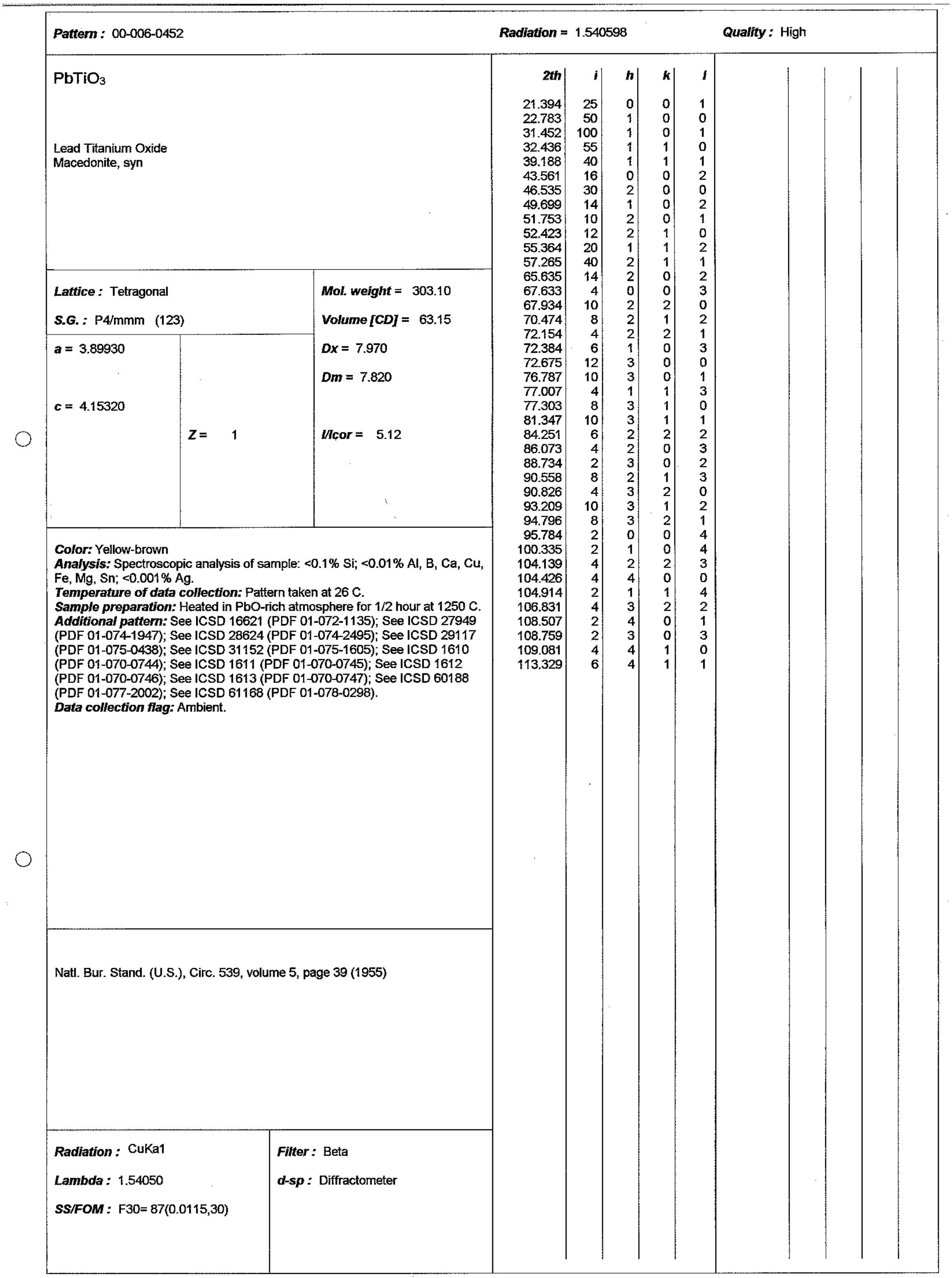

Pattern : 00-006-0452

Radiation = 1.540598

Quality : High

PbTiO$_3$

Lead Titanium Oxide
Macedonite, syn

Lattice : Tetragonal

S.G. : P4/mmm (123)

a = 3.89930

c = 4.15320

Z = 1

Mol. weight = 303.10

Volume [CD] = 63.15

Dx = 7.970

Dm = 7.820

I/Icor = 5.12

Color: Yellow-brown
Analysis: Spectroscopic analysis of sample: <0.1% Si; <0.01% Al, B, Ca, Cu, Fe, Mg, Sn; <0.001% Ag.
Temperature of data collection: Pattern taken at 26 C.
Sample preparation: Heated in PbO-rich atmosphere for 1/2 hour at 1250 C.
Additional pattern: See ICSD 16621 (PDF 01-072-1135); See ICSD 27949 (PDF 01-074-1947); See ICSD 28624 (PDF 01-074-2495); See ICSD 29117 (PDF 01-075-0438); See ICSD 31152 (PDF 01-075-1605); See ICSD 1610 (PDF 01-070-0744); See ICSD 1611 (PDF 01-070-0745); See ICSD 1612 (PDF 01-070-0746); See ICSD 1613 (PDF 01-070-0747); See ICSD 60188 (PDF 01-077-2002); See ICSD 61168 (PDF 01-078-0298).
Data collection flag: Ambient.

Natl. Bur. Stand. (U.S.), Circ. 539, volume 5, page 39 (1955)

Radiation : CuKa1

Lambda : 1.54050

SS/FOM : F30= 87(0.0115,30)

Filter : Beta

d-sp : Diffractometer

2th	**i**	**h**	**k**	**l**
21.394	25	0	0	1
22.783	50	1	0	0
31.452	100	1	0	1
32.436	55	1	1	0
39.188	40	1	1	1
43.561	16	0	0	2
46.535	30	2	0	0
49.699	14	1	0	2
51.753	10	2	0	1
52.423	12	2	1	0
55.364	20	1	1	2
57.265	40	2	1	1
65.635	14	2	0	2
67.633	4	0	0	3
67.934	10	2	2	0
70.474	8	2	1	2
72.154	4	2	2	1
72.384	6	1	0	3
72.675	12	3	0	0
76.787	10	3	0	1
77.007	4	1	1	3
77.303	8	3	1	0
81.347	10	3	1	1
84.251	6	2	2	2
86.073	4	2	0	3
88.734	2	3	0	2
90.558	8	2	1	3
90.826	4	3	2	0
93.209	10	3	1	2
94.796	8	3	2	1
95.784	2	0	0	4
100.335	2	1	0	4
104.139	4	2	2	3
104.426	4	4	0	0
104.914	2	1	1	4
106.831	4	3	2	2
108.507	2	4	0	1
108.759	2	3	0	3
109.081	4	4	1	0
113.329	6	4	1	1

Annex 2:

Surface & Coatings Technology 201 (2007) 9340-9344

Available online at www.sciencedirect.com
ScienceDirect
Surface & Coatings Technology 201 (2007) 9340–9344
SURFACE & COATINGS TECHNOLOGY
www.elsevier.com/locate/surfcoat

Ferroelectric $PbTiO_3$ films grown by pulsed liquid injection MOCVD

A. Bartasyte [a,b,*], R. Bouregba [c], E. Dogheche [d], M. Boudard [e], G. Poullain [c],
O. Chaix-Pluchery [a], C. Jimenez [a], V. Plausinaitiene [b], D. Remiens [d],
A. Abrutis [b], Z. Saltyte [b], F. Weiss [a]

[a] *Laboratoire des Matériaux et du Génie Physique, CNRS, INP Grenoble-Minatec, 3 parvis Louis Néel, BP 257, 38016 Grenoble Cedex 1, France*
[b] *Vilnius University, Dept. of General and Inorganic Chemistry, Naugarduko 24, LT-03225 Vilnius, Lithuania*
[c] *Laboratoire CRISMAT, CNRS-Université de Caen, Boulevard Maréchal Juin, 14050 Caen Cedex, France*
[d] *Institut d'Electronique, de Microélectronique et de Nanotechnologie Bat P3, Cité scientifique, 59655 Villeneuve d'Ascq Cedex, France*
[e] *Science et Ingénierie des Matériaux et Procédés, CNRS-INP Grenoble-UJF, 1130 Rue de la Piscine, BP75, 38402 St. Martin d'Heres Cedex, France*

Available online 10 May 2007

Abstract

The influence of deposition conditions (pressure, growth rate, solution concentration, etc.) on the growth of ferroelectric $PbTiO_3$ films by pulsed liquid injection MOCVD was examined. $Pb(thd)_2$ and $Ti(O^iPr)_2(thd)_2$ (thd=2,2,6,6-tetramethyl-3,5-heptanedionate) dissolved in toluene were used as precursors. Films were grown on $LaAlO_3$ (001) substrates for deposition process optimisation. $PbTiO_3/La_{1-x}Sr_xMnO_3/LaAlO_3$ heterostructures were elaborated at optimized deposition conditions. The microstructure of the heterostructures was characterized by X-ray Diffraction and by Raman spectroscopy. $Pt/PbTiO_3/La_{1-x}Sr_xMnO_3/LaAlO_3$ structures were used for ferroelectric, dielectric and piezoelectric characterisations of $PbTiO_3$ films.

© 2007 Elsevier B.V. All rights reserved.

Keywords: MOCVD; $PbTiO_3$ films; Ferroelectric and piezoelectric properties

1. Introduction

Ferroelectric $PbTiO_3$ (PTO) and $PbTi_{1-x}Zr_xO_3$ (PZT) thin films are extensively studied since their properties offer a great promise for various applications [1]. High-quality epitaxial ferroelectric films are needed in prospect of new devices; moreover, ferroelectrics can be combined with other functional oxides, such as high temperature superconductors and magnetic oxides. Heterostructures of ferroelectrics with manganites ($La_{1-x}Sr(Ca)_xMnO_3$) exhibiting colossal magnetoresistance are of interest due to the possibility of achieving electric-field-tuned metal-insulator phase transitions, an idea that is being explored for applications based on oxide channel field-effect transistors operating at room temperature [2]. For some applications, epitaxial ferroelectric films must be grown on electrode/substrate. Stresses in such lattice mismatched heterostructures significantly influence both the structural and electrical properties of the films [3]; therefore residual stresses should be evaluated in addition to electrical measurements.

Epitaxial PTO films have been grown by metalorganic chemical vapour deposition (MOCVD) [4,5], pulsed laser deposition [6] and rf-magnetron sputtering [7]. Among various deposition methods, MOCVD has been recognized as the most promising technique due to simple apparatus, excellent film uniformity, good control of composition and possibility to grow films on large area with high growth rate and good conformal step coverage. Most of PTO film studies are related to structural properties; some papers deal with ferroelectric and dielectric properties [8–12] and a few ones about piezoelectric properties are available [11,12].

In the present paper, we report on the role of system pressure, solution concentration and injection frequency on the growth rate and composition of $PbTiO_3$ films grown by pulsed liquid injection MOCVD. Further, the $Pt/PbTiO_3/La_{1-x}Sr_xMnO_3/LaAlO_3$ (Pt/PTO/LSMO/LAO) heterostructures were grown and their microstructure, morphology and electrical properties were studied and discussed.

---

* Corresponding author. LMGP, INP Grenoble-Minatec, 3, parvis Louis Néel, BP 257, 38016 Grenoble Cedex 1, France. Tel.: +33 4 56 52 93 00; fax: +33 4 56 52 93 01.
E-mail address: Ausrine.Bartasyte@gmail.com (A. Bartasyte).

0257-8972/$ - see front matter © 2007 Elsevier B.V. All rights reserved.
doi:10.1016/j.surfcoat.2007.05.006

2. Experimental details

Film depositions were carried out in a vertical hot wall pulsed injection MOCVD reactor. This technique is largely described elsewhere [13]. A computer controlled injector repeatedly injects microdroplets of organic solution containing a mixture of metalorganic precursors into a hot evaporation zone. After flash evaporation of microdroplet, resulting vapour is carried to a deposition zone by an Ar+O_2 gas flow. Deposition conditions of PTO and LSMO films are summarized in Table 1. More details and discussions on the influence of solution composition, deposition temperature, oxygen partial pressure and film annealing in different atmospheres on PTO film properties can be found in previous paper [14]. Details about deposition, structural and physical properties of LSMO films are given in Ref. [15].

Film composition was determined by wavelength dispersion spectroscopy (WDS) using Cameca S×-50. The film texture and microstructure were studied by XRD using a SIEMENS D5000 4-circle diffractometer with monochromatic CuKα radiation (λ=0.15418 nm). Analysis of the microstructure was carried out through standard ω-, χ-, φ-scans. More details concerning this analysis can be found in Ref. [14]. Percentage of a-axis oriented domains in the films was calculated by peak integration of (102) reflection in φ-scans measured at different χ angles, corresponding to *a*- and *c*-axis oriented crystallites (i.e. *a*- and *c*-domains respectively) [14]. The c-parameter of PTO c-domains was calculated from the position of three (00*l*) peaks in $\theta/2\theta$ scans. 3D mapping of the reciprocal space was performed with an automatic Nonius Kappa CCD diffractometer (Mo Kα radiation λ=0.7071 Å). Film morphology was examined by atomic force microscopy (AFM) using a Digital Instruments Multimode Scanning Probe Microscope, in the taping mode. Thickness of films was determined from cross-section images obtained by SEM Philips XL30.

Table 1
Deposition conditions for $PbTiO_3$ and $La_{1-x}Sr_xMnO_3$ layers by PI MOCVD

	$PbTiO_3$	$La_{1-x}Sr_xMnO_3$
Substrates	$LaAlO_3$ (001 — in a pseudo-cubic setting)	$LaAlO_3$ (001 — in a pseudo-cubic setting)
Substrate temperature, °C	600 or 650	800
Evaporation temperature, °C	280	310
Transport gas	Ar+O_2	Ar+O_2
Total gas flow rate, l/h	60	95
Oxygen fraction, %	37.7	35
Total pressure, Torr	2–10	5
Precursors *	$Pb(thd)_2$, $Ti(thd)_2(O^iPr)_2$	$La(thd)_3$, $Mn(thd)_3$, $Sr(thd)_2$
Solvent	Toluene	Monoglyme
Solution concentration (total), mol/l	0.02–0.08	0.049; with proportion of the precursors: $Sr(thd)_2$:$La(thd)_3$:$Mn(thd)_3$=1:1.5:1.58
Injection frequency, Hz	1 or 2	2
Thickness, nm	200–340	200

* All the precursors were synthesized in Vilnius University.

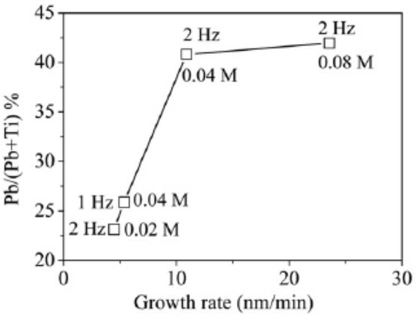

Fig. 1. PTO/LAO film composition evolution as a function of growth rate.

Raman spectra were collected using Jobin Yvon/Horiba Labram spectrometer equipped with liquid nitrogen cooled CCD detector. Experiments were conducted in the micro-Raman mode at room temperature, in a backscattering geometry. The Raman spectra were recorded from the film surface. The 514.5 nm line of an Ar^+ laser was focused to a spot size smaller than 1 μm. Spectra from different experiments were calibrated using Si spectra at ambient temperature.

To characterise the ferroelectric properties of PTO films from an electrical point of view, 235×235 μm^2 square capacitors were designed by UV photolithography using a metallic shadow, and then top contacts were patterned by lift off. Ferroelectric hysteresis loops were observed using a Sawyer–Tower circuit driven at 50 kHz by a sine wave. Capacitance–voltage (*C*–*V*) curves and dielectric constants ε_r were determined from small signal capacitance measurements performed at 50 kHz with a HP Agilent LCZ meter. Piezoelectric coefficients d_{33} were measured by laser Doppler vibrometry using a Polytec OFV512 as described in Ref. [16].

3. Results

3.1. *Effects of film growth rate*

As shown in our previous paper [14], Pb fraction in the film grown at higher temperatures (≥600 °C) increases until near stoichiometric value and after remains almost stable with further increase of the Pb content in the solution; thus, Pb excess cannot be reached in the film. In order to observe the maximum Pb/Ti ratio in the film which can be reached by varying the growth rate, lead deficient films were studied. Series of PTO films were deposited at 600 °C by varying the total solution concentration (0.02 M, 0.04 M or 0.08 M) and injection frequency (1 Hz or 2 Hz) while the precursors' ratio in solution (Pb/(Pb+Ti)=28.1%) and other deposition conditions were kept constant as given in Table 1. The variation of film composition with growth rate is shown in Fig. 1. Pb content in the film increases with increasing growth rate from 4.9 to 10.9 nm/min and saturates when

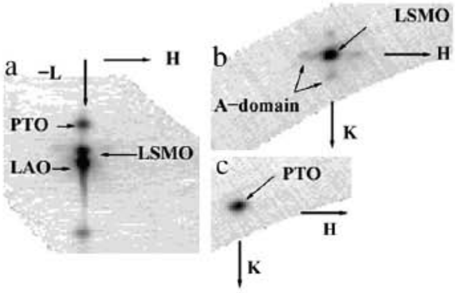

Fig. 2. 2D sections of the reciprocal space of a PTO/LSMO/LAO structure: (a) $k=0$ plane; (b) $l=-3.9$ plane; (c) $l=-3.7$ plane.

sufficiently high growth rates (>10.9 nm/min) are reached. Deposition with low growth rate results in high Pb desorption from the film. For high growth rates, Pb loss highly decreases and film composition becomes defined mainly by Pb/Ti ratio in solution and precursors' decomposition rates at deposition temperature. In order to obtain Pb/Ti = 1 in the films grown with rates >10.9 nm/min, Pb/(Pb + Ti) ratio in the precursor solution should be increased from 28.1% to 31.3% or more. The 0.04 M total concentration and 2 Hz injection frequency were chosen as optimal conditions for further deposition investigation.

3.2. Effects of deposition pressure

In order to test the influence of deposition pressure on PTO film growth, films were grown at 650 °C at three different pressures (2, 5 and 10 Torr). The surface of layers deposited at 2 Torr of pressure was completely covered by spherical particles, probably due to precursor decomposition in the reactor volume, thus this pressure was discarded from further investigation. Stoichiometric film was reached using 0.020 M and 0.023 M Pb$(thd)_2$ concentrations (at 0.04 M total concentration of solution) for depositions carried at 5 Torr and 10 Torr pressure, respectively. The growth rates of stoichiometric PTO films at 5 Torr and 10 Torr were 20.6 nm/min and 18.8 nm/min, respectively. P. Lu et al. also reported a growth rate decrease of PZT films with increasing pressure [17]. As lower growth rate enhances Pb desorption, higher concentration of lead precursor was needed to obtain stoichiometric PTO at higher pressures.

The results of our present and previous studies on PTO deposition suggest the possibility to control accurately the film growth rate and film composition is important for reproducing stoichiometric PTO films. Therefore, PI MOCVD is a promising method as it offers an easy control of precursor feeding rate, vapour and film composition.

3.3. PTO/LSMO/LAO heterostructures

PTO/LSMO heterostructures consisting of stoichiometric 300 nm thick PTO film and 200 nm LSMO film were grown on LAO at 650 °C and 5 Torr using optimal conditions described above and given in Table 1. The microstructure, surface roughness, residual stresses and electrical properties of the PTO/LSMO/LAO heterostructure are presented and discussed below.

3.3.1. Microstructure and surface roughness

XRD 2D reciprocal space mapping of this heterostructure (Fig. 2a) shows successive epitaxial growth of probably rhombohedral LSMO and tetragonal PTO on LAO substrate along the [00l] direction (referred to pseudo-cubic settings for LSMO). More precise investigations are needed to confirm rhombohedral LSMO structure. Weak reflections in Fig. 2b indicate the presence of PTO crystallites with *a*-axis oriented almost perpendicular to the substrate plane (a-domains). The c-parameter (4.111 ± 0.005 Å) of c-domains was reduced compared to the bulk value (4.1532 Å), indicating that PTO film is under tensile stress in-plane. As it is known, the a- and c-domains are bounded by the (101) twin plane and this results in a tilt of domains by angle from the substrate plane normal depending on the cell tetragonality and domains fraction [18]. The split into four peaks (Fig. 2b) confirms the existence of twinning resulting in the tilt of a-domains by ~2° angle with respect to the substrate plane. No split was observed for the central reflection in Fig. 2c corresponding to c-domains of PTO. The volume fraction of a-domains in PTO film was 13.7%. FWHM of PTO and LSMO rocking curves were 0.64° and 0.22° respectively, indicating a good texture of the heterostructure. Heterostructure had good in-plane orientation, as FWHM of PTO and LSMO φ-scans were 1.7° and 1° respectively.

Film surface roughness was evaluated by AFM. Higher roughness of PTO films in heterostructure (Ra = 4.3 nm), in comparison with PTO films on LAO (Ra = 0.96 nm), may result from LSMO film roughness (Ra = 2.6 nm). Roughness values are comparable to reported ones for similar heterostructures grown by pulsed laser deposition [19].

3.3.2. Residual stresses

Polarized Raman spectra of PTO/LSMO/LAO heterostructure measured in crossed polarization configuration (VH) confirmed the presence of pure tetragonal PTO phase (Fig. 3), as only *E*(TO) modes are observed [20]. PTO *E*(1TO) soft mode is very pressure sensitive and, as a consequence, its

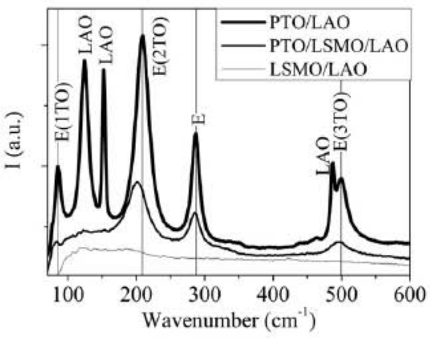

Fig. 3. Polarized Raman spectra of PTO/LAO, PTO/LSMO/LAO and LSMO/LAO films measured in VH polarization configuration.

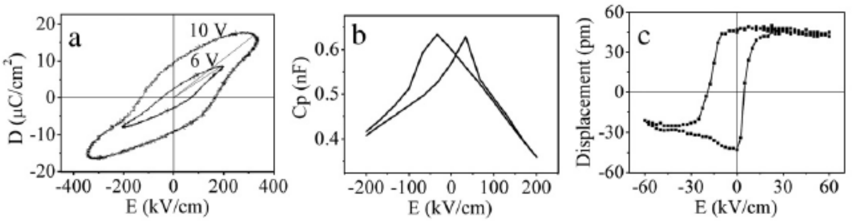

Fig. 4. Electrical characterizations of PTO/LSMO/LAO films: (a) polarization hysteresis loop; (b) capacitance–electric-field curve; (c) piezoelectric displacement versus E_{dc} loop.

wavenumber shifts as a function of increasing pressure according to the following relation:

$$\omega[E(1TO)] = \omega_0 + (\partial\omega/\partial P)P \qquad (1)$$

where $\omega_0 = 89$ cm^{-1} is the soft mode wavenumber at zero pressure and room temperature, and $\partial\omega/\partial P = -5.8$ cm^{-1} GPa^{-1} is the pressure coefficient [21,22]. The shift value is used to evaluate the residual stress σ in PTO films. PTO E(1TO) mode was observed at 81 cm^{-1} for PTO/LSMO/LAO and at 86.6 cm^{-1} for PTO/LAO. These values, as well as all other E (TO) mode wavenumbers are quite below those observed in single crystal (89 cm^{-1} for E(1TO)). This gives evidence that PTO films on LSMO/LAO and on LAO are under tensile stress in-plane in agreement with XRD results. Corresponding stress values calculated from Eq. (1) are closed to 1.38 and 0.41 GPa in PTO/LSMO/LAO and PTO/LAO, respectively. Despite bigger misfit strain in PTO/LAO system, PTO films on LSMO/LAO were more stressed than PTO/LAO films probably due to distortion induced by rhombohedral structure of LSMO.

3.3.3. Electrical properties

Ferroelectric properties of PTO films on LSMO/LAO were characterized by measuring polarization hysteresis (Fig. 4a). The films displayed hysteresis loops typical of ferroelectric materials for an applied voltage of 6 V. Remanent polarization and average coercive field values were 2.4 μC/cm^2 and 65 kV/cm, respectively. Quite low remanent polarization values comparing to reported ones [8,9,11] can be due to incomplete reversal of the switching domains [11]. However, increasing the applied voltage up to 10 V led to inflating loops typical of non linear lossy dielectrics [23]. The saturation of polarization was not achievable and it was indeed difficult to reach the coercive field due to the leakage currents. The coercive fields are expected to be rather high (>100 kV/cm) due to the strain in the film resulting from epitaxial growth. This fact combined with the leakage current made difficult to observe large polarization in the range of applied voltage. Deposition of stoichiometric PTO films on LSMO/LAO at 10 Torr resulted in films characterized by elliptical hysteresis loops, which is characteristic of excessive leakage currents in the film [24]. Hence, leakage current can be reduced by decreasing lead desorption and then probably the resulting defects.

PTO film deposited at lower pressure displayed capacitance–electric-field curve (Fig. 4b) typical of ferroelectric materials. The dielectric constant of this film reached 325, which is higher than reported values for bulk materials (210 perpendicular to and 120 along polarization direction [25,26]) and than values published by many authors for PTO films [8–10]. However, Kighelman et al. measured dielectric constant higher than 300 [11]. Higher dielectric constant in our films in comparison with bulk value may be consistent with an increased number of domain walls and with film stresses. Raman spectroscopy results confirmed that PTO films on LSMO/LAO are under tensile stress in the plane parallel to the substrate, despite negative misfit stress. Unlike our results, Haeni et al. reported enhancement of dielectrical permittivity of SrTiO$_3$ films in case of positive misfit strain but information about stresses was not specified [27]. Dielectric losses (tgα = 0.02) obtained in our films were similar to the reported values.

Using the procedure described in Ref. [16] for an accurate measurement, a small top electrode and a clamped sample have been used to reduce the substrate bending and eliminate the resonant effects. We can illustrate the evolution of the piezoelectric properties of PTO thin films in Fig. 4c. The d_{33} versus E_{dc} loop, measured by laser Doppler vibrometry, was rectangular, with some asymmetry. The piezoelectric coefficient d_{33} measured in PTO films was around 50 pm/V ($V_{ac} = 1$ V, 48.5 kHz), which is comparable to values reported for PTO films [11] and even for Pb$_{1-x}$Ca$_x$TiO$_3$ or PZT films [28,29]. The asymmetry of piezoelectric and ferroelectric hysteresis and C–V loop resulted from the different nature of bottom (LSMO) and top (Pt) electrodes. In fact, the film properties are correlated to the film orientation and control of the film growth results in optimum piezoelectric activity.

4. Conclusions

The growth rate and composition of PTO films were studied as a function of deposition pressure, solution concentration and injection frequency. It was shown, that Pb desorption can be governed by changing film growth rate. Epitaxial PTO/LSMO/LAO were elaborated at optimized deposition conditions. PTO films in such heterostructure were under tensile stress in-plane; they showed piezoelectric activity and very good dielectric properties, but remanent polarization values were quite low.

Acknowledgements

This work was supported by the European Community in the framework of the NoE FAME (Functional Advanced Materials and Engineering of hybrids and ceramics).

References

[1] N. Setter, L. Eng, S. Gevorgian, S. Hong, A. Kingon, H. Kohlstedt, N.Y. Park, G.B. Stephenson, I. Stolitchnov, A.K. Tagantsev, D.V. Taylor, T. Yamada, S. Streiffer, J. Appl. Phys. 100 (2006) 051606.
[2] C.H. Ahn, J.-M. Triscone, J. Mannhart, Nature 424 (2003) 1015.
[3] S.B. Desu, Phys. Status Solidi, A Appl. Res. 141 (1994) 119.
[4] C. Schmidt, E.P. Burte, Microelectron. Reliab. 39 (1999) 257.
[5] H. Funakubo, K. Nagashima, K. Shinozaki, N. Mizutami, Thin Solid Films 368 (2000) 261.
[6] Y.K. Kim, S.S. Kim, H. Shin, S. Baik, Appl. Phys. Lett. 84 (25) (2004) 5085.
[7] K. Wasa, Y. Haneda, T. Sato, H. Adachi, K. Setsune, Vacuum 51 (4) (1998) 591.
[8] K. Nishida, T. Sugino, M. Osada, M. Kakihana, T. Katoda, Appl. Surf. Sci. 216 (2003) 312.
[9] D. Bao, X. Yao, N. Wakiya, K. Shinozaki, N. Mizutani, Mater. Sci. Eng., B, Solid-State Mater. Adv. Technol. 94 (2002) 269.
[10] H. Huang, X. Yao, X. Wu, M. Wang, L. Zhang, Microelectron. Eng. 66 (2003) 688.
[11] Z. Kighelman, D. Damjanovic, M. Cantoni, N. Setter, J. Appl. Phys. 91 (3) (2002) 1495.
[12] B. Jaber, D. Remiens, E. Cattan, P. Tronc, B. Thierry, Sens. Actuators, A, Phys. 63 (1997) 91.
[13] J.P. Senateur, C. Dubourdieu, V. Galindo, F. Weiss, A. Abrutis, Innovative processing of films and nanocrystalline powders, Imperial College Press, London, 2002.
[14] A. Bartasyte, A. Abrutis, C. Jimenez, F. Weiss, O. Chaix-Pluchery, Z. Saltyte, Ferroelectrics 353 (2007) 1.
[15] A. Abrutis, V. Plausinaitiene, V. Kubilius, A. Teiserskis, Z. Saltyte, R. Butkute, J.P. Senateur, Thin Solid Films 413 (1–2) (2002) 32.
[16] R. Herdier, D. Jenkins, E. Dogheche, D. Remiens, M. Sulc, Rev. Sci. Instrum. 77 (2006) 093905.
[17] P. Lu, H. Li, Y.-M. Wang, S. Sun, B. Tuttle, J. Cryst. Growth 181 (1997) 348.
[18] M. de Keijser, D.M. de Leeuw, P.J. van Veldhoven, A.E.M. De Veirman, D.G. Neerinck, G.J.M. Dormans, Thin Solid Films 368 (2000) 261.
[19] J. Yin, X.S. Gao, Z.G. Liu, Y.X. Zhang, X.Y. Liu, Appl. Surf. Sci. 141 (1999) 21.
[20] M.D. Fontana, H. Idrissi, G.E. Kugel, K. Wojcik, J. Phys:, Condens. Matter 3 (1991) 8695.
[21] J.A. Sanjurjo, E. Lopez-Cruz, G. Burns, Phys. Rev., B 28 (12) (1983) 7260.
[22] F. Cerdeira, W.B. Holzapfel, D. Bauerle, Phys. Rev., B 11 (3) (1975) 1188.
[23] M.E. Lines, A.M. Glass, Principles and Applications of Ferroelectrics and Related Materials, Oxford University Press, Oxford, 1977, p. 104, reprinted 1996.
[24] R. Bouregba, G. Poullain, Ferroelectrics 274 (2002) 165.
[25] Z. Li, M. Grimsditch, X. Xu, S.K. Chan, Ferroelectrics 141 (1993) 313.
[26] V.G. Gavrilyachenko, E.G. Fesenko, Sov. Phys. Crystallogr. 16 (1971) 549.
[27] J.H. Haeni, P. Irvin, W. Chang, R. Uecker, P. Reiche, Y.L. Li, S. Choudhury, W. Tian, M.E. Hawley, B. Craigo, A.K. Tagantsev, X.Q. Pan, S.K. Streiffer, L.Q. Chen, S.W. Kirchoefer, J. Levy, D.G. Schlom, Nature 430 (2004) 758.
[28] A. Kholkin, A. Seifert, A. Setter, Appl. Phys. Lett. 76 (2000) 1615.
[29] S. Hiboux, P. Muralt, T. Maeder, J. Mater. Res. 14 (1999) 4307.

List of publications

Invited article:

1. **A. Bartasyte,** O. Chaix-Pluchery, J. Kreisel, J. Santiso, M. Boudard, C. Jimenez, A. Abrutis, F. Weiss, Raman Spectroscopy and X-ray Diffraction Studies of Stress Effects in $PbTiO_3$ Thin Films, *IEEE TUFFC.*, Vol. 54, No. 12, pp. 2623-2631, Dec. 2007.

Articles in international journals:

2. A.Bartasyte, O. Chaix-Pluchery, J. Kreisel, M. Boudard, C. Jimenez, A. Abrutis, F. Weiss, Z. Saltyte, “Investigation of stress and relaxation mechanisms in $PbTiO_3$ thin films”, *J. Appl. Phys.,* Vol. 103, pp. 014103-11, Jan. 2008.

3. **A.Bartasyte**, R. Bouregba, E. Dogheche, M. Boudard, G. Poullain, O. Chaix-Pluchery, C. Jimenez, V. Plausinaitiene, D. Remiens, A. Abrutis, Z. Saltyte, F. Weiss, “Ferroelectric $PbTiO_3$ films grown by pulsed liquid injection MOCVD”, *Surf. Coat. Tech*., Vol. 201, pp. 9340-9344, May, 2007.

4. **A.Bartasyte**, A. Abrutis, C. Jimenez. F. Weiss. O. Chaix-Pluchery, Z. Saltyte, “Ferroelectric $PbTiO_3$ films grown by pulsed liquid injection metalorganic chemical vapour deposition”. *Ferroelectrics,* Vol. 353, No. 1, pp. 104-115, June, 2007.

5. S. Pasko, L. G. Hubert-Pfalzgraf, A. Abrutis, **A. Kizienė (**ex-family name), “Metal 2,7,7-trimethyl-3,5-octanedionates as new MOCVD precursors for oxide films”. *Electrochemical Society Proceedings*, Vol. 2005-09, pp. 921-927, September, 2005. The Electrochemical Society, Inc., Pennington, NJ, USA, ISBN 1-56677-427-6. Proc. of EUROCVD15 conf., Bochum, Germany, 5-11 September, 2005.

6. A.Abrutis, M. Lukosius, **A. Kiziene (**ex-family name), P.K. Baumann, M. Schumacher, J. Lindner, “MOCVD growth and properties of high-k dielectric praseodymium oxides layers on silicon”, *Electrochemical Society Proceedings*, Vol. 2005-09, pp. 936-943, September, 2005. The Electrochemical Society, Inc., Pennington, NJ, USA, ISBN 1-56677-427-6.

7. A.Abrutis, **A. Bartasyte**, A. Teiserskis, Z.Saltyte, P.K. Baumann, M. Schumacher, J. Lindner, T. McEntee, “Growth of Pr_2O_3 layers by pulsed injection MOCVD”, in *Integration of Advanced Micro- and Nanoelectronic Devices—Critical Issues and Solutions*, (Mater. Res. Soc. Symp. Proc. 811, Warrendale, PA, 2004), D9.9.

8. A.Abrutis, **A. Bartasyte**, Z. Saltyte, A. Zukova, S. Donet, F. Weiss, “Thick SmBCO layers and SmBCO/YBCO structures grown by pulsed injection MOCVD”, *Physica C*,Vol. 415, pp. 21-28, October, 2004.

9. A.Abrutis, L.G. Hubert-Pfalzgraf, S.V. Pasko, **A. Bartasyte**, F. Weiss, V. Janickis, “Hafnium oxoneopentoxide as a new MOCVD precursor for hafnium oxide films”, *J. Cryst. Growth*, Vol. 267, pp. 529-537, June, 2004.

10. S. V. Pasko, L.G. Hubert-Pfalzgraf, A. Abrutis, Ph. Richard, **A. Bartasyte**, V. Kazlauskiene, “New sterically hindered Hf, Zr and Y β-diketonates as MOCVD precursors for oxide films”, *J. Mater. Chem.*, Vol. 14, pp. 1245-1251, August, 2004.

11. A.Abrutis, **A. Bartasyte**, G. Garcia, A. Teiserskis, V. Kubilius, Z. Saltyte, V. Faucheux, A. Figueras, S. Rushworth, “Metal-organic chemical vapour deposition of mixed-conducting perovskite oxide layers on monocrystalline and porous ceramic substrates”, *Thin Solid Films*,Vol. 449, pp. 94-99, February, 2004.

12. J.J. Robles, **A.Bartasyte**, H.P. Ng, A. Abrutis, F. Weiss, “On the possibility of growing unidirectionally twinned $YBa_2Cu_3O_{7-\delta}$ thin films on $YAlO_3$”, *Physica C*, Vol. 400, pp. 36-42, December, 2003.

13. A.Abrutis, **A. Bartasyte**, V. Kubilius, A. Teiserskis, P. Baumann, J. Lindner, M. Schumacher, C. Dubourdieu, “Growth of Al_2O_3 films by pulsed injection MOCVD: comparative study of precursor materials”, *Electrochemical Society Proceedings*, Vol. 2003-8, pp. 771-776, 2003. The Electrochemical Society, INC, Pennington, USA.

14. A.Abrutis, V. Plausinaitiene, A. Teiserskis, Z. Saltyte, V. Kubilius, **A. Bartasyte**, J.P. Senateur, “$YBa_2Cu_3O_7$ and $La_{1-x}Sr_xMnO_3$ thin films grown by pulsed injection MOCVD”, *J. Phys IV France*, Vol. 11, pp. Pr11-215-219, December, 2001.

Résumé

Cette étude réalisée par Spectroscopie Raman, Diffraction de Rayons X et Microscopie Electronique en Transmission porte sur l'origine et l'effet des contraintes sur la transition de phase dans des couches épitaxiées de $PbTiO_3$ (PTO). Des films minces de PTO de différentes épaisseurs ont été déposés sur plusieurs substrats de façon à faire varier le désaccord de maille film-substrat pour générer des films sous contrainte de compression ($SrTiO_3$ et $LaAlO_3$) et sous tension (MgO).

Les contraintes résiduelles dans les films PTO ont été déterminées à partir des spectres Raman mesurés exclusivement en configuration de polarisation VH pour éliminer les modes obliques; le mode dur *E(3TO)* est apparu le seul mode fiable pour l'estimation des contraintes. Pour caractériser les domaines c qui sont prépondérants, les spectres ont dû être mesurés sur la tranche des films. Les contraintes résiduelles proviennent non seulement du désaccord de maille, mais aussi de contraintes thermiques ou liées à la transition de phase.

Les transitions de phase et les changements d'états de domaines dans les films ont été analysés par diffraction des RX et spectroscopie Raman à haute température. Il est apparu que la taille des clusters ferroélectriques à haute température est plus grande et Tc plus élevée dans les films très contraints.

Mots clés : Couches minces de $PbTiO_3$, MOCVD, contraintes, transitions de phase, structure de domaines

Abstract

Raman spectroscopy, X-ray diffraction (XRD) and Transmission Electron Microscopy were used to investigate the origin and stress effects on phase transitions in $PbTiO_3$ (PTO) epitaxial thin films. A thickness series of epitaxial PTO films were deposited on substrates inducing compressive ($SrTiO_3$ and $LaAlO_3$) and tensile (MgO) misfit stresses to vary the stress level in the films.

We showed that the VH polarization configuration is essential for Raman investigation of residual stress in PTO thin films as oblique modes are absent, and that *E(3TO)* hard mode is the unique reliable mode. In order to obtain information about the dominant *c*-domains, spectra must be collected on the film cross section. The residual stress originates not only from misfit stresses, but also from thermal and phase transformation stresses.

Phase transitions and domain state transformations were investigated using high temperature XRD and Raman spectroscopy. It was found that ferroelectric cluster size in high temperature phase is increased and T_c is higher in highly stressed films.

Keywords: $PbTiO_3$ thin films, MOCVD, stress, phase transition, domain structure